Modélisation multi-échelle d'écoulements sanguins et application à des pathologies congénitales du cœur

Grégory Arbia

Modélisation multi-échelle d'écoulements sanguins et application à des pathologies congénitales du coeur.

THÈSE DE DOCTORAT

Présentée par

Grégory ARBIA

pour obtenir le grade de

DOCTEUR DE
L'UNIVERSITÉ PIERRE ET MARIE CURIE - Paris VI

Spécialité : Mathématiques Appliquées

Soutenue publiquement le 16 décembre 2014 devant le jury composé de:

Pascal Frey	Examinateur
Jean-Frédéric Gerbeau	Directeur de thèse
Alain Kassab	Rapporteur
Bertrand Maury	Rapporteur
Anne-Virginie Salsac	Examinateur
Irène Vignon-Clémentel	Directrice de thèse

Après avis favorables des rapporteurs: Alain Kassab et Bertrand Maury

Thèse préparée au sein de l'équipe-projet REO
Laboratoire Jacques-Louis Lions
Université Pierre et Marie Curie - Paris 6
et **Centre de Recherche INRIA Paris-Rocquencourt**
Domaine de Voluceau, BP 105
78153 Le Chesnay CEDEX

The research leading to these results has received funding from the Leducq Transatlantic Network of Excellence Grant, Fondation Leducq, Paris, France.

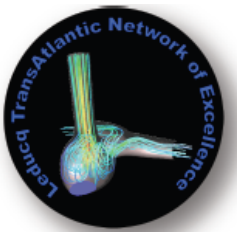

Modélisation multi-échelle d'écoulements sanguins et application à des pathologies congénitales du coeur.

Resumé: Dans cette thèse nous traitons de la simulation numérique des écoulements sanguins dans le contexte des maladies cardiaques congénitales. Nous nous concentrons d'une part sur l'intégration de données cliniques, et d'autre part sur les aspects de couplages multi-échelles. Dans l'introduction, nous présentons les pathologies structurelles du coeur et les traitements chirurgicaux nécessaires dans certaines cardiopathies sévères. Puis, nous consacrons un chapitre aux challenges liés à la simulation numérique des écoulements sanguins. Dans les deux chapitres suivants nous présentons une méthodologie permettant d'estimer des paramètres de modèles réduits modélisant l'arbre artériel pulmonaire, en y intégrant des mesures cliniques prises pour chaque patient à différents endroits avant intervention chirurgicale. Cette méthode est appliquée sur neuf patients et permet de représenter l'hémodynamique dans les artères pulmonaires pour chacun des patients. Le chapitre suivant est consacré au couplage des équations de Navier-Stokes 3D avec un modèle réduit, qui soulève des problèmes d'instabilités numériques dans nombre d'applications. Nous présentons d'abord un état de l'art des couplages 3D-0D communément utilisés pour ce type de problème. Nous présentons de plus une étude de stabilité pour montrer quels sont les avantages et inconvénients de chacun d'eux. Ensuite, nous présentons une nouvelle méthode de couplage 3D-3D qui est similaire, d'un point de vue énergétique, au couplage avec un modèle réduit. Nous comparons enfin les méthodes existantes à ce couplage 3D-3D sur trois cas de patients, côtés systémique et pulmonaire. Dans le dernier chapitre de cette thèse, nous nous intéressons à la propagation des incertitudes des données cliniques sur la simulation de l'hémodynamique dans le cadre de chirurgie virtuelle.

Mots-clés: modélisation multi-échelle, modèles réduits, couplage Navier-Stokes 3D-modèle réduit, cardiopathies congénitales, planification de chirurgies, propagation d'incertitude.

Multiscale modeling of blood flow in the context of congenital heart disease.

Abstract: In this thesis, we deal with numerical simulation of blood flow in the context of congenital heart diseases. We focus on clinical data integration into reduced models, and from a numerical point view on the coupling of blood flow (3D Navier-Stokes equations) and reduced models. In the introduction, we present congenital heart diseases and the surgical palliations needed for severe pathologies. We then present a chapter on challenges in numerical simulations of blood flow. In the next chapters, we present a methodology to estimate parameters of reduced models taking into account the effect of the pulmonary vasculature and the clinical measurements performed at different locations prior to surgical intervention of each patient. This method is applied to nine patient-specific cases and provides a representation of the hemodynamics in pulmonary arteries at different palliation stages. The next part of this thesis is devoted to numerical coupling between 3D blood flow and reduced models, which leads to numerical instability in a number of applications. We first present the state of the art for the different coupling methods, and perform a stability analysis of each coupling approach, highlighting the pros and cons. Moreover we present the new 3D-3D coupling method which presents the same energy balance as the 3D-reduced model. We compare all these methods on three systemic or pulmonary patient-specific cases to assess the robustness and accuracy of each one. In the last part of this manuscript we present a framework to investigate the effect of uncertainty of clinical measurements on our methodology to estimate reduced models for surgery planning: we focus on the impact of clinical data uncertainty to estimate blood flow distribution and pressure loss due to a stenosis to assess if it should be removed or not.

Keywords: multiscale modeling, reduced models, 3D Navier-Stokes-reduced model coupling, congenital heart diseases, surgery planning, uncertainty propagation.

Contents

Introduction

Chapter 1

Introduction

In this chapter, we introduce the motivations and main aims of this thesis. We first describe congenital heart diseases and the three palliative procedures (Norwood, Glenn or Hemi-Fontan, and Fontan). We then present numerical challenges and modeling potential difficulties of this thesis. Finally, we present the way of working within the MOdeling of Congenital Heart Alliance group and collaborative aspects of this thesis.

Contents

1.1 Motivations of this thesis

1.1.1 Healthy heart

A healthy heart is pump made of tissue, divided in two separated parts containing each an atrium and a ventricle (see Figure 1.1). Left and right atrium are separated by atrial septum, while left and right ventricle are separated by ventricular septum. Blood poor in oxygen (colored in blue in Figure 1.1) comes from upper and lower body through the superior and inferior vena cava respectively. It enters into the right heart (left in Figure 1.1) by crossing right atrium and right ventricle. It then goes towards the lungs through the pulmonary artery to be oxygenated (and discharge carbon dioxide), and comes back to the left heart (right side on Figure 1.1) through

left atrium and left ventricle. Finally, blood full of oxygen (colored in red in Figure 1.1) is carried towards the organs through the aorta.

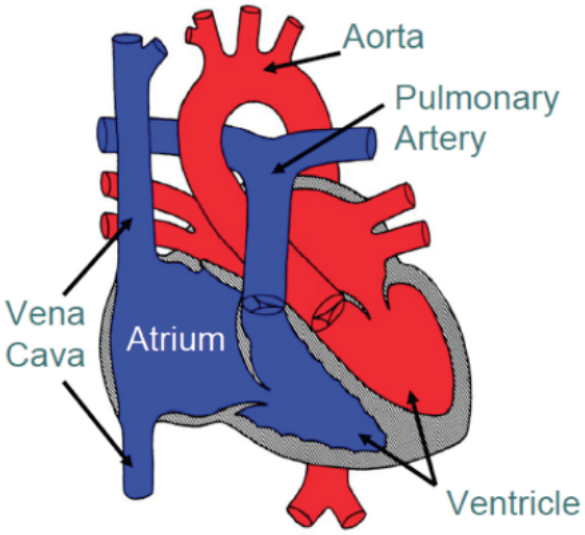

Figure 1.1: Healthy heart.

The healthy heart thus contains four chambers and four valves separating atrium and ventricle or ventricle and artery. Each valve has a set of leaflets that let or not pass the blood during cardiac cycle. The valve between right atrium and right ventricle is the tricuspid valve, while the valve between right ventricle and pulmonary artery is the pulmonary valve. The valve separating left atrium and left ventricle is the mitral valve, and the valve between left ventricle and aorta is the aortic valve.

1.1.2 Congenital heart diseases

Congenital heart defects (CHD) are structural problems with the heart present at birth. The most commonly reported incidence of congenital heart defects is around 8 per 1000, 7 per 1000 and 9 per 1000 respectively in the United States, in Europe and in Asia (American Heart Association). Congenital cardiovascular defects are the most common cause of infant death resulting from birth defects.

In Figure 1.2, we present possible common defects. In fact, defects can be holes between chambers of the heart (upper left in Figure 1.2). In this

configuration, blood from right ventricle poor in oxygen is mixing with blood from left ventricle rich in oxygen because of a hole in ventricular septal defect. This defect involves transport of non totally oxygenated blood towards the organs. Moreover, another possible defect is a significant narrowing in main vessels (center right in Figure 1.2). Such a blockage causes high heart pressure and possible heart failure. Finally, a severe defect is the non development of one of the chambers that induces breathing and feeding insufficiency. This heart defect is usually fatal within the first days of life without treatment.

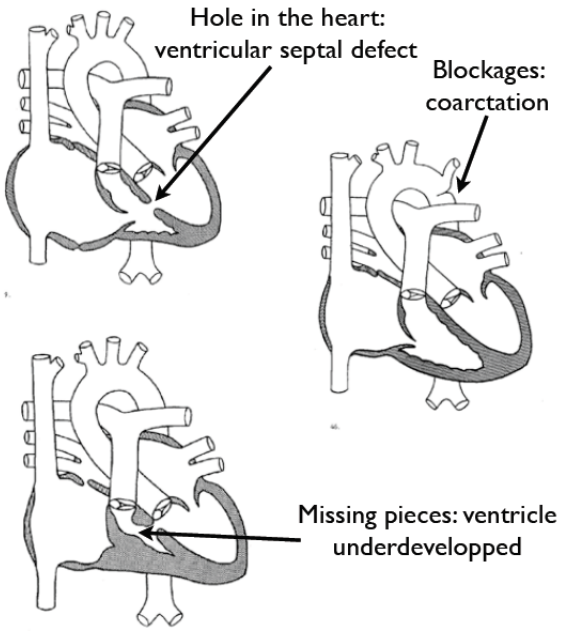

Figure 1.2: Possible defects in congenital heart diseases.

For example, the Tetralogy of Fallot is cumulated four defects in the structure of the heart: 1) pulmonary stenosis which is an underdevelopment of the pulmonary valve and a narrowing of the main pulmonary artery, 2) ventricular septal defect which is a hole between the two ventricles, 3) right ventricular hypertrophy, and 4) overriding aorta where aortic valve and entrance of aorta are between the two ventricles.

1.1.3 Treatment for congenital heart defects

Babies born with congenital heart defects do not necessary require treatment and some of them need to be observed. But for the most severe pathologies, several structural defects in the heart are accumulated and surgery is

warranted to repair the defects and increase life expectancy. In this thesis, we concentrate mainly on single ventricle physiology, in which there is only one ventricle that can effectively pump, either because of a heart valve defect, a ventricle not being able to pump well or other complex CHD for which bi-ventricular repair is not possible. The patient receive usually three palliative surgeries during childhood (from birth to three or five years old).

The first surgery is the stage 1 procedure and must be performed soon after birth. One of them is the Norwood procedure. This procedure was firstly described in 1981 by W.I. Norwood [NLCC81] (left in Figure 1.3). The main pulmonary artery is separated from the left and right portions of the pulmonary artery and joined with the upper portion of the aorta. Widening of the pulmonary artery is often necessary. This allows the blood, a mixture of oxygenated and non oxygenated, to be pumped to the body. Since the remainder of the pulmonary artery is now disconnected from the heart, a second step must be performed to supply blood to the lungs using usually a Gore-Tex conduit to connect the subclavian artery to the pulmonary artery. In this case, blood comes from the heart, through the pulmonary valve, the reconstructed aorta, the subclavian artery, and the conduit, to the lungs. There are variations on this procedure where the origin of the shunt is elsewhere in the systemic circulation (e.g. from the aorta itself) rather than the subclavian artery.

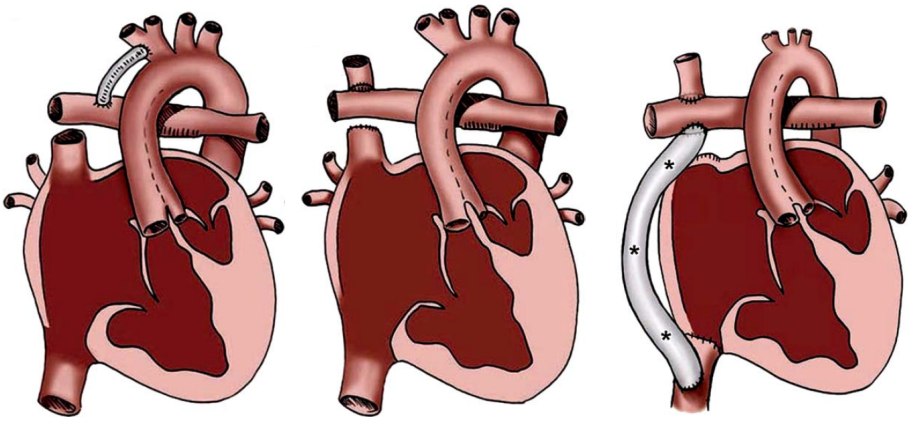

Figure 1.3: Scheme of the Norwood procedure. Illustration by Anne Phillips, University of Michigan Health System, Department of Radiology Media Services [DDA+10].

The second surgery is a cavo-pulmonary connection and is usually per-

formed between 4 and 12 months. It is an open heart procedure usually using the heart lung bypass machine. After removing the artificial shunt included during the first surgery, non oxygenated blood is carried from the upper body to the lungs, through the right pulmonary artery (center in Figure 1.3). After this procedure, the blood coming from upper body is going straight to the lungs for oxygenation without going through the heart. This increases the blood flow to the lungs and decreases the work of the heart.

The last surgery is a total cavo pulmonary connection, called Fontan procedure. This is usually the last palliative surgery and is undertaken between three and five years old. This procedure consists of linking non oxygenated blood returning from the lower part of the body directly to the pulmonary artery without passing through the heart (right in Figure 1.3). This surgery separate pulmonary and systemic parts. By this way, the heart is pumping oxygenated blood coming from the lungs and leads it towards the organs of the upper and lower body.

1.1.4 Challenges and aim of this thesis

For each procedure there are different ways to connect arteries and artificial grafts or to reconstruct tissues. Therefore, modeling of blood flow becomes a tool for understanding the single ventricle physiology at each repair stage, or to simulate different surgical options. The magnetic resonance imaging can give a three-dimensional geometry and flow measurements. Moreover, using a catheter, blood pressure measurements are performed. Then the main challenges of this thesis are 1) to simulate blood flow in the discretized geometrical model, and 2) to model the effect of the downstream vasculature that reflect clinical hemodynamics measurements. To this end a coupling between the partial differential equations of Navier-Stokes equations and ordinary differential equation is performed at each outlet of three dimensional domain. Issues of this thesis are thus numerical and clinical. On the one hand it is necessary to deal with problems related to coupling instabilities, and on the other hand clinicians want a reliable representation of the flow of blood in the area of interest.

1.2 Thesis context

1.2.1 Collaborative project

Modeling Of Congenital Heart Alliance (http://modelingventricle.clemson.edu/) is a transatlantic network involving clinical and academic partners from US, UK, Italy and France working on: 1) developing computational tools for multi scale simulations, and 2) gathering and use patient-specific data with the goal of better understand congenital heart disease and help surgeons for surgery planning. Key aspects of the MOCHA project are the incorporation of clinical measurements for 3D simulations of blood flow, virtual surgery planning and robustness of the modeling, which includes measurement uncertainty quantification and validation.

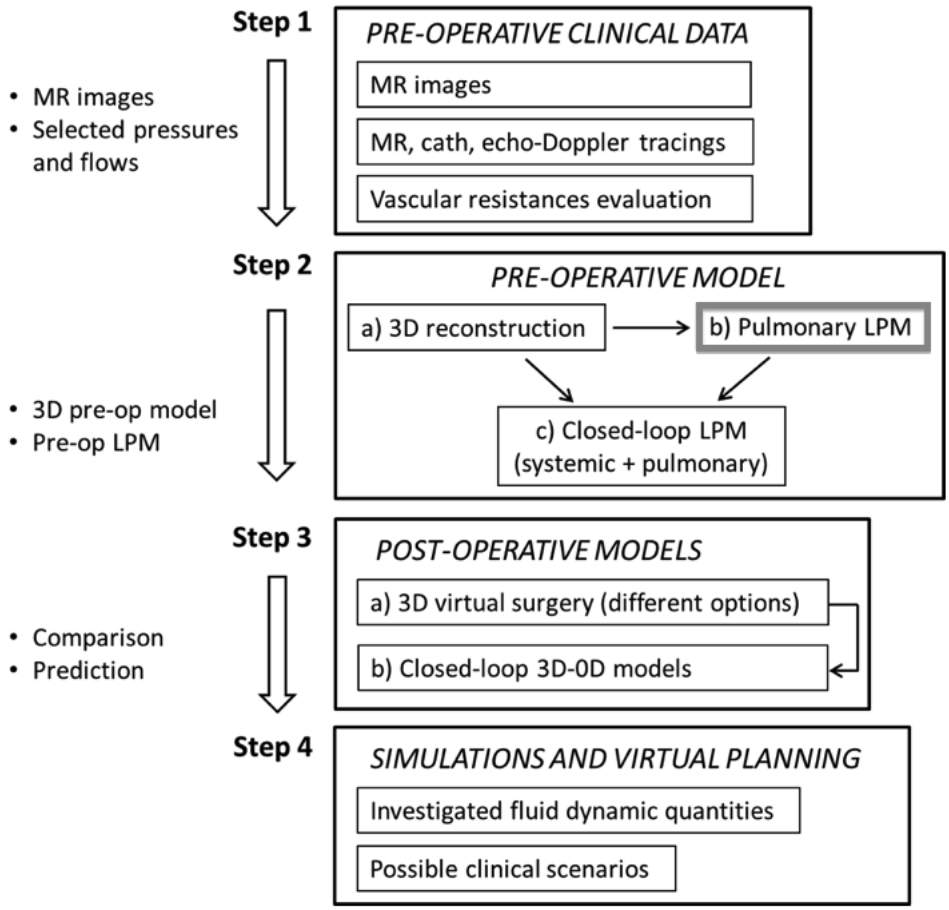

Figure 1.4: Workflow in the Leducq collaboration.

For each selected patient, we follow the same way of working in order to prepare palliative surgery (see Figure 1.4). The first step is realized in hospitals in charge of treatments for the selected patients. These hospitals are at University of Michigan (Ann Arbor, MI, USA), at the Medical University of South Carolina (Charleston, SC, USA), and at the Great Ormond Street Hospital (London, UK). It consists of measurements of pre-operative clinical data: images for defining three dimensional geometrical models, selected pressures and flow rates. The second step is divided in three parts: 1) Geometrical models are built from images at the University College of London (London, UK). 2) From this geometry adding the clinical measurements, a three dimensional representation of hemodynamics in pulmonary arteries is computed taking into account the effect the arterial and venous trees between pulmonary arteries and left atrium of the heart. This latter is realized at INRIA Paris-Rocquencourt (France) and leads to estimate parameters of reduced models. 3) The reduced model is sent to a team from Politecnico di Milano (Italy) to simulate the whole circulatory system with an electric analog of the hemodynamics, called a 0D model, lumped parameter model or also reduced model (see Figure 1.5). The third step is the virtual surgery planning. Indeed, several possible surgical configurations of virtual post-operative surgery are built and numerical simulations of blood flow in these geometries are performed taking into account model of the whole circulatory system generated previously. This last step is realized at University of California of San Diego (CA, USA) and leads to the step 4) that helps clinicians to better understand each option and in a longer term take a decision for the best procedure to be done for each patient.

The INRIA's REO team was in charge of preoperative multiscale modeling of blood flow in pulmonary arteries coherent with clinical measurements (flow and pressure data). The main goals of this thesis are thus 1) the development of numerical tools for coupling 3D incompressible Navier-Stokes equations to reduced models, and 2) calibration of resistances and capacitances to model the effects of the vasculature.

Various meetings took place with several partners in order to, firstly, define the concrete clinical questions, and secondly, to setup the different technical developments and to exchange the clinical data. In particular, as shown in Chapters 3 and 4 and in Appendix, this fruitful collaboration allowed to validate and apply the methodologies presented throughout the manuscript.

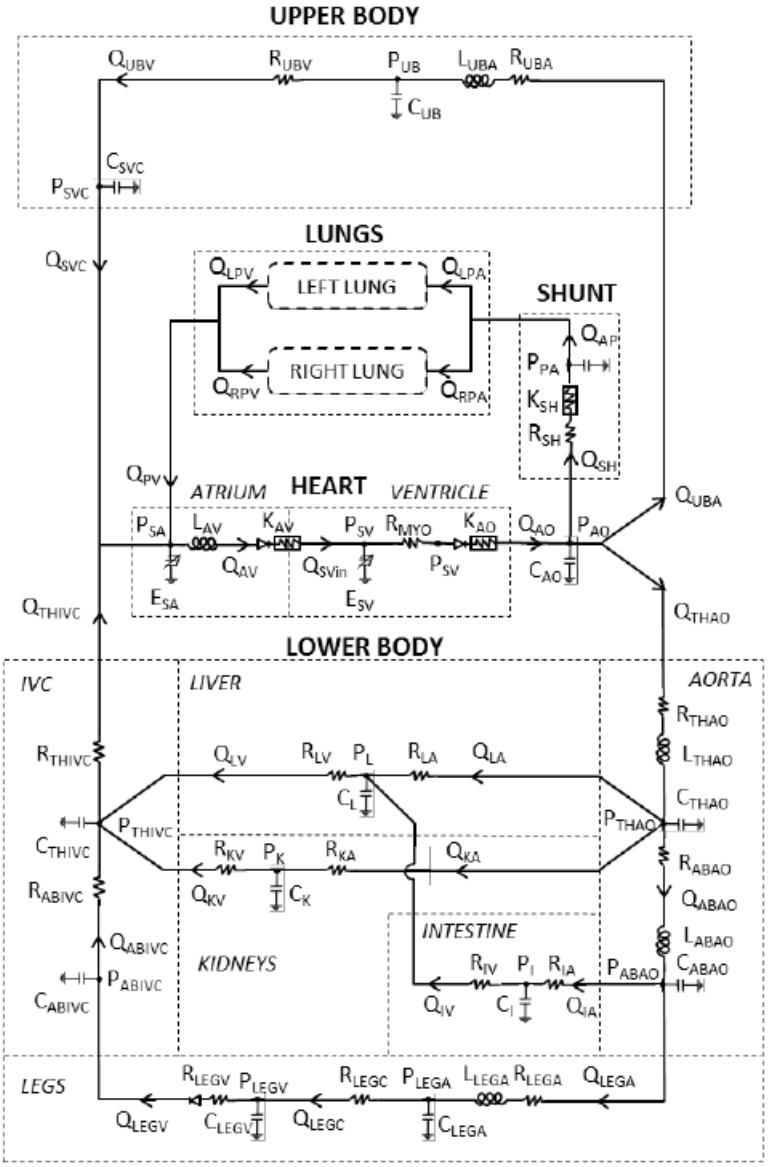

Figure 1.5: Reduced model of the whole circulatory system, where left and right lungs (upper part) are reduced models generated at INRIA, during numerical simulation of blood flow into pre-operative geometrical model.

1.2.2 Software

As mentioned at the beginning of each Chapter, the different parts of this work were the result of an active collaboration. In particular, the following softwares were used in this thesis:

- The Navier-Stokes solver PHASTA, within the open source software package Simvascular (http://www.simtk.org).
- The Navier-Stokes solver FELiScE, developed by the M3DISIM and REO teams implemented in C++.
- Tuning of parameters of reduced models from clinical measurements was performed by self-implemented Python routines.
- Mesh processing and editing were done using the software 3-matic (Materialise, Leuven, Belgium), Gmsh [GR09] and in-house Matlab routines.
- Postprocessing was done using Ensight (CEI Software) and Paraview (Sandia National Laboratory, Kitware Inc, Los Alamos National Laboratory).

Pursuing a close collaboration between the REO members, a contribution of this work has been in developing new capabilities within FELiScE code (mainly the new coupling method presented in Chapter 5).

1.3 Outline of the thesis

In chapter 2, we present underlying challenges in three-dimensional simulations of blood flow taking into account mesh generation from images, numerical solver, and boundary conditions. We compare simulation results obtained by the in-house code PHASTA and the commercial software ANSYS Fluent. We present results for a Poiseuille flow in a cyclinder, a cavopulmonary patient-specific anastomosis, and a patient-specific central shunt multibranch model with reduced model coupled at outlets.

In chapters 3 & 4 there are two aims: 1) derive and parameterize 0D models (boundary conditions of the 3D model) in order to reflect the effect of the pulmonary vascular tree according to clinical measurements that are not taken at boundaries of the 3D domain, and 2) provide to clinicians a three-dimensional qualitative representation of hemodynamics in patient-specific stage 1 (Norwood or other surgical options) and stage 2 (Glenn or Hemi-Fontan) patient-specific models. We iteratively tune a 0D

model for each outlet in agreement with clinical measurements by coupling three-dimensional Navier-Stokes equations to a set of resistances. We then use a morphometric model and empirical laws to transform this set of resistances to a set of 3 or 5-element 0D model parameters. The framework is general enough to accomodate different types of measurements, that are in general not taken where boundary conditions need to be specified, and be done under steady or pulsatile conditions. Furthermore, the presence of collateral vessels is included in the distal reduced model if necessary. This methodology is successfully applied to six patient-specific stage 1 cases and 3 patient-specific stage 2 cases. We show how this process also helps to check the coherence of the clinical measurements and give additional insights to clinicians that are not easy to measure, such as kinks effects.

In chapter 5, we propose to treat the outflow boundary conditions by coupling the 3D Navier-Stokes equations with another 3D compartment as a new method to palliate numerical instabilities. Indeed, the latter arise often when complex swirling flow or flow reversal occur at the 3D domain extremities, as is typical of stage 1 simulations or other cardiovascular patient-specific CFD. This artificial compartment involves modified Navier-Stokes equations that mimic a three-element 0D (Windkessel) model. The advantages of such approach are that the coupling does not enforce the traction at the interface to be uniform, and is energetically close to the usual 3D Navier-Stokes - Windkessel model, without the potentially destabilizing convective boundary term that emerge from an energy analysis. Numerical tests are presented to compare existing methods to this new approach in patient-specific geometries of various pathophysiological complexities.

In chapter 6, we present a method to determine the impact of uncertainty of the clinical measurements on surgical planning. Clinical measurements are taken using PC MRI for the velocity fields and catheterization for the pressure. On one hand these devices have a limited measurement accuracy. On the other hand these data are not acquired at the same time, and the child's physiological state may have changed. For theses reasons, these clinical data are prone to noise and uncertainty. This methodology is applied to a stenosed patient-specific virtual stage 3 model, from preoperative uncertain measurements. The goal is to quantify to which extend the decision to remove or not the stenosis during the surgery would have been impacted by the preoperative clinical measurements.
In Appendix, we present two articles where we integrate methodologies developed in chapters 3 & 4 in a joined work with the Modeling for the Congenital Hearts Alliance.

Chapter 2

Numerical simulations of blood flow

In this chapter, we present the keypoints in numerical simulations of blood flow. We compare simulation results obtained by using in-house code PHASTA and commercial software ANSYS Fluent. We first describe the principles of mesh generation, boundary conditions and numerical methods and then we present results for a Poiseuille flow in a cyclinder, a Glenn anastomosis, and a central shunt multibranch model with reduced model coupled at outlets. We conclude by defining the minimum needed to reach accuracy and stability.

The work presented in this chapter was performed in collaboration with Mahdi Esmaily Moghadam (numerical simulations in cylinder and glenn models using PHASTA), and Chiara Corsini (numerical simulations in both models using ANSYS Fluent). Moreover this chapter lead to the article:
Gregory Arbia, Chiara Corsini, Mahdi Esmaily Moghadam, Alison L. Marsden, Francesco Migliavacca, Giancarlo Pennati, Tain-Yen Hsia and Irene E. Vignon-Clementel **Numerical blood flow simulation in surgical corrections: what do we need for an accurate analysis ?** Journal of Surgical Research, Volume 186, Issue 1, pages 44–55, 2014.

Contents

2.1 Introduction

Computational fluid dynamics (CFD) has been increasingly used in cardiovascular research to model how hemodynamics change due to a pathology [YKA+06],[TTFVC11],[LDF+11],[TO12], predict hemodynamic change due to surgical repair [VCMF10],[CBK+13], explore different scenarios for treatment [HCC+11],[YVCT+12],[KBB+13],[MMVC+12], plan therapy [MKV+11], for example by noninvasively computing indices that are otherwise invasively measured such as fractional flow reserve [KED+11], and design artificial devices or conduits that are subject to stress and pressure from blood flow [PTG+11],[PLCB11],[YFS+13].

The Food and Drug Administration is integrating computational modeling into its evaluation and testing processes with increasing frequency and mandate [SPB+12]. Commercially developed numerical codes have increased the availability of such tools to a wider range of research, desing, and clinical users. In parallel but independently, a number of research specific codes have been developed, some of which have been made available as open sources. A few studies or simulation challenges have thus now emerged to compare codes of simulation approaches [SPB+12],[PDZG+05],[RAC+08],[SHF+13] to ascertain the validity and accuracy of these various codes.

To achieve effective solution, there are several necessary steps to numerically simulate blood flow: geometrical mesh generation from image data, choice of boundary conditions for the blood flow equations, and choice of numerical algorithm to compute the pressure and flow solution. These steps will be defined in section 2.2. Any misstep or inaccurate performance along the simulation algorithm can lead to erroneous results and potentially misleading conclusions. Therefore, we sought to systematically examine the choices of each of these steps to assess whether the choice of solver code remains an important determinant on the reliability and accuracy of the solution. Because of the early adaptation of computational fluid dynamics (CFD) in the field of congenital cardiac surgery as a tool to guide operative techniques and evaluate hemodynamic and physiological consequences, we have chosen three representative cases of palliative operations for congenital heart defects (CHD) as the clinical problem to achieve our investigative objectives.

To highlight the importance of the different steps in the cardiovascular modeling process, we first summarize the main steps in section 2.2. Previously, we have demonstrated the importance of defining accurate boundary conditions [VCMF10] as a prerequisite for accurate simulation. We also note the recent review on considerations for the numerical modeling of the pulmonary, especially on hypertension, which focuses primarily on the geometry reconstruction and on boundary conditions [KOS+13]. Therefore, in this chapter, the focus is on mesh generation and choice of numerical methods to solve the equations governing blood flow and pressure in the region of interest and the resulting impact on clinically relevant parameters derived from the simulation. These concepts are illustrated in the results section with increasing complexity, from the simplest example of a blood flow through a rigid tube, to realistic cases in the context of single ventricle palliations. In each case, the results from two different numerical codes are compared. The results are then discussed to draw conclusions on the main points medical researchers should be aware of for numerical analysis of blood flow.

2.2 Methods

Blood flow numerical simulations involve, at a minimum, three steps following reconstruction of the three-dimensional (3D) geometry from cross-sectional imaging data: (1) geometrical mesh generation, (2) choice of boundary conditions for the blood flow mass and momentum balance equations, and (3) numerical computation of the solution. We recall here only what is necessary to understand the essence of each step. For more detailed description we can refer to [VCMF10],[TF09]. These steps each have significant influence on the results and must thus be carried out with care, as will be shown in the results.

2.2.1 Discretization of the geometry: mesh generation

The 3D geometry of the vessels of interest can be drawn with CAD softwares or in case of patient-specific cases, reconstructed from imaging data such as magnetic resonance angiography (Figure 2.1). In most geometries and flow conditions, the mathematical, or exact, solution to the flow equations cannot be found analytically, that is, by hand or simple calculations. Hence, the solution must be approcimated by breaking down the equations in time and space in such a way that the computed solution can approach the exact solution if the simulation is carried out sensibly and correctly. This defines an algorithm that computes the solution numerically over successive time steps at a

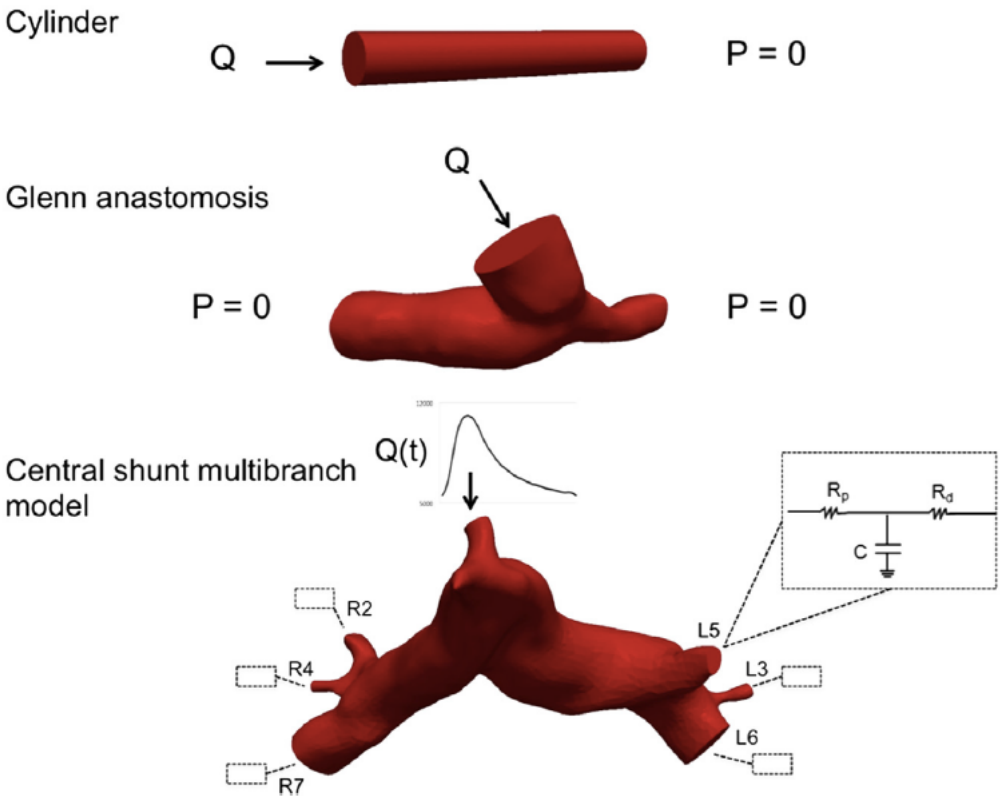

Figure 2.1: Examples of increasing geometrical (red) and physiological (inlet flow Q, outlet constant reference pressure P_{ref}, or Windkessel boundary condition) complexity. Zero velocity is imposed on the vessel walls. Top: cylinder for which the solution is known. Middle: simple patient-specific case. Bottom: realistic patient-specific configuration.

finite number of locations in the blood vessels. The 3D geometry is thus discretized into small volumes or elements (tetrahedra, hexahedra, and so forth) defined by nodes (or connection points of each element) where the solution is computed (Figures 2.2 & 2.6). The ensemble of volumes or elements and nodes constitutes the mesh that thus represents the 3D geometry. The more elements a mesh contains, the finer solution is. The disadvantage of mesh refinement is, however, the increase in computational cost: for instance, when the number of volumes or elements is doubled and the same computational power is used, the computational time can increase up to 10x, translating to simulations that may last several days or weeks. Mesh adaptation is a way to obtain a higher accuracy mesh, yet keep the number of elements, and thus the simulation time, reasonable [SMJ+06]. This is particularly important for challenging patient-specific simulations, where blood flow shows complex structures and for geometries with disparate length scales. The geometry is first discretized into an isotropic (i.e., uniform in all orientations) mesh. An initial simulation is performed, producing a metric of local flow gradients. An anisotropic, that is, with a preferential refinement orientation, mesh is then created by adaptively placing elements in areas of high-velocity gradient that need better refinement. These steps can be repeated a number of times to increase the quality of the mesh until the desired level of accuracy is reached. Here the isotropic and anisotropic meshes were generated using tetrahedral elements with the mesh generation software MESHSIM (Simmetrix Inc, Clifton Park, NY) [SMJ+06],[MSL+05] except for one isotropic hexahedral element mesh, which was generated with GAMBIT (Ansys Inc, Canonsburg, PA).

2.2.2 Solved equations and boundary conditions

Pressure and velocity are computed as solutions in space and time to the Navier-Stokes equations, which solve for the majority of the real-world fluid flow problems by assuming blood behaves as a Newtonian (viscosity: 0.004 Pa s), incompressible fluid (density: 1060 kg/m^3). These partial differential equations necessitate that appropriate boundary conditions are prescribed on the whole boundary. The vessel walls are assumed to be rigid, and a zero velocity no slip boundary condition is thus imposed there. On the inflow boundary, velocity is prescribed: in this chapter, it is assumed perpendicular to the surface, following a given steady (average behavior) or pulsatile (taking into account cardiac or respiratory variations) flow rate. At the outflow boundaries, one way impose a pressure (or traction) value or a simplified representation of the downstream vascular trees (here with a Windkessel model). For more information about typical boundary conditions, how they relate to physiological or patient-specific data, see the review [VCMF10] and references therein or

more recently [TTFVC11] and for related numerical issues [MVCF+13].

2.2.3 Flow solver numerical methods

As mentioned above, the governing equations must be discretized in time and space in such a way that the computed solution is as close as possible to the exact solution. Finite volumes and finite elements are two families of space discretization methods, within whom many variants exist for the Navier-Stokes equations [GSE98]. In addition, different schemes have been developed to match the solution in time. These choices depend on the trade-off between case of implementation, computational cost, stability, and accuracy of the computed solution. This trade-off needs to be evaluated for each application, accounting for values of blood density and viscosity, flow rates and pressure ranges, complexity of the flow, and precision needed to answer the medical question of the study.

In this chapter, we highlight how this can be done numerically, with examples of increasing complexity. In each of example, two codes are compared: the commercial ANSYS Fluent and the code PHASTA, the flow solver within the open source software package Simvascular (www.simtk.org) [SDS+08].

Although both codes require mesh discretization to solve the fluid dynamics problem, they adopt different numerical solution methods. Moreover, being a general purpose CFD code, Fluent provides various numerical options and models to solve problems of different nature (e.g. laminar, turbulent, diffusion, heat transfer) and in different fields (e.g. biomechanics, energetics, aerospace, chemistry). For example, first-order or second-order approximations can be chosen for both spatial and time discretization of the Navier-Stokes equations: the former is usually faster to reach convergence of the solution, although with lower precision than the latter. If such options are not known in detail or the default settings are used, they may lead to inappropriate and risky choices. As an example, first order is the default option in Fluent, but it is usually inappropriate for most cardiovascular CFD problems. PHASTA, instead, is an in-house code specificially designed for solving complex CFD problems, thus using numerical options (e.g. second-order approximation in time) already optimized for such problems. Open source and in-house solvers such as this offer the advantage of greater user control over numerical scheme and flexibility to implement new capabilities. Solutions from the two codes are vizualized at each mesh element (Fluent) or node (PHASTA) with the software Paraview (www.paraview.org).

2.2.4 Setup of the three examples

A summary of the geometry and boundary conditions is explained in Figure 2.1 for each example of increasing complexity.

2.2.4.1 Simple "SVC" tube with Poiseuille flow

The conditions in the first example are representative of a superior vena cava (SVC) in an adult CHD patient, simplified enough so that an exact solution can be calculated, the well-known "Poiseuille flow". The geometry is a cylinder of radius 2 cm and length 30 cm. Three unstructured tetrahedral meshes of increasing refinement were tested (6 10^3, 2.4 10^4 and 10^5 elements), as well as a hexahedral mesh of 5.4 10^4 elements oriented along the direction of flow. Two different steady flow regimes were tested, with a Reynolds number (Re) of 530 and 1060, that is, with lower and higher flow rates, respectively. The corresponding flow was imposed at the inlet, with a parabolic axial velocity profile. In all simulations, zero velocity at the wall and a constant reference pressure at the outlet were imposed. Calculated pressures were then interpreted as differences with respect to the reference value. As a consequence, the mathematical solution is, in this simple case, analytically known and can be compared with the numerical simulations. It is the Poiseuille solution, with a Parabolic axial velocity solution that is constant along the length of the cylinder, and a pressure solution which is uniform on a given cross-sectional area but decays linearly along the length of the cylinder. The resistance to the flow, which is the ratio of the pressure loss along the tube divided by the flow, can then be compared between the analytical and the numerical solutions.

2.2.4.2 Steady superior cavopulmonary connection, or Glenn anastomosis, model

As the second stage palliation for single ventricle hearts, the SVC is disconnectd from the right atrium and connected directly to the pulmonary artery to provide pulmonary blood flow. Contrary to the previous case, the exact solution of the flow equation in a Glenn anastomosis cannot be derived analytically, due to its complex geometry and flow characteristics and compulsory three-dimensionality. To compare the differences between codes and between meshes is thus more difficult as the mathematical exact solution is unknown. The SVC anastomosis to the left pulmonary artery (LPA) and right pulmonary artery (RPA) was reconstructed from magnetic resonance imaging data of a single ventricle patient following the Glenn operation. The SVC averaged diameter is 12.2 mm. In this example, only the geometrical complexity

is increased to see its influence on the solution in the simplest hemodynamics setting. Steady flow (2.6 10^{-5} m^3/s) with a flat axial velocity profile was imposed at the inlet (SVC), zero flow at the wall, and the same reference pressure at the outlets. It is worth noting that, with rigid walled models, CFD results are identical regardless of obvious to use a reasonable value for mean pulmonary artery pressure, but zero pressure could be indifferently applied, without affecting the solution in terms of flow distribution and pressure gradients. A uniform mesh was created (2.4 10^5 elements, indicated as "240K") and adapted first with 5.4 10^5 elements and then with 1.4 10^6 elements (indicated as "1.4M").

2.2.4.3 Pulsatile multidomain central shunt pulmonary model

This case presents a realistic and patient-specific simulation for both geometry and physiology (Figure 2.1). Constructed from magnetic resonance imaging data, the geometry consists of a systemic to pulmonary shunt connected between the aorta and the pulmonary arteries (PA) as the first stage of single ventricle palliation. The inlet shunt flow was imposed with typical cardiac pulsatility (as measured by ultrasound) for several cardiac cycles, with a flat velocity profile. The average flow was 7.5 10^{-6} m^3/s (corresponding to an average inlet Re of about 10^3). To model the pressure drop relationship of the pulmonary arterial trees downstream of the outlets, three-element Windkessel models, each composed of a proximal resistor in series with a capacitor and a distal resistor in parallel, are coupled to these outlets. Proximal and distal resistances represent the viscous effects of blood flowing through the pulmonary arterial and capillary venous bed, respectively, whereas the capacitance accounts for vessel wall deformability. The distal pressure was taken as the average atrium pressure (6 mmHg). The parameters can be automatically tuned based on the magnetic resonance left/right pulmonary flow split, catheter based transpulmonary gradient, diameter of each outlet , and morphometric data. This mehtod allows one to obtain realistic pressure and flow values [TTFVC11]. The mesh was first adapted in a steady simulation from a 5 10^6 isotropic element mesh to an anisotropic 2.7 10^6 element mesh and then further adapted in a pulsatile simulation to an anisotropic 1.9 10^6 element mesh, with a target error reduction of 20% each time [SMJ+06]. The time step was 0.001 s and two cycles were enough to reach stable waveforms.

2.3 Results

2.3.1 Simple tube with Poiseuille flow

The simulation results were compared for the different meshes and codes (Figure 2.2, upper panel). In general, the results get closer to the analytical exact solution as the mesh is refined. ANSYS Fluent overestimates the resistance, whereas PHASTA underestimates it, regardless of flow rate; but both codes converge to the analytical solution. The convergence to the analytical solution is faster for low flow (Re = 530) than for high flow (Re = 1060). Note that for higher flow, the coarsest mesh (6 10^3 element mesh noted 6K) run with ANSYS Fluent appears to be closer to the analytical solution for the resistance. However, the pressure map (Figure 2.2, lower panel, top left) reveals that the pressure is spotty and not linearly decreasing, contrary to the analytical solution. This is also the case for the 6K-mesh PHASTA simulation (Figure 2.2, lower panel, bottom left). This stresses the importance of selecting a relevant criterion to assess mesh convergence.

One way to construct a mesh that provides a better solution, while limiting the number of elements, is to align the elements with the flow. In this simple unidirectional flow, a hexahedral mesh is particularly well suited: the 54K element mesh, which has about half the number of nodes compared with the finer mesh, leads to a solution much closer to the analytical solution (Figure 2.2, upper panel for the resistance value and lower panel top for the linear pressure decay with Re=1060).

Moreover, selecting the "first-order method" as a numerical discretization method in ANSYS Fluent lead to pressure drop double the analytical solution (Figure 2.2, upper panel).

2.3.2 Steady Glenn anastomosis model

To show the influence of mesh refinement, a mesh comparison was performed with three increasingly refined meshes, and the differences between codes were compared (Figure 2.3). The SVC pressure for PHASTA is going toward an asymptote with about 2% increase (corresponding to about 0.01 mmHg) when refining the mesh (i.e. more than doubling the number of elements at each adaptation). On the other hand, with Fluent, it oscillates around a value (about 0.55 mmHg) with changes of around 1% (corresponding to about 0.005 mmHg). For both solvers, the flow split between the two pulmonary arteries (PAs) quickly converges to the same value (0.703).

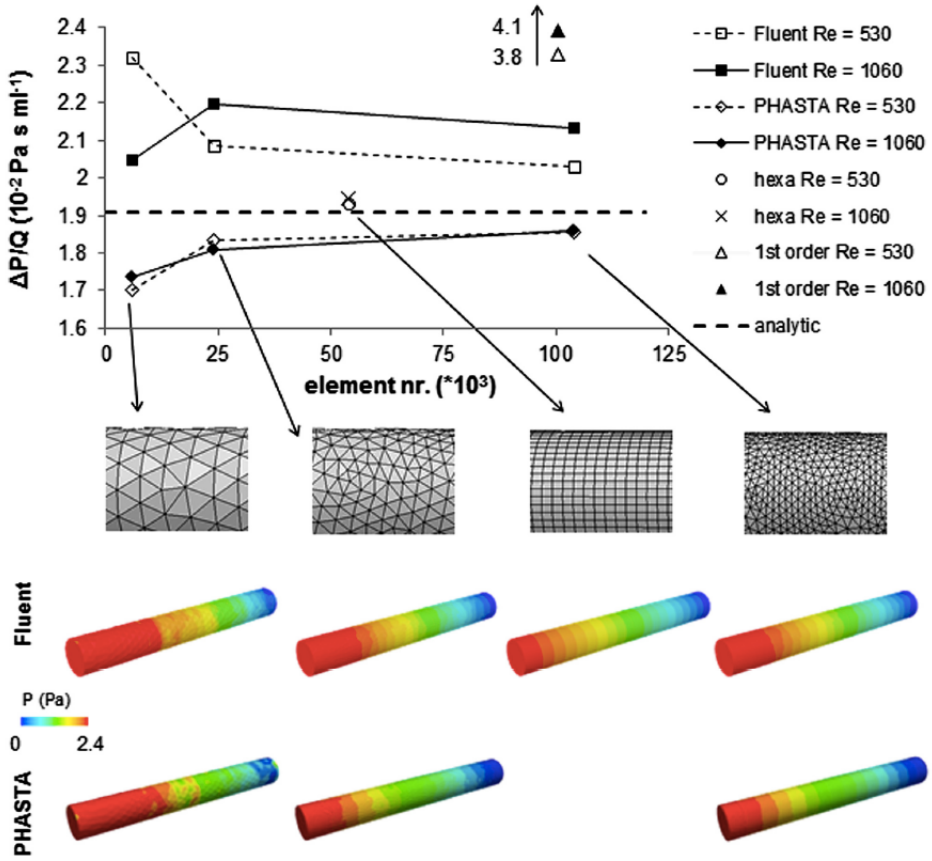

Figure 2.2: Upper panel: mesh convergence results shown as resistance ($\Delta P/Q$) computed with the solution of meshes of increasing size (shown below). The dashed straight line corresponds to the analytical Poiseuille resistance. The upper curves correspond to ANSYS Fluent solutions, whereas the lower ones to PHASTA solutions, for both simulated Re. Solutions of Fluent hexahedral mesh ad Fluent first-order method are also reported. Lower panel: Pressure (Pa) maps corresponding to the different meshes computed with Fluent (top) and PHASTA (bottom), for the case with Re=1060.

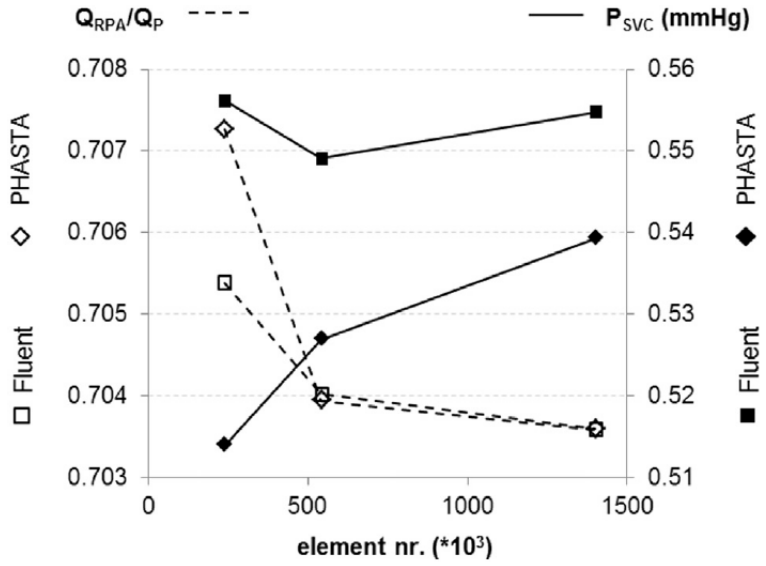

Figure 2.3: Numerical solutions with PHASTA (diamonds) and ANSYS Fluent (squares). Flow split (Q_{RPA}/Q_P) to the right PA (left axis, open symbols) and SVC inlet pressure (in mmHg, right axis, filled symbols) for meshes of increasing refinement (number of elements on x-axis). 1 mmHg = 133 Pa.

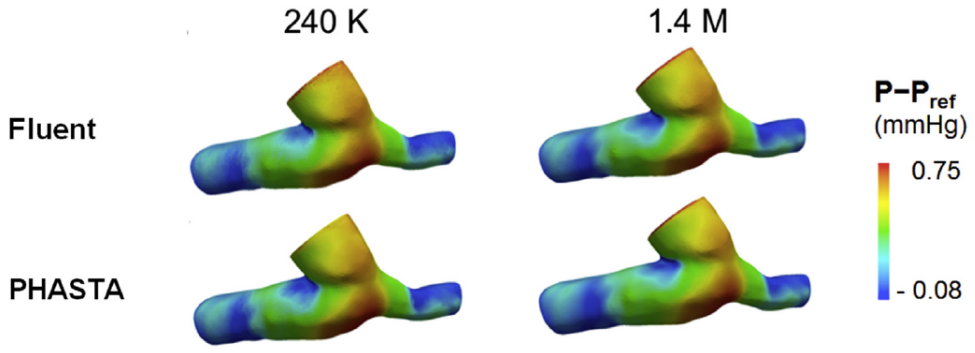

Figure 2.4: Pressure (mmHg) maps for meshes with 240K (left) and 1.4M (right) elements, computed with Fluent (top) and PHASTA (bottom). Depicted pressure is relative to the reference pressure P_{ref} applied to the models outlets.

The 3D pressure (Figure 2.4) and velocity (Figure 2.5) maps demonstrate minimal differences between the two solvers' solutions. Moreover, the maps confirm that the differences between meshes are minimal and that the coarsest mesh (240K) is thus appropriate for this type of geometry and flow conditions.

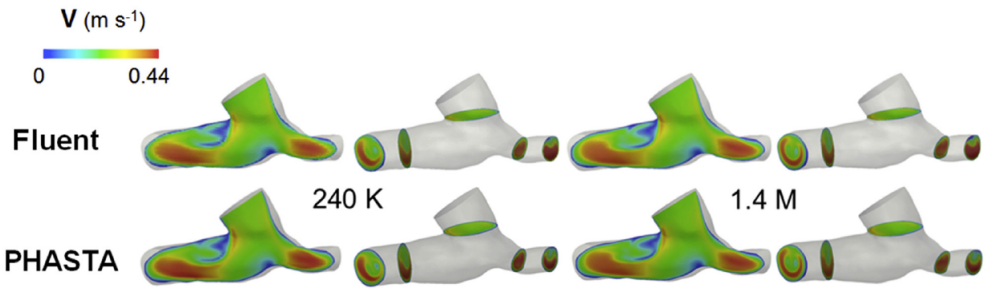

Figure 2.5: Velocity magnitude (m/s) cuts for meshes with 240K (first two columns on the left) and 1.4M (last two columns on the right) elements, computed with Fluent (top) and PHASTA (bottom).

The mesh was adapted to the flow structures, creating a boundary layer at the SVC inlet, where a flat flow profile was imposed, and a swirling pattern on the RPA outlet section (Figure 2.6), where the flow swirls.

Note that the computed flow split shows a right dominance. This is a consequence of applying an equal pressure at the two outlets and a larger RPA diameter. However, if the flow split is measured clinically (e.g. by phase-contrast magnetic resonance imaging), the boundary conditions should incorporate this data, for example, directly imposing the outflows or setting dowstream resistances such that the measured flow split is obtained. Furthermore, taking into account unsteadiness has been shown to influence the results (due to nonlinear effects) [MVCC+07].

2.3.3 Pulsatile multiscale central shunt pulmonary model

In this realistic multibranched model, the aforementioned limitations are alleviated. Results are shown as velocity cuts and pressure maps on the final adapted mesh (1.9 10^6 elements) at end diastole and peak systole (Figure 2.7). They illustrate how complex the hemodynamics are in such an anatomy. Blood enters at high speed through the shunt (Figure 2.7A) and impacts the

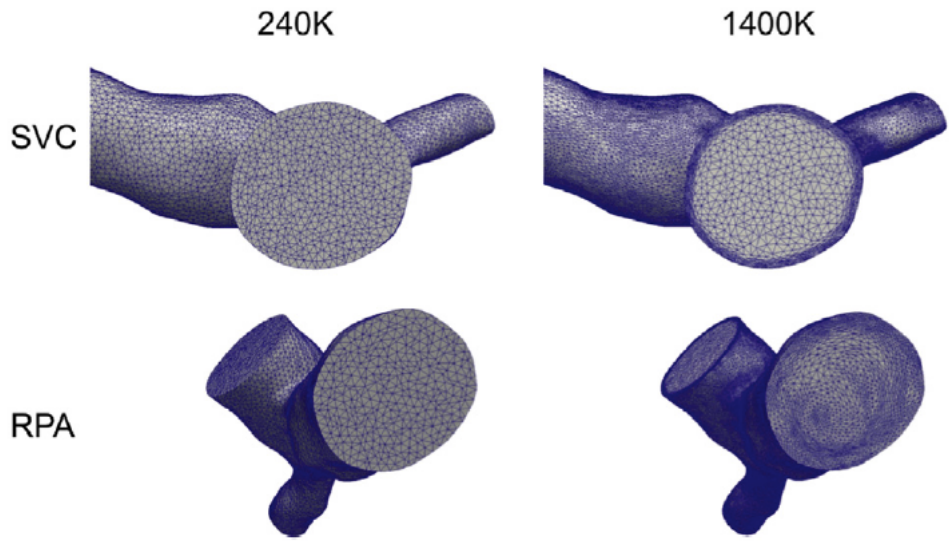

Figure 2.6: Uniform initial mesh (240K elements) and refined mesh (1.4M elements) that adapted to the flow structures, as shown at the inlet (SVC), where a flat profile is imposed, and at largest outlet (RPA), where the flow swirls.

branch name	R2	L3	R4	L5	L6	R7
Pressure (mmHg)						
PHASTA	12.37	11.94	12.69	12.28	12.26	12.32
Fluent	12.35	11.95	12.53	12.29	12.28	12.32
Flow (ml/s)						
PHASTA	0.659	0.120	0.176	0.299	2.326	3.914
Fluent	0.659	0.120	0.172	0.300	2.330	3.910

Table 2.1: Time average pressure and flow at the six branches

pulmonary wall (red in Figure 2.7C), causing a high-pressure region (circular patched on the right of the main pulmonary artery stump in Figure 2.7B). Blood swirls downstream into the PAs (cyan structures in Figure 2.7C and D).

The interaction between the 3D geometry and the high flow in the narrow shunt spreading into the PAs generates flow dynamics that are not completely periodic over time. This is reflected by the flow and pressure tracings over time at two outlets (Figure 2.8).
Because this case includes 3D model characterized by multiple pulmonary branches and relatively high inlet velocity, generating complex fluid dynamics, it is interesting to compare the two codes in terms of flow distribution at the outlets and of local velocities and pressures. The Table 2.1 shows, for the two solvers, how closely flow rates and pressures match at the outlets, on average over time, with relative difference $<2.4\%$. The comparison of pressure and velocity maps shows that the results are very similar between the two solvers, at low (end systole) and high (peak systole) flows: both of them detect flow impingement on the pulmonary wall at the exit of the shunt, with local maximal velocity values (3.5 m/s in Figure 2.7C), and swirling flow in the PAs. Note that the maximum pressure actually occurs not at the inlet but at the impingement on the pulmonary wall, where the two codes computed the same value (76 mmHg; Figure 2.7B).

2.4 Discussion

The first example (simple tube with Poiseuille flow) illustrates that, even for a simple Poiseuille flow, selecting the mesh impacts the results. Here the hexahedral mesh leads to better results: this mesh is the most axisymmetric and aligned with the flow among all the other meshes. Generalization of this observation to more complex geometries and flows is the subject of another study. The better suitability of hexagonal *versus* tetrahedral meshes is a

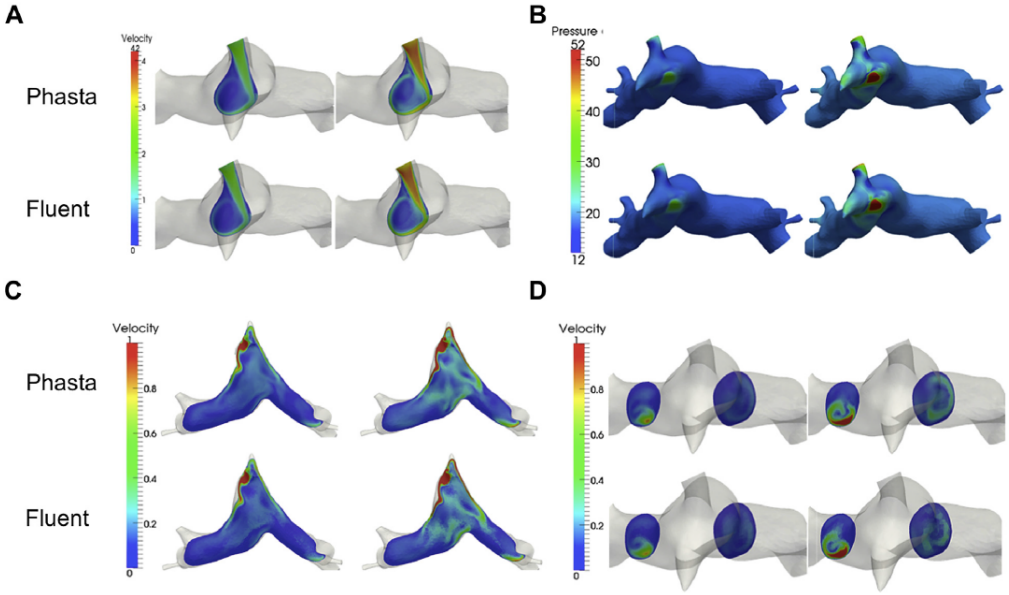

Figure 2.7: Comparison between the two codes (PHASTA and Fluent) of pressure (mmHg) (B) and velocity magnitude (m/s) at the anastomosis (A), on an axial cut (C) and on sagital cuts through the pulmonary arteries (D), in end diastole (first and third columns) and peak systole (second and fourth columns). The maximum legend values were chosen as a compromise between showing the high values and visualizing flow and pressure structures.

matter of debate in fluid mechanics [DSMDB+10] that is beyond the scope of this article. However, the results do highlight that the fineness of the mesh should be determined based on the relevant output: taking into account just a global measure rather than local phenomena may be misleading. It is thus necessary to define a convergence criterion to assess when to stop the mesh refinement.

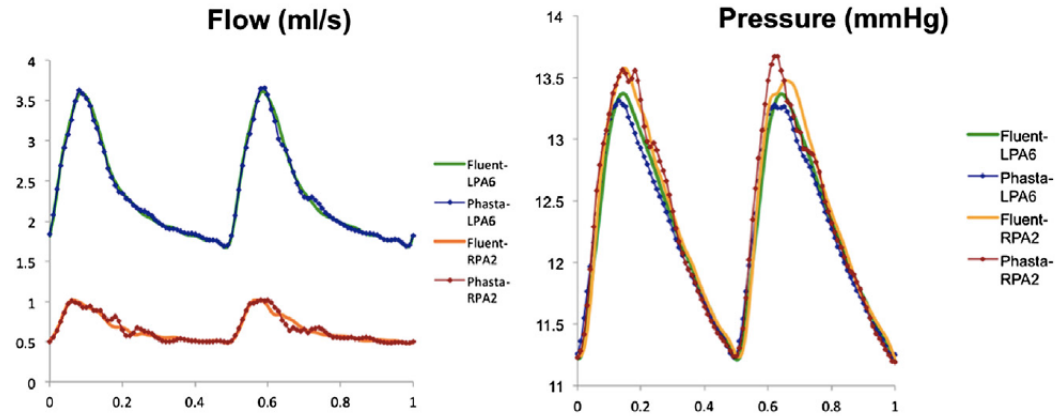

Figure 2.8: Comparison of flow (left) and pressure (right) over time (in seconds) at one small branch on the RPA and one large branch on the LPA, between the two codes (Fluent, PHASTA, dotted lines).

The chosen level of refinement depends on the flow conditions and numerical methods of the code at hand. The first-order method on a fine mesh in Fluent, which is the default and faster method, had a 100% error in the pressure drop. This is likely due to the added energy dissipation to achieve numerical stability of the numerical method. This stresses the importance of testing the numerical method according to the application. The mesh can, however, be refined anisotropically based on how the blood flows, to keep the computational time reasonable while improving the solution quality.

Indeed, in the second example (steady Glenn anastomosis model), appropriate mesh adaptation was performed. However, the results show that for these meshes and simple hemodynamic conditions, the mesh had little impact on the SVC pressure and the flow split between the two lungs. Changes in the SVC pressure of about 2% for PHASTA and 1% for Fluent (Figure 2.4) are clinically negligible because they correspond to very small fractionsof mmHg (about 0.01 and 0.005 mmHg respectively). Changes in flow split with mesh refinement are even slighter if compared with SVC pressure. The 3D maps (Figure 2.5 and 2.6) confirm this point. The first mesh is thus fine enough

for these conditions and these convergence criteria.

The difference between the codes, although very small compared with pressure measurement uncertainties, decreases with the refinement of the mesh: for the SVC pressure, it decreased from 8% to 4% and then to 3%. Note that in this case, the "true" solution is not known, so it can only be obtained by such a convergence study. From a practical point of view, the appropriate refinement is defined by metrics that depend on the purpose of the hemodynamic simulations, for example, pressure drop, flow repartition, of finer information such as wall shear stress, which usually requires a significant increase in mesh quality.

The third example adopting solution to a pulsatile multidomain central systemic pulmonary shunt is a simulation with realistic geometry and physiological conditions. The mesh was adapted to the solution. The complexity of the flow and the associated effects on pressure distribution were captured by both codes. This observation is noteworthy from a clinical perspective, as complex hemodynamics with increased turbulence, increased particle residence time, and abnormal shear stresses may have important impact on potential for thromboembolic phenomenon, flow distribution to the right and left lungs, and vascular wall remodeling. The solutions over time and in space were largely similar. It is thus expected that the chosen numerical methods for each code would give comparable differences on similar patient-specific hemodynamics simulations.

Another consideration in choosing a CFD method is the overall computational time. In fact, the latter may vary according to time and space discretization methods, the mesh size, the programming language, the computing power at hand, and so forth. As with the mesh refinement study, a time step refinement study should be performed. In both cases, there is a tradeoff between computational cost and accuracy of the solution. Reducing computational complexity is yet a matter of intense research.

One factor that increases computational time but may be necessary for some applications is to take into account the elastic or viscoelastic nature of the vessel walls when solving the blood flow equations. To take into account such a fluid-solid interaction necessitates proper algorithms (e.g. [CGN05],[FVCJ+06]) and additional modeling parameters to select or estimate from patient data [MBX+13]. As for boundary conditions, such choices need to be consistent with the clinical question being addressed and the patient data or population data available in the literature [VCMF10].

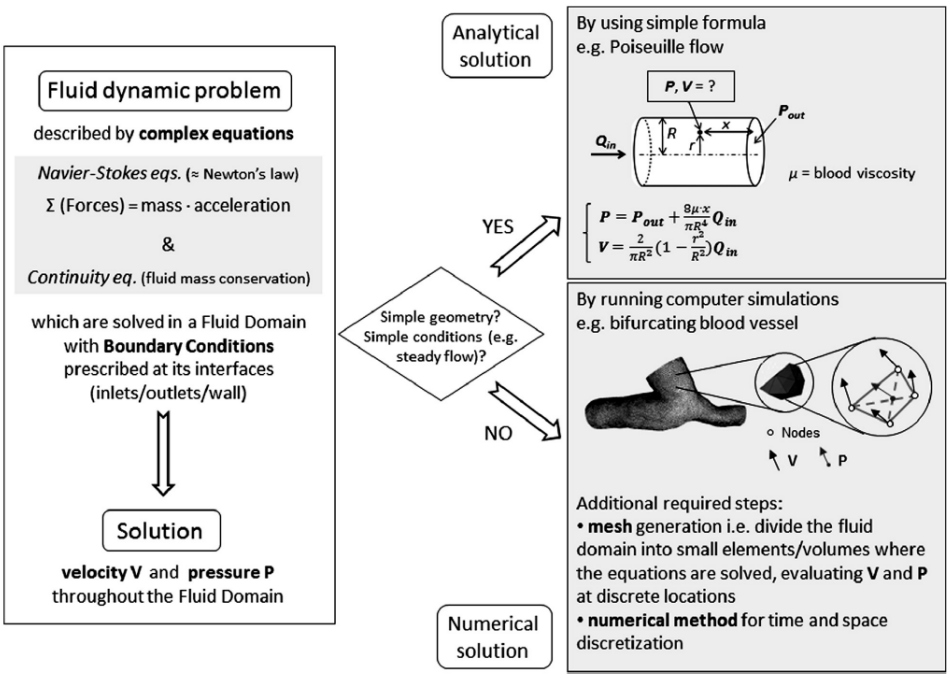

Figure 2.9: Schematic summarizing key basic concepts for readers less familiar with CFD numerical tools.

Other considerations may also drive the choice of flow solvers. Commercial solvers are designed to be easier to use, with intuitive user interfaces and training courses. This facilitates the entrance into the simulation field for new users. In traditional engineering applications, these codes have been tested in R&D companies in the context of product design. In cardiovascular research, the CFD community is still growing, with a wide spectrum of CFD conditions, ranging for low Re flow in small animals [GLT+06] to near-turbulent flow in patient congenital or acquired diseases [LDF+11],[LSF+10]. For each application, numerical methods need to be tested. In fact, the interaction of patient-specific 3D multibranched geometry and the hemodynamics conditions can create a highly complex flow, with unsteady swirling structures that are far from unidirectional flow. This can cause numerical challenges for which traditional approaches, found in commercial codes, sometimes fail. Specific numerical methods are, in such case, warranted and implemented in in-house research codes [MBH+11]. Moreover, in hemodynamics simulations, the 3D region of interest is part of the global circulation. To take into account the interaction between the local hemodynamics effect and the rest of the circulation, the 3D hemodynamics equations can be coupled to reduced models (e.g. lumped parameter models [CBK+13],[LDM+02],[MBP+06],[KVCC+10],[BF13],[BCM+12]) of the entire circulation instead of just a Windkessel model as was done here. Such a coupling can be numerically challenging. Commercial codes offer limited possibilities to do it, whereas in-house codes, with more developmental work, can be tailored for efficiency and robustness [MVCF+13],[MBDQ11],[LBB10]. For example, in commercial codes, the reduced model can be coupled to the 3D domain with a user-defined routine. But the coupling is done explicitly in time, which requires uning a smaller time step size to maintain numerical stability and thus longer simulation times.

2.5 Conclusion

The take home points are summarized in Figure 2.9 for readers less familiar with CFD numerical tools. Even in very simple fluid dynamics conditions (Poiseuille flow), expertise and careful numerical choices are mandatory to obtain a robust and accurate solution. At least a basic numerical knowledge is thus required to appropriately use codes or formulas [VCMF10],[YCS+88]. For example, a mesh sensitivity study is warranted, based on a chosen convergence criterion, usually a threshold of change in an output quantity, that depends on the accuracy necessary for the medical question at hand. Other choices are important in addition to the numebr or the location of the ele-

ments: elements shape (hexehedra *versus* tetrahedra) and numerical schemes (time and space discretization methods). These choices depend on both the hemodynamic conditions (low flow or high flow, interaction with more or less complex geometry) and the output relevant for the application. In fact, meshes and numerical parameters chosen for simulations under resting conditions. Similarly, to evaluate a pressure loss may capture 3D flow features or wall shear stress. Finally, with the present chapter, we underlined that the choice of proper numerical settings is more important than the solver (code) choice [SHF+13].

Part I

Multiscale modeling of palliative surgery from clinical data

Chapter 3

Multiscale modeling of stage 2 surgery

We present a method to iteratively tune parameters of reduced models from clinical measurements. The method is based on a fixed-point algorithm to tune total resistances [TTFVC11] and leads to estimation of 5-element reduced model parameters, taking into account pulmonary and venous vascular trees. We also adapt this method to reflect the effect of collateral vessels linking systemic to pulmonary vasculatures. We illustrate our methodology for three patient-specific models of stage 2 palliative surgery.

This work has been performed in collaboration with Catriona Baker, Silvia Schievano and Tain-Yen Hsia (clinical background of patients, clinical data gathering and reconstruction of the 3D geometrical models at Great Ormond Street Hospital in London).

Contents

3.1 Introduction

Congenital heart defects are the most common birth defects. These patients are born with one functional part of the heart and require several operations

during childhood. The stage 2 procedure is the second palliative surgery, and consists of linking the superior vena cava to pulmonary arteries. This palliative surgery occurs generally during the second semester of the life. Modeling blood flow into pulmonary arteries is challenging from a computational point of view and useful for surgery planning from clinical point of view. Then, integrating patient-specific clinical information into numerical simulations is critical to yield results which accurately represent a patient specific condition [VCMF10].

A lot of effort was previously performed to model and better understand the third palliative surgery, especially postoperatively [DeG08],[dZMFY10], [VCFJT10],[dLD10], which consists of linking the inferior vena cava to the pulmonary artery leading to a well known total cavopulmonary connection. Less work has been done on stage 2 patients (see [TTFVC11] and references therein). Computational fluid dynamics studies of single-ventricle conditions (e.g [BdLM$^+$03, VCFJT10, dZMFY10], have presented the crucial interest of specifying the relevant boundary conditions.

The main challenge of this study within the Leducq consortium is, as in [TTFVC11] to determine outflow boundary conditions for each patient-specific model that are consistent with the clinically measured data: 1) flow distribution between left and right sides (flow split) denoted by fs and 2) arterial pressure close to the SVC inlet denoted by P_t, which is the target pressure that we want to reach according to clinical measurements. In Figure 3.1 we present a scheme of the global circulation before the third surgery, which includes the clinical measurements.

In order to reflect the effect of the downstream vascular tree it would not be relevant to apply pressure boundary conditions for the following reasons: 1) we could not recover the flow split or the inlet measured pressure, and 2) the pressure measurements are not performed at the same locations in the pulmonary arteries. A common way to take into account the effect of the downstream domain is to couple 3D Navier-Stokes equations to lumped parameter models or one-dimensional models of the peripheral circulation [PCC$^+$11], [VCFJT06], [VCFJT10], [VCMF10]. This gives information about local fluid dynamics with changes in anatomical features [CBK$^+$13], [KBB$^+$13]. We thus couple 3D Navier-Stokes equations to reduced models including resistances and capacitances. We present in this chapter a method to iteratively tune these parameters.

For more general background on 0D parameter tuning, see the introduction

of chapter 4. A previous work [TTFVC11] introduced a method to iteratively tune reduced order parameters of the 3D model to match clinical inlet average pressure, inlet average flow and outlets' flow repartition. The method was illustrated on coupling of 3D steady Navier-Stokes equations to total outlet resistances of dozens of branches in stage 2 (Glenn) patient-specific simulations. From these resistances, 3-parameter Windkessel models were generated to represent the downstream arterial tree, neglecting the venous circulation. In this chapter we use the same methodology but extend 3-parameter Windkessel models to 5-element reduced models containing 3-element Windkessel model for the arterial side, in series with in parallel capacitance and resistance for the venous side. We also take into account the effect of collateral vessels created by the body linking systemic to pulmonary vasculature.

We present the framework in section 3.2, then we use this method for three patient-specific models of stage 2 procedure in section 3.3. We highlight the interest of this method regarding pressure, blood flow behavior and wall shear stress. Finally we discuss about the results and limitations of this method and present possible extensions and future work.

3.2 Methods

The Methods section presents the type of clinical data that define the patient-specific geometry and hemodynamics target values. The automatic reduced model parameters tuning to reach these target values is explained, followed by the 5-parameter reduced model description. In this chapter three patient-specific computational models were built to describe hemodynamics into the corresponding three-dimensional regions of interest, reflecting the patient state in coherence with the clinical measurements acquired before stage 1 surgery. In order to understand hemodynamics in stage 2 geometries and reflect the effect of the vascular tree, rigid-wall Navier-Stokes equations were solved in three-dimensional models, coupled to zero-dimensional (0D) models. All simulations were performed using a custom version of finite element Navier-Stokes solver with SimVascular (http://simtk.org), assuming blood as a newtonian fluid with a density of 1060 kg m^{-3} and a dynamic viscosity of 0.004 Pa s, with monolithic coupling between the 3D and 0D models [VCFJT06], [VCFJT10]. A new challenge is to generate reduced model parameters from these resistances.

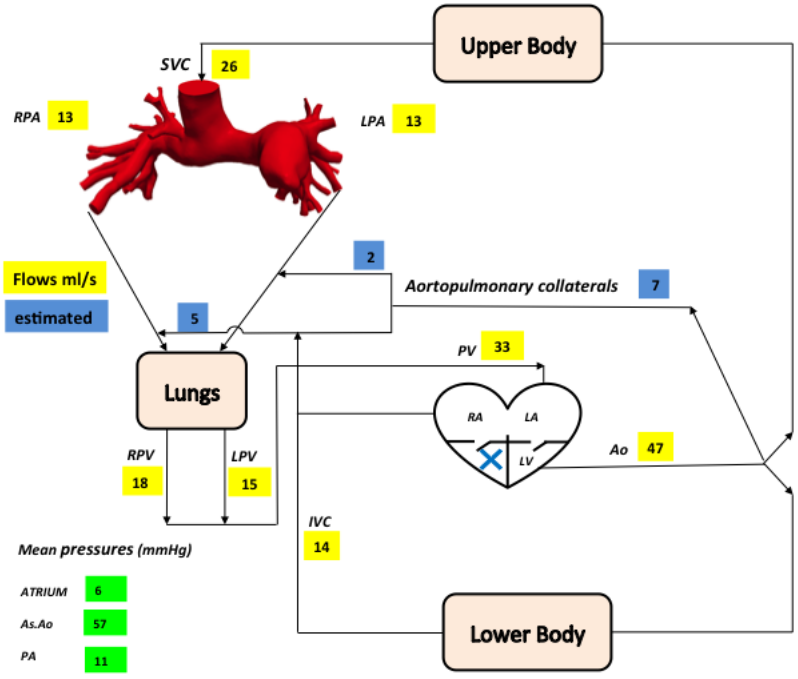

Figure 3.1: Scheme summarizing the global circulation to prepare the third surgery. Blue and yellow values are measured flow rates (ml/s) and green values are pressure measurements (mmHg).

3.2.1 Clinical cases and measurements

Patients A and B were recruited to the Great Ormond Street Hospital, London. Patient C was recruited to the Medical University of South Carolina, Charleston, SC. The study was approved by the institutional review board at each institution and consent was obtained from the subject's parents. Patient A was born with pulmonary atresia with intact ventricular septum. The patient underwent surgical placement of 3.5mm right modified BT shunt and atrial septectomy during the second day of his/her life and a surgical bi-directional stage 2 stage 2 at 7 months old. This patient was 3 years and 7 months old at time of CRM, with body surface area (BSA) of 0.62 m^2. Patient B was born with hypoplastic left heart syndrome. This patient underwent surgical placement of 3.5mm right modified BT shunt and atrial septectomy during the second day of his/her life and a surgical bi-directional stage 2 at 7 months old. This patient was 3 years and 2 months old at time of CRM with BSA of 0.59 m^2. Patient C was born with hypoplastic left heart syndrome. This patient underwent surgical placement of 3.5mm right modified BT shunt and atrial septectomy during the second day of his/her life and a surgical bi-directional stage 2 at 7 months old. This patient was 3 years and 5 months old at time of CRM with BSA of 0.61 m^2. See Table 3.1 for a summary.

For patients A, B and C the cardiovascular magnetic resonance (CMR) was performed respectively 5, 7 and 6 months prior to the third surgery, and cardiac catheterization was performed respectively during surgery, 7 months and 6 months prior to the third surgery, giving the pressures in the superior vena cava (SVC) or the pulmonary (considered as equivalent pressures as there were no restrictions) and in the common atrium. The total pulmonary flow (SVC flow), as well as right (RPA) and left (LPA) pulmonary artery flows were measured from CMR. The SVC flow was imposed at the inlet surface assuming a velocity parabolic profile.

3.2.2 Tuning of total resistances

The automatic tuning of outflow boundary condition was introduced in [TTFVC11] for patient-specific simulations of the stage 2 procedure. This method was developed to obtain 3-element Windkessel parameters containing proximal resistance (R_p) to describe viscous effects into large arteries, capacitance (C) representing the ability of large arteries to store and return blood during a cardiac cycle, and distal resistance (R_d) representing viscous effects into small vessels. A first part consisted of iteratively tune a total resistance

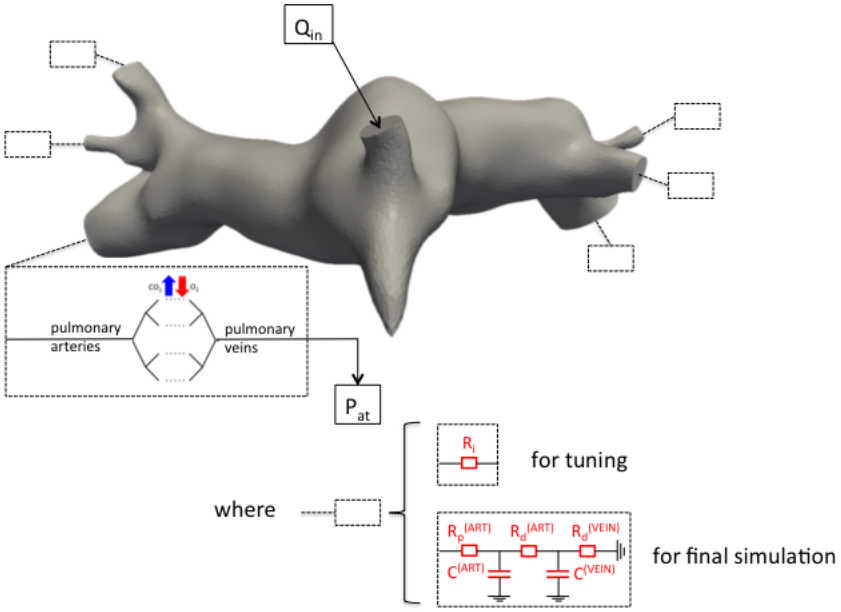

Figure 3.2: Multiscale set-up, with the 3D domain (here a stage 1 case as in the next chapter), its inlet face on which the inflow Q_{in} is prescribed, and the distal pulmonary circulation for each outlet that all merge in the single atrium defined by its pressure P_{at}. At each outlet (dashed rectangle), the pulmonary arteries, capillaries and veins are represented either by a resistance for tuning, or by a more complete 5-parameter reduced model for the future pulsatile simulations.

at each outlet by coupling 3D Navier-Stokes equations to a resistance by using a fixed point method until recovering: 1) the measured transpulmonary gradient between the superior vena cava and the left atrium, and 2) the flow split.

The flow split (fs) is computed from CMR flow rates of the right pulmonary artery (RPA) and left pulmonary artery (LPA) as follow:

$$\text{fs} = \frac{Q_{\text{RPA}}}{Q_{\text{LPA}} + Q_{\text{RPA}}} \tag{3.1}$$

The mean flow rate (Q_i) that we want to reach through an outlet i is assumed to be proportional to the surface area of this outlet (S_i):

$$Q_i \propto S_i \tag{3.2}$$

An expected value for the flow rate at outlet i is thus a fonction of the inlet flow rate (Q_{in}) coming from clinical measurements:

$$Q_i = Q_{\text{in}}\Big(\delta_{i\text{r}}\text{fs} + (1-\delta_{i\text{r}})(1-\text{fs})\Big)\frac{S_i}{\sum\limits_j S_j\delta_{ij}} \tag{3.3}$$

where $\delta_{i\text{r}}$ is kronecker symbol equal to 1 if outlet i is on the right side and 0 if not, and δ_{ij} is kronecker symbol equal to 1 if outlet j is on the same side as outlet i and 0 if not.

We denote by P_{at} the atrial pressure and P_{in} the inlet pressure measured from catheterization. We then define a transpulmonary gradient by $\text{TPG} = P_{\text{in}} - P_{\text{at}}$.

We estimate a first value of R_i at each outlet, that we couple to the 3D incompressible Navier-Stokes equations.

By post-processing the results, we compute the averaged pressure at the inlet denoted by $P_{\text{in}}^{\text{3D}}$, the average pressure at each outlet i denoted by (P_i^{3D}), and the flow rate at each outlet i denoted by Q_i^{3D}. We thus deduce a resulting flow split, and compare these results to the target values, by defining errors on pressure and flow rate,

$$\begin{aligned} \varepsilon_P &= \frac{|\mathrm{TPG} - (P_{\mathrm{in}}^{3\mathrm{D}} - P_{\mathrm{at}})|}{\mathrm{TPG}} \\ \varepsilon_Q &= \left(\frac{1}{N} \sum_{i=1}^{N} \left(\frac{Q_i^{3\mathrm{D}} - Q_i}{Q_i} - \frac{1}{N} \sum_{i=1}^{N} \frac{Q_i^{3\mathrm{D}} - Q_i}{Q_i} \right)^2 \right)^{\frac{1}{2}} \end{aligned} \tag{3.4}$$

where N is the number of outlets.
If the convergence is not reached, we update resistance at each outlet as follow:

$$R_i = \frac{\mathrm{TPG} - (P_{\mathrm{in}}^{3\mathrm{D}} - P_{\mathrm{at}})}{Q_i} \tag{3.5}$$

And we run a 3D simulation of incompressible Navier-Stokes equations by coupling a new set of resistances R_i, where $i \in [0, N]$ for N outlets. This process is repeated until convergence.

3.2.3 Reduced model parameters for pulsatile simulation

From the pulmonary arteries to the left atrium the vascular tree is carrying blood though the lung where gas exchanges occur. We divide this vasculature in three parts: the arteries downstream of the 3D geometry, the smaller arteries and capillaries, and the veins; representing the viscous effects and the ability of the larger vessels (both arteries and veins) to store and return blood during the cardiac cycle. The resulting parameters described on Figure 3.2 need thus to be determined. Assuming that pressures return periodically to the same values in the 5-parameter reduced model, the proximal arterial resistance R_p^{ART}, the distal arterial resistance R_d^{ART} and the venous resistance R_d^{VEIN} can be summed to recover the total resistance at outlet i,

$$R_i = R_p^{\mathrm{ART}} + R_d^{\mathrm{ART}} + R_d^{\mathrm{VEIN}} \tag{3.6}$$

Next, empirical laws determine the distribution of the equivalent resistance and capacitance over the arterial or venous sides [BSD68, OLFH96, PAH+98]. Thus for each outlet, $R_d^{\mathrm{VEIN}} = 0.52R_i$. The total pulmonary artery resistance ($R_p^{\mathrm{ART}} + R_d^{\mathrm{ART}} = 0.48R_i$) leads to the localization of the branch within a morphometric pulmonary artery tree, and to the definition of the corresponding arterial sub-tree. A Windkessel model consisting of two resistances (R_p^{ART}, R_d^{ART}) and one capacitance (C^{ART}) is generated from the Womersley-based impedance of this sub-tree [SFP+07],[TTFVC11]. Hence the proximal to distal pulmonary artery resistance ratio is different for each outlet. The capacitance in the venous tree is 5.7 bigger than in the arterial side. Combining all these

relations determines a unique set of reduced parameters for each outlet i based on its total resistance.

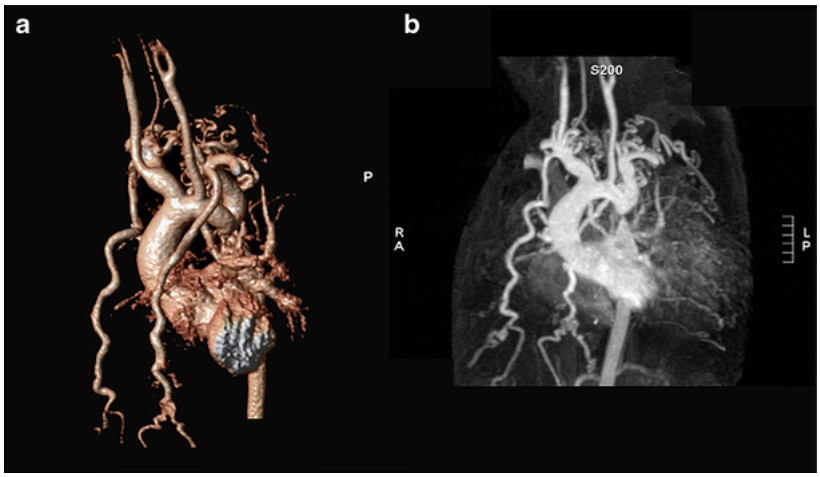

Figure 3.3: Magnetic resonance imaging representing collaterals in aortic coarctation pathology [LBMdW12].

Collaterals vessels The last point that we have to take into account is the added mass of fluid due to the collaterals vessels. In this context, the blood vessel collateralization is the growth of blood vessel between systemic and pulmonary circulatory systems (Figure 3.3). In fact, small vessels are linked from ascending aorta to the pulmonary arterioles and pulmonary veins. We do not know with accuracy in which proportion the collaterals are joined to the artery versus venous sides, but as they join in the smaller vessels, their localization within the reduced model was decided with the clinicians as after the second resistance. The only quantity that we know is the added flow coming from collaterals into the left and right lungs. Theses values are deduced from CMR in pulmonary veins. We then have the following quantities: the blood flow into the left pulmonary artery (Q_{LPA}) and the right pulmonary artery (Q_{RPA}), and the blood flow into the left pulmonary vein (Q_{LPV}) and the right pulmonary vein (Q_{RPV}). Then, we deduce the flow coming from collaterals in the left (Q_{LC}) and right (Q_{RC}) sides as follow:

$$\begin{aligned} Q_{\text{LC}} &= Q_{\text{LPV}} - Q_{\text{LPA}} \\ Q_{\text{RC}} &= Q_{\text{RPV}} - Q_{\text{RPA}} \end{aligned} \tag{3.7}$$

We assume that collaterals are uniformly distributed in the arterial side. We then define P_i the pressure at outlet i obtained by 3D simulations at the end

of tuning, and Q_i^c the equivalent blood flow rate due to the collaterals into the arterial subtree of the outlet i computed as follow,

$$\begin{aligned} Q_i^c &= \frac{S_i}{\sum_j S_j \delta_{ij}} Q_{\mathrm{LC}}, \text{ on the left side} \\ Q_i^c &= \frac{S_i}{\sum_j S_j \delta_{ij}} Q_{\mathrm{RC}}, \text{ on the right side} \end{aligned}$$

where $\delta_{ij} = 1$ if the outlet i is in the same side as outlet j and $\delta_{ij} = 0$ if not.

In addition we define an equivalent pressure at lung level by P_{L}, the atrial pressure P_{at} coming from clinical measurements, and the total resistance R_i^{tot} due to the arterial and venous tree downstream the outlet i taking into account the collaterals. We obtain the following model,

$$R_i^{\mathrm{tot}} = \frac{P_i - P_{\mathrm{L}}}{Q_i} + \frac{P_{\mathrm{L}} - P_{\mathrm{at}}}{Q_i + Q_i^c} \tag{3.8}$$

Using (3.8) and since we assume that the collaterals are linked to the pulmonary circulation between arterial and venous sides (after R_d^{ART}), (3.6) becomes,

$$R_i = 0.48 R_i^{\mathrm{tot}} + 0.52 R_i^{\mathrm{tot}} \left(1 + \frac{Q_i^c}{Q_i}\right) \tag{3.9}$$

In the equation above, only R_i^{tot} is unknown. Once it is computed, on can deduce the total resistance on the arterial side ($0.48 R_i^{\mathrm{tot}}$). The latter leads as without collaterals to the localization of the branch within a morphometric PA tree, and to the definition of the corresponding arterial sub-tree. An impedance consisting of two resistances and one capacitance is generated as before. The capacitance of the venous tree is assumed to be unchanged by the presence of collaterals, and thus still 5.7 bigger than that of the arterial side. We thus calibrate 3-element Windkessel parameters in the arterial side and venous resistance and capacitance taking into account the effect of collaterals.

In a next step, the three dimensional Navier-Stokes equations can be coupled to these reduced models at the outlets for more complete pulsatile simulations. A preoperative overview of the hemodynamics in the pulmonary arteries of each patient is thus generated in order to investigate several palliative surgical options (work in progress within the Leducq network).

3.3 Results

The Results section presents the demonstration of this framework on three stage 2 single ventricle patients, defining their specific simulations parameters and reporting their 3D pressure, flow and wall shear stress.

3.3.1 Outputs of simulation set up for each patient

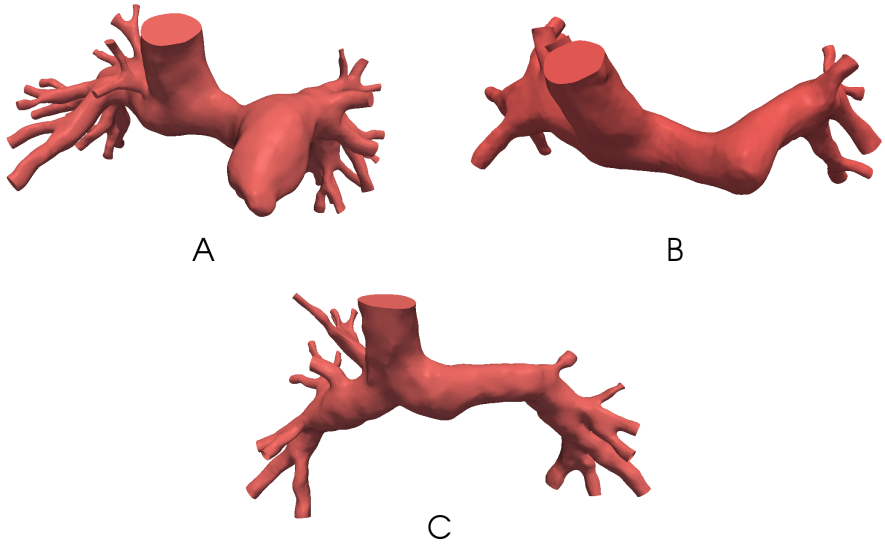

Figure 3.4: 3D geometrical model of patients A, B and C

Anatomy of each patient was reconstructed from CMR data with the commercial software Mimics (Materialise, NV, Leuven, Belgium). After selection of the vasculature of interest, based on the geometric constrains that might affect stability and accuracy of numerical simulations of blood flow, a three-dimensional volume was obtained for each of the components, following operations of segmentation and region-growing described in details in [ABD+07],[SMC+07]. In Figure 4.1, we present the resulting 3D geometries of patients A, B and C done by the London group. Furthermore the geometry includes the region where the future virtual surgery will be performed.

For each of these 3D models, finite element meshes were created with the commercial software MeshSim (Simmetrix Inc., Clifton Park, MY). All 3D geometrical models included an inlet which is the SVC and a number of pulmonary branch outlets depending on the CMR images resolution. 3D meshes of patients A, B and C contain respectively 614K, 845K and 744K tetrahe-

dra. The clinical data that we want to match are the flow split and the SVC pressure. For patients A, B and C we should recover a flow split equal to 0.50, 0.615 and 0.54 respectively, and an SVC pressure equal to 11, 12 and 10 mmHg respectively. Table 3.1 presents the tuning results: for the three patients, flow splits are the same as the target ones, and the target pressures are reached within at most 0.5 mmHg.

Patient	A	B	C
Age (months)	43	38	41
BSA (m^2)	0.62	0.59	0.61
Inflow (cm^3/s)	26	17.9	12.5
Re_{max}	1350	1250	800
fs	0.5	0.61	0.54
SVC pressure (mmHg)	12.8	12.7	13.5
fs^{3D}	0.5	0.61	0.54
P_{in}^{3D} (mmHg)	12.3	12.7	13.4

Table 3.1: Clinical measurements and numerical results (red) obtained by using tuning approach.

3.3.2 Pressure

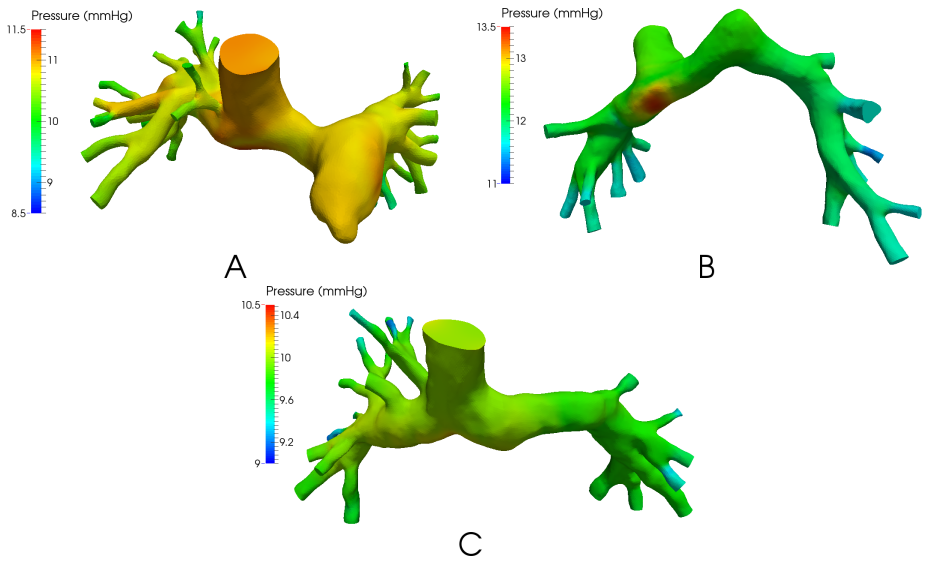

Figure 3.5: Pressure maps for patients A, B and C.

We present in Figure 3.5 pressure map for each patient at the end of the tuning. There is a peak of pressure on the wall in front of the SVC for patient B while for patients A and C the maximal pressure is reached close to the inlet of the SVC. The maximal pressure for patients A, B and C are respectively 11.2, 13.6 and 10.4 mmHg. The patients A, B and C have homogeneous pressure at both pulmonary arteries respectively around 10.4, 11.1 and 9.4 mmHg.

3.3.3 Velocity streamlines

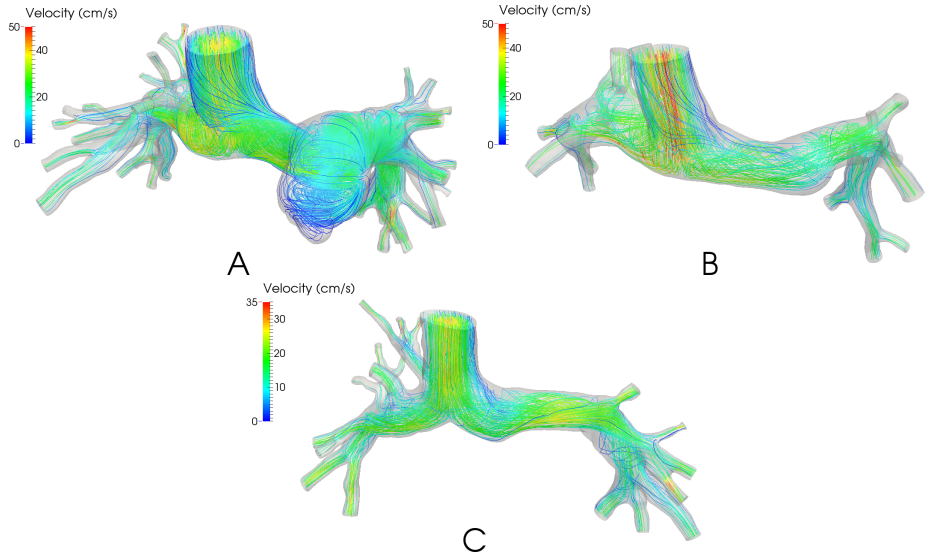

Figure 3.6: Streamlines of patients A, B and C colored by velocity magnitude.

We present in Figure 3.6 blood flow behavior for each patient at the end of the tuning. We can observe complex flow in the 3D domain. Indeed, the maximal flow is obtained in the center of the SVC because we impose parabolic velocity profile and there is no downstream constriction. The inlet surface areas of patients A, B and C are respectively 1.30, 7.17 10^{-1} and 8.79 10^{-1} cm^2. Highest velocity is respectively equal to 39, 49 and 28 cm/s. For patients A, B, and C the blood is swirling in the pulmonary arteries close to the SVC and goes toward the outlets smoothly with less complexity. We can also see a recirculation into the main pulmonary artery stump for patient A. This information provides an important information to the clinicians because blood recirculation can involve clots responsible for pulmonary embolism.

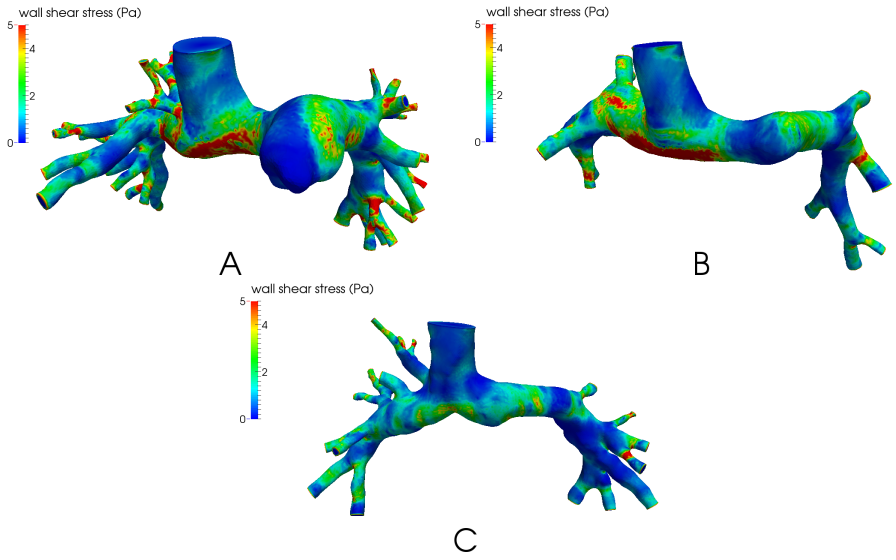

Figure 3.7: Wall shear stress map of patients A, B and C in Pa. Maximum color scale is fixed at 5 Pa but the maximal wall shear stress is in fact larger.

3.3.4 Wall shear stress

We present in Figure 3.7 the wall shear stress for each patient at the end of the tuning. For patients A and B the maximal wall shear stress is reached where there is a peak of pressure and for patient C the maximal wall shear stress is reached in smallest branches close to outlets and are respectively equals to 7.8, 9.3 and 5.9 Pa. These values are in agreement with typical stage 2 wall shear stress values [TTFVC11].

3.4 Conclusion

In Table 3.1 we recall the clinical measurements and we compare it to the numerical results obtained after tuning: an excellent match is reached, well below the measurement uncertainty. Patients taken into account for this work are between 38 and 43 months old with BSA between 0.59 and 0.62 m^2. We can see a large difference between imposed flow rates (from 12.5 to 26 cm^3/s) leading to Reynolds numbers (from 800 to 1350) computed at the SVC with the maximum velocity much lower than for stage 1 patients (next chapter).

Our methodology to tune reduced model parameters allows to accurately recover clinical measurements. Moreover, we provide three-dimensional

hemodynamics at the level of the SVC anastomosis and downstream, that are difficult to 'see' by imaging, although 4D MRI techniques are improving to get the velocity information.

Moreover we obtain homogeneous distribution of pressure at both pulmonary arteries. Regarding blood flow behavior we highlight the complexity of the flow in the 3D domain. In particular, we show a recirculation into the main pulmonary artery stump for patient which receive ligation of the main pulmonary artery.

Here we assume that the walls of the 3D geometrical models are rigid because we do not know the data for the heterogeneous assessment of the wall parameters. Moreover, the anastomosis is rigidified because of sutures.

A last point concerns the using of reduced models composed by three resistances and two capacitances generated with our methodology. These parameters are integrated as input into a reduced model representing the whole circulatory system described in Figure 1.5, and then coupled to three dimensional Navier-Stokes equations in possible stage 3 geometrical models (step 4 in Figure 1.4).

In the next chapter, we enrich this methodology for the first palliative surgery in congenital heart disease, extending it to pulsatile simulations. At this stage, the geometry is smaller and the maximal Reynolds number is higher. Moreover the clinical measurements are more difficult to accurately obtain, and only averages over certain regions are given. Tuning parameters of reduced model is then much more challenging.

Chapter 4

Multiscale modeling of stage 1 procedure

We present a method to iteratively tune parameters of reduced models from clinical measurements. This method is based on the one presented in chapter 3, and extended for steady state and pulsatile 3D simulations taking into account different locations of clinical measurements in pulmonary circulatory system. We illustrate our methodology with the estimation of the parameters of 5-element reduced models for six patient-specific models.

The work of chapter 3 and this chapter lead to the article:
Gregory Arbia, Chiara Corsini, Catriona Baker, Giancarlo Pennati, Tain-Yen Hsia and Irene E. Vignon-Clementel **Multiscale modeling of pulmonary hemodynamics in first stage single ventricle patients: integrating clinical data and simulations** *submitted*

Contents

4.1 Introduction

Single ventricle defects are a spectrum of congenital heart disorders resulting in only one functional ventricle. Several stages of palliative surgery are required to connect the systemic and pulmonary circulations to the single ventricular power source. The first stage commonly utilises a shunt between the aorta, or its branches, and the pulmonary arteries. Accurate modeling of patient-specific physiology for clinical decision-making requires the integration of the patient's clinical data into numerical simulations [VCMF10].

Computational fluid dynamics studies of single-ventricle conditions [BdLM+03],[dZMFY10],[VCFJT10], have presented the crucial interest of specifying the relevant boundary conditions. More specifically in [MPD+01] authors investigated the effect of clinical parameters such as shunt, vasculature and heart rate on stage 1 procedure. Taking into account the effect of the downstream domain by coupling 3D Navier-Stokes equations to 0D models, local fluid dynamics due to changes in anatomical features were investigated for this stage or their virtual surgical options [CBK+13], [KBB+13]. In [QLI+10] the authors presented computational hemodynamics simulations but in the systemic circulation of one specific stage 1 case with aortic arch repair and Damus-Kay-Stansel anastomosis. The distribution of flows among the outlets was not directly controlled since a zero pressure gradient method was applied at the end of very long extensions to recover a physiological pressure level. The pressure results were compared with pressure measurements at three locations in the aorta.

A first idea consists of manually tuning parameters, which requires hemodynamics intuition [PCC+11] and has been experienced to be out of reach if there are many branches. Automatic parameter estimation methods have thus been developed. In [ST10], six parameters of an aortic model were estimated with a quasi-Newton method to achieve some pressure and flow waveform features inside the 3D model. In [IWG13], the Windkessel parameters of 3D bifurcating aneurysm were estimated with an adjoint-based method to match systolic, diastolic and average pressure differences. In [BMG12], wall displacement values were used to estimate the stiffness of the 3D fluid-solid interaction idealized aneurysm model and its outlet proximal

resistance, based on a sequential estimation approach. In [PFGVC14], a dozen of Windkessel parameters in a 3D coarctation model were estimated with a Kalman filter approach on a corresponding 0D surrogate model of the 3D-0D model, to match given flow and pressure waveforms inside the 3D domain.

In this chapter we present a CFD analysis of the blood flow behavior in the distal anastomosis of the systemic-to-pulmonary shunt and the connected pulmonary arteries over several bifurcations, in six different patients. At the 3D outlets, it would not be relevant to apply pressure boundary conditions for the following reasons: 1) the measured flow distribution between the two different lungs cannot be easily matched, and 2) the pressure measurements were not performed at these locations in the pulmonary arteries. Sometimes, applying the same pressure at all outlets can even lead to unphysiological reverse average flow in some of the branches. Applying time-varying flow boundary conditions would also be difficult because the flow distribution between the different outlets is not necessarily constant, and would not guaranty to be coherent with the pressure measurements. Moreover, prescribing pressure or flow reduces the predictive potential such as in virtual surgery planning. We thus aim at coupling 3D Navier-Stokes equations to reduced models including resistances and capacitances. A previous work [TTFVC11] introduced a method to iteratively tune reduced order parameters of the 3D model to match clinical inlet average pressure, inlet average flow and outlets' flow repartition. The method was illustrated on coupling of 3D steady Navier-Stokes equations to total outlet resistances of dozens of branches in Stage 2 (Glenn) patient-specific simulations. From these resistances, 3-parameter Windkessel models were generated to represent the downstream arterial tree, neglecting the venous circulation. In chapter 3, the results were based on the former work [TTFVC11] to iteratively tune reduced model parameters to match clinical inlet average pressure, inlet average flow and outlets flow repartition. The methodology was illustrated on coupling of 3D steady Navier-Stokes equations to total outlet resistances. Moreover, the downstream reduced models of the pulmonary circulation was enriched to a 5-element parameter model representing more specifically the arterial and venous circulations.

In this chapter we extend the method to iteratively tune reduced parameters for more general pressure clinical data localization, as clinical data are rarely given at the specific 3D boundaries. The methodology is demonstrated for steady and pulsatile cases, with clinical data of stage 1 patients. The highly complex fluid dynamics of this stage is analyzed. Moreover, the downstream

reduced models of the pulmonary circulation is enriched as in chapter 3 to a 5-parameter model representing more specifically the arterial and venous circulations.

The chapter continues with section 4.2 to present the different steps of the algorithm, from clinical data, automatic parameters tuning to the final reduced pulmonary model generation for each outlet. The Results section presents then the demonstration of this framework on six stage 1 single ventricle patients, reporting their specific 3D hemodynamics. A discussion follows on methodological, biomechanical and clinical aspects.

4.2 Methods

The Methods section presents the type of clinical data that define the patient-specific geometry and hemodynamics target values. The automatic reduced model parameters tuning to reach these target values is explained. In this work six patient-specific computational models were built to describe hemodynamics into the corresponding three-dimensional regions of interest, reflecting the patient state in coherence with the clinical measurements acquired before stage 2 surgery.

4.2.1 Clinical cases

Patients A, B and C were recruited at the University of Michigan, Ann Arbor, MI, USA; patients D and E at Medical University of South Carolina, Charleston, SC, USA; and patient F recruited at Great Ormond Street Hospital, London, UK. The study was approved by the institutional review board at each institution and consent was obtained from the subject's legal guardian.

Patient A had a diagnosis of pulmonary atresia with intact ventricular septum. The stage 1 surgery comprised a central shunt, from the ascending aorta (AoA) to the main pulmonary artery (MPA). This patient was 6 months old at time of cardiovascular magnetic resonance imaging (CMR), with body surface area (BSA) of 0.34 m^2. Patients B, C, D and F had hypoplastic left heart syndrome. Their stage 1 operations were all 3.5 mm right modified Blalock-Taussig shunts (rmBT). These patients were 4, 5, 5 and 4 months old at time of CMR, with BSA of 0.28, 0.34, 0.30 and 0.27 m^2 respectively. Patient E had tricuspid and pulmonary atresia, and underwent stage 1 surgery of a 4 mm rmBT, with additional left pulmonary artery patch to treat a left pulmonary artery stenosis. This patient was 3 months old at time of CMR, with BSA of 0.26

m^2.

4.2.2 Clinical measurements

For patients A, B and C, CMR was performed immediately prior to the second surgery under the same general anesthetic, and cardiac catheterization was performed respectively 3 days, 1.5 months and 1 week prior to the second surgery. CMR and cardiac catheterization were performed on the same day, 1.5 months prior to the second surgery for patient D; and 1 month prior for patients E, and F. Flows were quantified by cardiac-gated CMR, and thus they give in the best case cycle-averaged time-varying information. For patients A and D, flows were measured in the branch pulmonary arteries; and for patients B, C, E and F, in the pulmonary veins, for which only time-averages are equal to the corresponding arterial flows. The total pulmonary flow (inflow) was obtained by adding the left and right sided pulmonary flows, and was imposed at the inlet surface (shunt). The mean values are reported in Table 4.1. Catheterizations were performed in the common atrium and on the venous side, by a pulmonary venous wedge pressure as a surrogate of the pulmonary artery pressure. Pressure differences between left and right sides were either measured or considered negligible (0-1mmHg), except for patient D. The values defined as target pulmonary arterial pressures are reported in Table 4.1.

The main challenge of this study is to determine outflow boundary conditions for each patient-specific model that are consistent with the clinically measured data: 1) time-average flow distribution between left and right sides (flow split) denoted by fs and 2) pulmonary arterial pressure denoted by P_t, which is the target pressure to match, and which location and definition vary for each patient.

4.2.3 Numerical methods

The pre-operative anatomy of each patient was reconstructed from three-dimensional contrast enhanced CMR data using commercial software (Mimics, Materialise, NV, Leuven, Belgium). The vascular region of interest (the distal shunt and the pulmonary arteries extending to their first branches) was selected to include enough branches to avoid numerical instabilities or to largely include the future virtual stage 2 operative anastomosis [CBK+13, KBB+13], without going beyond the branches for which the image resolution would affect the simulation accuracy. A three-dimensional surface was thus obtained, following operations of segmentation and region-growing

described in details in [ABD+07, SMC+07].

For each of these 3D models, finite element meshes were generated with the commercial software MeshSim (Simmetrix Inc., Clifton Park, MY). Resulting meshes were anisotropically adapted to the flow in several steps [MSL+05, SMJ+06].

In order to understand hemodynamics in these single ventricle geometries and reflect the effect of the downstream vascular trees, rigid-wall Navier-Stokes equations were solved in three-dimensional models, coupled to zero-dimensional models (Figure 3.2). This multidomain approach and its monolithic numerical implementation are described in details in [VCFJT06, VCFJT10]. All simulations were performed with a custom version of finite element Navier-Stokes solver, SimVascular (http://simtk.org), assuming blood as an incompressible Newtonian fluid with a density of 1060 kg m^{-3} and a dynamic viscosity of 0.004 Pa s.

4.2.4 Tuning of total resistances

We place ourselves in the framework of the section 3.2.2 in order to iteratively tune total resistances at each outlet of the 3D domain. A first part consisted of iteratively tuning a total resistance at each outlet by coupling 3D Navier-Stokes equations to a resistance with a fixed point method until recovering: 1) the measured transpulmonary gradient between the superior vena cava and the left atrium, and 2) the pulmonary flow split. Here this method is extended in order to take into account the different locations of measured pulmonary arterial pressure: instead of only handling situations where the measured pressure coincides with the pressure at one boundary of the 3D domain (the inlet), the former can be more general as will be explained below. This changes the way the outlet parameters are updated at each tuning iteration, and possibly the algorithm convergence. The framework presented below is the same for steady and pulsatile simulations.

We take the same notations for the flow split (fs) defined in (3.1), the proportionality law between flow (Q_i) at outlet i and surface area of the latter (3.2), and the target flow rate at outlet i (3.3).

A first value of R_i at each outlet is estimated to initialize the algorithm. This serves as the boundary condition for a first 3D Navier-Stokes simulation that is run during enough time steps in order to reach stable state results, typically a few 100 time steps for steady simulations and four cardiac cycles

for pulsatile simulations. Note here that even in case of steady inlet flow (so called "steady simulations"), the resulting 3D flow is unsteady due to its complex interaction with the patient-specific geometry. Therefore, we use a transient formulation even for steady boundary conditions.

By post-processing the results over the last stable period, time-averaged (and mean in space) pressure (P_i^{3D}) and flow rate (Q_i^{3D}) are computed at each outlet. A flow split (fs^{3D}, based on the sum of the flows Q_i^{3D} on each side), and a controlled pressure (P_c^{3D}) that varies according to the measurement location and clinician input, are then calculated. Note that the exact pressure measurement location was unknown, hence this controlled pressure could not be related to the output pressure at a specific location in the 3D domain. Rather, if catheterization was performed on the left pulmonary side, P_c^{3D} is the average pressure over all the outlets of the left side (P_i^{3D}, $i \in [0, N]$ for N the number of left pulmonary outlets). Sometimes, there were several measurements done on one or both sides; P_c^{3D} is then defined with the clinical expert as being the maximum or the minimum value over all the corresponding branches of number N, e.g.

$$P_c^{3D} = \min_i P_i^{3D}, i \in [0, N] \tag{4.1}$$

These different options define *the measurement for tuning* and *control method* reported in Table 4.1.

The results are then compared to the target values, by defining error on pressure and flow rate,

$$\begin{aligned} \varepsilon_P &= \frac{|P_t - P_c^{3D}|}{P_t} \\ \varepsilon_Q &= \left(\frac{1}{N} \sum_{i=1}^{N} \left(\frac{Q_i^{3D} - Q_i}{Q_i} - \frac{1}{N} \sum_{i=1}^{N} \frac{Q_i^{3D} - Q_i}{Q_i} \right)^2 \right)^{\frac{1}{2}} \end{aligned} \tag{4.2}$$

where N is the number of outlets.

If convergence is not reached within a certain tolerance, the resistance at each outlet is updated as follows:

$$R_i = \frac{P_t - (P_c^{3D} - P_i^{3D})}{Q_i} \tag{4.3}$$

Another 3D simulation is run coupled to the new set of resistances R_i, where

$i \in [0, N]$ for N outlets. This process is repeated until convergence.

When pulsatile tuning simulations are performed, which can be important to better capture nonlinear effects across the 3D domain, resistances are also applied as boundary conditions, while pulsatile flow is imposed at the inlet. The controlled variables (P_c^{3D}, Q_i^{3D}) are then the time-averaged values over the last cardiac cycle.

The steady tuning simulations were performed for all the six patients, whereas the pulsatile ones only for patients A and E due to time-varying arterial inflow issues.
An additional step could be naturally included between the update of equation 4.3 and the next 3D iterative run, to update and impose more complex downstream reduced models, such as the one presented in the next section. This was not done here because the time-varying target pressure measurements were not available. Hence for each outlet, the 5-parameter reduced model was derived from the total resistance, with a combination of modeling and literature data, as in chapter 3. In a next step, the three dimensional Navier-Stokes equations can be coupled to these reduced models at the outlets for more complete pulsatile simulations. A preoperative overview of the hemodynamics in the pulmonary arteries of each patient is thus generated in order to investigate a palliative surgery [CBK+13, KBB+13].

4.3 Results

The Results section presents the demonstration of this framework on six stage 1 single ventricle patients, defining their specific simulations parameters and reporting their 3D pressure, flow and wall shear stress.

4.3.1 Outputs of simulation set up for each patient

Figure 4.1 shows the reconstructed 3D geometries of patients A, B, C, D, E, and F.
All 3D geometrical models included an inlet which is the distal shunt and a number of pulmonary branch outlets as described in the methods. The inlet surface areas of patients A, B, C, D, E, and F are respectively 3.39 10^{-2}, 1.27 10^{-1}, 1.83 10^{-1}, 6.21 10^{-2}, 6.29 10^{-2} and 5.93 10^{-2} cm2. The 3D meshes of patients A, B, C, D, E and F contain respectively 715K, 970K, 1050K, 1500K, 710K and 1540K tetrahedra. Recall that the clinical data are the flow split between the right and left lungs and a pulmonary pressure. For

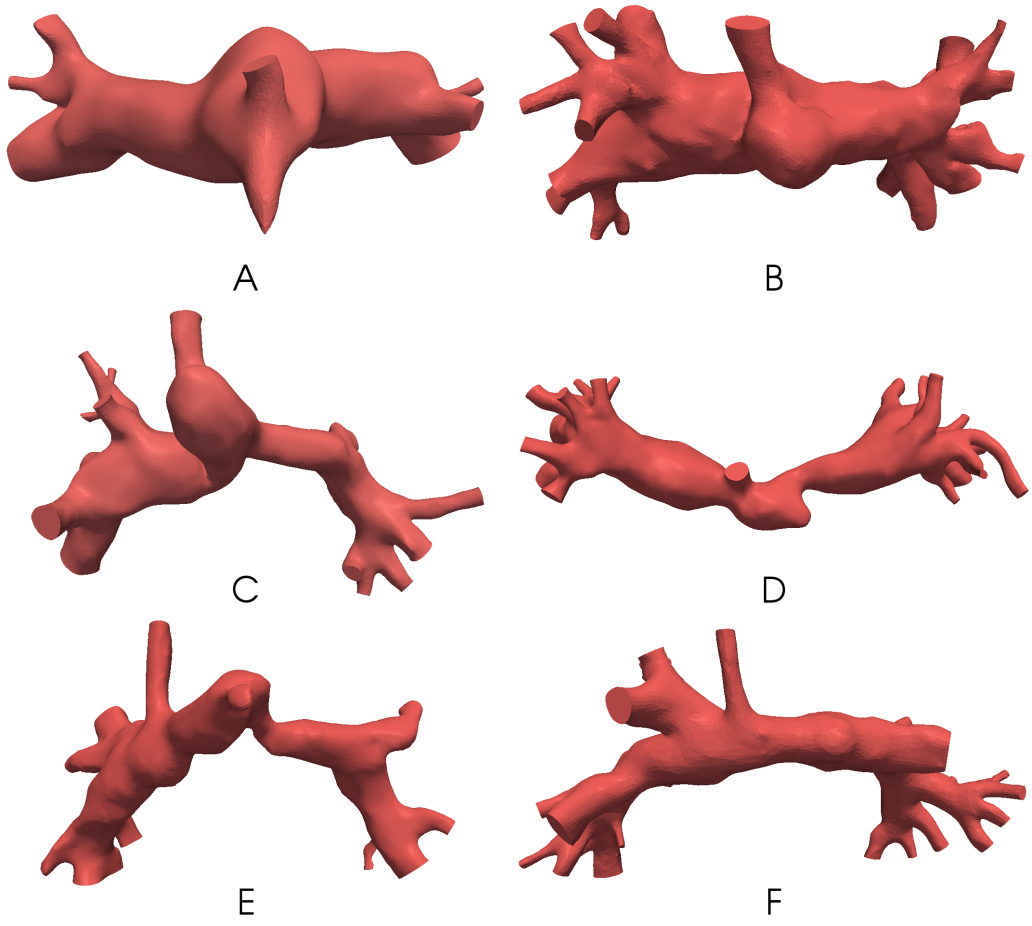

Figure 4.1: 3D geometrical model of patients A, B, C, D, E, F.

patients A, B, C, D, E, and F, we should recover a flow split equal to 0.64, 0.46, 0.55, 0.46, 0.67 and 0.52 respectively, and a pulmonary arterial pressure equal to 12.8, 12.7, 13.5, 12, 14 and 11 mmHg respectively, depending on the location where the clinical measurements were performed. Table 4.1 reports the pressure measurement location chosen for the tuning and the controlled value (average, minimum or maximum over branches of the measurement location) that was set by the clinicians. The pressure difference between the right and left pulmonary artery sides was negligible, except for patient D where it was 3 mmHg. Table 4.1 also reports the tuning results. Steady tuning was run for every patient: the results are very close to the targeted clinical data. For the first patient, pulsatile tuning was also performed for patient A and led to results of 0.64 for the flow split, 12.4 mmHg for the pulmonary pressure and 0.4 mmHg for the pressure difference, all very close to both steady tuning and targeted clinical values. For patient E, who was the only case with significant pressure difference between right and left lungs, results are 0.67, 17 mmHg and 3 mmHg respectively, also very close to both steady tuning and targeted clinical values. As a consequence, the next paragraphs only report the 3D results of the steady tuning.

Patient	A	B	C	D	E	F
Age (months)	6	4	5	5	3	4
BSA (m^2)	0.34	0.28	0.34	0.30	0.26	0.27
Inflow (cm^3/s)	7.5	12	20	9.7	12	16.6
Re_{max}	2300	1750	2900	2500	3000	4150
fs	0.64	0.46	0.55	0.46	0.67	0.52
PA pressure (mmHg)	12.8	12.7	13.5	12	17	11
$\Delta P_{L/R}$ (mmHg)	negl.	negl.	negl.	negl.	3	negl.
Meas. location for tuning	both	LPA	LPA	both	RPA	both
Control method	average	average	average	average	min	max
fs^{3D}	0.64 (0.64)	0.46	0.55	0.46	0.66 (0.67)	0.52
P_c^{3D} (mmHg)	12.3 (12.4)	12.7	13.4	12.0	17.0 (17)	11.0
$\Delta P_{L/R}^{3D}$ (mmHg)	0.4 (0.4)	0.7	0.5	6.0	3.0 (3)	0.2

Table 4.1: Clinical measurements, numerical method and results. For each patient, clinical data (age, BSA, average pulmonary inflow, deduced Reynolds number Re_{max}, flow split fs, target pulmonary artery pressure value, negligible or not left/right pulmonary pressure difference), tuning set-up (left or right pulmonary side, and control method to define P_c^{3D}), and numerical results in red (obtained flow split fs^{3D}, controlled pressure P_c^{3D} and pressure difference between left and right sides $\Delta P_{L/R}^{3D}$). Numbers are for the steady tuning and in parenthesis for the pulsatile tuning.

4.3.2 Pressure distribution

We present in Figure 4.2 the pressure map for each patient at the end of the tuning. We observe a high peak of pressure on the wall. The maximal pressure for patients A, B, C, D, E and F are respectively 52, 26, 25, 45,

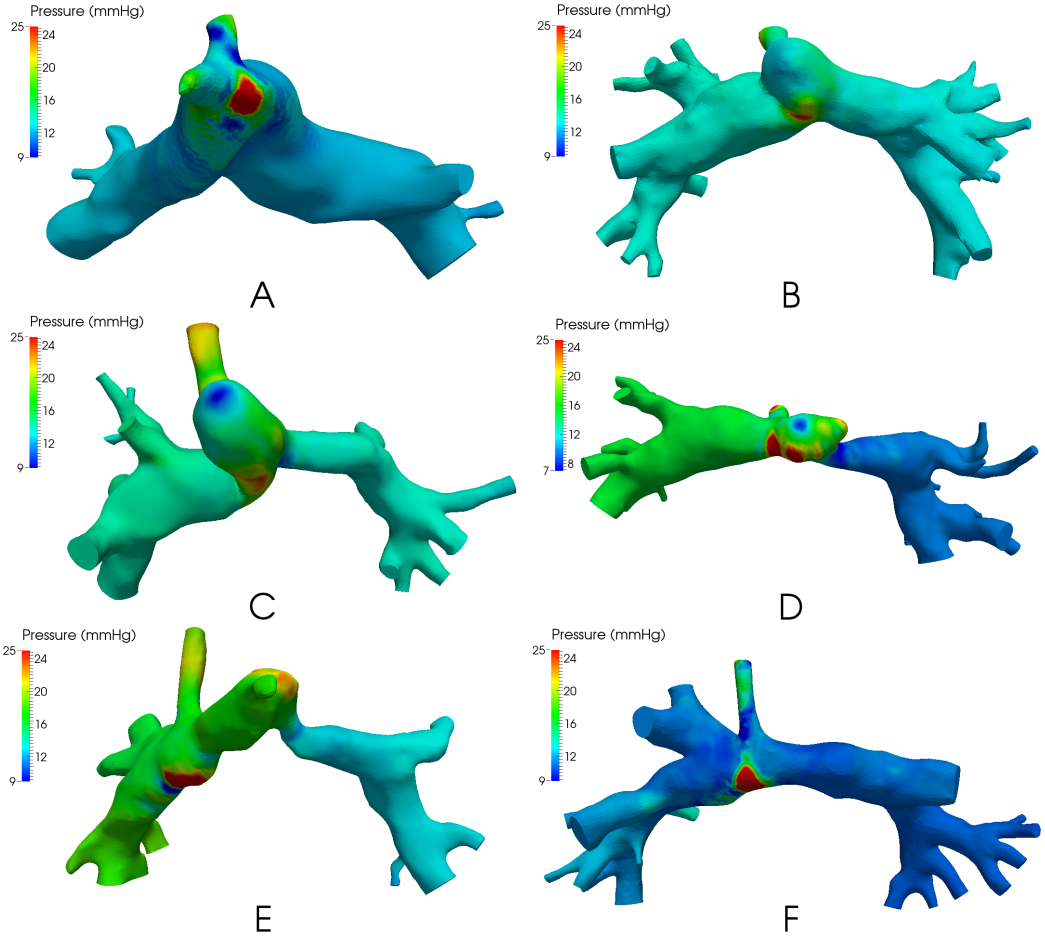

Figure 4.2: Pressure maps for patients A-F. Maximum pressure is equals to 25 mmHg on the color scale, even if the real maximal pressure is larger. 1 mmHg = 133.3 Pa.

62 and 74 mmHg. The patients A, B and F have homogeneous pressure in both pulmonary arteries respectively, approximately 12, 13 and 11 mmHg. Moreover, patients D and E have a left pulmonary artery (LPA) stenosis which involves a significant pressure loss of approximately 3 mmHg across the stenosis, while homogeneous pressure is found in the right pulmonary artery (RPA). A last remark concerns patient C who has a kink in the RPA close to the shunt. The kink does not generate a significant pressure loss and pressure is homogeneous in both PAs, around 13.5 mmHg.

4.3.3 Velocity patterns

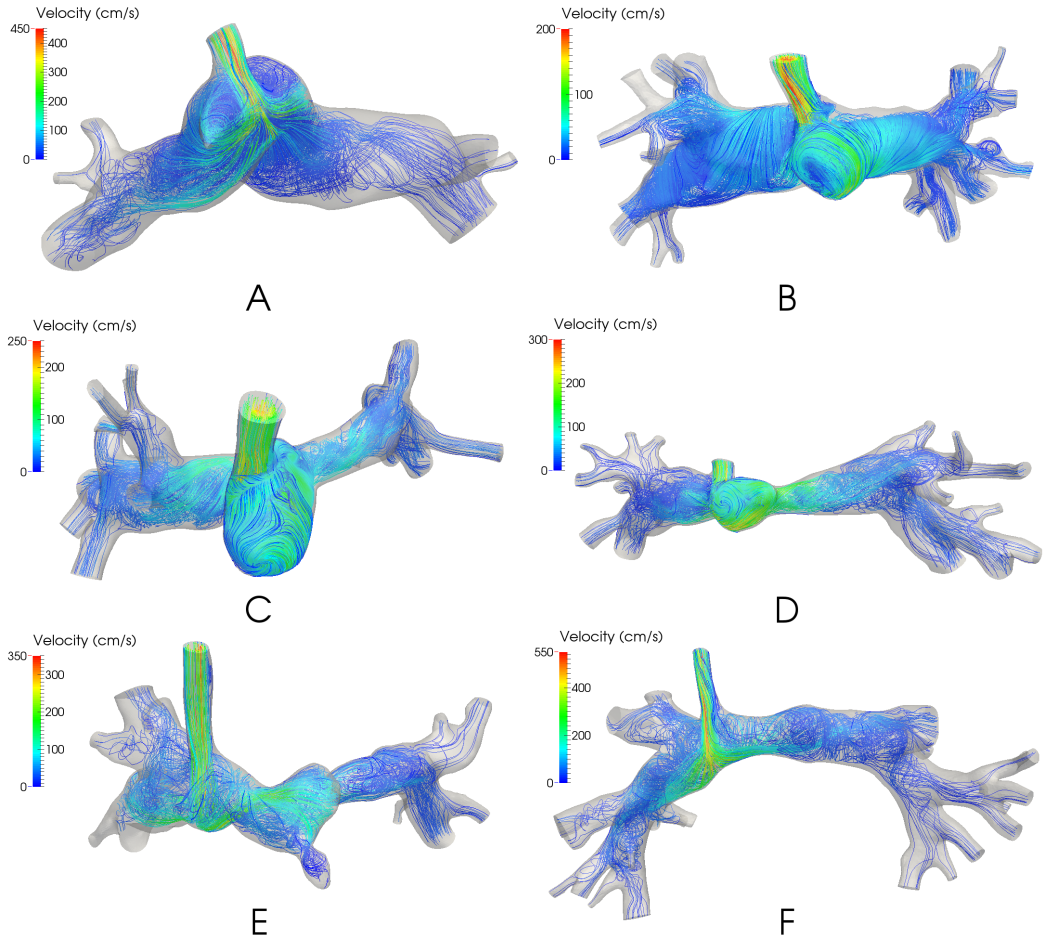

Figure 4.3: Streamlines of patients A-F colored by velocity magnitude.

In Figure 4.3 blood flow patterns for each patient are presented at the end of the tuning. A very complex flow can be observed in the 3D geometrical domain, especially close to the shunt where blood flow is the highest. Highest

velocity is obtained in the center of the shunt and is respectively equal to 470, 250, 265, 319, 377 and 570 cm/s. For patients A, B, and F the blood is swirling in the pulmonary arteries close to the shunt and goes towards the outlet smoothly with less complexity. This mixing flow behavior occurs into the main pulmonary artery stump for patients B, C, and D where the anastomosis of the ligated main pulmonary artery is prominent. For patient E, swirling reflects the tortuous geometry on the left side, where there are a constricted anastomosis of the ligated main pulmonary artery, followed by a stenosis.

4.3.4 Wall shear stress maps

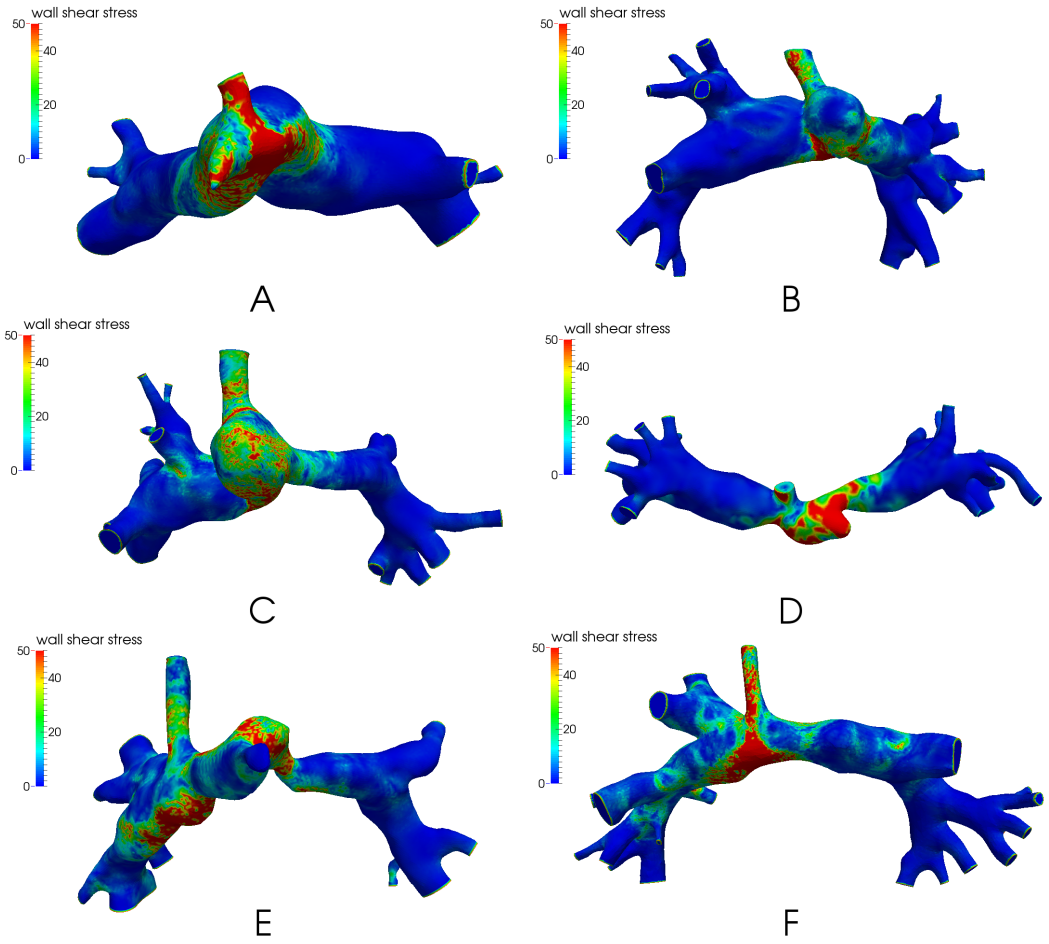

Figure 4.4: Wall shear stress map of patients A-F in Pa. Maximum color scale is fixed at 50 but the real maximum value is larger.

In Figure 4.4 the wall shear stress surface maps are represented for each

patient. For all patients the maximal wall shear stress is reached either in the shunt, or where there is a peak of pressure, respectively equal to 73.8, 55.3, 52.9, 66.3, 67.1, and 69.7 Pa.

Moreover, for patients D and E, the stenosis involves a large wall shear stress respectively equal to 54.3 and 61.4 Pa. Regarding patient A, where the main pulmonary artery was ligated the mean wall shear stress is 57.8 Pa, which is high compared to the rest of the domain. In contrast, in the corresponding location of patient E, the mean wall shear stress is close to 0.

Comparing patients B and C, which have a similar shape, the obtained mean wall shear stress is respectively equal to 17 and 40 Pa.

4.4 Discussion

4.4.1 Significance of the Results

The proposed methodology to tune reduced model parameters accurately replicates clinical measurements 4.1, at least within acceptable clinical measurement tolerance. Moreover, we highlight the high complexity of the blood flow patterns in pulmonary arteries in the context of the stage 1 single ventricle procedure.

Patients have a BSA between 0.26 and 0.34 m^2. The variability of the pulmonary flow rate - between 7.5 and 20 cm^3/s - leads to very high Reynolds numbers, between 1750 and 4150 when computed at the shunt inlet with the maximum velocity.

This leads to values of wall shear stress that are very high. They are in the same order of magnitude as in the aorta of a typical Norwood patient [QLI+10] (keeping in mind that the shunt is a direct connection from the aorta or brachial artery). In the Glenn circulation [TTFVC11], a typical wall shear stress is more than 10 times lower. For patients B and C, the main pulmonary artery was ligated, forming a sphere bulging out of the anastomosis, which might foster recirculation and thus low wall shear stress. Yet, the computed wall shear stresses were quite different. The relative differences in wall shear stress between patients may have some bearing on the development of the PAs, however, the stage 1 circulation is only present for a few months before second stage palliative surgery is required. Therefore, these effects will be of a fairly short duration.

The importance of the severe stenosis for the pressure drop and the swirling behavior of the blood flow was also shown. This complexity is induced by the high Reynolds number is in the shunt. For these stenosis cases and patient C with its kinks, computational fluid dynamics is a a complement to clinical measurements. One potential clinical application for this technique is to aid clinicians understanding of the significance of anatomical abnormalities in these complex patients. For example, patient C appears to have a significant geometric 'kink' or restriction in their RPA just distal to the shunt. Only a distal LPA pressure measurement was obtained clinically, so the hemodynamic effect of this lesion was unknown. However, simulation results clearly indicate that the pressure difference between the shunt anastomosis and the PAs are equal on the left and right sides. This was of interest to the clinicians, as the consensus was that judging by the anatomy alone, they would expect a pressure loss across the RPA. Indeed, at stage 2 surgery, patients A, C, D, and E all underwent patch augmentation of their central PAs or proximal LPAs judged on the appearance of the geometry alone. This work suggests that in some cases the clinician's perception of what constitutes a geometric abnormality may actually not result in a hemodynamically significant pressure difference, as in case C. Although, the tortuous course of the PA appears to constitute a stenosis, it is partly an illusion due to the distal PA having a relatively large cross-sectional area.

For patient D, a first attempt was to match the measured flow split of 0.46 and a pressure at both LPA and RPA side equal to 12 mmHg. Unfortunately, targeting the flow split to be 0.46 induced a pressure difference between left and right sides around 6 mmHg which was not acceptable from a clinical point of view. Discussions with clinicians led us to disregard the clinically measured flow split. By imposing the same pressure on average on each side, a flow split of 0.54 (more flow to the right side) was then found, which was clinically acceptable. The differences in flow split would correspond to an error of 0.78 ml/s (i.e. 8 %) in estimating flow with CMR. This example highlights the impact of uncertainty of measurements on the numerical simulations. It could be interesting to investigate more precisely the effect of uncertainties of pressure and flow split measurements on the pressure loss through the stenosis. This patient-specific example was thus challenging and required a close collaboration with clinicians. On the other hand, performing simulations underlined the incoherence between the original clinical measurements, and helped to assess together with the clinical experts which data made more sense to trust.

4.4.2 Methodology Discussion

The tuning methodology introduced in this work consists of coupling Navier-Stokes equations to reduced models (here resistances) at the outlets and running steady or pulsatile simulations. The *a priori* interest of running pulsatile simulation is the integration of all non linearities due to the 3D geometrical model and obtain a more accurate set of reduced model parameters. However, to achieve periodic stability, pulsatile simulations need to be run over 4 cardiac cycles (around 2000 time steps) and the iterative process is converging in 5 iterations, thus around 10000 time steps. In comparison, 100 time steps for a steady stimulation were enough and the iterative process converges in 4 iterations, thus around 400 time steps were necessary in total. Furthermore, pulsatile tuning for patients A and E were performed and both matched targeted clinical values and were very close to the steady tuning results. Moreover, the reduced model parameters were very close to those obtained by steady tuning. Indeed, for patients A and E the difference between steady and pulsatile tuning are respectively 6.37% and 7.82% in resistances, computed by the formula (4.2). Note that the same framework could be used to tune total capacitance values for example or even more parameters, if pulsatile pressure measurements were available in synchrony with the flow measurements [PFGVC14].

For sake of brevity, the 5 parameters of each branch for the six patients considered in this study are not presented in the results section. Such reduced models of the pulmonary circulation for each outlet have been incorporated into preoperative closed-loop simulations representative of the patient state before surgery. They have been then used to investigate different surgical options as in [CBK+13, KBB+13], keeping all these outlet blocks the same while changing the 3D part and its connecting inflow. Deriving this 5-parameter model of the arterial and venous pulmonary circulation has lead to more successful matching clinical time-varying tracings in the closed-loop simulations than the previous 3-component Windkessel model that neglected in particular the venous compliance.

A first source of uncertainty comes from the geometrical reconstruction for these young babies. The typical pixel size from 3D CMR angiography is $1 * 1\text{mm}^2$. In addition 3D CMR angiography may suffer from signal loss in areas of turbulent or complex flow. Thus including or excluding a pixel in a small area region, such as a shunt stenosis, may lead to errors in the 3D geometry. This kind of uncertainty should be addressed in future work. Where available, 2D CMR black blood imaging sequences were used

to check diameters at specific locations since spatial resolution is higher in this sequence. As a final check for each patient, a visual comparison was made between the 3D reconstruction and the 2D cardiac catheter angiography sequences. Patient D had the appearance of luminal narrowing with an obvious distal stenosis on catheter angiographic sequences. The 2D measurements were used to adjust the 3D reconstruction to give an accurate representation of the geometry in this region.

Branching bifurcations were included evenly on both sides, coherently with image resolution. Although a large number of branches increases computational time, cutting the branches before the first bifurcations on each side often leads to numerical instabilities, as was tested for patient A. Stabilizing the numerical scheme is then warranted [AGHVC], [MBH+11]. Note that sometimes, as was the case for patient F, the robust convective stabilization was not enough to avoid numerical divergence in the short model. Besides, as cutting branches or stabilization can change flow features close to the boundary, it is necessary to include enough branches to not affect the flow close to the current anastomosis or the one of the next stage virtual surgery.

Furthermore, in this work walls of the 3D geometrical models were assumed rigid because data for the heterogeneous assessment of the wall parameters were not known. Moreover, the shunt is a rigid graft and the anastomosis is also quite rigid because of sutures. If time-varying geometry data were available, the elasticity parameters could also be inferred [BMG12]. However, it has been shown that FSI has little effect at rest at least at later stage of the palliation [BGH+09].

Regarding the inlet boundary condition, since the velocity profile was not available, a parabolic profile was imposed at the inlet, which is commonly used for blood flow in arteries. We verified on one case that changing the profile to a flat velocity profile did not significantly change the pressure or the velocity fields.

The clinical hemodynamics measurements have uncertainties and it would be interesting to take it into account in a future work [TTFVC11]. Indeed it would be useful to investigate their effect on the pressure loss through stenosis and on the set of reduced model parameters.
A last comment regarding uncertainties of clinical measurements: in Figure 4.5 simulated velocity vectors for patient D are shown at the same locations as where flow measurements were done in CMR. We highlight the complexity of the blood flow patterns at these locations, which might explain the difficulty

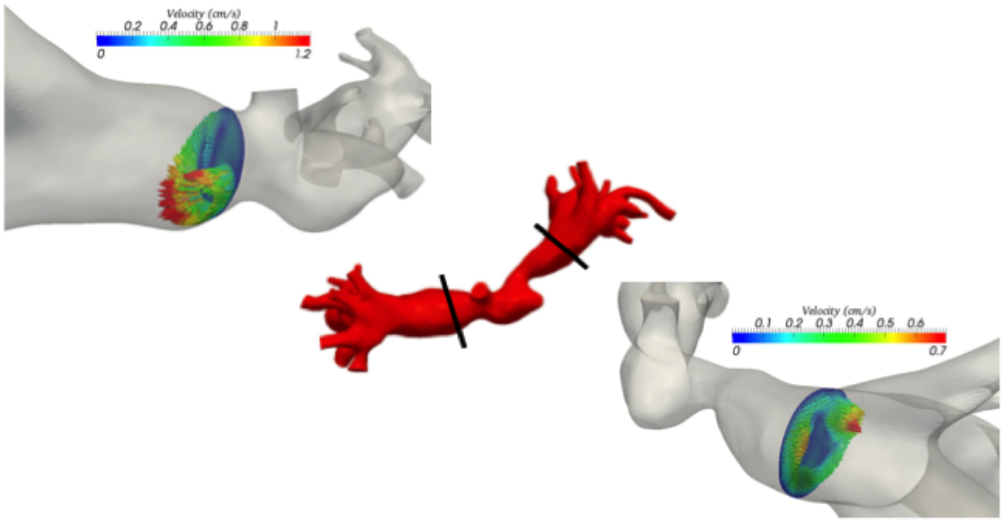

Figure 4.5: Velocity vectors (coloured by their magnitudes) from the 3D simulation shown at the locations where the CMR flow measurements were performed.

to get accurate clinical time-varying velocity measurements by CMR at these locations. The PAs are relatively small, and are receiving flow from the aorta, or one of its branches, at high pressure. CMR flow measurements are typically less reliable in areas of complex flow because unpredictable phase shifts occur. This often leads to signal loss (voiding) and inaccurate flow measurements [OKP95]. Typically, the PA flow measurements in this location would be underestimated in stage 1 patients. The pulmonary veins may represent a more stable location to measure the pulmonary flow split, however, the physiology of these patients sometimes leads to the pulmonary veins receiving additional blood flow external to the pulmonary arteries. It is only through the iterative process of comparing simulation results to clinical measurements that suitable strategies for managing measurement uncertainty are reached.

4.5 Conclusion

In this work we develop a method to iteratively tune parameters of reduced models of 3D blood flow simulations in order to reflect the effect of the downstream vasculature, taking into account clinical measurements of stage 1 single ventricle patients before they underwent the next palliative operation. This method was effectively demonstrated on six patients. It can be useful in other multi-branched blood flow simulations for which pressure or flow measurements are taken at various locations, and chosen to be matched as a minimum, maximum, average or other combinations of values in a given region.

Simulations in these stage 1 cases highlighted the complexity of the blood flow patterns into the shunt anastomosis and the pulmonary arteries, as well as the very specific pressure map. The wall shear stress was found to be very high in magnitude, but varying in space differently according to the patients anatomy, not necessarily leading to a low value in the ligated main pulmonary stump. Simulations also assessed the effects of anatomical kinks or stenoses, demonstrating the potential use of the technique: clinicians do not always know whether a lesion is hemodynamically significant. These types of simulations could be helpful when planning whether to intervene on a PA anatomical problem. It involves a lot more surgery to intervene on a PA stenosis so if clinicians better understood the difference between a significant stenosis and an anatomical anomaly that does not have an effect, it would save time and danger intervening when it was not necessary.

This methodology is moreover helpful for virtual surgical planning testing

different surgical approaches [CBK+13, KBB+13]. It is also shown to be a tool for clinicians to assess coherence of clinical measurements : the iterative approach between comparing clinical data and the simulation results emerged as efficient to understand the limitations in clinical measurements and decide upon a strategy to replicate the clinical case that makes sense to clinicians. This process raises the issue of the impact of uncertainty quantification of the clinical measurements.

Finally, this first work on single ventricle shunt anastomoses at stage 1 could be used to compare hemodynamics of different stages of the Fontan palliation.

4.6 Applications to predictive surgeries for congenital heart diseases

We present in Appendix possible applications of methodologies developed in chapters 3 and 4 for predictive modeling of single ventricle palliation. Theses two studies were done within the Modeling Of Congenital Hearts Alliance supported by the Leducq Foundation as part of the Transatlantic Network of Excellence for Cardiovascular Research.

A first study lead to the article:

Chiara Corsini, Catriona Baker, Ethan Kung, Silvia Schievano, Gregory Arbia, Alessia Baretta, Giovanni Biglino, Francesco Migliavacca, Gabriele Dubini, Giancarlo Pennati, Alison L. Marsden, Irene E. Vignon-Clementel, Andrew Taylor, Tain-Yen Hsia, Adam Dorfman, **An integrated approach to patient-specific predictive modeling for single ventricle heart palliation.** *Computer Methods in Biomechanics and Biomedical Engineering*, http://www.tandfonline.com/doi/pdf/10.1080/10255842.2012.758254, pages 1–18, 2013.

In this article, an integrated approach between clinicians and engineers has been developed, based on patient-specific multiscale models, and was applied to predict stage 2 surgical outcomes. This approach involved four distinct steps: (1) collection of pre-operative clinical data from a patient presenting for SV palliation, (2) construction of the pre-operative model, (3) creation of feasible virtual surgical options which couple a three-dimensional model of the surgical anatomy with a lumped parameter model (LPM) of the remainder of the circulation and (4) performance of post-operative simulations to aid clinical decision making. Two surgical options (bi-directional

stage 2 and hemi-Fontan operations) were virtually performed and coupled to the pre-operative LPM, with the hemodynamics of both options reported. This article presented the first patient-specific predictive modeling of stage 2 palliation using virtual surgery and closed-loop multiscale modeling.

A second study lead to the article:

Ethan Kung, Alessia Baretta, Catriona Baker, Gregory Arbia, Giovanni Biglino, Chiara Corsini, Silvia Schievano, Irene E. Vignon-Clementel, Gabriele Dubini, Giancarlo Pennati, Andrew Taylor, Adam Dorfman, Anthony M. Hlavacek, Alison L. Marsden, Tain-Yen Hsia, Francesco Migliavacca, **Predictive modeling of the virtual Hemi-Fontan operation for second stage single ventricle palliation: Two patient-specific cases.** *Journal of Biomechanics*, Volume 46, Issue 2, pages 423–429, 2013.

In this article, based on pre-operative data obtained from two patients prior to stage 2 surgery, we developed two patient-specific multi-scale computational models, each including the 3D geometrical model of the surgical junction constructed from magnetic resonance imaging, and a closed-loop systemic lumped-parameter network derived from clinical measurements. "Virtual" Hemi-Fontan surgery was performed on the 3D model with guidance from clinical surgeons, and a corresponding multi-scale simulation predicts the patient's post-operative hemodynamic and physiologic conditions. For each patient, a post-operative active scenario with an increase in the heart rate (HR) and a decrease in the pulmonary and systemic vascular resistance (PVR and SVR) was also performed. Results between the baseline and this "active" state were compared to evaluate the hemodynamic and physiologic implications of changing conditions. Simulation results revealed a characteristic swirling vortex in the Hemi-Fontan in both patients, with flow hugging the wall along the SVC to Hemi-Fontan confluence. One patient model had higher levels of swirling, recirculation, and flow stagnation. However, in both models, the power loss within the surgical junction was less than 13% of the total power loss in the pulmonary circulation, and less than 2% of the total ventricular power. This implies little impact of the surgical junction geometry on the SVC pressure, cardiac output, and other systemic parameters. In contrast, varying HR, PVR, and SVR led to significant changes in theses clinically relevant global parameters. Adopting a work-flow of customized virtual planning of the Hemi-Fontan procedure with patient-specific data, this study demonstrates the ability of multi-scale modeling to reproduce patient specific flow conditions under differing physiological states. Results demonstrate that the same operation performed in two different patients can lead

to different hemodynamic characteristics, and that modeling can be used to uncover physiologic changes associated with different clinical conditions.

Part II

Numerical aspects of outflow boundary conditions

Chapter 5

3D-3D coupling model for numerical simulations of blood flow

In this chapter, we present a new approach to couple the three-dimensional Navier-Stokes equations to a reduced model. We first describe some existing 3D-0D coupling methods and highlight benefits and disadvantages of each of them. We then introduce a new method that consists of adding a 3D artificial part where the Navier-Stokes equations are modified to obtain an equivalent energy balance to a classical coupling with for example a 3-element Windkessel model. We investigate theoretically the stability of the system and compare it to previously introduced methods. Finally we compare these coupling methods for numerical simulations of blood flow in three patient-specific models, which represent different flow regimes in the pulmonary and systemic circulations.

The work presented in this chapter lead to the article:
Gregory Arbia, Jean-Frédéric Gerbeau, Tain-Yen Hsia and Irene E. Vignon-Clementel **A new approach for the outflow boundary conditions in the three-dimensional hemodynamics** *to be submitted.*

Contents

5.1 Introduction

The three-dimensional Navier-Stokes simulation of blood flow and pressure in large vessels requires inlet or outlet boundary conditions that represent hemodynamics at these locations. However, in patient-specific settings, pressure or velocity are rarely clinically measured exactly there or can be part of the desired output [VCMF10]. Thus, boundary conditions rather consist in reduced models of the rest of the circulation. This typically involves coupling to 1D models (e.g. [FGNQ01, VCFJT06, BWF12, OTT+12]), and/or simple (seen in many applications, e.g. [VCFJT10, PTG+11, YVCT+12, FI14]) or closed loop lumped parameter 0D models (e.g. [MBP+06, KVCF+10, MMVC+12, CBK+13, BF13]). This coupling methodology transfers in various forms pressure and flow rate between 3D and reduced models, for which there is a loss of information. Moreover, reverse flow may occur in parts of or on entire coupling boundaries due to physiological conditions or complex interactions between the 3D geometry and the flow. This warrants careful coupling conditions, so that the scheme is stable, without artificially altering the local flow dynamics.

A first coupling method consists of enforcing the pressure at this coupling boundary to be uniform, that is, the pressure resulting from the reduced model. However, such a condition does not appear as the standard boundary condition in most formulations. In fact, in the latter, the traction appears as the natural boundary condition (e.g.[HRT96]) and its normal component is thus enforced to be the uniform reduced model pressure. But stability analyses show that the convective term on the boundary can be responsible for numerical instabilities in the presence of reverse flow. Other Navier-Stokes formulations rather involve the total pressure (e.g. [BCMO88]), which has been shown to lead to an energetically stable coupling between 3D and reduced models of blood flow (e.g. [FMN07, FQV13]). Some of these authors have been expecting instabilities when the dynamic pressure is not included in the boundary conditions but have not seen them numerically [FQV13, BDM13]. A dissipative stabilization has been proposed to counteract the destabilizing effect of the convective boundary term in such a case (e.g. [BGH+09]). A boundary condition based on enforcing the continuity of pressure on the one hand and of a linear combination of flow and energy fluxes on the other hand, has been proven to be energetically stable, but it does not necessarily conserve mass [DO13]. More recently, a local regularization of the fluid velocity along the tangential directions has been developed in [BC14], with interesting results. In all these methods, the reduced model pressure is imposed as a uniform boundary condition for the Navier-Stokes

equations. But in complex flow, such as with reverse flow, there is *a priori* no reason that the normal traction or the total pressure is uniform on a coupling boundary. For stabilized methods, the added term introduces some non-uniformity that has also no obvious reason to correspond to the flow at hand. In this chapter, we propose to handle the outflow boundary conditions by coupling the 3D Navier-Stokes equations with another 3D compartment. This artificial compartment involves modified Navier-Stokes equations that mimic a three-element Windkessel model (as an example of reduced model). The advantages of such an approach are that the coupling 1) does not enforce the traction at the interface to be uniform, and 2) is energetically close to the usual 3D Navier-Stokes - Windkessel solution, without the potentially destabilizing convective boundary term.

Note that the idea of introducing an artificial 3D part is not new. It was for example used in [BNAL05] to model dissipative boundary conditions in a commercial code that did not allow the users to implement the usual 0D boundary conditions. Our contribution with respect to the existing works is twofold: first, our artificial compartment is more complex since it includes two different kinds of dissipation and one term representing an elastic potential energy; second, we investigate how this artificial compartment affects outflow instabilities typically encountered in hemodynamics.

In the first part of this chapter we introduce existing coupling methods with strong formulations of the Navier-Stokes equations for the coupled system, weak form of the considered coupled system and numerical analysis of the energy balance to highlight the theoretical benefits and disadvantages of each method. Furthermore, we present a new 3D-3D coupling method and analyze its stability. In the second part we describe the numerical implementation of these coupling methods. The results are then illustrated on three patient-specific cases of numerical blood flow simulations in arteries in the pulmonary and the systemic sides for healthy or diseased configurations. The different methods are compared qualitatively, looking at the velocity fields at the coupling interface, and quantitatively on the flow and pressure tracings. When available, the results at that location of an extended geometrical model are given for reference. Finally, the results are compared and contrasted with the literature and possible extensions discussed.

5.2 Methods

5.2.1 Problem formulations

Blood is assumed to be a Newtonian fluid flowing in a rigid domain Ω_1. The incompressible Navier-Stokes equations are solved with no-slip condition on the wall Γ and with a Dirichlet boundary condition on the velocity at the inlet Γ_{in} (the notation is defined in Figure 5.1):

$$\rho\frac{\partial \boldsymbol{u}}{\partial t} + \rho(\boldsymbol{u}\cdot\nabla\boldsymbol{u}) + \nabla p - 2\mu\nabla\cdot\boldsymbol{\varepsilon}(\boldsymbol{u}) = 0 \tag{5.1}$$

$$\nabla\cdot\boldsymbol{u} = 0 \tag{5.2}$$

$$\boldsymbol{u}_{|\Gamma} = 0 \tag{5.3}$$

$$\boldsymbol{u}_{|\Gamma_{\text{in}}} = \boldsymbol{u}_{\text{in}} \tag{5.4}$$

where $\boldsymbol{u} : \Omega_1 \times \mathbb{R}^+ \to \mathbb{R}^3$ is the velocity, $p : \Omega_1 \times \mathbb{R}^+ \to \mathbb{R}$ is the pressure, and $\boldsymbol{\varepsilon}(\boldsymbol{u}) = \frac{1}{2}(\nabla\boldsymbol{u} + \nabla\boldsymbol{u}^T)$ denotes the strain rate tensor.

The system (5.1)-(5.4) has to be complemented with boundary conditions at the outlet Γ_{out}, where the Navier-Stokes equations are coupled to a reduced-order model which takes into account the rest of the vessels. Here inlet (where a velocity Dirichlet condition is imposed) and outlet (where a coupling with another model is performed) are taken in a generic sense. Besides, any of these can have some positive or negative flow rate over time. Three possible approaches that have been proposed in the literature to perform this coupling are presented below. Then, the main contribution of this study, based on a 3D-3D coupling, is introduced.

Formulation 1: 3D-0D The most common idea consists of enforcing a uniform normal stress at the outlet, equal to a pressure p_{c} given by a reduced model:

$$\boldsymbol{\sigma}\cdot\boldsymbol{n} = -p_{\text{c}}\boldsymbol{n}, \quad \text{on } \Gamma_{\text{out}}, \tag{5.5}$$

where $\boldsymbol{\sigma} = -p\mathbf{I} + 2\mu\varepsilon(\boldsymbol{u})$. In a finite element framework, this is easily done with a Neumann boundary condition. The advantage of this formulation is its simplicity. Although stable in many practical situations, instabilities can be observed in presence of complex reverse flow. It will be shown in Section 5.2.2 that an uncontrolled term appears in the energy balance. This is a possible reason of the observed instabilities. In addition, enforcing a uniform normal stress on a section where the flow is complex may generate spurious vortices that can also lead to instabilities.

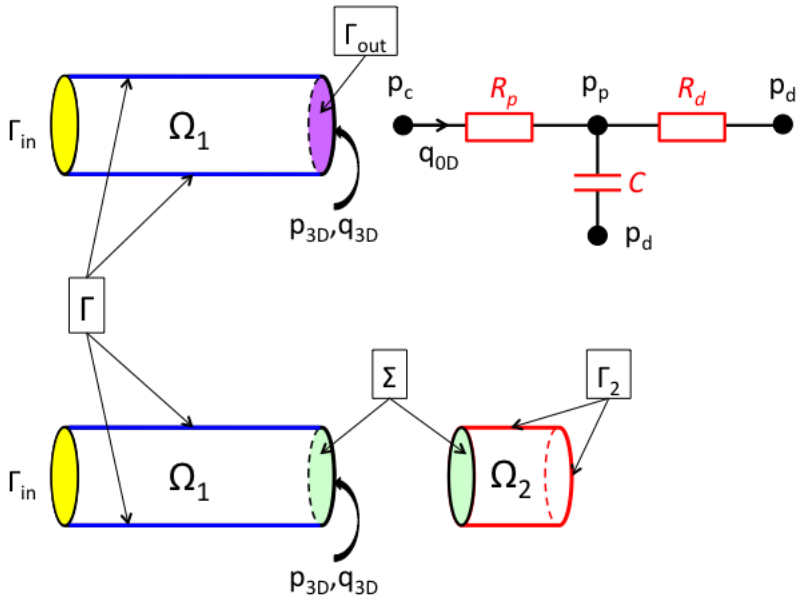

Figure 5.1: top: 3D-0D coupling scheme, bottom: 3D-3D coupling scheme.

Formulation 2: 3D-0D-Stab To cure the instabilities that may appear during backflow with Formulation 1, a stabilization method was proposed in [BGH+09]. This approach consists of modifying (5.5) as follows, here written in a more general form:

$$\boldsymbol{\sigma} \cdot \boldsymbol{n} = -p_c \boldsymbol{n} - \rho\theta(\boldsymbol{u} \cdot \boldsymbol{n})_- \boldsymbol{u}, \qquad \text{on } \Gamma_{\text{out}}, \tag{5.6}$$

where $(\boldsymbol{u} \cdot \boldsymbol{n})_-$ is equal to $-(\boldsymbol{u} \cdot \boldsymbol{n})$ if $\boldsymbol{u} \cdot \boldsymbol{n} \leq 0$, and is equal to 0 if not, and where θ has to be fixed.

This method is simple to implement and can be shown to be stable in the energy norm for $\theta \geq 0.5$. In practice, it proves to be very efficient at reducing the outlet instabilities. It was successfully tested in particular in [MBH+11, PZVP12]. If $\theta = 0.5$, it exactly cancels the convective energy entering the domain through the outlet during backflow. Two situations have to be distinguished here. When the backflow is due to spurious vortices induced by the presence of an artificial boundary, this effect is desirable. But it is well-known that a *physical* backflow can appear in some vessels during diastole. In those cases, the stabilization term artificially takes out of the

system an energy that should enter through the outlet.

Formulation 3: 3D-0D-Ptot Another approach consists of considering a formulation of the Navier-Stokes equations that involves the total pressure (e.g. [BCMO88, HRT96]):

$$\boldsymbol{\sigma}\cdot\boldsymbol{n}-\frac{\rho}{2}|\boldsymbol{u}|^2\boldsymbol{n}=-p_c\boldsymbol{n},\qquad \text{on } \Gamma_{\text{out}}. \tag{5.7}$$

This formulation, advocated in particular in [FMN07, FQV13], can be proved to be stable in the energy norm (see below). But in blood flow, the *total* stress is far from being uniform on a section.

Note that this is even not true for Poiseuille or Womersley flows. As a consequence, this formulation leads to large parasite velocity vectors at the core of the interface that converge towards the center, even for simple configurations [HRT96]. As in Formulation 1, spurious vortices can be generated at this interface and can eventually trigger instabilities.

Formulation 4: 3D-3D A possible alternative to the previous approaches consists of coupling system (5.1)-(5.4) to a modified Navier-Stokes system. Instead of a 0D model, an artificial 3D domain Ω_2 is added to the 3D domain of interest Ω_1 (bottom of Figure 5.1). In Ω_2, the Navier-Stokes equations are modified by adding terms to recover an energy balance similar to the one obtained with Formulation 3. The resulting system can be written in a compact form in $\Omega_1\cup\Omega_2$:

$$\rho\frac{\partial\boldsymbol{u}}{\partial t}+\rho\boldsymbol{u}\cdot\nabla\boldsymbol{u}+\nabla p-2\mu\nabla\cdot\boldsymbol{\varepsilon}(\boldsymbol{u})+\gamma\boldsymbol{u}+\rho\frac{\boldsymbol{u}}{2}\nabla\cdot\boldsymbol{u} = 0 \tag{5.8}$$

$$\alpha\frac{dp}{dt}+\beta p+\nabla\cdot\boldsymbol{u} = 0 \tag{5.9}$$

$$\boldsymbol{u}_{|\Gamma\cup\Gamma_2} = 0 \tag{5.10}$$

where α, β and γ vanish in Ω_1, to recover the standard equations (5.1)-(5.4), and are positive in Ω_2.

Parameter α is a distributed version of the capacitance in the Windkessel model. Parameters γ and $1/\beta$ play the role of the proximal and distal resistances respectively. Their values will be discussed in Section 5.2.2. The additional term $\rho\frac{\boldsymbol{u}}{2}\nabla\cdot\boldsymbol{u}$ is necessary to ensure stability in the energy norm, because the fluid is no longer incompressible in the artificial domain Ω_2. The equations in the two domains Ω_1 and Ω_2 are coupled through the usual trans-

mission conditions:

$$\boldsymbol{u}_1 = \boldsymbol{u}_2, \text{ and } \boldsymbol{\sigma}_1 \cdot \boldsymbol{n} = \boldsymbol{\sigma}_2 \cdot \boldsymbol{n}, \quad \text{on } \Sigma. \tag{5.11}$$

Note that these conditions are automatically satisfied when a standard variational formulation of equations (5.8)-(5.10) is set on the whole domain $\Omega_1 \cup \Omega_2$.

Contrary to what happened with the three previous formulations, the information coming from the "external part" is not uniform on the outflow section Γ_{out}. Contrary to Formulation 1, an inequality can be proved to control the energy of the system Compared to Formulation 2, it can let energy enter into the system through Γ_{out} in the presence of a physical backflow. Compared to Formulation 3, it is not based on the total pressure, and is thus expected to avoid the associated spurious velocity behavior.

5.2.2 Stability analysis

In this Section, the energy equations of the various formulations presented above are derived. Without loss of generality, the reduced-order model providing the pressure p_c in Formulations 1, 2 and 3, is assumed for now to result from a standard RCR Windkessel model (Figure 5.1, top):

$$C\frac{dp_p}{dt} + \frac{p_p - p_v}{R_d} = q \tag{5.12}$$

$$p_c - p_p = R_p q \tag{5.13}$$

where $q = \int_{\Gamma_{\text{out}}} \boldsymbol{u} \cdot \boldsymbol{n}$. For the sake of simplicity, $p_v = 0$ is assumed.

Multiplying (5.13) by q and (5.12) by p_p leads to the energy equation of the lumped parameter model:

$$p_c q = C\frac{d}{dt}\left(\frac{p_p^2}{2}\right) + R_p q^2 + \frac{p_p^2}{R_d} \tag{5.14}$$

We introduce the following notation:

$$E_{K_{\Omega_1}} = \int_{\Omega_1} \frac{\rho}{2}|\boldsymbol{u}|^2 \tag{5.15}$$

$$P_{V_{\Omega_1}} = 2\mu \int_{\Omega_1} \varepsilon(\boldsymbol{u}) : \varepsilon(\boldsymbol{u}) \tag{5.16}$$

$$P_{\text{in}} = \int_{\Gamma_{\text{in}}} \boldsymbol{\sigma} \cdot \boldsymbol{n} \cdot \boldsymbol{u} - \rho \int_{\Gamma_{\text{in}}} \frac{|\boldsymbol{u}|^2}{2} \boldsymbol{n} \cdot \boldsymbol{u} \tag{5.17}$$

denoting the kinetic energy, the viscous power and the energy entering through Γ_{in}, respectively.

Energy balance of Formulation 1 (3D-0D coupling) Multiplying (5.1) by $\boldsymbol{u}$ and integrating over Ω_1:

$$\frac{d}{dt}\int_{\Omega_1}\frac{\rho}{2}|\boldsymbol{u}|^2+\rho\int_{\Omega_1}\boldsymbol{u}\cdot\nabla\left(\frac{|\boldsymbol{u}|^2}{2}\right)+2\mu\int_{\Omega_1}\boldsymbol{\varepsilon}(\boldsymbol{u}):\boldsymbol{\varepsilon}(\boldsymbol{u})+\int_{\Omega_1}\nabla p\cdot\boldsymbol{u}=0 \tag{5.18}$$

and enforcing the incompressibility of the fluid (5.2) and the no-slip condition on the wall, the energy equation in Ω_1 reads:

$$\frac{d}{dt}E_{K_{\Omega_1}}+P_{V_{\Omega_1}} \;=\; P_{\text{in}}+\int_{\Gamma_{\text{out}}}\boldsymbol{\sigma}\cdot\boldsymbol{n}\cdot\boldsymbol{u}-\rho\int_{\Gamma_{\text{out}}}\frac{|\boldsymbol{u}|^2}{2}\boldsymbol{n}\cdot\boldsymbol{u} \tag{5.19}$$

Considering the coupling condition (5.5) and the energy equation of the 0D model (5.14), the global energy balance of the **3D-0D** coupling method is obtained:

$$\frac{d}{dt}E_{K_{\Omega_1}}+P_{V_{\Omega_1}}+C\frac{d}{dt}\frac{p_p^2}{2}+\frac{p_p^2}{R_d}+R_pq^2 \;=\; P_{\text{in}}-\rho\int_{\Gamma_{\text{out}}}\frac{|\boldsymbol{u}|^2}{2}\boldsymbol{n}\cdot\boldsymbol{u} \tag{5.20}$$

In the presence of reverse flow at an outlet ($\boldsymbol{u}\cdot\boldsymbol{n}<0$) the last term may thus have a destabilizing effect.

Energy balance of Formulation 2 (3D-0D-Stab coupling): With the same computation as in Formulation 1, but considering (5.6) instead of (5.5) as a coupling condition, the energy equation of Formulation 2 reads:

$$\begin{aligned}\frac{d}{dt}E_{K_{\Omega_1}}+P_{V_{\Omega_1}}+\;& C\;\frac{d}{dt}\frac{p_p^2}{2}+\frac{p_p^2}{R_d}+R_pq^2\\ &=\begin{cases}P_{\text{in}}-\rho\int_{\Gamma_{\text{out}}}\frac{|\boldsymbol{u}|^2}{2}(\boldsymbol{u}\cdot n), \text{ if } \boldsymbol{u}\cdot\boldsymbol{n}\geq 0\\ P_{\text{in}}+\rho(\theta-\frac{1}{2})\int_{\Gamma_{\text{out}}}|\boldsymbol{u}|^2(\boldsymbol{u}\cdot\boldsymbol{n}), \text{ if } \boldsymbol{u}\cdot\boldsymbol{n}<0\end{cases}\end{aligned} \tag{5.21}$$

If $\theta=0.5$, as in [MBH+11, PZVP12], the potentially destabilizing term of (5.20) is exactly balanced by the artificial dissipation when $\boldsymbol{u}\cdot\boldsymbol{n}<0$. In some publications, a stronger dissipation is chosen (e.g. $\theta=1$ in [BGH+09]). This formulation is therefore for $\theta\geq 0.5$ stable in the energy norm.

Energy balance of Formulation 3 (3D-0D-Ptot coupling): When coupling is done with the total pressure (5.7), the potentially destabilizing term of (5.20) disappears in the energy balance:

$$\frac{d}{dt}E_{K_{\Omega_1}} + P_{V_{\Omega_1}} + C\frac{d}{dt}\frac{p_p^2}{2} + \frac{p_p^2}{R_d} + R_p\boldsymbol{q}^2 = P_{\text{in}} \tag{5.22}$$

This formulation is therefore stable in the energy norm.

Energy balance of Formulation 4 (3D-3D coupling): As in Formulation 1, the energy equation in the domain of interest Ω_1 reads:

$$\frac{d}{dt}E_{K_{\Omega_1}} + P_{V_{\Omega_1}} = P_{\text{in}}^{\Omega_1} + \int_{\Gamma_\Sigma} \boldsymbol{\sigma}\boldsymbol{n}\cdot\boldsymbol{u} - \rho\int_{\Gamma_\Sigma}\frac{|\boldsymbol{u}|^2}{2}\boldsymbol{n}\cdot\boldsymbol{u} \tag{5.23}$$

Similarly, in the artificial domain Ω_2, from the modified Navier-Stokes equation (5.8)-(5.9)-(5.10):

$$\frac{d}{dt}E_{K_{\Omega_2}} + P_{V_{\Omega_2}} + \gamma\int_{\Omega_2}|\boldsymbol{u}|^2 - \int_{\Omega_2} p \quad \nabla\cdot\boldsymbol{u} = -\int_{\Gamma_\Sigma}\boldsymbol{\sigma}\boldsymbol{n}\cdot\boldsymbol{u} + \rho\int_{\Gamma_\Sigma}\frac{|\boldsymbol{u}|^2}{2}\boldsymbol{n}\cdot\boldsymbol{u} \tag{5.24}$$

Using equation (5.9),

$$\frac{d}{dt}E_{K_{\Omega_2}} + P_{V_{\Omega_2}} + \alpha\frac{d}{dt}\int_{\Omega_2}\frac{p^2}{2} + \quad \beta \quad \int_{\Omega_2}p^2 + \gamma\int_{\Omega_2}|\boldsymbol{u}|^2 = -\int_{\Gamma_\Sigma}\boldsymbol{\sigma}\boldsymbol{n}\cdot\boldsymbol{u} + \rho\int_{\Gamma_\Sigma}\frac{|\boldsymbol{u}|^2}{2}\boldsymbol{n}\cdot\boldsymbol{u} \tag{5.25}$$

Adding these two relations, the boundary terms in the right-hand side cancel out, due to the transmission condition (5.11), and the energy balance of Formulation 4 is obtained:

$$\frac{d}{dt}E_K^{\Omega_1\cup\Omega_2} + P_V^{\Omega_1\cup\Omega_2} + \alpha\frac{d}{dt}\int_{\Omega_2}\frac{p^2}{2} + \beta\int_{\Omega_2}p^2 + \gamma\int_{\Omega_2}|\boldsymbol{u}|^2 = P_{\text{in}}^{\Omega_1}. \tag{5.26}$$

This formulation is therefore stable in the energy norm. Comparing (5.26) with (5.20) triggers an analogy between α, β, γ and the standard Winkessel parameters: $\alpha \approx C/V$, $\beta = 1/(R_d V)$, and $\gamma \approx R_p S/L$.

5.2.3 Numerical schemes

The RCR Windkessel model is discretized with a first order scheme: assuming that p_p^n and q^n are known, then p_p^{n+1} and p_c^{n+1} are defined by

$$\begin{aligned} C\frac{p_p^{n+1}-p_p^n}{\Delta t}+\frac{p_p^{n+1}}{R_d} &= q^n, \\ p_c^{n+1} &= p_p^{n+1}+R_p q^n. \end{aligned} \tag{5.27}$$

Denoting $R_d C$ by τ, the pressure transmitted to the 3D model at time t^{n+1} is given by:

$$p_c^{n+1} = \frac{\frac{\tau}{\Delta t}p_p^n + R_d q^n}{1+\frac{\tau}{\Delta t}} + R_p q^n. \tag{5.28}$$

The 3D formulations are also discretized with a first order time scheme. The nonlinear advection term of the Navier-Stokes equations is treated semi-implicitely.

Formulation 1 (3D-0D) Defining the bilinear form:

$$\begin{aligned} A_1^{\Omega}(\boldsymbol{u}_h^n;(\boldsymbol{u}_h^{n+1},p_h^{n+1}),(v_h,q_h)) &= \int_\Omega \left(\frac{\rho}{\Delta t}\boldsymbol{u}_h^{n+1}+\rho\boldsymbol{u}_h^n\cdot\nabla\boldsymbol{u}_h^{n+1}\right)\cdot v_h \\ &+ \int_\Omega \mu\left(\nabla\boldsymbol{u}_h^{n+1}:\nabla v_h\right) \\ &- \int_\Omega \left(p_h^{n+1}\nabla\cdot v_h + q_h\nabla\cdot\boldsymbol{u}_h^{n+1}\right), \end{aligned} \tag{5.29}$$

the variational formulation of **3D-0D** method reads:

$$A_1^{\Omega_1}(\boldsymbol{u}_h^n;(\boldsymbol{u}_h^{n+1},p_h^{n+1}),(v_h,q_h)) = \int_{\Omega_1}\frac{\rho}{\Delta t}\boldsymbol{u}_h^n v_h - \int_{\Gamma_{\text{out}}} p_c^{n+1}\boldsymbol{n}\cdot v_h \tag{5.30}$$

***Remark* 5.2.1.** *Note that the weak form of the viscous term is based on the relation $\mu\Delta\boldsymbol{u} = 2\mu\nabla\cdot\boldsymbol{\varepsilon}(\boldsymbol{u})$, valid for an incompressible fluid. The natural condition corresponding to this formulation is compatible with Poiseuille and Womersley flows contrary to the one based on $\varepsilon(\boldsymbol{u})$ (e.g. [HRT96]). We made this choice to avoid perturbations of the velocity field at the outlet, but the formulation based on $\varepsilon(\boldsymbol{u})$ can also be used in practice.*

Formulation 2 (3D-0D-Stab) Considering the bilinear form (5.29) and boundary conditions (5.6) with $\theta = 0.5$ to ensure stability of energy of the

coupled system, the **3D-0D-Stab** method variational formulation reads:

$$\begin{aligned} A_1^{\Omega_1}(\boldsymbol{u}_h^n;(\boldsymbol{u}_h^{n+1},p_h^{n+1}),(v_h,q_h)) &= \int_{\Omega_1}\frac{\rho}{\Delta t}\boldsymbol{u}_h^n v_h - \int_{\Gamma_{\text{out}}} p_c^{n+1}\boldsymbol{n}\cdot v_h \\ &- \int_{\Gamma_{\text{out}}}\frac{\rho}{2}(\boldsymbol{u}_h^n\cdot\boldsymbol{n})_-(\boldsymbol{u}_h^{n+1}\cdot v_h) \end{aligned} \quad (5.31)$$

Formulation 3 (3D-0D-Ptot) Defining the bilinear form:

$$\begin{aligned} A_2^{\Omega}(\boldsymbol{u}_h^n;(\boldsymbol{u}_h^{n+1},p_h^{n+1}),(v_h,q_h)) &= \int_{\Omega}\left(\frac{\rho}{\Delta t}\boldsymbol{u}_h^{n+1}+\rho\ \vec{\text{rot}}(\boldsymbol{u}_h^{n+1})\times\boldsymbol{u}_h^n\right)\cdot v_h \\ &- \int_{\Omega}\frac{\rho}{2}\left(\boldsymbol{u}_h^{n+1}\cdot\boldsymbol{u}_h^n\right)\nabla\cdot v_h + \int_{\Omega_1}\mu\left(\nabla\boldsymbol{u}_h^{n+1}:\nabla v_h\right) \\ &- \int_{\Omega}\left(p_h^{n+1}\nabla\cdot v_h + q_h\nabla\cdot\boldsymbol{u}_h^{n+1}\right). \end{aligned} \quad (5.32)$$

The variational formulation of the **3D-0D-Ptot** method reads:

$$A_2^{\Omega_1}(\boldsymbol{u}_h^n;(\boldsymbol{u}_h^{n+1},p_h^{n+1}),(v_h,q_h)) = \int_{\Omega_1}\frac{\rho}{\Delta t}\boldsymbol{u}_h^n v_h - \int_{\Gamma_{\text{out}}} p_c^{n+1}\boldsymbol{n}\cdot v_h \quad (5.33)$$

***Remark* 5.2.2.** *In this formulation, the total pressure only appears in the boundary condition but the pressure unknown is still the static pressure. It is also possible to consider a formulation, based on the relation* $\boldsymbol{u}\cdot\nabla\boldsymbol{u}^T = \nabla\left(\frac{|\boldsymbol{u}|^2}{2}\right)$*, where the static pressure is replaced by the total pressure as an unknown [HRT96].*

Formulation 4 (3D-3D) Defining the bilinear form:

$$\begin{aligned} A_3^{\Omega}(\boldsymbol{u}_h^n;(\boldsymbol{u}_h^{n+1},p_h^{n+1}),(v_h,q_h)) &= \int_{\Omega}\left(\frac{\rho}{\Delta t}\boldsymbol{u}_h^{n+1}+\rho\boldsymbol{u}_h^n\cdot\nabla\boldsymbol{u}_h^{n+1}\right)v_h \\ &+ \int_{\Omega}\mu\left(\nabla\boldsymbol{u}_h^{n+1}:\nabla v_h\right) \\ &- \int_{\Omega}\left(p_h^{n+1}\nabla\cdot v_h + q_h\nabla\cdot\boldsymbol{u}_h^{n+1}\right) \\ &+ \int_{\Omega}\gamma\left(\boldsymbol{u}_h^{n+1}v_h\right) + \int_{\Omega}\frac{\rho}{2}\left(\boldsymbol{u}_h^{n+1}\left(\nabla\cdot\boldsymbol{u}_h^n\right)v_h\right) \\ &- \int_{\Omega}\left(\frac{\alpha}{\Delta t}+\beta\right)p_h^{n+1}q_h \end{aligned} \quad (5.34)$$

where, $\alpha=\beta=\gamma=0$ in Ω_1.

The variational formulation of the **3D-3D** method reads:

$$A_3^{\Omega_1\cup\Omega_2}(\boldsymbol{u}_h^n;(\boldsymbol{u}_h^{n+1},p_h^{n+1}),(v_h,q_h)) \;=\; \int_{\Omega_1\cup\Omega_2}\Big(\frac{\rho}{\Delta t}\boldsymbol{u}_h^n v_h - \frac{\alpha}{\Delta t}p_h^n q_h\Big) \tag{5.35}$$

5.3 Results

As a preamble we define a hybrid **3D-3D-0D** coupling method where the Navier-Stokes equations are coupled to the modified Navier-Stokes model, which is itself coupled to a 3-element Windkessel reduced model, as shown in Figure 5.2 .

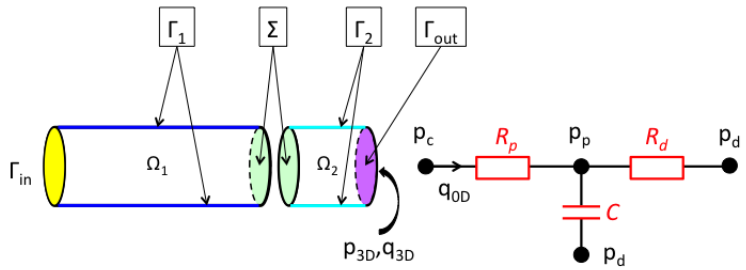

Figure 5.2: **3D-3D-0D** coupling approach, where Ω_1 is the domain of interest, Ω_2 is an artificial added part, coupled to a 3-element Windkessel model.

In the whole domain $\Omega_1 \cup \Omega_2$,

$$\rho\frac{\partial \boldsymbol{u}}{\partial t} + \rho(\boldsymbol{u}\cdot\nabla\boldsymbol{u}) + \nabla p - \nabla\cdot\boldsymbol{\varepsilon}(\boldsymbol{u}) + \gamma\boldsymbol{u} \;=\; 0 \tag{5.36}$$

$$\nabla\cdot\boldsymbol{u} \;=\; 0 \tag{5.37}$$

$$\boldsymbol{u}_{|\Gamma_1\cup\Gamma_2} \;=\; 0 \tag{5.38}$$

$$\boldsymbol{u}_{|\Gamma_{\text{in}}} \;=\; \boldsymbol{u}_{\text{in}} \tag{5.39}$$

where $\gamma = 0$ in Ω_1, with the usual transmission conditions (5.11). We finally couple a 3-element Windkessel model to the system (5.36)-(5.37)-(5.38)-(5.39)

with the **3D-0D** coupling method,

$$\boldsymbol{\sigma} \cdot \boldsymbol{n} \;=\; -p_c \boldsymbol{n}, \quad \text{on } \Gamma_{\text{out}}, \tag{5.40}$$

In this section we present results of all these coupling methods for patient-specific cases in the systemic and the pulmonary sides where the flow regimes are very different. In order to test a large domain of validity for each of them, we highlight differences and reflect their benefits and disadvantages.

5.3.1 Adult patient-specific pulmonary artery

This patient specific geometrical model is an adult pulmonary artery (PA). Velocity is prescribed at the inlet of the model, as a plug profile following the flow tracing of Figure 5.3. There is around 16% of reverse flow, leading to a highest Reynolds number of 2400. The flow rate maximum is around $378 cm^3/s$. During the deceleration after systole, physical reverse flow occurs with a minimal flow rate around $-66 cm^3/s$. Figure 5.3 also shows on the left side the original geometrical model containing 107K tetrahedra, with both outlets coupled to 3-element Windkessels by successively the **3D-0D**, **3D-0D-Stab** and **3D-0D-Ptot** methods. On the right side, the geometrical model with the added artificial parts consists of 127K tetrahedra: there the coupling is done with the **3D-3D** and **3D-3D-0D** methods.

Table 5.1 summarizes the parameters of the different coupling methods. On the left side, the 3-element Windkessel parameters are the ones of the **3D-0D**, **3D-0D-Stab** and **3D-0D-Ptot** coupling approaches. They were chosen to represent physiological PA pressure pulses, assuming symmetry between the two lung vasculatures [GMC+13]. The **3D-3D** parameters in the artificial added parts are given in the middle section, following the same symmetry. Finally, parameters of the hybrid **3D-3D-0D** method are given on the right: in the artificial parts, $\boldsymbol{\gamma}$ is obtained by computing 10% of $\boldsymbol{\gamma}$ in the **3D-3D** model, while correspondingly the proximal resistance of the 3-element Windkessel is decreased by 10% compared to the original value.

	LPA	RPA		Lc	Rc		Lout	Rout		Lc	Rc
R_p	$4\ 10^1$	$4\ 10^1$	$\boldsymbol{\alpha}$	$2\ 10^{-4}$	$2\ 10^{-4}$	R_p	$3.6\ 10^1$	$3.6\ 10^1$	$\boldsymbol{\gamma}$	4.9	4.9
C	$1\ 10^{-3}$	$1\ 10^{-3}$	$\boldsymbol{\beta}$	$6.7\ 10^{-4}$	$6.7\ 10^{-4}$	C	10^{-3}	10^{-3}	$\boldsymbol{\alpha}$	0	0
R_d	$3\ 10^2$	$3\ 10^2$	$\boldsymbol{\gamma}$	$4.9\ 10^1$	$4.9\ 10^1$	R_d	$3\ 10^2$	$3\ 10^2$	$\boldsymbol{\beta}$	0	0

Table 5.1: R_p and R_d in g cm^{-4} s^{-1}, and C in g^{-1} cm^4 s^2, $\boldsymbol{\alpha}$ in g^{-1} cm s^2, $\boldsymbol{\beta}$ in g^{-1} cm s, and $\boldsymbol{\gamma}$ in g cm^{-3} s^{-1}.

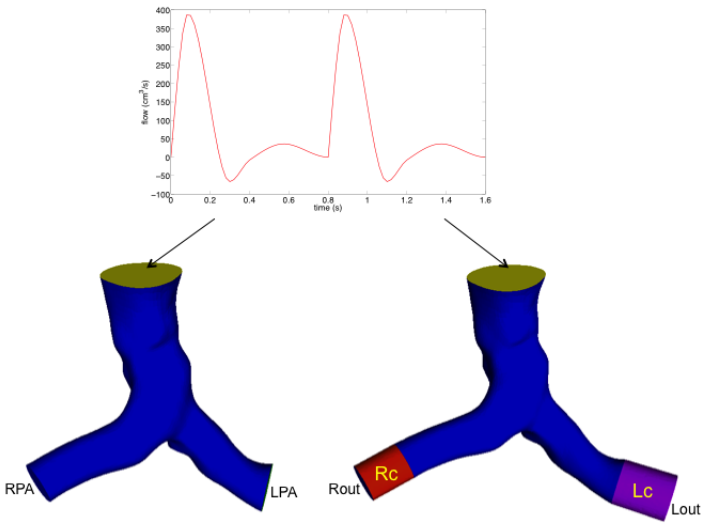

Figure 5.3: Original geometrical model in blue (left) and geometrical model with the added outlet 3D artificial parts in red and purple (right). Inlet flow tracing over two cardiac cycles (red).

This example is a typical PA physiological case. In Figure 5.4 velocity fields are shown during forward peak flow (top) and in presence of backflow (bottom), comparing the **3D-0D**, **3D-0D-Stab** and **3D-3D** coupling methods. During forward flow, the three approaches lead to very similar velocity fields. In fact, in this configuration the convective stabilization is off, which is verified by the same results obtained for the **3D-0D** or **3D-0D-Stab** methods. During backflow, the **3D-0D** coupling method exhibits perturbations with for a few time steps inward vectors which are large relative to the flow rate. The **3D-0D-Stab** method, while stable, impacts the hemodynamics by reducing the velocity vectors to almost zero. The **3D-3D** approach allows to recover backflow and warrants stability of the computation.

In Figure 5.5, the **3D-0D-Ptot** method exhibit velocity vectors with strong spurious radial components at the outlet surface [HRT96]. Spurious in and out of plane vectors can also be seen, even though flow is maximally forward. Moreover, computations are not diverging but lead to a very large in-plane pressure gradient ($\Delta P = 26.50$ mmHg), which is not relevant from a clinical point of view.

Finally, in Figure 5.6 the velocity fields of the **3D-3D-0D** method are

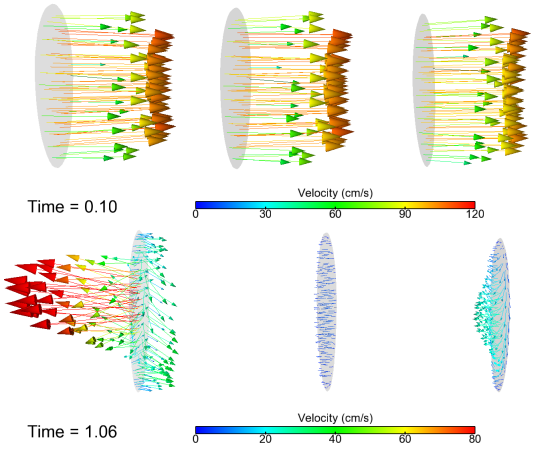

Figure 5.4: Velocity fields at the LPA interface, when flow at the inlet is maximal forward (top, t=0.10s, $Q_{\max} = 378$ cm^3/s) and is reverse (bottom, t=1.06s, $Q_{\min} = -66$ cm^3/s) with the **3D-0D**, **3D-0D-Stab** and **3D-3D** coupling methods from left to right.

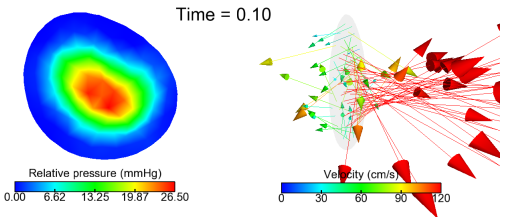

Figure 5.5: In-plane pressure gradient (left) and velocity fields (right) at the LPA interface during maximal forward flow (t=0.1s) with the **3D-0D-Ptot** coupling method.

analyzed. During forward flow, velocity fields are close to those obtained by the **3D-0D**, **3D-0D-Stab** and **3D-3D** models. Furthermore, during reverse flow stable velocity vectors are observed, with at the center higher inward vectors, similarly to the **3D-3D** model.

Figure 5.6: Velocity fields during maximal forward flow (left, t=0.10s) and reverse flow (right, t=1.06s) at the LPA interface with the **3D-3D-0D** coupling approach.

The time-varying flow rates (Figure 5.7) and average pressure (Figure 5.8) at the two coupling surfaces are now analyzed. For each coupling method, similar flow and pressure results are found on both the left and right sides. Pressure and flow from the **3D-0D-Ptot** method are not represented as the obtained values were non-physiological. Even if the simulation did not diverge, obtained pressure and flow were too high with spurious high-frequency tracings. Flow varies over time very similarly for all coupling methods. Pressure varies over 3 to 20 mmHg, in exactly the same way for the **3D-0D** and **3D-0D-Stab** methods, but a few mmHg lower for the **3D-3D** model, while for the **3D-3D-0D** model it is closer to the other couplings.
For each of these methods, the observed behaviors are actually the same on both PA sides. At this point however, it is hard to conclude on which method is best reproducing the real flow behavior, because we do not have access to the three dimensional downstream domain. But this case is highlighting the robustness of the **3D-0D-Stab** and **3D-3D** coupling methods to avoid large numerical artefacts due to physiological reverse flow in a patient-specific case.

5.3.2 Child patient-specific pulmonary arteries with CHD

This patient specific geometry is the first generation of a pulmonary arterial tree of a child affected by a congenital heart disease, the single ventricle pathology. This patient underwent a so-called stage 1 surgical procedure consisting of an anastomosis between the systemic and pulmonary circula-

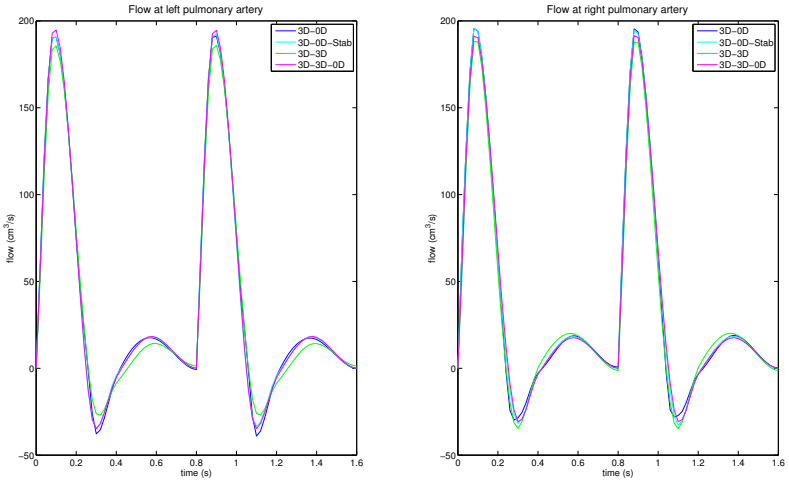

Figure 5.7: Flow rate over two cardiac cycles in both PAs for the different coupling models.

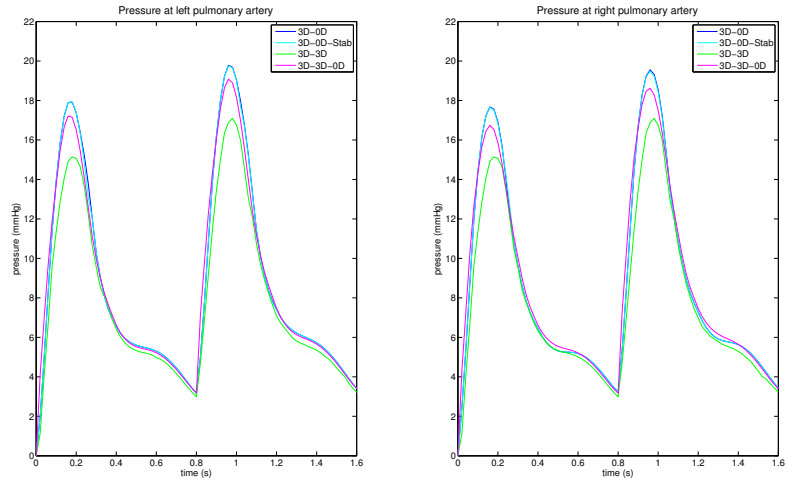

Figure 5.8: Average pressure over two cardiac cycles at both interfaces for the different coupling methods

tory systems *via* a small artificial shunt. This patient is patient A in chapter 4.

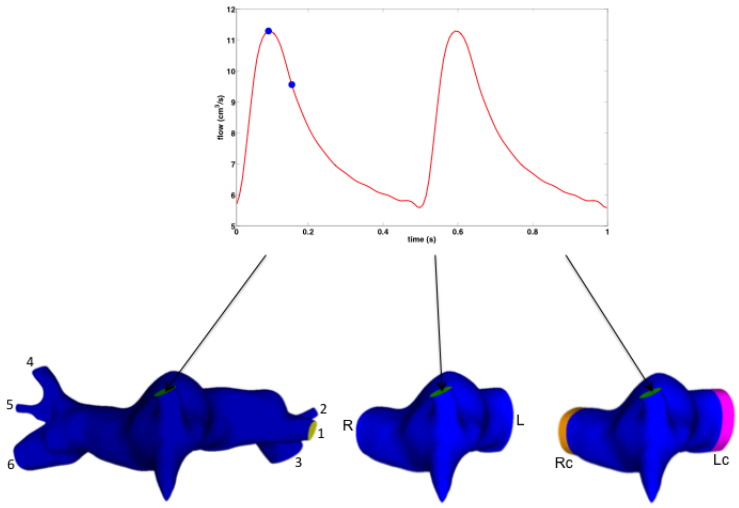

Figure 5.9: From left to right: complete model (with outlets 1−6), short model (two outlets, R for the RPA and L for the LPA), and short model with the two artificial three dimensional parts on each side, R_c and L_c. Top: imposed inflow shown over two cycles, with the two dots representing maximum flow and decelerating flow respectively.

Figure 5.9 represents the complete geometrical model (918K tetrahedra, six outlets), the short model with cut pulmonary artery branches (471K tetrahedra, two outlets), and the short model with its artificial parts to the outlet surfaces (505K tetrahedra, 2 outlets). As in the previous case, velocity was prescribed at the inlet with a plug profile, following a typical shunt flow tracing. The highest Reynolds number is 3000. The flow rate varies over one cardiac cycle between $5.8cm^3/s$ and $11.2cm^3/s$: there is thus no physical flow reversal prescribed at the inlet. The main advantages of this case are first that the effect of artificially cutting the geometry can be assessed, and second that, due to the bifurcation close to the inlet, it is a case of more complex flow than previously.

In Table 5.2 the values of proximal and distal resistances, and capacitances are given for each of the six outlets of the complete geometrical model. These values were generated to reflect clinical measurements [ACEM+14]. A first simulation is run with the **3D-0D** coupling approach. All the coupling

methods with the short models are then compared to this reference simulation.

	1	2	3	4	5	6
R_p	$3.19\ 10^{1}$	$4.73\ 10^{1}$	$6.38\ 10^{0}$	$1.71\ 10^{1}$	$4.26\ 10^{1}$	$5.75\ 10^{0}$
C	$4.40\ 10^{-4}$	$1.79\ 10^{-4}$	$5.50\ 10^{-3}$	$1.14\ 10^{-3}$	$2.35\ 10^{-4}$	$1.06\ 10^{-2}$
R_d	$2.45\ 10^{2}$	$6.13\ 10^{2}$	$2.95\ 10^{1}$	$1.11\ 10^{2}$	$4.63\ 10^{2}$	$1.58\ 10^{1}$

Table 5.2: R_p and R_d in g cm^{-4} s^{-1}, and C in g^{-1} cm^4 s^2 for the six 3-element Windkessel outlets of the reference simulation in the complete geometrical model.

In Table 5.3, the reduced model parameters for the short geometries are given. They were generated from the reference model parameters: at both outlets, an equivalent impedance is computed from the three distal outlet 3-element Windkessel of the complete model. 3-element Windkessel parameters are then optimized to match this impedance. This 3-element Windkessel is then coupled to the 3D Navier-Stokes equations with the **3D-0D** , **3D-0D-Stab** and **3D-0D-Ptot** methods. The parameters implemented in the **3D-3D** model are also reported.

	R	L		Rc	Lc
R_p	$4.44\ 10^{0}$	$5.28\ 10^{0}$	$\boldsymbol{\alpha}$	$1.96\ 10^{-1}$	$6.35\ 10^{-2}$
C	$1.29\ 10^{-2}$	$6.20\ 10^{-3}$	$\boldsymbol{\beta}$	$1.14\ 10^{0}$	$4.09\ 10^{-1}$
R_d	$1.33\ 10^{1}$	$2.51\ 10^{1}$	$\boldsymbol{\gamma}$	$7.13\ 10^{0}$	$1.29\ 10^{1}$

Table 5.3: Parameters for the different coupling methods in the short models: R_p and R_d in g cm^{-4} s^{-1}, and C in g^{-1} cm^4 s^2, $\boldsymbol{\alpha}$ in g^{-1} cm s^2, $\boldsymbol{\beta}$ in g^{-1} cm s, and $\boldsymbol{\gamma}$ in g cm^{-3} s^{-1}.

In Figure 5.10 velocity fields in the RPA are compared between the different methods at the same location during maximal forward flow (left) and deceleration flow (right). The **reference** case (top) was run with a **3D-0D** method. It presents no instability because the flow is smoother at its distal outlets, which is typical of bifurcations quite downstream of complex flow [TTFVC11]. The other three methods were run in the cut model. At maximal forward flow, the **reference** model shows complex flow in the RPA. This behavior is retrieved with the **3D-0D** coupling method but with inwards velocity vectors. However, computation is close to divergence. The **3D-0D-Stab** coupling method efficiently kills the reverse velocity vectors at the coupling surface so that a similar forward flow motion to the **3D-0D** coupling method is retrieved without backflow. Note that coupling three-dimensional **3D-3D** model to the Navier-Stokes equations leads to a

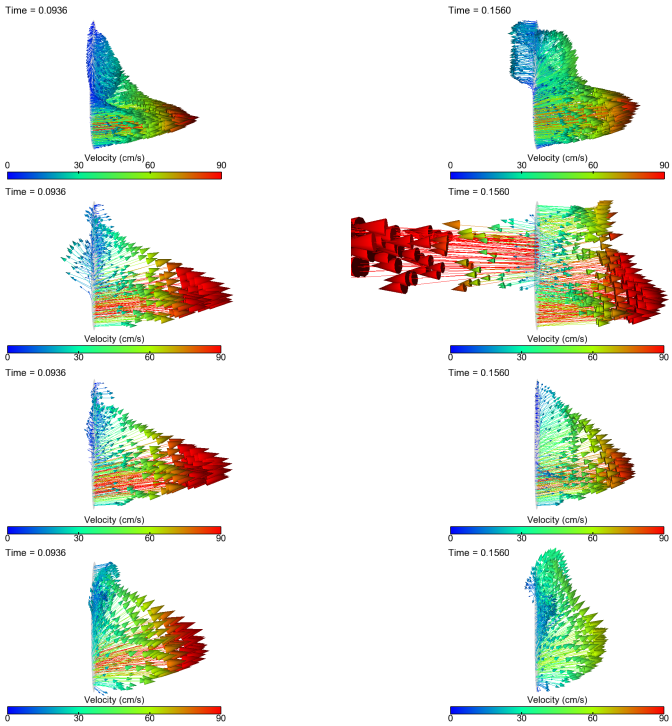

Figure 5.10: Velocity fields in RPA at peak inlet flow (left, t=0.0936s, Q_{max} = 11.2 cm^3/s) and during decelerating flow (right, t=0.1638s) comparing the **reference**, **3D-0D**, **3D-0D-Stab** and **3D-3D** coupling methods from top to bottom. The two times are shown as dots on the inflow Figure 5.9.

velocity profile closer to the reference case.

Regarding blood flow behavior during the decelerating phase in Figure 5.10 (right column), there is reverse flow in **reference** case and a large proportion of the forward flow is located at the bottom of the surface area. With the **3D-0D** coupling method at outlet surfaces of the cut model, computation is diverging, but the **3D-0D-Stab** coupling method leads to a blood flow behavior where velocity vectors are underestimated at the center and top of the coupling surface area. In the **3D-3D** coupling approach, flow motion is more homogeneous in terms of size and direction of the velocity vectors.

In Figure 5.11 the velocity field for the **3D-0D-Ptot** coupling method behaves as in the previous patient-specific case of adult pulmonary arteries. Moreover, computation is diverging.

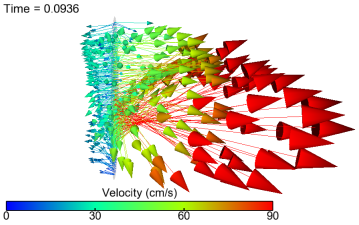

Figure 5.11: The RPA velocity field during peak flow with the **3D-0D-Ptot** coupling method.

In Figure (5.12), the **3D-3D-0D** coupling method leads during maximal forward flow to a velocity field close to the coupling of reduced model with the **3D-0D-Stab** method. During deceleration the majority of flow is located at the bottom of the coupling surface and backflow is authorized in the upper part. The obtained flow behavior is thus close to the **reference** case.

Figure 5.12: RPA velocity fields during peak flow (left) and decelerative flow (right) with the **3D-3D-0D** method.

In the figures above, the RPA side is presented. In fact, the LPA is turning in the downstream 3D domain of the **reference** case in such a way that hemodynamics are even more different between the reference on the one hand and the cut models on the other hand than for the RPA. Next, in Figure 5.13, the resulting flow rates are compared at both coupling surfaces, between the **3D-0D** , **3D-0D-Stab** , **3D-3D** and **3D-3D-0D** coupling models. In all cases, most of the flow goes to the RPA, following a dynamics close to that of the inlet flow, with a peak in systole followed by a rapid decay. The flow rates oscillate in time in diastole due to the complex flow structures created by the interaction of the impinging inflow and the patient-specific geometry. However, for the **3D-0D** case the flow rates largely oscillate before the simulation diverges. In terms of magnitude, the coupling method that is closer to the **reference** case is the **3D-0D-Stab** method, on both sides. The **3D-3D** coupling approach is leading to a satisfying blood flow behavior but changes the distribution of flow between the left and right sides for this choice of parameters: it slightly underestimates flow in the LPA and thus overestimates flow in the RPA. However, the hybrid coupling method **3D-3D-0D** is close to the **reference** case. The diverging **3D-0D-Ptot** results are not represented because the simulation diverged early on (t=0.0936s).

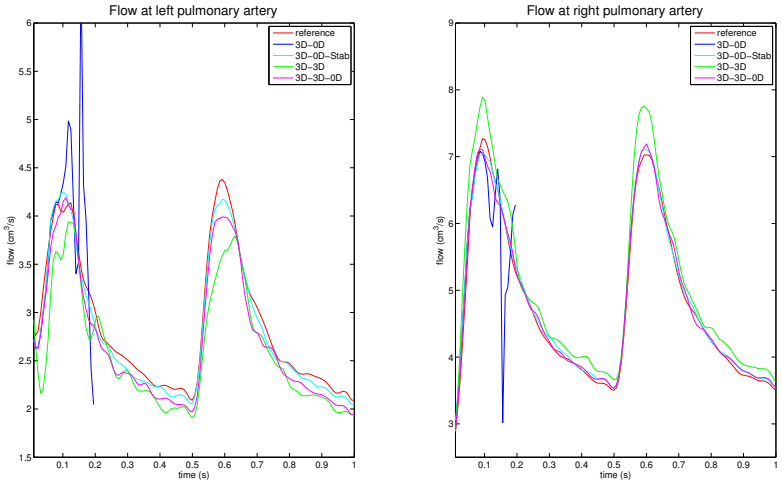

Figure 5.13: Flow rates over two cardiac cycles in the LPA (left) and RPA (right) for the different coupling methods.

Lastly, Figure 5.14 shows the corresponding pressure waveforms. The time dynamics are similar for all cases and on both sides, except for the **3D-0D** case which diverges in the first cardiac cycle. After the transitory

first cycle, the second cycle is closer to a periodic solution with a sharp rise in systole, followed by a smooth diastole decay. The closest results to the **reference** case is the **3D-0D-Stab** method for both sides. The **3D-3D** approach underestimates pressure for both sides. However the hybrid **3D-3D-0D** coupling approach more closely reproduces the **reference** results.

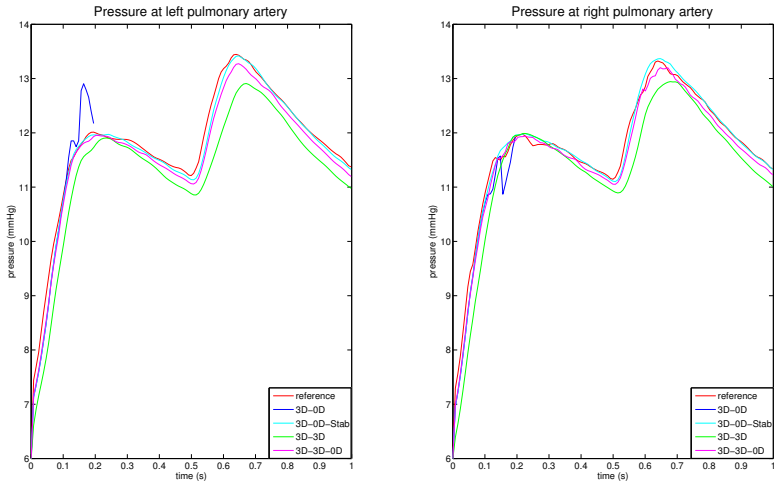

Figure 5.14: Surface averaged pressure over two cardiac cycles at the LPA (left) and RPA (right) interfaces for the different coupling methods.

To summarize this case, one can observe that both **3D-0D** and **3D-0D-Ptot** couplings lead to divergence of the simulation, although there is negative flow rate neither at the inlet nor at the outlets, and although the **reference** case does not diverge, despite it uses the same **3D-0D** method at its outlets. This is highlighting the need for robust numerical methods in the presence of complex flow, such as the **3D-0D-Stab** and **3D-3D** or **3D-3D-0D** coupling methods. The three presented similarities and differences with the **reference** case, which is the ground truth, **3D-3D-0D** being the best compromise in this example.

5.3.3 Adult patient-specific aorta

This last patient-specific case is an abdominal adult aorta. Figure 5.15 consists of the inlet flow rate over time and the three tested geometrical models: the complete 3D model containing 608K tetrahedra and 9 outlet surfaces, the short model containing 473K tetrahedra and 6 outlet surfaces

where the abdominal aorta was cut to remove the iliac branches, and the same cut model but with an artificial 3D part at its descending aorta outlet, containing 499K tetrahedra. Velocity is prescribed at the inlet of the model, as a plug profile following the flow tracing of Figure 5.15. As is typical in the supra celiac descending aorta, this flow rate does not contain reverse flow over the entire cardiac cycle. The maximal flow is $Q_{\max} = 177$ cm^3/s and the minimal flow is $Q_{\min} = 7$ cm^3/s. Deceleration is large enough to generate complex flow behavior in all the geometrical models regardless of the outlets coupling methodology at hand. The complete model is the **reference** where three dimensional Navier-Stokes equations are coupled to reduced models at every outlet with the **3D-0D** coupling method.

Table 5.4 contains the values of the proximal and distal resistances, and capacitances for each of the nine outlets of the complete geometrical model. These values are coming from clinical measurements [VCFJT06].

	1	2	3	4	7	8	9	10	11
R_p	9.63 10^2	2.96 10^2	5.98 10^2	3.57 10^2	1.46 10^3	1.08 10^3	4.86 10^2	2.70 10^1	1.59 10^3
C	6.21 10^{-5}	7.67 10^{-4}	3.80 10^{-6}	1.40 10^{-6}	3.03 10^{-5}	6.91 10^{-5}	3.70 10^{-6}	2.13 10^{-5}	3.09 10^{-5}
R_d	3.36 10^4	1.03 10^4	1.48 10^4	2.51 10^4	1.14 10^5	4.35 10^4	1.49 10^4	1.55 10^4	1.15 10^5

Table 5.4: Reduced model parameters for each outlet of the **reference** model, as labeled in the full model of Figure 5.15. R_p and R_d in g cm^{-4} s^{-1}, and C in g^{-1} cm^4 s^2.

Table 5.5 contains values of proximal and distal resistances, and capacitances for each of the six outlets of the cut geometrical model. These reduced model parameters for the cut abdominal outlet surface (cut2) were not generated from the ones of the four outlet surfaces of the reference model (labeled 1,7, 8 and 11) as was done in the previous test case, as this was leading to too inaccurate results. Instead, the 3 Windkessel parameters of this cut outlet were identified by a Kalman filtering approach based on the flow and pressure tracings from the reference simulation [PFGVC14].

	cut1	cut2	cut3	cut4	cut6	cut7
R_p	4.86 10^2	8.21 10^2	3.57 10^2	2.96 10^2	2.70 10^1	5.98 10^2
C	3.70 10^{-6}	2.05 10^{-4}	1.40 10^{-6}	7.67 10^{-4}	2.13 10^{-5}	3.80 10^{-4}
R_d	1.49 10^4	2.13 10^4	2.51 10^4	1.03 10^4	1.55 10^4	1.48 10^4

Table 5.5: Reduced model parameters for each of the six outlet of the cut model (for the **3D-0D** and **3D-0D-Stab** coupling methods), as labeled in Figure 5.15. R_p and R_d in g cm^{-4} s^{-1}, and C in g^{-1} cm^4 s^2.

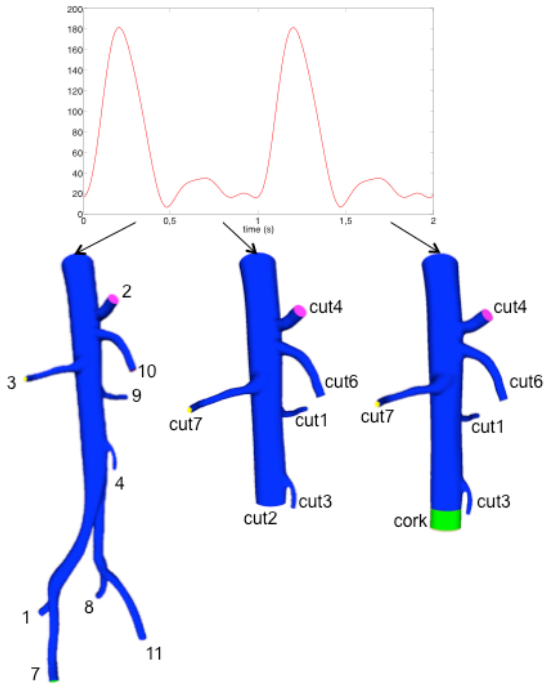

Figure 5.15: Top: imposed inflow (cm^3/s) shown over two cycles. Below, from left to right: the complete 3D model, the cut 3D model and the cut 3D model with its artificial 3D part tagged cork. The outlets are all labeled for future reference.

Table 5.6 contains values of proximal and distal resistances, and capacitances for each of the five outlets of the original part and coefficient α, β and γ for the **3D-3D** model in the artificial cork part. Similarly, Table 5.7 reports the same values for the five outlets of the original part, but coefficients α, β and γ and the 3-element Windkessel distal interface for the artificial cork part of the **3D-3D-0D** model.

	cut1	cut3	cut4	cut6	cut7		cork
R_p	$4.86\ 10^{2}$	$3.57\ 10^{2}$	$2.96\ 10^{2}$	$2.70\ 10^{1}$	$5.98\ 10^{2}$	γ	$1.49\ 10^{3}$
C	$3.70\ 10^{-6}$	$1.40\ 10^{-6}$	$7.67\ 10^{-4}$	$2.13\ 10^{-5}$	$3.80\ 10^{-6}$	α	$1.13\ 10^{-4}$
R_d	$1.49\ 10^{4}$	$2.51\ 10^{4}$	$1.03\ 10^{4}$	$1.55\ 10^{4}$	$1.48\ 10^{4}$	β	$2.60\ 10^{-5}$

Table 5.6: Reduced model parameters for each outlet of the **3D-3D** coupling model, as labeled in the cut model with cork in Figure 5.15. R_p and R_d in g cm^{-4} s^{-1}, and C in g^{-1} cm^4 s^2, $\boldsymbol{\alpha}$ in g^{-1} cm s^2, $\boldsymbol{\beta}$ in g^{-1} cm s, and $\boldsymbol{\gamma}$ in g cm^{-3} s^{-1}.

	cut1	cut3	cut4	cut6	cut7	cork		cut	
R_p	$4.86\ 10^{2}$	$3.57\ 10^{2}$	$2.96\ 10^{2}$	$2.70\ 10^{1}$	$5.98\ 10^{2}$	γ	$1.49\ 10^{2}$	R_p	$7.39\ 10^{2}$
C	$3.70\ 10^{-6}$	$1.40\ 10^{-6}$	$7.67\ 10^{-4}$	$2.13\ 10^{-5}$	$3.80\ 10^{-6}$	α	0	C	$2.05\ 10^{-4}$
R_d	$1.49\ 10^{4}$	$2.51\ 10^{4}$	$1.03\ 10^{4}$	$1.55\ 10^{4}$	$1.48\ 10^{4}$	β	0	R_d	$2.13\ 10^{4}$

Table 5.7: Reduced model parameters for each outlet of the **3D-3D-0D** coupling model, as labeled in the cut model with cork in Figure 5.15. R_p and R_d in g cm^{-4} s^{-1}, and C in g^{-1} cm^4 s^2, $\boldsymbol{\alpha}$ in g^{-1} cm s^2, $\boldsymbol{\beta}$ in g^{-1} cm s, and $\boldsymbol{\gamma}$ in g cm^{-3} s^{-1}.

Hemodynamics are compared through the cut abdominal aortic surface of the reference simulation with the abdominal aortic outlet of the other models. On the left column of Figure 5.16, i.e. during forward flow, the velocity field behavior is closer to the **reference** for the **3D-0D** coupling and thus also for **3D-0D-Stab** method since the vectors are all pointing outwards. The **3D-3D** approach leads to a flatter velocity profile. However, during reverse flow, the **reference** case concentrates the higher velocity magnitudes on the exterior part of the surface area. The **3D-0D** coupling method results in high central velocity vectors, eventually leading to divergence of the simulation. This time, the **3D-0D-Stab** coupling exhibits some backflow but with a homogeneous distribution of velocity vectors on the surface area. The **3D-3D** model is similar, but with velocity magnitude closer to the average **reference** case.

Figure 5.17 shows the **Ptot** coupling method results, with spurious radial velocity vectors, the well known effect of the total pressure coupling [HRT96]. In this case the simulation actually diverges.

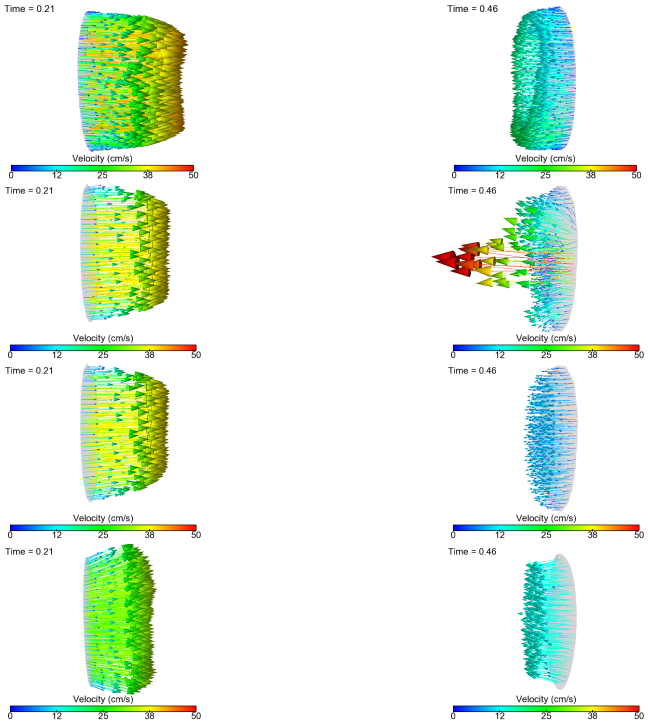

Figure 5.16: Velocity fields at two different times, t=0.21s (maximal forward inlet flow) on the left side and t=0.46s (maximal reverse flow at outlet) on the right side for from top to bottom: **reference**, **3D-0D**, **3D-0D-Stab** and **3D-3D** coupling models.

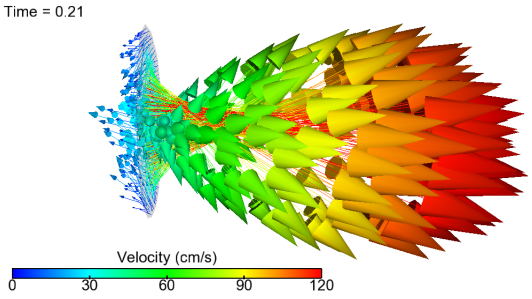

Figure 5.17: Velocity fields during maximal forward flow by using **3D-0D-Ptot** coupling model.

By contrast, in Figure 5.18, the velocity field with the **3D-3D-0D** coupling method is close to the one obtained with the **3D-0D-Stab** coupling method, during both maximal forward flow and during reverse flow.

Figure 5.18: Velocity fields at two different time points (t=0.21s (maximal forward flow at inlet) on the left side and t=0.46s (maximal reverse flow at outlet) on the right side) by using **3D-3D-0D** model.

Next, in Figure 5.19, the resulting time-varying flow rates are compared at the same surface, between the **3D-0D** , **3D-0D-Stab** , **3D-3D** and **3D-3D-0D** coupling models. All cases follow a dynamics with a peak in systole followed by a rapid deceleration with significant flow reversal and then forward flow again in the last part of diastole. The curves are neither completely synchronized in time nor matching completely in amplitudes. This time, for the **3D-0D** case the flow rate does not largely oscillate before the simulation diverges. Moreover the **3D-0D-Stab** coupling method is disturbing the blood flow behavior, with a flow rate amplitude lower than the reference one, where maximum flow is lower and minimum flow is higher than reference flow rate. The **3D-3D** follows closely. The coupling method that reproduces as best as possible the flow tracing from the reference case is the **3D-3D-0D** coupling method even if the minimum flow is overestimated.

In Figure 5.20, the corresponding pressure curves are compared: although they all follow the same typical pressure dynamics of a peak in systole followed by a smooth decay in diastole, all coupling methods overestimate the reference pressure. They are all shifted in time differently than for the flow rates. The **3D-0D** case overestimates the last pressure, but it diverges in diastole. For this test case, the **3D-0D-Stab** method is the furthest from the reference case whereas the **3D-3D-0D** coupling model is the closest. The **3D-3D** coupling approach is in between in terms of magnitude, but with an additional time shift.

In summary for this case, one can observe that both **3D-0D** and **3D-0D-Ptot** couplings lead to divergence of the simulation, due to the negative

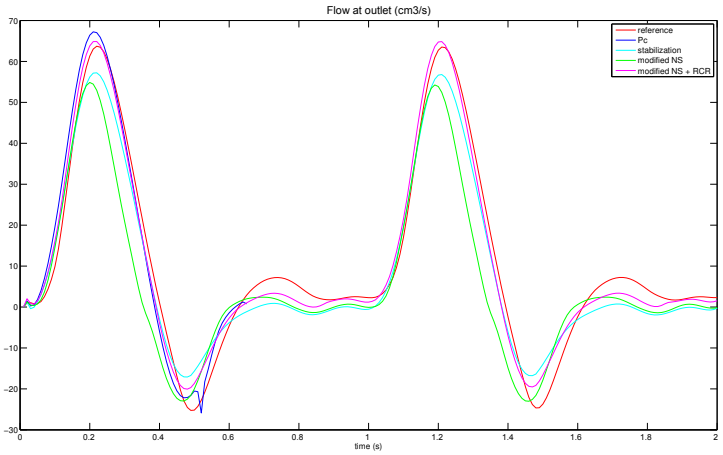

Figure 5.19: Flow rates over two cardiac cycles at the infrarenal (cut2) coupling interface, with the different coupling methods.

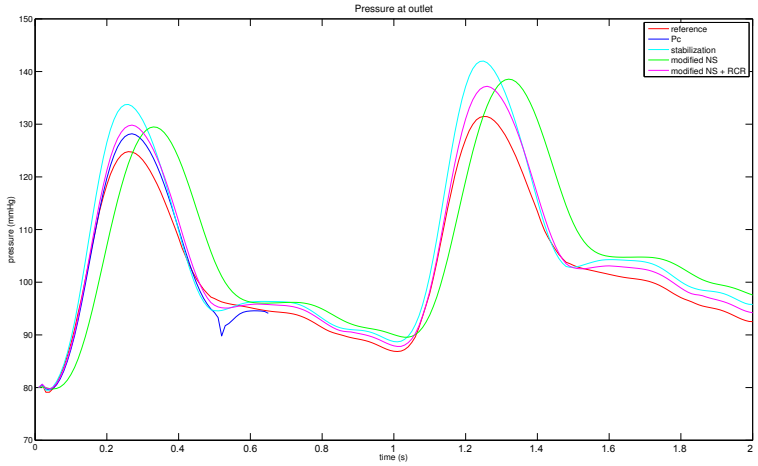

Figure 5.20: Surface-averaged pressure over two cardiac cycles at the infrarenal (cut2) coupling interface with the different coupling methods.

flow rate at the outlet, although the flow is entering at the inlet. Such a flow rate difference is typical of these abdominal aorta locations [VCFJT06]. Note however that the **reference** case does not diverge, despite using the same **3D-0D** method at its outlets. This is underlying the sensitivity of such flow simulations to divergence. In all the converging cases during back flow, the velocity vectors are all aligned in the same inward direction. The **3D-0D-Stab** , **3D-3D** and **3D-3D-0D** coupling methods presented similarities and differences with the **reference** case, which is the ground truth, **3D-3D-0D** being again the best compromise in this example.

5.4 Discussion

In this chapter different existing methods have been implemented and compared to couple three-dimensional finite element Navier-Stokes simulations to lumped parameter models, and in particular to the 3-element Windkessel model. Differences in numerical implementations that might also affect numerical stability (e.g [MVCF+13]) and references therein) are not discussed here, but rather coupling approaches at the continuous level. The first (standard) idea has been to impose weakly that at the coupling interface the normal component of the stress tensor is equal to a surface-homogeneous pressure computed from the reduced model. Such a coupling was shown above to lead to an (uncontrolled) convective boundary energy term, potentially destabilizing with flow reversal at the interface. In presence of complex flow at that location, simulations are diverging in the patient-specific examples presented above. This behavior is consistent with other examples from the literature [IE06, ACB+]. Note that for the two last patient-specific cases, although the same **3D-0D** coupling was imposed in the full 3D-models, the simulations did not diverge: as the geometry branches off, flow gets more streamlined as observed in [TTFVC11, IE06]. To get rid of this potentially destabilizing boundary convective term, the **3D-0D-Ptot** coupling method was also implemented. It imposes the normal component of the stress to be equal to the total pressure. This coupling approach was considered for example in [BCMO88, HRT96]. Similarly to what [HRT96] observed already for stationary flow in a pipe, abnormally large radial components of the velocity vectors at the coupling surface was observed during forward flow. Likely because of higher Reynolds numbers and more complex flow in these patient-specific cases, spurious peripheral inward and out of plane velocity vectors were seen, even in case of forward flow. This generated abnormally large in-plane pressure gradient and eventually lead to divergence of the

simulations when forward flow became too high.

These two methods highlighted the sensitivity of the simulation stability to the choice of coupling method. It is not a priori possible to predict which simulation will be stable throughout or diverge. Since the first coupling only diverges typically with some inward and non-zero tangential velocity vector or complete back flow at the coupling interface, natural ideas are to enforce the tangential component to be zero or to even constrain the whole velocity profile. As these have been shown to be non-ideal [MBH+11], here the convective **3D-0D-Stab** method was retained. Recall that it only acts when velocity vectors point inwards at the coupling interface. It was introduced in [BGH+09] for cardiovascular applications with an energetically over-stabilizing effect as discussed above, and successfully tested with a smaller energy-dissipative coefficient (a value of θ of 0.5 or less was found enough to ensure stability) in [MBH+11, MVCF+13, OMG+14] in cardiovascular and respiratory contexts. In these papers, without this stabilization the simulations would have diverged. Here the version that exactly annihilates the energetically destabilizing convective term was implemented. It leads in fact to a similar stabilizing behavior. The present results highlight the robustness of this method under different conditions of complex and back flows. However such a coupling involves enforcing an ad-hoc inhomogeneous normal stress over the interface area and in practice generally induces an over-killing of the inward velocity vectors. Besides, as noted by [PZVP12], this leads to a weak formulation that is not consistent with the original strong boundary condition of the reduced model coupling. A consistent formulation (with a value of θ of one) has been proposed by [GCY+12] in respiratory mechanics (see this reference for earlier references about imposition of total momentum flux) but it requires to also prescribe the convective term and thus to know the velocity vectors at the coupling boundary or to make some further assumption on the velocity profile at the boundary [GCY+12, IGCW14]. The convective stabilization with $\theta = 1$ resulted in single tube cases in a flatter velocity profile than in their total momentum flux case. It is interesting to note that in respiratory applications for which the back flow is very significant (whole expiration phase), the necessity to stabilize the convective term one way or another was found crucial [KKC+13, IGCW14, OMG+14].

One of our main aims was thus to develop a new three-dimensional finite element coupling method where reduced model parameters were three-dimensionally distributed in a modified Navier-Stokes equation into a small outer portion. The goal was to obtain a blood flow behavior as close as possible to a **3D-0D** coupling into an extended geometrical model with more

branches. From a theoretical point of view, this approach has the advantage that it does not necessitate a coupling condition at the interface: it thus does not enforce the normal component of the stress to be homogeneous as in the **3D-0D** method or inhomogeneous in an ad-hoc way as in the **3D-0D-Stab** method. Another advantage is that it generates an energy balance that is similar to the **3D-0D** method, but if the distal boundary of the modified part is set to zero velocity (as was done in the **3D-3D** simulations), it does not include the potentially destabilizing convective boundary term. If this distal velocity is not zero (as was the case in the **3D-3D-0D** simulations), this term is however controlled in the sense that the velocity field is regularized by the modified portion before it reaches the boundary.

This new method was also numerically compared to existing coupling methods qualitatively and quantitatively. As a general trend, the results suggest that the **3D-0D-Stab** coupling method is more accurately reproducing forward blood flow whereas during deceleration or reverse flow it is less invasive to use the three-dimensional coupling **3D-3D** approach than the robust **3D-0D-Stab** model. An excellent compromise was reached by the **3D-3D-0D** method, a hybrid method which regularizes the flow in an artificial portion, with a small dissipative term, representing a small fraction of the proximal resistance. The rest of the reduced model is then coupled as usual at the end of the three-dimensional model. It effectively stabilized the simulations, without significantly affecting forward flow but allowing more freely inward velocity vectors than the **3D-0D-Stab** method. Regarding pressure and flow tracings at the coupling interfaces of the three patient-specific cases, all coupling methods could reproduce the general temporal dynamics, unless they diverged. However, quantitative pressure and flow differences could be observed. In fact, in biomedical applications, the existing coupling methods and the ones developed in this chapter all involve tuning of the distal parameters in order to be as coherent as possible to clinical hemodynamics measurements [VCMF10]. Such tuning was not the focus of this work, and is matter of intense recent research (e.g [ST10, TTFVC11, BMG12, IWG13, PFGVC14, CBK+13, ACB+]). Here, when the reference model (extended model with Windkessel reduced models at its ends) was available, it was quite simple to deduce or automatically tune the corresponding Windkessel model at the coupling interface of the cut model. This made sure that the **3D-0D** and **3D-0D-Stab** results were close to the **reference** case. However, such equivalence or tuning was less obvious to do for the new **3D-3D** parameters ($\boldsymbol{\alpha}$, $\boldsymbol{\beta}$ and $\boldsymbol{\gamma}$). Actually in general the reference model would not be available (otherwise it would be used without cutting) and the modified Navier-Stokes parameters (in its original or hybrid version) could be tuned in order to match clinical hemodynamics

measurements instead of matching reduced model parameters R_p, C and R_d. This approach is not developed at this time and could be part of future work.

Interestingly, several methods lead to more similar results between each other than compared to the non-cut reference model. This is particularly true when the downstream part is geometrically different than the upstream, as was the case of the LPA in the child pulmonary example. The distribution of flow rates among the different downstream vessels can also affect the flow in the non-cut upstream region. This highlights the importance of including enough downstream geometry to not affect the area of interest in the three-dimensional part in biomedical applications [TTFVC11, ACB+].

Finally, this **3D-3D** method could be extended to couple a more extensive lumped parameter model through the $\boldsymbol{\beta}$ term. The latter could include a distal pressure, representing the link with the rest of the reduced model. Furthermore, it would be interesting to implement a space-varying $\boldsymbol{\gamma}$ parameter. This dissipative term in the Navier-Stokes equation is known to regularize the velocity profile to a plug-like profile (like at the interface with a porous medium), which helps here to stabilize the simulation but is also responsible for a significant impact on the velocity field at the interface. The coupling approach would be less invasive in particular during forward flow if this parameter was changing more smoothly. This is probably why the **3D-3D-0D** was found to be the best compromise between robustness and non-invasiveness.

5.5 Conclusion

In this chapter we have developed and implemented a new approach to improve the stability of the incompressible three-dimensional Navier-Stokes equations for patient-specific simulations of blood flow: it adds a modified Navier-Stokes artificial domain that models in a distributed way the reduced Windkessel model. Hence, there is no need for coupling conditions, and in particular it does not constrain the normal component of the stress at the interface, nor adds an ad-hoc boundary stabilization term. The total system gives an energy norm in essence similar to that of the usual Navier-Stokes to reduced model coupling, without the potentially destabilizing outlet convective term, or in the hybrid implementation stable in numerical practice.

Qualitative and quantitative comparisons of existing coupling methods of

three-dimensional Navier-Stokes equations to 0D reduced models with this modified Navier-Stokes approach have been made in three patient-specific cases of healthy adult and diseased child pulmonary arteries and healthy adult descending aorta. The **3D-0D** and **3D-0D-Ptot** methods are sensitive to instabilities, depending on where the 3D domain is artificially cut, while the other methods remain stable in all tests. Results from earlier coupling methods match those from the literature. Numerical results from the modified Navier-Stokes approach are especially less invasive during deceleration or reverse flow. The hybrid form of this new method, the **3D-3D-0D** method, is particularly promising as it effectively stabilizes the simulations, without significantly affecting forward flow but allowing more freely inward velocity vectors than the **3D-0D-Stab** method.

The comparison of the cut-models with the reference, more extended model highlights the importance of including enough downstream geometry to not affect hemodynamics in the area of interest of the three-dimensional part in biomedical applications.

The dynamics accuracy of the proposed method can be increased by better tuning parameters to match clinical data. This method could also be improved, although it would increase the development cost, with a space-varying dissipative term. Finally, this method can be extended to other biological patient-specific simulations, like more extensive reduced models or air flow into the lungs.

Part III

Uncertainty quantification for surgery planning

Chapter 6

Uncertainty quantification in a stenosed patient-specific pre-stage 2 palliation

In this chapter, we present a cost-reduced modeling framework to translate uncertainties of flow split and pressure measurements into uncertainty on reduced model parameters of the multi scale 3D-0D simulations presented in chapter 4. The first step is to build 0D surrogates of these 3D-0D models to generate a set of 0D boundary conditions for the 3D simulations that reflect the measurement uncertainties. Then, 3D-0D simulations are performed to verify that this set indeed reflects the uncertainty ranges of clinical measurements. We apply this methodology to a stenosed pre-operative stage 2 patient-specific case for which preliminary work by the Leducq consortium on different surgical options included the removal or not of the stenosis.

The work presented in this chapter is being performed in collaboration with Catriona Baker at the Great Ormond Street Hospital, London (clinical data), and Daniele Schiavazzi and Alison Marsden at UCSD (propagation of uncertainties into stage 2) and discussed with the clinicians involved in the Leducq network.

Contents

6.1 Introduction

A significant increase in the sophistication and clinical applicability of computational tools has lead to more representative patient-specific modeling

of blood flow. The latter is based on the capacity to build realistic three dimensional models directly from image data and to obtain reliable blood velocity and pressure information from clinical data, in order to perform simulations that are physiologically meaningful, as described in chapters 2, 3, 4. The confidence in the data output from cardiovascular simulations directly depends on the level of certainty in simulation input parameters. In this context, determining the effect of uncertain inputs on simulation results makes the models more reliable and becomes a more useful tool for surgical planning.

The methodological aim of this study is to provide a numerical tool able to automatically propagate uncertainties in hemodynamics clinical measurements from clinically based pre-stage 2 to virtual post-stage 2 simulations. In particular, we want to investigate the effect of pulmonary flow split and venous wedge pressure measurements uncertainties on hemodynamics quantities such as 1) pressure difference between left and right pulmonary arteries, 2) pressure drop through the stenosis, and also on hemodynamics (blood flow behavior, pressure, etc.) in different virtual post-operative cases.

We present in Figure 6.1 the 3D stage 1 (i.e. pre-stage 2) patient-specific model corresponding to patient D in 4. This preoperative model contains a significant stenosis in the left pulmonary artery. When tuning of the reduced model parameters in the 3D-0D simulations was first performed based on the measured flow split, the model prediction for the pressure difference between RPA:LPA was not consistent with the clinical observations (see 4.4). The set of parameters that were coherent with all the pressure measurements thus led to a different flow split than measured. In the study of different virtual surgical options, it was found that the removal of the stenosis was not significantly affecting the ratio between the power loss in the model and the total pulmonary power loss that the diseased heart has to pump for. Besides, a rather small - 10 % - flow split difference was found with and without the stenosis. Hence, it was concluded based on these simulation results, that removal of the stenosis - as was actually surgically done - may in fact not have been necessary. The clinical aim here is thus the answer to the following question: how much are the above statements affected by the uncertainty in the preoperative clinical measurements?

In this chapter we focus on the first step of the study, i.e. to translate uncertainties of flow split and venous wedge pressure measurements into uncertainties on reduced model parameters of the preoperative multi scale 3D-0D simulations presented in chapter 4. A cost-reduced framework is proposed. First, 0D surrogates of the 3D-0D preoperative model are built.

Their outputs lead to a set of 0D boundary conditions for the 3D simulations that reflect the measurement uncertainties. Then, 3D-0D simulations are performed to verify that this set indeed reflects the uncertainty ranges of clinical measurements. By this process, a question from the clinicians is then addressed: to assess the blood flow through the narrowing in the left pulmonary artery (Figure 6.1 right side, close to the shunt) that is consistent with the clinically believed measurements or their tolerated deviations. From a modeling point of view, it is possibly important to take into account this narrowing, as well as other 3D effects, when setting the 0D boundary conditions.

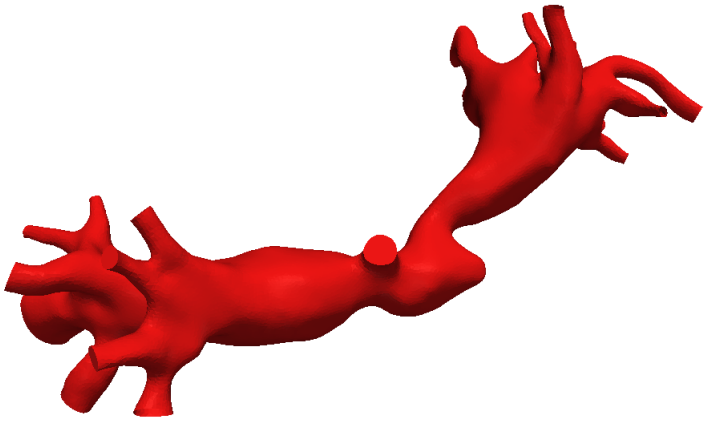

Figure 6.1: 3D patient-specific model of pre operative stage 2

In section 6.2, we iteratively build the 0D surrogates to convert uncertainties of pressure and flow split into uncertainty of reduced model parameters (sets of total resistances later translated into 5-parameter reduced models as in 3.2.3) taking into account non linear effects due to narrowings. In section 6.3 we present simulation results by coupling three dimensional incompressible Navier-Stokes equations to these sets of resistances and verify that these sets indeed reflect the uncertainty ranges of clinical measurements, hence assessing the validity of the 0D surrogates. Finally, on-going work to answer the clinical aim based on these results is briefly given as an outlook in 6.4.

6.2 Methods

A schematic representation of the pulmonary circulation is shown in Figure 6.2. Values of resistances (Ri) are computed from flow rates (Qi) and pressures (Pi) at the model outlets, given the downstream atrium pressure P_a, i.e

$$R_i = \frac{P_i - P_a}{Q_i} \tag{6.1}$$

Resistances thus represent as usual the distal pulmonary vasculature not included in the multi-branched domain of interest. This domain can either be represented in 3D (for 3D-0D multi scale simulations) or by a 0D surrogate consisting of an arrangement of resistances, possibly nonlinear. The inflow Q_in and the atrium pressure P_a are considered here as the time-averaged clinically measured values and not subject to uncertainties. This first uncertainty study is thus based on steady blood flow simulations.

If the uncertainties were directly known on the boundary resistances (R_i), one could thus directly propagate them by 3D-0D simulations with the given inlet flow rate, in terms of output uncertainties (flow (Q_i) and pressure (P_i) results at various locations in the model). This is a well-defined problem that can be solved, e.g., by non-intrusive sparse grid approaches.

However, to characterize the uncertainty in the boundary resistances (R_i) cannot easily be deduced from the uncertainties in the clinical measurements. Recall that these are the flow split between right and left lungs fs_m, and the venous wedge pressure as surrogate for an average arterial pulmonary pressure P_m (see 4.2.2). Clinical experts can set uncertainty ranges and probability density functions based on their expertise. Then, collocation points need to be computed to know which discrete pairs (fs_m, P_m) should be considered. Indeed, for each pair of these uncertain measurements, tuning involving several 3D simulations is warranted as was done in 4. This would rapidly be very costly. For this reason, the current framework is rather based on 0D surrogates, where such uncertainty propagation is more straightforward.

We thus start with the simplest 0D surrogate, which means that pressure loss in the 3D model is neglected and the surrogate consists solely on the set of downstream R_i all in parallel. This leads to the first approximation of (R_i).

We first define the flow split fs_m which is the ratio of blood going towards the

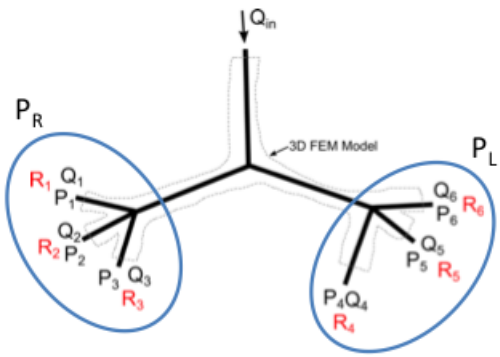

Figure 6.2: Schematic representation of the pulmonary circulation models. Inlet and outlet variables are shown together. P_i, Q_i and R_i are respectively pressures, flows and resistances ($i \in [1;6]$), and P_R and P_L are averaged pressures over the right and left sides respectively.

right pulmonary artery over the total flow entering into the 3D domain,

$$\mathrm{fs}_m = \frac{Q_{\mathrm{right}}}{Q_{in}} \tag{6.2}$$

We then define as in 3 a target flow at outlet i proportional to the surface area of the latter (S_i), and depending on the flow split,

$$Q_i = \frac{Q_{in} S_i \Big(\delta_{iR} \mathrm{fs}_m + (1 - \delta_{iR})(1 - \mathrm{fs}_m) \Big)}{\sum_j S_j \delta_{ij}} \tag{6.3}$$

where fs_m is the flow split generated by a collocation method, $\delta_{ij} = 1$ if outlets i and j are on the same side and 0 if not, $\delta_{iR} = 1$ if outlet i is on the right side and 0 if not.

The most simplified 0D surrogate model thus defines an approximation of R_i with 6.3 as follows,

$$R_i = \frac{P_m - P_a}{Q_i} \tag{6.4}$$

where P_m is the pulmonary arterial pressure computed from a collocation method knowing the atrium pressure P_a. It is assumed from now on to be representative of the average pressure over all the 20 outlets.

However, a first 3D-0D simulation can quickly convince that this simplest surrogate model is in fact too simple. Indeed, it does not consider the 3D nonlinear effects, especially for the pressure loss through narrowings such as a stenosis. The 0D surrogate is thus enriched to take into account the pressure losses due to narrowings. An empirical model [SY76] to quantify pressure loss in a stenosis as a function of the blood velocity is incorporated,

$$\Delta P_{\mathrm{stenosis}} = \frac{\mu L_{stenosis} 32 S_{vessel}^2}{D_{vessel}^2 S_{stenosis}^2} V + 0.76 \rho \left(\frac{S_{vessel}}{S_{stenosis}} - 1 \right)^2 V^2 \tag{6.5}$$

where V is the mean velocity of the blood through the narrow section, μ and ρ are respectively viscosity and density of the blood, $L_{stenosis}$ and $S_{stenosis}$ are respectively the length and the surface area of the narrowing, D_{vessel} and S_{vessel} are respectively the diameter and the surface area of the blood vessel upstream of the stenosis.

We denote by P_L and P_R the average outlet pressures respectively on the

left and right sides, ΔP_s^L and ΔP_s^R the pressure losses through stenoses respectively in the left and right sides. We then build two different surrogate models.

6.2.1 Stenosis in the left pulmonary artery

An obvious stenosis was detected by the clinicians priori to the surgery. This second surrogate model thus consists in a nonlinear resistance on the left side, and for the rest, it is as in the simplest models: all the distal branches are in parallel on each side. This model thus assumes that all other pressure differences are negligible, i.e.

$$\begin{aligned} P_L - P_a &= \frac{3}{2}P_m - \frac{1}{2}\Delta P_s^L \\ P_R - P_a &= \frac{1}{2}P_m + \frac{1}{2}\Delta P_s^L \end{aligned} \tag{6.6}$$

Recall that P_m is the pulmonary arterial pressure computed from a collocation method, representative of the average pressure over all the 20 outlets.
From (6.4),(6.5),(6.6) and a given pair of (fs_m,P_m), a set of resistances R_i is then generated that takes into account the stenosis in the left pulmonary artery,

$$\begin{aligned} R_i^L &= \frac{P^L - P_a}{Q_i} \\ R_i^R &= \frac{P^R - P_a}{Q_i} \end{aligned} \tag{6.7}$$

where R_i^L and R_i^R are new approximations of resistances R_i at each outlet i respectively in the left and right sides.

6.2.2 Stenosis in both pulmonary arteries

If we want to model resistances to take into account the stenosis in the left pulmonary artery and the narrowing in the right pulmonary artery, we define left and right pressures based on (6.5),

$$\begin{aligned} P^L - P_a &= \frac{1}{2}\left(\Delta P_s^R - \Delta P_s^L\right) + P_m \\ P^R - P_a &= \frac{1}{2}\left(\Delta P_s^L - \Delta P_s^R\right) + P_m \end{aligned} \tag{6.8}$$

and use (6.7) to compute a corresponding set of resistances. There are thus as many sets for each surrogate model as number of collocation points.

6.3 Results

Recall that this patient-specific model is patient D from chapter 4 with a left pulmonary wedge venous pressure measured equal to 12 mmHg and a flow split equal to 0.46. The pressure difference between right and left lung was considered negligible. The tuning of resistances in that chapter showed the incoherence of these data, pointing out the need for their uncertainty assessment. Based on the medical expertise about the difficulty of flow and pressure measurements in such a small child with turbulent flow and pressure only accessible via venous wedge, possible ranges of pressure and flow are respectively considered here as [9 mmHg,15 mmHg] and [0.45,0.65]. A plausible pressure difference between right and left lungs was estimated to be 2 mmHg.These ranges should covered by the outputs from the methods described above.

One option is to manually perturb different parameters. However, if we need to compute sensitivities over a wide range of parameters, and if there are a large number of parameters, this method involves an expensive computational cost. Monte-Carlo techniques have been employed for performing probabilistic analysis. However, it is not convenient to employ them for computationally expensive three-dimensional problems involving complex geometries. In this chapter, we use stochastic spaces to represent the variability in the average pressure and flow split parameters. We represent a stochastic field using its values at specific collocation points in the stochastic space. The Smolyak algorithm is a method for choosing the collocation points, and allow to significantly reduce the number of points necessary for interpolation in multi-dimensional random space [GZ07]. Further details of the algorithm are given in [Kli06],[Kli07].

For each pair of pulmonary pressure and flow split, a set of resistances was generated with the methods described in sections 6.2.1 and 6.2.2. This theoretical pair was then compared to the numerical results obtained by coupling 3D Navier-Stokes equations to these resistances. More precisely, theoretical and numerical average pressures over all the outlets and flow splits were thus compared.

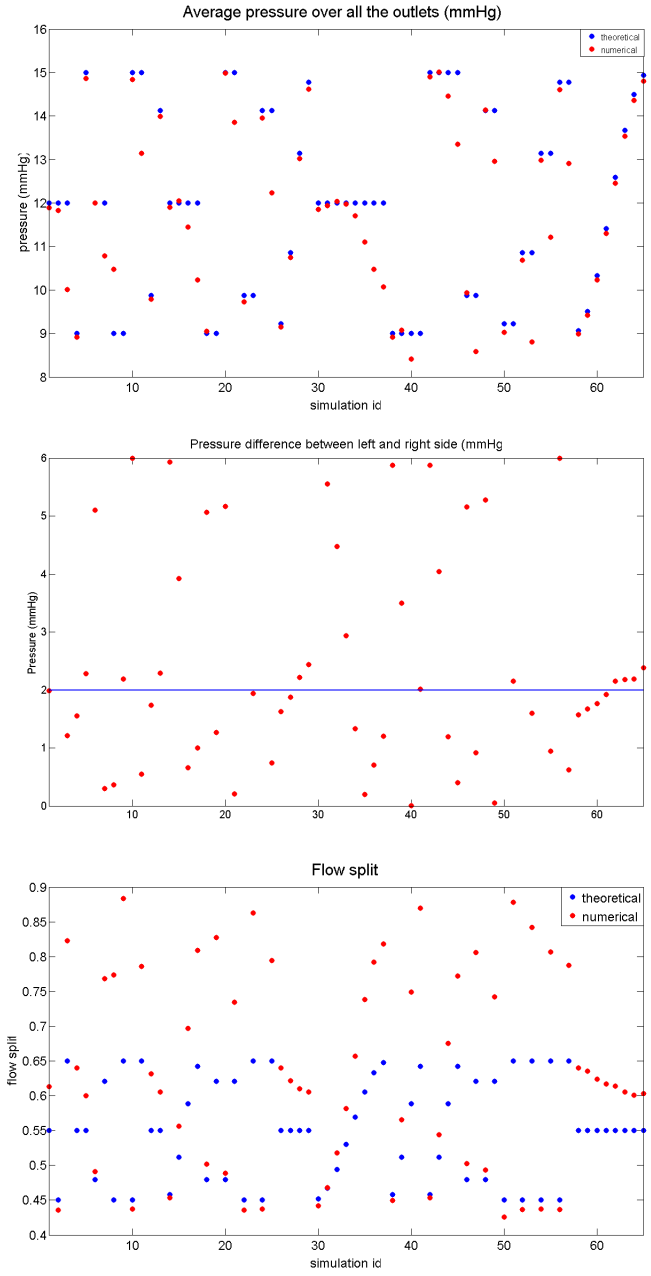

Figure 6.3: Expected (theoretical) and numerical results using the 0D surrogate model defined in 6.2.1. Pressure (upper), Difference pressure between left and right pulmonary artery (center), Flow split (lower). Here theoretical means the target values that we want to reach, based on the uncertain measurements, and numerical values are obtained by numerical simulations coupled to resistances.

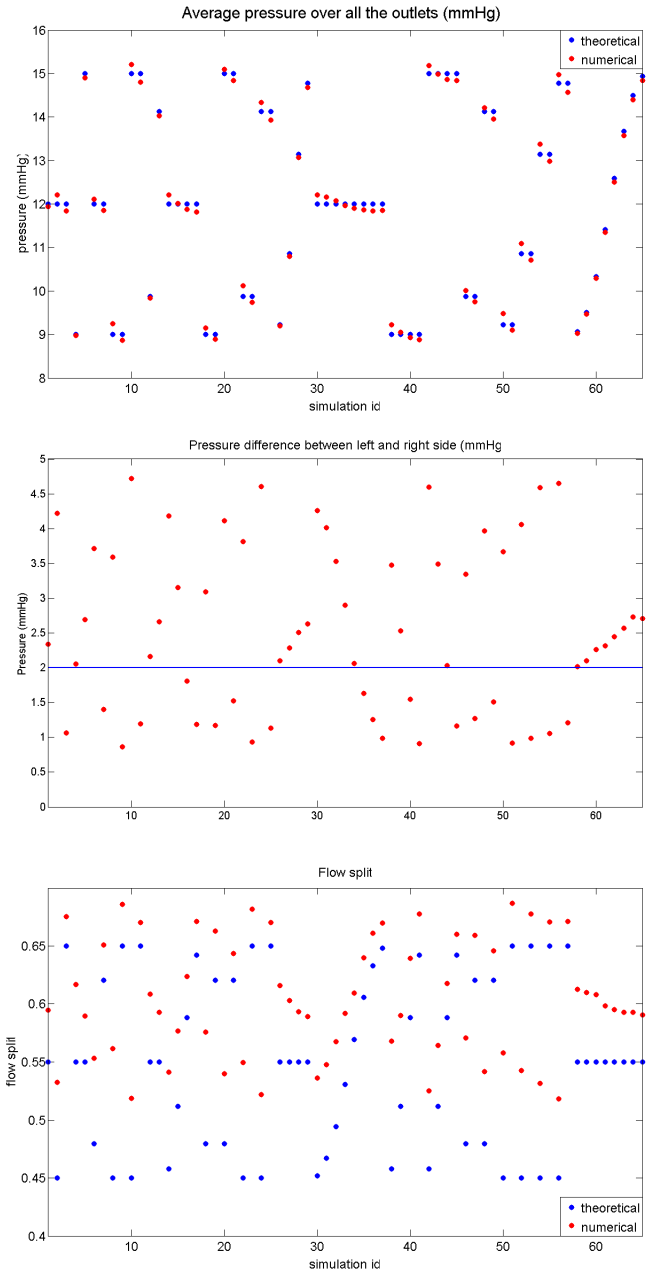

Figure 6.4: Expected (theoretical) and numerical results with the 0D surrogate model defined in 6.2.2. Pressure (upper), Difference pressure between left and right pulmonary artery (center), Flow split (lower)

In Figure 6.3 upper, we present expected (theoretical, blue points) and numerical (red points) average pressure over all the outlets, when using the left stenosis 0D surrogate model (6.2.1). The numerical pressure is between 8.4 and 15 mmHg which is close to the expected range (between 9 and 15 mmHg), but most of the simulations underestimate the expected outlet average pressure.

On the same figure, we also compare expected and numerical flow splits. The numerical flow split ranges between 0.4 and 0.9 which is much higher than the expected one (between 0.45 and 0.65).

Therefore, the procedure was repeated with the double-sided stenosis model. In Figure 6.4 upper, we present expected (blue points) and numerical (red points) average pressure over all the outlets. We can see that the numerical pressure is between 8.8 and 15.2 mmHg which is close to the expected range (between 9 and 15 mmHg) and most of numerical results are close to the expected ones.

As previously, we compare expected and numerical flow splits. The numerical flow split ranges between 0.52 and 0.69 which is closer to the expected flow split (between 0.45 and 0.65). Numerical simulations lead to a less overestimated flow split than with the previous surrogate model but this time fails to reach the lower bound of the targeted flow split range.

As a consequence, the sets of resistances R_i generated from both surrogate models are kept as results representing the ranges of measurement uncertainties. Note that in both cases, only a number of them are however consistent with the allowable left-right pressure difference of 2 mmHg (as can be seen at the center of Figures 6.3 and 6.4).

6.4 Conclusions and on going work

In this chapter, we developed a framework to quantify the impact of uncertainties of clinical measurements on the blood flow behavior in stage 1 pulmonary artery. We first translated measurement uncertainties of pulmonary pressure and flow distribution in the lung in terms of resistance uncertainties via nonlinear 0D surrogate models of various degrees of complexity. Then we coupled 3D Navier-Stokes equations to those sets of resistances and verified that the uncertainty ranges were indeed reached.

This framework reduces the number of 3D numerical simulations that would otherwise have been necessary with a more direct propagation of input uncertainties. The results provide an input for uncertainty propagation of preoperative clinical measurements into different virtual stage 2 surgical options (see Figure 6.5).

In this process, it was shown that nonlinearities were important to take into account to build these 0D surrogate models of 3D-0D models to capture more accurately non linear effects due to the 3D geometry, in particular to account for pressure losses through narrowings. These surrogate models were based on a nonlinear empirical model of stenosis. This model was actually successfully tested with results from 3D simulations of chapter 4 prior to its use in this uncertainty study. Although not completely representative of the 3D geometry, the 0D surrogates led in fine reasonable reach of the measurements uncertainty ranges.

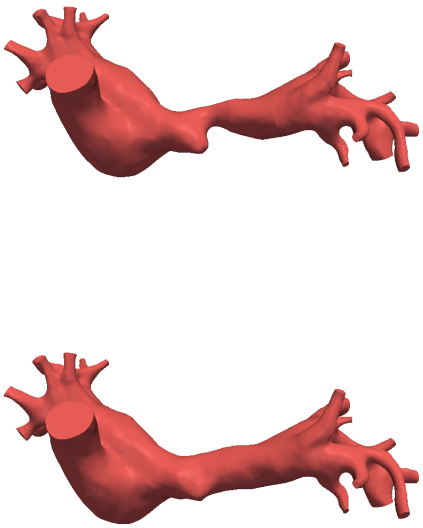

Figure 6.5: Post operative stage 2 patient-specific geometry where the superior vena cava is linked to the main pulmonary artery, and where the left pulmonary artery stenosis is repaired (lower) or left in state (upper).

Let us briefly explain now how the results are being applied to answer the medical aim. Discussing with clinicians, two post-operative stage 2 patient-

specific model are possible (Figure 6.5). The goals are now to 1) measure the effect of different ranges of the preoperatively defined resistances on postoperative flow distribution, 2) quantify the impact of the left pulmonary stenosis on the pressure loss in the 3D domain, and 3) provide an answer to the clinical question: should the stenosis during the stage 2 procedure be repaired or not?

To reach this final step, we firstly transform the sets of resistances into 5-parameter reduced models composed by resistances and capacitances, as described in chapter 3. Then, each set of reduced models is added in a whole circulatory reduced model (Figure 1.5) that is then coupled to the 3D Navier-Stokes equations. Pulsatile simulations of blood flow are then run in the 3D geometries. Another set of simulations is also run on the stenosed postoperative geometry with the same inlet and outlet resistances as in the steady preoperative study. Some of the results are described in Figures 6.6 and 6.7. We show in Figure 6.6 that flow split is higher for pre-stage 2 geometry while for pulsatile simulation in stage 2 geometry with repaired stenosis the blood flow is higher in left pulmonary artery. However pressure difference between left and right pulmonary artery is higher in pre-stage 2 geometry than in stage 2 geometry with repaired stenois. Regarding flow split Moreover we obtain (averaged over each set) 3D representation of pressure maps (see Figure 6.7) to investigate the impact of repairing the stenosis during stage 2. In fact, pulsatile simulations coupling Navier-Stokes equations to the whole circulatory system model (right in Figure 6.7) seems to be the best geometry to reduce pressure difference between left and right side. This is due to a combination of the lowering of the input flow that goes into the 3D model (effect of the whole circulation model) and a change of flow split due to the stenosis removal. This information is important from a clinical point of view to prepare stage 2 surgeries.
This methodology accounts for clinical data uncertainty in the context of surgical planning. It allows to estimate a level of confidence on biomedical conclusions based on simulation results (see Figure 6.6).

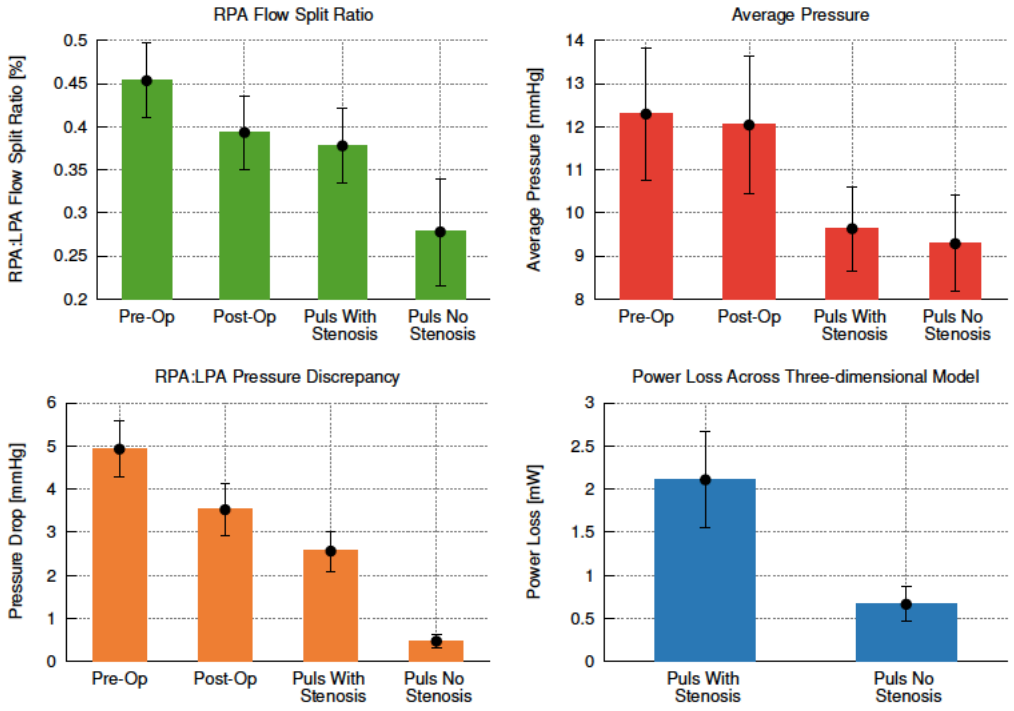

Figure 6.6: Analysis of simulation results regarding flow split (upper left), pressure (upper right), pressure discrepancy (lower left) and power loss (lower right).

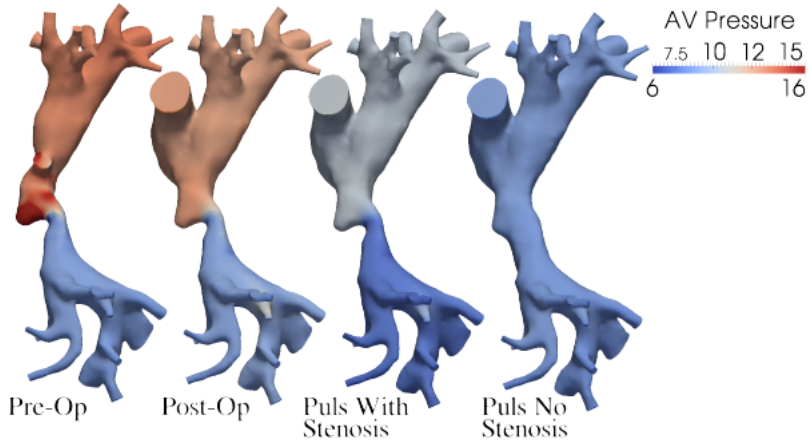

Figure 6.7: Averaged pressure distribution from left to right: steady simulation in pre-operative stage 2 model, steady simulation in stage 2 model with LPA stenosis, pulsatile simulation in stage 2 model with LPA stenosis, pulsatile simulation in stage 2 model with repaired stenosis.

Conclusions and Perspectives

Chapter 7

Conclusion

In this chapter we give a general overview of the work and contributions of this thesis and some perspectives for future research.

Contents

In chapter 2, we presented the key points in numerical simulations of blood flow regarding mesh generation, equations, boundary conditions, and numerical methods for incompressible Navier-Stokes solvers. In this thesis we focused more specifically on reduced model boundary conditions parametrization for 3D Navier-Stokes equations and stability of coupling methods between these reduced models and the 3D equations. These scientific questions stemmed out of the biomedical context of single ventricle pathophysiology and repair, a severe form of congenital heart disease.

7.1 Multiscale modeling of palliative surgery from clinical data

In chapters 3 and 4 we presented a method to iteratively tune parameters of these reduced models in multi-scale 3D-0D simulations to match averaged in time clinical hemodynamics measurements, such as mean pressure in a certain location and how much flow rate goes into each lung. Validation included the pressure difference between left and right lungs. The algorithm is the same for steady or pulsatile tuning. The method was extended to accommodate different types of pressure measurements (maximum, minimum, average over one or both lungs), depending on the patient-specific case. Moreover, arterial and venous vascular trees downstream to the 3D domain were better taken into account compared to previously, leading to estimation of 5-element reduced model parameters. We also adapted this

method to reflect the effect of collateral vessels linking systemic to pulmonary vasculature. This methodological framework was applied to three stage 2 and six stage 1 preoperative patient-specific models. One benefice was that this process demonstrated if clinical hemodynamics data were coherent or not.

3D simulations in these stage 1 and stage 2 cases highlighted the complexity of blood flow patterns into the shunt or SVC anastomosis and the pulmonary arteries, as well as their very specific pressure maps. Wall shear stress maps were especially patient-specific, although the average level was much higher in stage 1. Simulations also assessed the effects of anatomical kinks or stenoses, demonstrating the potential use of the technique: help clinicians decide whether a lesion is hemodynamically significant or not. These types of simulations could be helpful when planning whether to intervene on a PA anatomical problem. It involves a lot more surgery to intervene on a PA stenosis so if clinicians better understood the difference between a significant stenosis and an anatomical anomaly that does not have an effect, it would save time and danger to not intervene when it is not necessary.

7.2 Numerical aspects of outflow boundary conditions

In chapter 5, we presented a new approach to couple the three-dimensional Navier-Stokes equations to a reduced model. The first (standard) idea has been to impose weakly that at the coupling interface the normal component of the stress tensor is equal to a surface-homogeneous pressure computed from the reduced model. Such a coupling was shown to lead to an uncontrolled convective boundary energy term, potentially destabilizing with flow reversal at the interface. In presence of complex flow at that location, simulations were diverging in the patient-specific examples presented. To get rid of this potentially destabilizing boundary convective term, the **3D-0D-Ptot** coupling method was also implemented. It imposed the normal component of the stress to be equal to the total pressure. This coupling approach was introduced in [BCMO88, HRT96]. Similarly to what [HRT96] observed already for stationary flow in a pipe, the typical crossing of abnormally large velocity vectors at the coupling surface center was observed during forward flow. Likely because of higher Reynolds numbers and more complex flow in these patient-specific cases, spurious peripheral inward and out of plane velocity vectors were seen, even in case of forward flow. This generated abnormally large in-plane pressure gradient and eventually lead to divergence of the simulations when forward flow becomes too high.

In [BGH+09], a method was introduced to stabilize simulations in presence of back flow. The results obtained with this approach in several publications highlighted its robustness under different conditions of complex flows. Although very efficient at avoiding instabilities, this method has the drawback to also dissipate physiological back flow.

We have developed and implemented a new approach to improve the stability of the incompressible three-dimensional Navier-Stokes equations for patient-specific simulations of blood flow: it adds a modified Navier-Stokes artificial domain that models in a distributed way the reduced Windkessel model.

$$\rho\frac{\partial \boldsymbol{u}}{\partial t} + \rho\boldsymbol{u}\cdot\nabla\boldsymbol{u} + \nabla p - 2\mu\nabla\cdot\boldsymbol{\varepsilon}(\boldsymbol{u}) + \gamma\boldsymbol{u} + \rho\frac{\boldsymbol{u}}{2}\nabla\cdot\boldsymbol{u} = 0 \quad (7.1)$$

$$\alpha\frac{dp}{dt} + \beta p + \nabla\cdot\boldsymbol{u} = 0 \quad (7.2)$$

$$\boldsymbol{u}_{|\Gamma\cup\Gamma_2} = 0 \quad (7.3)$$

where α, β and γ vanish in the domain of interest, to recover the standard equations (5.1)-(5.4), and are positive in the added artificial domain, and where Γ is the wall of the domain of interest and Γ_2 is the union of the wall and the outlet of the added artificial part.

With this formulation, the coupling conditions are implicitly present in the variational formulation. In particular it does not constrain the normal component of the stress at the interface, and it does not add any ad-hoc boundary stabilization term. The global system has an energy equation similar to that of the usual Navier-Stokes equation coupled to a reduced order model, without the potentially destabilizing outlet convective term.

Qualitative and quantitative comparisons of existing coupling methods of three-dimensional Navier-Stokes equations to 0D reduced models with this modified Navier-Stokes approach have been made in three patient-specific cases of healthy adult and diseased child pulmonary arteries and healthy adult descending aorta. The **3D-0D** and **3D-0D-Ptot** methods are sensitive to instabilities, depending on where the 3D domain is artificially cut, while the other methods remain stable in all tests. Results from earlier coupling methods match those from the literature. Numerical results from the modified Navier-Stokes approach are especially less invasive during deceleration or reverse flow. The hybrid form of this new method, the **3D-3D-0D** method, is particularly promising as it effectively stabilizes the simulations, without significantly affecting forward flow but allowing more freely inward velocity

vectors than the **3D-0D-Stab** method.

7.3 Future work

Methodology presented in chapters 3 and 4 can be applied in other multi-branched blood flow simulations for which time-averaged pressure or flow measurements are taken at various locations, and chosen to be matched as a minimum, maximum, average or other combinations of values in a given region.

The accuracy of the method presented in chapter 5 can be increased by better tuning parameters to match clinical data. This method could also be improved, although it would increase the development cost, with a space-varying dissipative term. Finally, this method can be extended to other biological patient-specific simulations, like more extensive reduced models or air flow into the lungs.

Finally, all the methods developed in this thesis could be applied systematically for surgery planning, in the context of congenital heart disease, to help surgeons to choose the best palliative procedure. Although preliminary work has been done on assessing how measurement uncertainties affect the developed methodology, much more work is warranted in this direction to assess the robustness of the results and applicative conclusions.

Appendix A

An integrated approach to patient-specific predictive modeling for single ventricle heart palliation

Computer Methods in Biomechanics and Biomedical Engineering, 2013
http://dx.doi.org/10.1080/10255842.2012.758254

Taylor & Francis
Taylor & Francis Group

An integrated approach to patient-specific predictive modeling for single ventricle heart palliation

Chiara Corsini[a1], Catriona Baker[b1], Ethan Kung[c], Silvia Schievano[b], Gregory Arbia[d], Alessia Baretta[a], Giovanni Biglino[b], Francesco Migliavacca[a]*, Gabriele Dubini[a], Giancarlo Pennati[a], Alison Marsden[c], Irene Vignon-Clementel[d], Andrew Taylor[b], Tain-Yen Hsia[b] and Adam Dorfman[e]; for the Modeling of Congenital Hearts Alliance (MOCHA)[2] Investigators

[a]*Laboratory of Biological Structure Mechanics, Department of Structural Engineering, Politecnico di Milano, Piazza Leonardo da Vinci, 32, 20133, Milano, Italy;* [b]*Cardiorespiratory Unit, UCL Institute of Cardiovascular Science and Great Ormond Street Hospital for Children, London, UK;* [c]*Department of Mechanical and Aerospace Engineering, University of California San Diego, San Diego, CA, USA;* [d]*INRIA Paris-Rocquencourt, Le Chesnay, France;* [e]*Division of Pediatric Cardiology, University of Michigan Medical School, Ann Arbor, MI, USA*

(*Received 6 June 2012; final version received 10 December 2012*)

In patients with congenital heart disease and a single ventricle (SV), ventricular support of the circulation is inadequate, and staged palliative surgery (usually 3 stages) is needed for treatment. In the various palliative surgical stages individual differences in the circulation are important and patient-specific surgical planning is ideal. In this study, an integrated approach between clinicians and engineers has been developed, based on patient-specific multi-scale models, and is here applied to predict stage 2 surgical outcomes. This approach involves four distinct steps: (1) collection of pre-operative clinical data from a patient presenting for SV palliation, (2) construction of the pre-operative model, (3) creation of feasible virtual surgical options which couple a three-dimensional model of the surgical anatomy with a lumped parameter model (LPM) of the remainder of the circulation and (4) performance of post-operative simulations to aid clinical decision making. The pre-operative model is described, agreeing well with clinical flow tracings and mean pressures. Two surgical options (bi-directional Glenn and hemi-Fontan operations) are virtually performed and coupled to the pre-operative LPM, with the hemodynamics of both options reported. Results are validated against postoperative clinical data. Ultimately, this work represents the first patient-specific predictive modeling of stage 2 palliation using virtual surgery and closed-loop multi-scale modeling.

Keywords: computational fluid dynamics; lumped parameter network; multi-scale model; congenital heart disease; virtual surgery

1. Introduction

Single ventricle (SV) circulations encompass a wide range of abnormalities in cardiac anatomy leading to one ventricle being poorly or non-functional. The aim of surgery is to bypass the non-functioning ventricle by connecting the systemic venous return to the pulmonary arterial (PA) system, leading to a circulation in series powered by a SV (Fontan and Baudet 1971). Typically, this is performed as three, staged procedures over the first few years of life, in order to provide adequate systemic oxygen delivery without severe volume overloading of the ventricle.

Stage 1 surgery (Figure 1(a)) occurs as a neonate. The aim is to provide an unrestrictive systemic outflow tract with unrestricted venous return to the ventricle. Balanced flow to the pulmonary circulation is provided through a systemic-to-pulmonary shunt or PA banding depending on the anatomy. In the first few months, pulmonary vascular resistance (PVR) decreases and lung surface area increases (Bardo et al. 2001), thus stage 2 surgery may be performed. At about 6 months, the shunt is taken down or PA is ligated, and the superior vena cava (SVC) is attached to the PA vasculature to provide pulmonary flow. This may be via a Glenn [Figure 1(b), SVC to right pulmonary artery (RPA)] or hemi-Fontan procedure (Figure 1(c), SVC remains connected to the right atrium with a homograft patch redirecting its flow to the PAs). The proportion of systemic venous return from the lower body (LB) increases with age; therefore at stage 3, the Fontan procedure, the inferior vena cava (IVC) is connected to the pulmonary vasculature.

Patients requiring SV surgery comprise a small, but highly complex population. There is wide variation in anatomy and physiology between individuals, with several alternative surgical procedures at each stage. In addition, patient-specific decisions are required to plan the timing and type of surgery. Differences in local hemodynamic effects with different procedures may affect global parameters such as pulmonary flow distribution and

*Corresponding author. Email: francesco.migliavacca@polimi.it

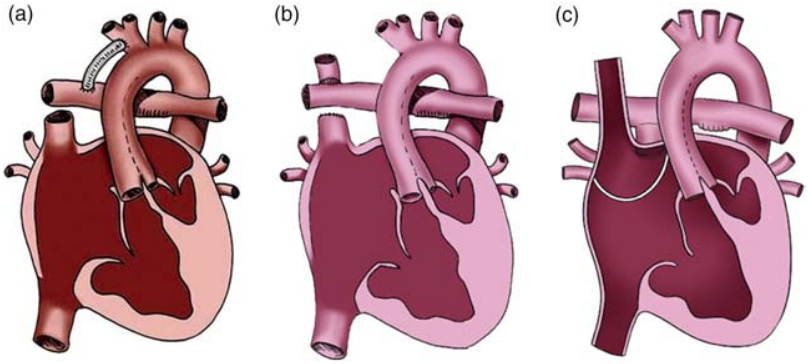

Figure 1. SV palliation surgical procedures: (a) stage 1, (b) stage 2 Glenn, (c) stage 2 hemi-Fontan. (a) republished with kind permission from Springer Science and Business Media, originally published in Dillman et al. (2010, p. 264, Figure 4) illustration by Anne Phillips, University of Michigan Health System, Department of Radiology Media Services; Figure (b),(c) produced by Carolyn Nowak, University of Michigan Health System, Department of Radiology Media Services.

systemic oxygen delivery, but these are difficult to predict clinically.

Patient-specific surgical planning involves the implementation of a pre-operative computational model that accurately reproduces patient hemodynamics, and the comparison of different surgical options through computational fluid dynamics (CFD) analysis. Several prior studies have shown the potential clinical application of virtual techniques for congenital heart disease (CHD) surgeries (Pekkan et al. 2008; Haggerty et al. 2009; Marsden et al. 2009; Vignon-Clementel, Marsden, et al. 2010), although two critical issues are the reproduction of the surgeon's anatomical manipulation and the prescription of model boundary conditions (BCs). Recently, an interactive tool for surgical planning of CHD has been developed combining cardiovascular magnetic resonance (CMR) imaging and CFD allowing free-form manipulation of anatomy with systematic geometric and hemodynamic optimization (Pekkan et al. 2008). Pre-operative blood flow rates have been adopted as inlet BCs while different pulmonary flow splits were imposed as outlet BCs (Pekkan et al. 2005; de Zelicourt et al. 2006, 2011). The limitation of this type of modeling is the inability to describe interactions with the rest of the circulation in post-operative scenarios since BCs are statically enforced without any two-way coupling to the rest of the circulation.

'Multi-scale' or 'multi-domain' models couple a three-dimensional (3D) model of the surgical region to a lumped parameter model [LPM or zero-dimensional (0D)] or a one-dimensional model of the peripheral circulation (Laganà et al. 2002; Vignon-Clementel et al. 2006; Vignon-Clementel, Figueroa, et al. 2010; Vignon-Clementel, Marsden, et al. 2010). This gives information about local fluid dynamics with changes in anatomical features, plus hemodynamic variables up or downstream. Presently, this approach has been applied in either a closed-loop model where the LPM (with detailed description of entire cardiovascular circulation) is coupled with geometrically simplified 3D models (Laganà et al. 2005; Bove et al. 2008; Corsini et al. 2011), or in an open-loop model that combines realistic 3D reconstructions with simple resistance BCs (Vignon-Clementel et al. 2006; Marsden et al. 2007; Spilker and Taylor 2010; Vignon-Clementel, Figueroa, et al. 2010). In these studies, while proper outflow impedances are applied to simulate the lung vasculature without assuming a flow split, the inlet BC is typically prescribed as velocity, potentially following a certain time-varying flow rate.

For patient-specific virtual planning it is essential that the 3D model and the LPM are customized based on pre-operative clinical data. The 3D model and LPM should be coupled in a closed-loop to avoid imposing BCs that would not account for the considerable circulatory changes post-operatively. A patient-specific, closed-loop, multi-scale approach has been applied to stage 3 virtual planning (Baretta et al. 2011), but an equivalent model for the earlier stage 2 is missing to date.

The role of virtual surgical prediction in CHD is to aid clinicians' decision-making for customized patient-specific treatments; however, it requires considerable interaction between clinicians and engineers. This study describes in detail a step-by-step integrated approach that could be applied to patient-specific virtual surgical planning of SV stage 2 or 3 operations. The workflow is illustrated for a patient undergoing stage 2 surgery. Two surgical options, Glenn and hemi-Fontan procedure, are compared, and both local and global hemodynamic effects are assessed using the coupled 3D-LPM approach. Model predictions are discussed on the basis of a number of clinical data collected post-operatively. This approach may be used as a workflow for future patients with CHD.

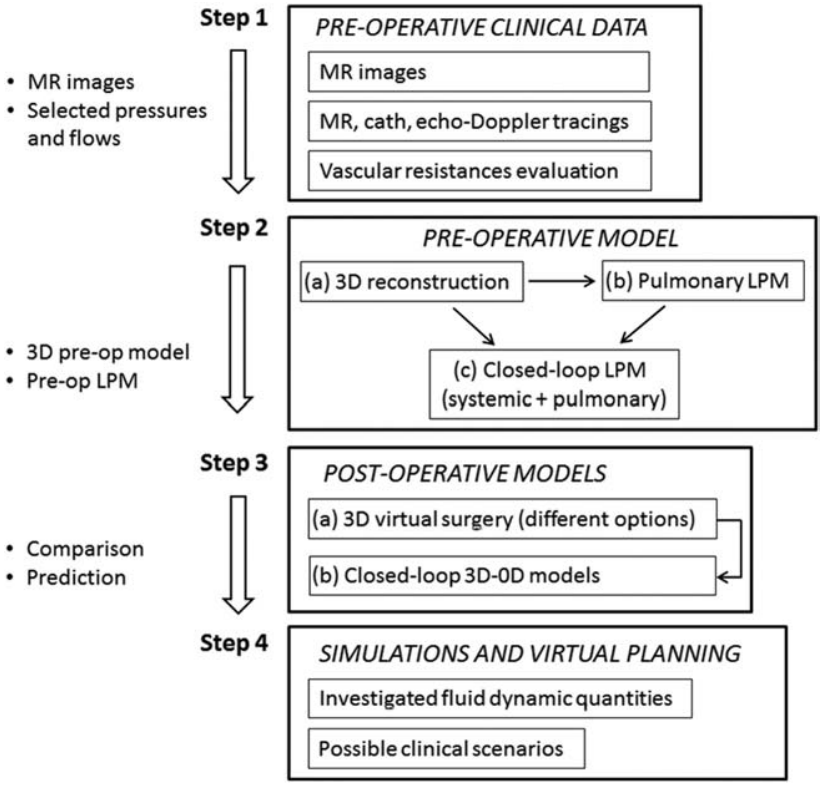

Figure 2. Workflow of the modelling process.

2. Materials and methods

The workflow (Figure 2) for virtual surgical planning presented in this study is comprised of four main steps. The first one is the collection and selection of pre-operative clinical data, based on its consistency and reliability. The processed anonymised data is submitted to a secure online data repository for analysis at multiple centers. The second step is the implementation of the pre-operative model, including the 3D patient-specific anatomical reconstruction to build the pulmonary LPM, and the coupling of the pulmonary and systemic LPMs in a closed-loop fashion. The third step is the virtual surgery for post-operative model construction of possible surgical options, i.e. a number of virtual 3D reconstructions based on the pre-operative anatomical model. The complete post-operative multi-scale model is then constructed by replacing the surgical domain in the LPM with the 3D surgical reconstruction, thus allowing coupling of the virtual 3D reconstruction with the LPM. The final step is to perform simulations of different scenarios for virtual surgical planning. Potentially, a number of different post-operative scenarios corresponding to different physiological states (e.g. exercise in older children, crying in younger children) may be analysed. All steps involve a strong interaction between surgeons, physicians and engineers, although the first step is mainly performed by clinicians and the others are engineer-led.

The above summarised approach includes several sub-steps that will be described in detail using a case study: stage 2 surgical planning for a baby with a previously constructed systemic-to-pulmonary shunt.

2.1 *Pre-operative clinical data*

Clinical data for the case study were collected at the University of Michigan C.S. Mott Children's Hospital (Ann Arbor, MI, USA), after institutional review board approval at the University of Michigan. Informed consent was obtained from the subject's parents. At the time of data collection, the patient was a 6-month old infant weighing 6.9 kg with a body surface area (BSA) of $0.34\,m^2$. The baby was born with pulmonary atresia with intact ventricular septum (hypoplastic right heart), not suitable for a two ventricle circulation. On the 5th day of life, the patient underwent surgical placement of a 3.5 mm central shunt, from the ascending aorta (AoA) to the main pulmonary artery (MPA). The patent arterial duct was divided at the time of the procedure.

Pre-operative echocardiogram was performed 5 weeks prior to surgery, under sedation with chloral hydrate,

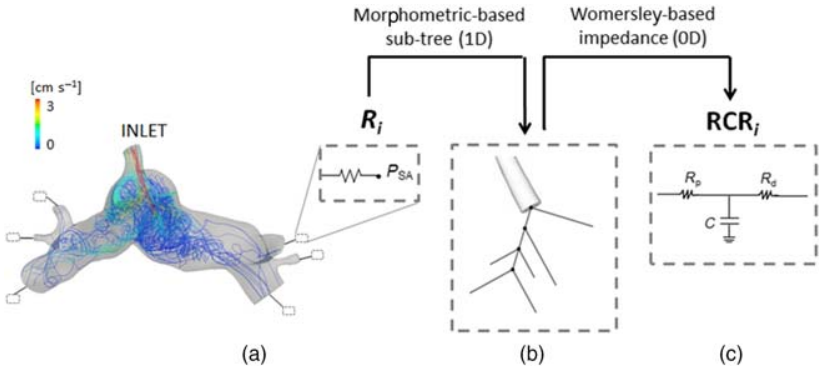

Figure 3. Pre-operative pulmonary LPM generation. A resistance R_i is computed for each ith outlet of the 3D model (a) by means of steady simulations (velocity-colored pathlines are displayed); R_i is first converted in a morphometric-based sub-tree (b), then in the corresponding Womersely-based impedance RCR_i (c). P_{SA} = single atrium pressure; R_p = proximal resistance; R_d = distal resistance; C = compliance.

using commercially available equipment (iE33, Philips, Best, Netherlands) and routine clinical protocols. Particular attention was paid to spectral Doppler signals in the superior and IVC, central shunt and branch PAs.

CMR was performed under general anesthesia immediately prior to surgery, on a commercially available 1.5 T scanner (Philips Intera Achieva, Best, Netherlands). Cine images were obtained with a breath-hold, electrocardiographic (ECG)-gated, segmented *k*-space, steady-state free precession sequence. Flow measurements were obtained in the AoA and descending aorta (AoD), transverse aortic arch, branch PAs, pulmonary veins, superior and inferior venae cavae, using an ECG-gated, free-breathing, cine-phase contrast velocity-encoded pulse sequence, and commercially available cardiac analysis software (ViewForum, Philips). Anatomy was assessed with a contrast-enhanced CMR angiography sequence, following the administration of 0.2 mmol kg^{-1} of gadoteridol (Prohance, Bracco, Princeton, NJ, USA). Blood pressure was recorded throughout the CMR using an automated blood pressure cuff applied to the right arm.

Cardiac catheterization for pre-operative testing was performed under conscious sedation, including meperidine, midazolam and ketamine, 3 days prior to surgery, using routine clinical protocols. The procedure was performed in a biplane fluoroscopy suite (Siemens Medical Solutions USA, Inc., Malvern, PA, USA). Hemodynamic assessment with intracardiac and vascular pressure measurements was obtained using a fluid filled catheter system and Witt Biomedical Calysto Series IV software (Philips Medical Systems, Best, Netherlands).

From the mean values of clinical flows and pressures collected, the patient-specific PVRs, and systemic vascular resistances of the upper and lower body (UBSVR and LBSVR, respectively) were calculated as follows:

$$\begin{aligned} \mathrm{PVR} &= \frac{P_{\mathrm{PA}} - P_{\mathrm{SA}}}{Q_{\mathrm{PA}}} \\ \mathrm{UBSVR} &= \frac{P_{\mathrm{SysA}} - P_{\mathrm{SA}}}{Q_{\mathrm{UBA}}} \\ \mathrm{LBSVR} &= \frac{P_{\mathrm{SysA}} - P_{\mathrm{SA}}}{Q_{\mathrm{LBA}}}, \end{aligned} \tag{1}$$

where P_{PA}, P_{SA}, P_{SysA} are the common pulmonary arterial pressure, single atrium pressure and systemic arterial pressure, while Q_{PA}, Q_{UBA}, Q_{LBA} are the flows in the pulmonary arteries, in the upper body (UB) arteries and in the LB arteries, respectively.

2.2 *Pre-operative geometry reconstruction*

The patient's anatomy was reconstructed from CMR data using commercial software (Mimics, Materialise NV, Leuven, Belgium). After selection of the vasculature of interest, based on the geometric constraints that might affect the surgical procedure, a 3D volume was obtained for each of the components, following operations of segmentation and region-growing described in detail elsewhere (Armillotta et al. 2007; Schievano et al. 2007).

2.3 *Pre-operative open-loop multi-scale pulmonary model*

A 3D rigid-walled sub-model of the PA vasculature (Figure 3(a)) was extracted from the reconstructed anatomy. This model included an inlet (i.e. the shunt) and a number of outlets (pulmonary branches) depending on the CMR images resolution, and was discretized using commercial mesh generation software (MESHSIM, Simmetrix, Inc., Clifton Park, NY, USA) into an isotropic

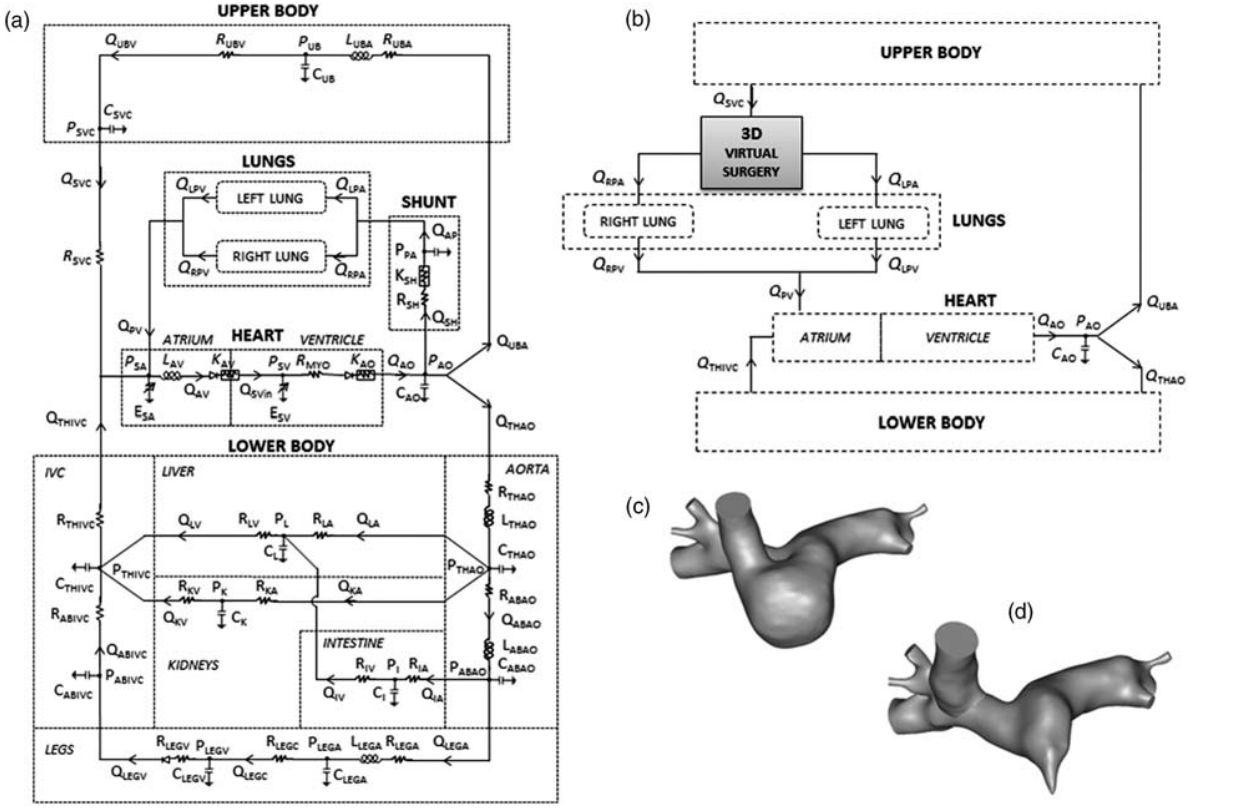

Figure 4. Detailed scheme of (a) pre-operative stage 1 LPM; (b) post-operative 3D model of the virtual surgery coupled to the LPM; 3D virtual surgery of (c) hemi-Fontan and (d) bi-directional Glenn.

finite-element mesh. The pulmonary vasculature downstream each outlet was represented by reduced models, built based on pre-operatively measured CMR and catheterisation data. Namely, the inflow (total pulmonary flow) was imposed in an open-loop configuration, while the flow split between the right and left lungs and the transpulmonary pressure gradient between the inlet of the 3D model and the left atrium were used as the target quantities. A resistance BC (Figure 3(a)) was computed for each outlet by an automatic tuning algorithm necessitating several 3D steady simulations (Troianowski et al. 2011). For each outlet, the resistance led to the localization of the branch within a morphometric PA tree, and thus to the definition of the corresponding arterial sub-tree (Figure 3(b)). An impedance consisting of two resistances and one compliance (RCR block) was then inferred from the Womersley-based impedance of this sub-tree (Figure 3(c)) (Spilker et al. 2007; Troianowski et al. 2011). Since the arterial side of pulmonary vasculature comprises only 20% of the total compliance (Dawson et al. 1988; Presson et al. 1998), compliance values were multiplied by a factor of four to account for the capillary and venous distensibility. The obtained values of resistances and compliances were used as initial values for additional tuning of the LPM described below (see Section 2.4). All simulations were performed using a custom version of the finite element Navier–Stokes solver released with SimVascular (http://simtk.org) and assuming blood as a Newtonian fluid with a density of $1060\,\mathrm{kg\,m^{-3}}$ and a dynamic viscosity of 0.004 Pa s, with a monolithic coupling between the 3D and 0D models (Vignon-Clementel et al. 2006; Vignon-Clementel, Figueroa, et al. 2010).

2.4 *Pre-operative closed-loop LPM of the patient's cardiovascular system*

2.4.1 *Model layout*

An LPM of the pre-operative SV cardiovascular system was used (Figure 4(a)) (Baretta et al. 2011). The model layout was derived from Snyder and Rideout (1969) who focused the lumped parameter representation on the LB circulation, especially the venous side, including the abdominal organs and the respiration. The LPM, indeed, was designed to be suitable for virtually planning stage 3 surgeries, i.e. when exercise conditions, combined with respiratory effects, and hepatic flow distribution to the lungs may become interesting to study. The detailed description of the LB allows one to alter only those parameter values that belong to specific regions of the

body (e.g. legs for vasodilation due to exercise, and thorax/abdomen for respiration).

The network comprised five main blocks to model the heart, the systemic UB and LB circulation, and the right and left lung circulation (see Appendix for equations). For the sake of simplicity and in absence of any clinical information, coronary circulation, gravity and respiratory effects were neglected in the present case study.

The heart was described by two time-varying elastances, representing the single atrium (SA) and the SV, as well as atrio-ventricular (AV) and aortic valves. The contractions of the two cardiac chambers were ruled by two activation functions, properly shifted in time, so that the ventricular activation function starts when atrial activation function reaches zero value. AV and aortic valves were described by non-linear diodes that allow unidirectional flow and exhibit resistances.

In the LB three abdominal organs (kidneys, liver and intestine) and legs vasculature were modelled; a venous valve was included by means of a diode in the leg venous block. Cerebral and brachial circulations were not distinguished within the UB portion of the model.

For the lungs, a number of RCR blocks, arranged in parallel, were used corresponding to the outlets of the 3D model, as described in Section 2.3. A resistive block mimicking the systemic-to-pulmonary shunt was added, including linear and non-linear components accounting for both distributed and concentrated energy dissipations.

The LPM resulted in a set of algebraic and ordinary differential equations, solved using a 4th order Runge–Kutta algorithm with an adaptive step, implemented in the software Simnon® (SSPA Maritime Consulting, Göteborg, Sweden) (version 3.00.011, 1998, Sweden).

2.4.2 *Model parameters*

The lumped parameter values included in the LPM were obtained after a manual tuning starting from 'first attempt' values. The systemic-to-pulmonary shunt parameters were not tuned, but were expressed as functions of the shunt diameter (Migliavacca et al. 2001 – see Appendix).

The 'first attempt' values were differently defined according to the different area in the LPM: the RCR values obtained at the end of 'Section 2.3' for the lungs, the data reported in Migliavacca et al. (2001) for the heart, while a scaling method was adopted for the systemic parameters. The scaling method is divided in two parts: (i) starting from a reference LPM of a healthy adult, based on the model by Snyder and Rideout (1969), differential scaling was applied according to the patient's BSA (Pennati and Fumero 2000) and (ii) the parameters obtained were then modified to account for the patient-specific vessels and organs development.

The model resulting from the first part of the method represents a generic subject with BSA equal to that of the considered patient (BSA*). Differential scaling was applied to derive the parameter values $x_{i\text{-}\,\mathrm{BSA}*}$ (with $x =$ resistance, compliance, inertance and i denoting the model block) with the following equation:

$$x_{i-\mathrm{BSA}*} = x_0 \cdot \left(\frac{\mathrm{BSA}*}{\mathrm{BSA}_0}\right)^b, \tag{2}$$

where x_0 and BSA_0 are the generic parameter and the BSA, respectively, of the reference adult LPM, and b is a constant coefficient depending on the parameter type (i.e. resistance, compliance, inertance) and on the organ/vessel (Baretta et al. 2011). Indeed, this BSA-based scaling approach enables one to account for the different organ/vessel growths with age (thus BSA), according to the region of the body (e.g. head, torso, legs) where the organ/vessel is located. Passing from an adult model (BSA_0) to a child one (BSA*), the values of the UB and LB systemic vascular resistances become representative of the BSA of the patient ($\mathrm{UBSVR}_{\mathrm{BSA}*}$ and $\mathrm{LBSVR}_{\mathrm{BSA}*}$), automatically giving the flow repartition between the UB and LB typical for a baby.

In the second part of the scaling method, each model resistance $R_{i\text{-}\,\mathrm{BSA}*}$ of the systemic circulation was modified (R_i with i denoting the model block) to obtain the global patient-specific resistance values UBSVR and LBSVR, as calculated in Equation (1), using the following equations:

$$R_i = R_{i-\mathrm{BSA}*} \cdot \frac{\mathrm{UBSVR}}{\mathrm{UBSVR}_{\mathrm{BSA}*}} \quad \text{or} \quad \mathrm{R}_i = \mathrm{R}_{i-\mathrm{BSA}*} \cdot \frac{\mathrm{LBSVR}}{\mathrm{LBSVR}_{\mathrm{BSA}*}} \tag{3}$$

depending on whether the resistance belongs to the UB or LB, respectively. Furthermore, the patient-specific compliances C_i (with i denoting the model block) were obtained accordingly to the change of R_i:

$$C_i = C_{i-\mathrm{BSA}*} \cdot \left(\frac{R_i}{R_{i-\mathrm{BSA}*}}\right)^{-4/3}, \tag{4}$$

where $C_{i\text{-}\,\mathrm{BSA}*}$ being the generic compliance of the systemic circulation. The adopted power expresses the dependence of resistances and compliances on vessel length and diameter (Pennati and Fumero 2000; Baretta et al. 2011). Since the cause of different development of the individual impedances is unknown, the repartition of resistances and compliances among the organs and vessels within the UB and LB was assumed to be the same in both parts of the method.

Once the 'first attempt' values were obtained for all the areas of the LPM, manual tuning was performed through a sequential process. First, the flow resistance of the 3D pulmonary model had to be represented in the closed-loop

Table 1. Clinical data pre-operatively collected from the patient.

	Magnetic resonance		Cardiac catheterization		
	Flow rate ($cm^3\,s^{-1}$)	HR (bpm)	Pressure (mmHg)	HR (bpm)	Other data
AoA	*24.4*	117	N.A.	N.A.	74/28 (*43*) [a]
Transverse aorta	10.6	116	N.A.	N.A.	
AoD	*5.7*	132	102/56 (82)[b]	N.A.	
SVC	9.8	115	9	143	3.06[c]
IVC	7.3	118	N.A.	N.A.	1.15[c]
RPA	*4.8*	116	*13*[d]	135 ÷ 170[e]	
LPA	*2.7*	115	12[d]	134	
Right pulmonary vein	7.4	117	N.A.	N.A.	
Left pulmonary vein	4.8	115	N.A.	N.A.	
Right atrium	N.A.	N.A.	6	143	
Left atrium	N.A.	N.A.	*5*	136	
SV	N.A.	N.A.	103/6[b]	167	

Notes: Flow and pressure values are averaged over several cardiac cycles. Values in *italic* are those selected for modeling.
[a] Max/min (mean) brachial cuff pressure in mmHg.
[b] Max/min (mean).
[c] Absolute value of the non-dimensional venous flow index S/A.
[d] Measured as pulmonary venous wedge pressure.
[e] Range covered by the right venous wedge pressure measured in three different locations. 1 mmHg = 133.32 Pa.

LPM, as disregarding this additional resistive term would provide a PVR and, potentially, a left/right pulmonary flow split different from the clinical ones. Therefore, the 3D contribution to the PVR was accounted for by properly increasing the total resistances of the lung blocks. Manual tuning was then applied to match the clinical cardiac output (CO) and the clinical time tracings available. In particular, the ventricular elastances were tuned to obtain the correct ventricular-circulatory coupling, verifying that the ventricle model worked at reasonable volumes and that the clinical atrial pressure was reproduced. This tuning enabled to reproduce the desired mean flow distribution among the various blocks and the mean pressures throughout the model. Furthermore, the atrial elastances and the venae cavae parameters were tuned to match the SVC and IVC flows, the aortic parameters to match aortic tracings (both flows and pressures), the lung distal-to-total resistance ratio and compliance to match the PA flow pulsatility. The tuning of the heart and circulatory parameters was based on a sensitivity analysis previously performed, showing the influence of different parameters on flow and pressure tracings (Pennati and Fumero 2000). The matching was not evaluated comparing values at any given time, but considering the morphology of the tracings (e.g. number of peaks, presence of reverse flow . . .) and a number of quantitative features of clinical interest (e.g. peak values, peaks ratios . . .).

2.5 Virtual reconstruction of different post-operative options

Using the same 3D volume generated to build the pre-operative model, various anatomies were virtually designed according to possible surgical options and to the geometric constraints given by the organs and vessels surrounding the region of the future cavo-pulmonary connection(s), e.g. the heart, aorta, SVC and IVC.

2.6 Post-operative closed-loop multi-scale models

The post-operative 3D models were then coupled to the pre-operative LPM, as depicted in Figure 4(b). Since the post-operative 3D models include the SVC and the first PA branches (as those in the 3D pre-operative model), the SVC resistance was removed from the LPM and each proximal resistance of the lung blocks (evaluated at the end of Section 2.4, 'Final LPM' in Table A2) was decreased to remove the resistive contribution of the 3D arterial branches from the 0D representation of the pulmonary vasculature.

Each of the post-operative 3D models was discretized using MESHSIM and a custom stabilized finite-element method with a rigid-wall assumption was used to solve the incompressible Navier–Stokes equations. Neumann BCs were prescribed in the 3D domain at the interfaces (i.e. inlets and outlets) with the LPM, and pressures were passed from the 0D domain to the 3D domain at the interfaces. The LPM equations were solved using a 4th order Runge–Kutta time-stepping scheme. Computed flows from the 3D domain were used as input parameters in solving the LPM equations, thus completing the two-way iterative coupling between the 3D and 0D domains. Coupling was performed using a stable and efficient semi-implicit algorithm, implemented in a custom solver, with negligible additional computational cost compared to the 3D simulation alone (Esmaily Moghadam et al. 2012).

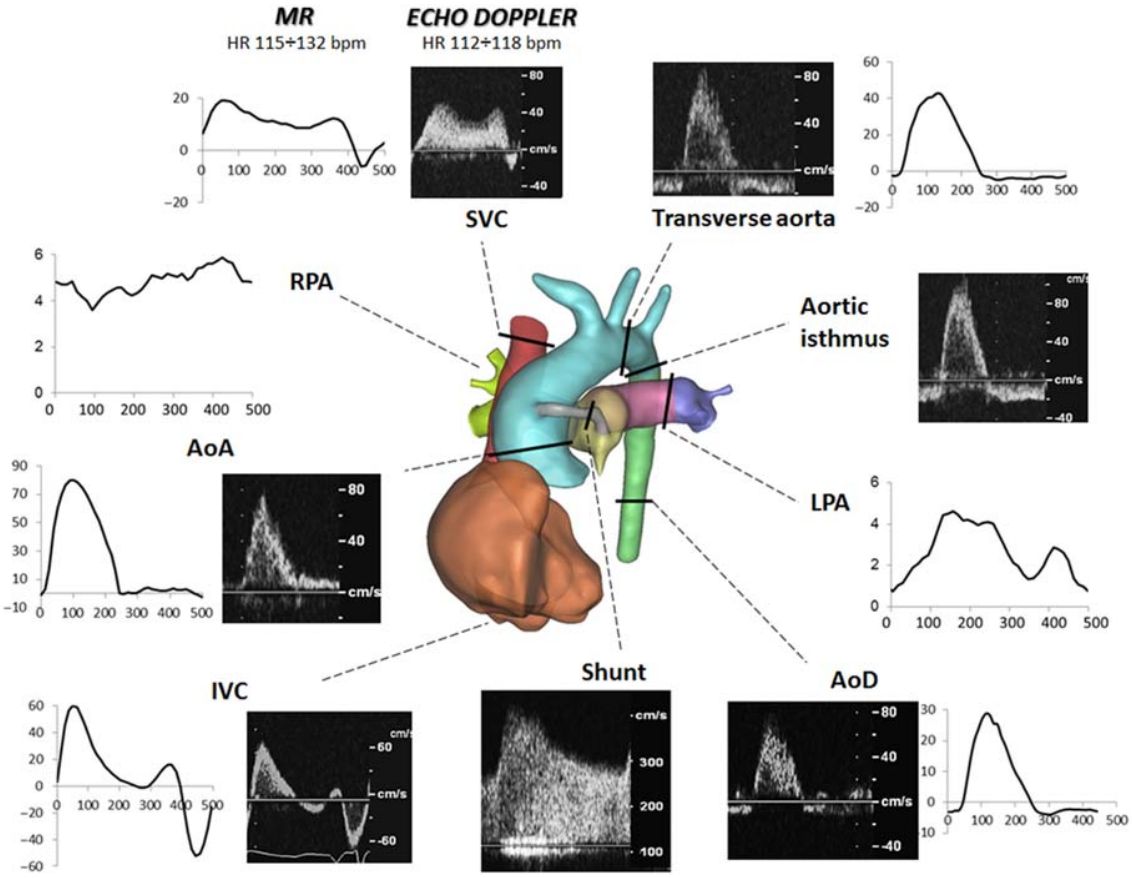

Figure 5. Pre-operative data: 3D reconstructed anatomy (centre), clinical MR ($cm^3\,s^{-1}$ vs. ms) and echo-Doppler ($cm\,s^{-1}$ vs. time) tracings. AoA/AoD, ascending/descending aorta; SVC/IVC, superior/inferior vena cava; RPA/LPA, right/left pulmonary artery.

Backflow stabilization was applied at each of the inlets and outlets, to prevent simulation divergence (Esmaily Moghadam et al. 2011). The assumptions regarding fluid properties were the same as for the pre-operative model.

2.7 *Simulations and virtual planning*

The post-operative simulations were performed using the models from *Section 2.6*. In this case study we have concentrated on a resting physiological state in order to illustrate the methodology. In predictive modelling the post-operative heart rate (HR) was unknown, therefore was assumed to be the same as the average during pre-operative data collection. This was used to set the cardiac cycle length for the simulations. Peripheral vascular parameters were assumed to be unchanged from the pre-operative situation.

In order to ensure clinical relevance, the reported simulation outputs were selected in conjunction with the clinicians. Global circulatory outputs were represented as both mean values and time tracings. The hemodynamic outputs most relevant to the clinicians were flow ratios, such as pulmonary-to-systemic flow and flow split to each lung, and parameters related to the heart, including CO, ejection fraction and pressure volume loops to estimate cardiac work and efficiency. Local effects were studied using 3D velocity and pressure maps at certain time instants of the cardiac cycle, maps of average wall shear stress (WSS) per cardiac cycle, and local energy losses.

The local power dissipation due to the hemodynamics in the surgical region was calculated as the difference between the inlet and the outlet energy fluxes of the 3D model, accounting for the potential and kinetic terms (Marsden et al. 2007). The local efficiency was defined as the ratio between the outlet and inlet energy fluxes.

3. Results

3.1 *Pre-operative clinical data*

Clinical data collected are listed in Table 1, underlining those selected for modelling. There was a normal HR range during acquisition of Doppler and CMR data (112–132 bpm). However, HR during catheterisation was higher and had greater variability, due to varying degrees of

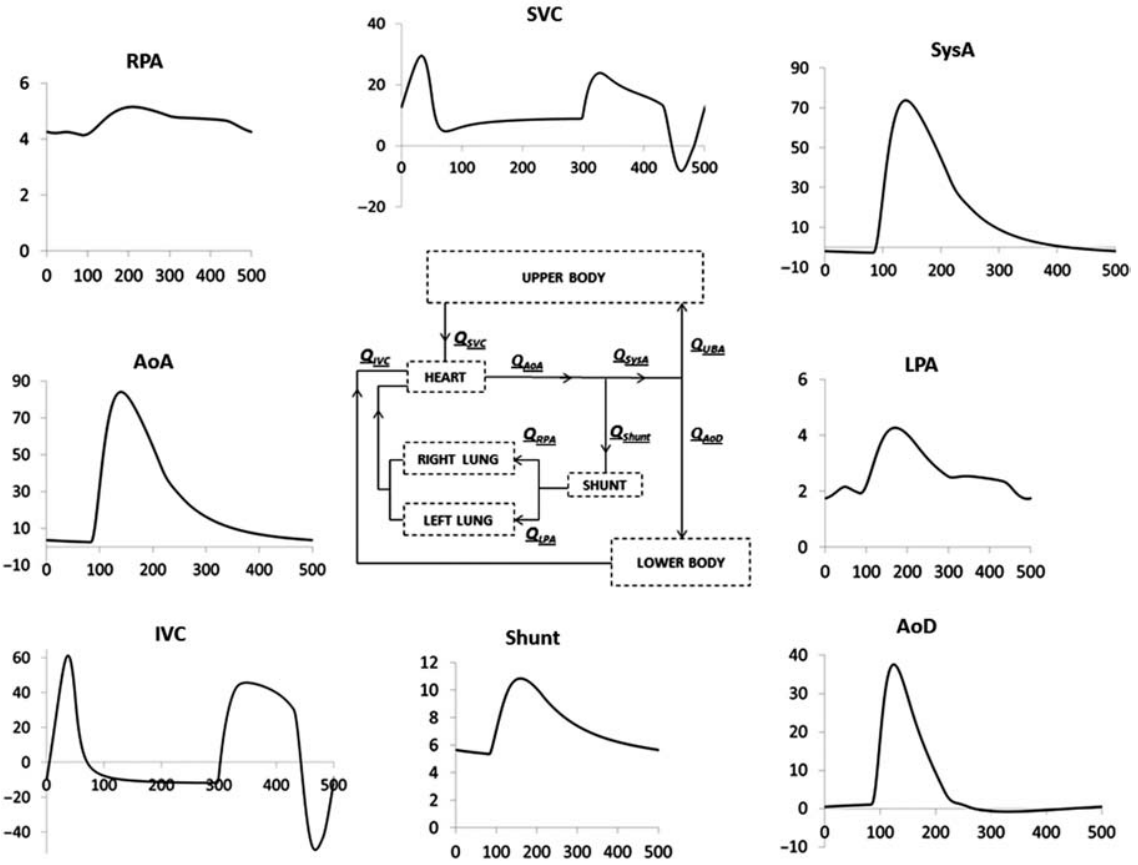

Figure 6. Flow time tracings ($cm^3\,s^{-1}$ vs. ms) resulting from the final pre-operative LPM (scheme in the centre). AoA/AoD, ascending/descending aorta; SVC/IVC, superior/IVC; RPA/LPA, right/left pulmonary artery; SysA, systemic artery.

agitation during the procedure, necessitating repeated doses of sedation. For this reason, modelling was performed using the HR of 120 bpm, selected as an average of CMR and Doppler HRs, and representing a resting clinical state. The average mean blood pressure as measured by cuff on either arm during the CMR was 43 mmHg. Aortic oxygen saturation was 69% during catheterisation. The CMR flows and catheter measurements represent averaging of several cardiac cycles and therefore respiratory influences were negligible.

Given the selected mean values of pressures and flows (Table 1), the PVR, UBSVR and LBSVR were calculated as described in Equation (1), obtaining 1.10, 3.39 and 6.67 mmHg s cm^{-3}, respectively. The UBSVR and LBSVR were calculated using the mean cuff pressure (see 'Other data' column in Table 1) as a measure of P_{SysA}, since the aortic pressure recorded during cardiac catheterisation did not correspond to a resting condition for the reasons explained above. The collected clinical CMR flow rates and echo-Doppler tracings are shown in Figure 5.

From the CMR and angiographic data collected, the shunt presented a non-circular area with a variable cross-section along the axis (diameter range: 2.3–3.0 mm), which was smaller than the original size of the shunt implanted at surgery (3.5 mm).

3.2 *Pre-operative model*

The reconstructed anatomy (Figure 5, centre) included: the aortic arch, the AoD), the main, RPA and left pulmonary artery (LPA) and pulmonary branching up to the second bifurcation, the right atrium, the SVC and the central shunt.

In the 3D sub-model used for the calculation of the downstream pulmonary impedances, the inlet was the distal part of the central shunt, and six outlets were included. The model was meshed with 7.15×10^5 elements. Figure 3(a) shows the resulting local hemodynamics in terms of pathlines when imposing an inlet flow equal to 7.5 $cm^3\,s^{-1}$, with a 64% flow to the right lung. The obtained values of pulmonary lumped parameters, corresponding to a transpulmonary pressure gradient of 8 mmHg (in agreement with Table 1), are reported in Table A2 (see 'Morphometric' columns).

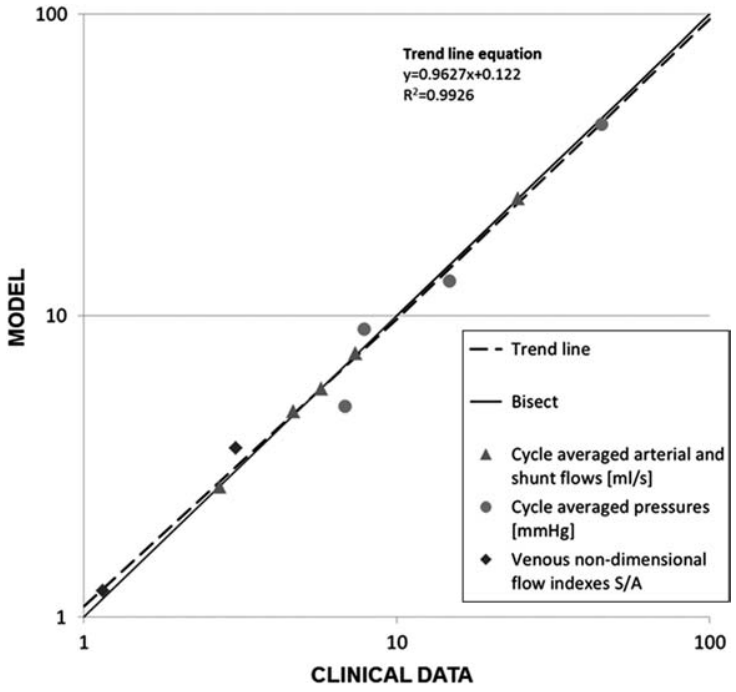

Figure 7. LPM results vs. clinical data: time-averaged (over cardiac cycle) arterial and shunt flows, pressures, SVC and IVC non-dimensional venous flow indexes S/A (calculated as the ratio between the S-wave and the A-wave during atrial contraction). The trend line (dashed) is obtained by best fitting the LPM results. The *x*- and *y*-axes are shown in a logarithmic scale.

In the pre-operative closed-loop LPM each resistance of the lung blocks derived from 'Section 2.3' was increased to obtain the clinical PVR (1.10 mmHg s cm^{-3}), thus corresponding to 30% PVR increase from the value calculated (Equation (1)) when neglecting the 3D additional resistance. The lumped parameter values of the whole pre-operative LPM, evaluated after the manual tuning which is described in Section 2.4, are listed in the Appendix (Table A1, for the heart and systemic parameters, and Table A2 – 'Final LPM' columns, for the pulmonary parameters).

Concerning the shunt lumped parameters, it was not straightforward to evaluate their values using the equation in the Appendix, due to the variable diameter along shunt length. Hence, they were determined with the measured difference between the mean systemic and PA pressures (i.e. $43-13=30$ mmHg), and the shunt flow rate (i.e. 7.5 $cm^3\,s^{-1}$). The corresponding diameter of the shunt was calculated to be 2.65 mm.

The LPM developed for the pre-operative circulation produced the flow tracings reported in Figure 6. A good agreement between clinical and model tracings can be observed comparing Figures 5 and 6: minimum and maximum flow values as well as the flow waveforms of the clinical tracings were acceptably reproduced by the model. In both clinical and model tracings, the aortic flow upstream of the shunt (AoA) showed positive values throughout the whole cardiac cycle, while the flow in the systemic arteries downstream the shunt (SysA) was positive during systole and negative in diastole, approaching values close to zero in the AoD at the end of the cardiac cycle, as reported by the CMR tracings.

Cycle-averaged flow values differed $<4\%$ from the clinical ones. Because of the different conditions of data acquisition during catheterisation (i.e. agitation, sedation and variable HR), averaged pressure values showed higher discrepancies ($<28\%$) than flow values, but on the whole the clinical tracings were reasonably matched by the model. In Figure 7 the simulated results of flows, pressures and non-dimensional venous flow indexes are plotted against clinical data. The non-dimensional index (S/A) is the ratio between the S-wave (corresponding to ventricular systole) and the A-wave (corresponding to atrial contraction) of the SVC and IVC flow tracings. The satisfactory agreement between clinical and model data is clearly visible.

3.3 *Post-operative models*

For the case study, the hemi-Fontan and bi-directional Glenn were virtually performed (hF and bG geometry, respectively). For the hF geometry, a portion of the atrium was removed from the 3D volume so to create the 'bulging patch' typical of this surgical configuration, the size of which was determined in agreement with the surgical team who performed the operation. This volume was

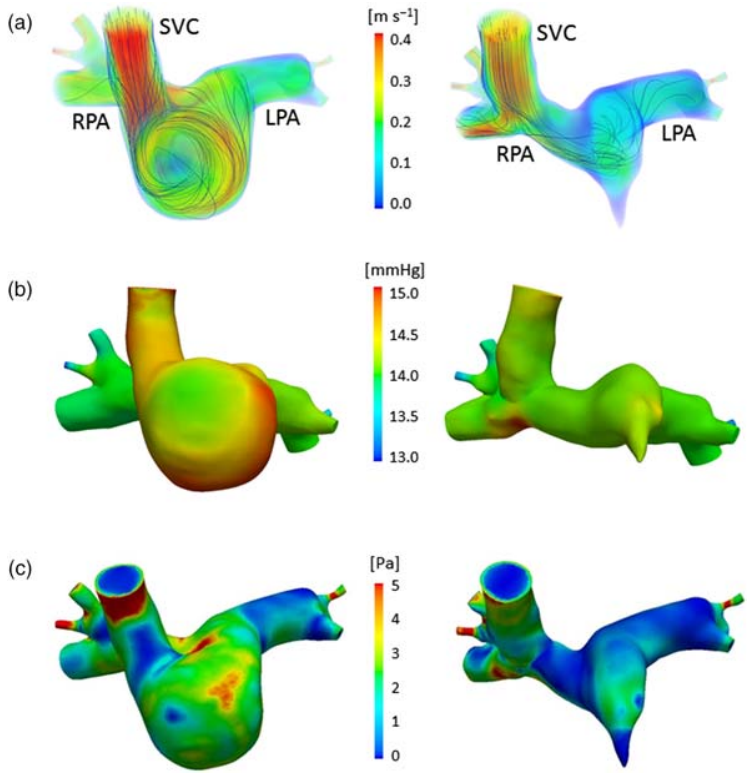

Figure 8. Comparison of the hemodynamics in the hF (left) and bG (right) models: (a) volume-rendered velocities at peak flow with streamlines, (b) wall pressure at peak flow, (c) time-averaged (over cardiac cycle) WSS magnitude. 1 mmHg = 133.32 Pa.

attached to the MPA and merged into a new, unique volume. The final anatomical model is shown in Figure 4(c). In the case of the bG geometry, the SVC–RPA anastomosis was recreated by virtually resecting the SVC from the atrium and adjoining it with minimal movement to the RPA. The two volumes were merged into a single one, as shown in Figure 4(d). In both cases, the central shunt was removed from the virtual models, to simulate the shift from stages 1 to 2 physiology.

The hF and bG model meshes used for simulation had a maximum edge size of 0.3 mm, containing 1.30×10^6 and 8.64×10^5 linear tetrahedral elements, respectively. The hF and bG geometries were coupled to the pre-operative LPM, as shown in detail in Figure 4(b).

3.4 Simulations and virtual planning

For both the hF and bG multi-scale simulations, 12 cardiac cycles were simulated with a time step size of 1 ms. A value of 120 bpm was used as the HR in the simulations, for the reason explained above (see Section 3.1). The results from the last cycle, after the pressures had stabilized, were used in the analysis.

For the case study, a number of results from the simulations carried out with the two post-operative models are reported below. Figures and numerical values are shown side by side to allow for comparison.

Figure 8(a) shows the time-averaged, volume-rendered flow velocities in the hF and bG geometries. The color map represents the velocity magnitude and the lines represent the velocity streamlines. In the hF geometry, the SVC inflow swirls along the side of the cavopulmonary junction, forming a vortex and maintaining a higher velocity (compared to that in the bG) before entering the PAs. In the bG geometry, the flow impacts the bottom of the RPA after entering from the SVC, and splits into the left and right directions.

In Figure 8(b) the pressure maps show higher values at the inlet for hF model compared to the bG model. Moreover, in both models areas of high pressure occur where the SVC flow impacts the vessel wall.

Figure 8(c) shows the time-averaged WSS magnitude in the hF and bG geometries. An area of high WSS close to the model inlet is present in both models, due to entrance effects and vessel curvature (in particular in the hF geometry). Moreover, in the hF model the area of high WSS persists throughout most of the surgical junction, due to the presence of a swirling vortex. Conversely, in the bG model a more limited area of high WSS is concentrated at the bottom of the RPA in the region where the inflow from

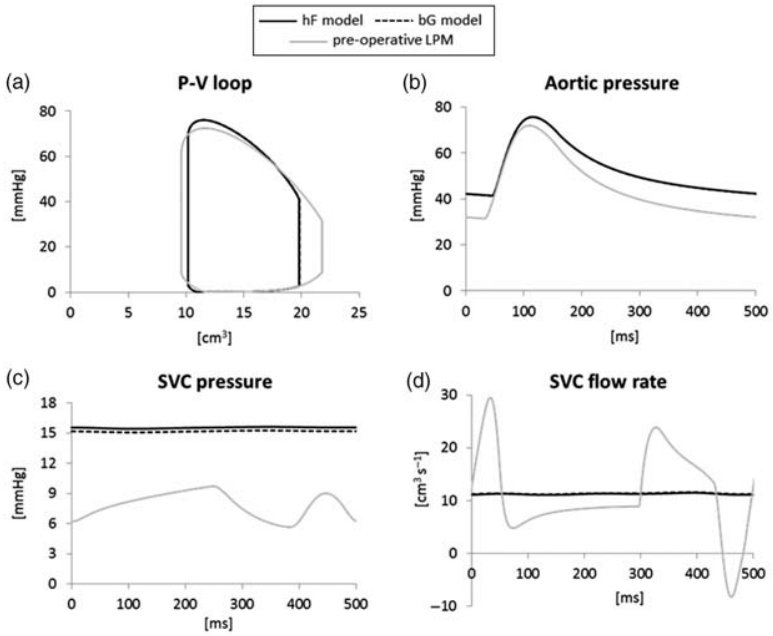

Figure 9. Comparison of the simulation results of the pre-operative LPM (grey lines) and post-operative hF (solid lines) and bG (dashed lines) models: (a) ventricular pressure-volume loop, (b) aortic pressure, (c) SVC pressure, (d) SVC flow rate. Except in graph (**c**), hF and bG curves overlap.

the SVC impacts. The mean WSS in the hF and bG is 2.11 and 1.48 Pa, respectively. These values are a little higher than those reported for older bG (Troianowski et al. 2011), but fall in the lower range of previously reported values of WSS in large arteries (Alevriadou and McIntire 1995; Tang et al. 2010).

The hemodynamics of the global circulation in the two post-operative configurations are very similar, and both are distinct from the pre-operative one (Figure 9). Only the SVC pressure shows slight differences between the hF and bG models, in agreement with the pressure maps in Figure 8. Similar considerations are found by examining the time-averaged flows, pressures, power losses and efficiencies obtained from the simulations (Table 2).

Table 2. Time-averaged flows, pressures and power losses of the post-operative models.

	hF model	bG model
SVC flow rate ($cm^3\,s^{-1}$)	11.3	11.4
IVC flow rate ($cm^3\,s^{-1}$)	7.89	7.87
LPA flow rate ($cm^3\,s^{-1}$)	4.21	4.17
RPA flow rate ($cm^3\,s^{-1}$)	7.07	7.21
SVC pressure (mmHg)	15.4	15.1
Aortic pressure (mmHg)	53.1	53.1
Atrial pressure (mmHg)	2.43	2.48
3D power loss (mW)	1.26	0.61
3D potential term (mW)	1.29	0.62
3D kinetic term (mW)	−0.03	−0.01
3D efficiency (−)	0.95	0.97
Ventricular power (mW)	166	166

Note: SVC/IVC, superior/inferior vena cava; LPA/RPA, left/right pulmonary artery. 1 mmHg = 133.32 Pa.

Comparing the post-operative and the pre-operative simulations (Figure 9), regardless of surgical option: (a) stroke volume (i.e. the CO, assuming no change in HR) significantly decreases (21%) together with a slight increase in the systolic pressure, thus reducing (12%) the ventricular work; (b) aortic pressure increases in the mean value (from 43.3 to 53.1 mmHg) as in both systolic and diastolic values; (c) mean SVC pressure roughly doubles (from 7.9 to about 15.3 mmHg) while damping its pulsatility and (d) SVC flow pulsatility is highly reduced, although its mean value does not significantly change from the pre-operative one.

Table 2 shows that the surgical junction power loss in the bG model (0.61 mW) is roughly half of that in the hF model (1.26 mW), with a higher contribution of the potential term compared to the kinetic term (0.62 vs. −0.01 mW for bG, 1.29 vs. −0.03 mW for hF). These values are in the same range as previously reported power loss values in the stage 2 junctions and consistent with previous observations that bi-directional Glenn tends to exhibit lower power loss compared to hemi-Fontan (Pekkan et al. 2009). High efficiencies were obtained, in the same range as in Troianowski et al. (2011). However, under resting conditions the power loss of both surgical junctions is very small in comparison to the inlet and cardiac powers: it is only 3% (in bG) and 5% (in hF)

of the time-averaged power calculated at the inlet (22.6 mW in bG and 23.1 mW in hF), and $<0.8\%$ of the ventricular power (166 mW in both models). Hence, the surgical junction geometry has very little impact on the behaviour of the overall circulation at rest, with differences in flows and pressures resulting from the two models not exceeding 2%.

4. Discussion

This study reports the first, patient-specific predictive modelling of SV palliation using virtual surgery, closed-loop multi-scale modelling and an integrated approach between clinicians and engineers. Our approach involves four distinct steps: collection of clinical data, creation of the pre-operative model, creation of feasible virtual surgical options, and modification of the LPM for post-operative simulations to aid clinical decision making. This approach is generally applicable to stages 2 and 3 of SV surgery. In this study, we applied our predictive surgical planning to patient-specific stage 2 surgery in order to demonstrate the applicability of the approach.

4.1 Pre-operative clinical data

Predictive modelling of stage 2 surgery represents a demanding challenge as patients at this stage have complex physiology. Patient physiological parameters are complex, difficult to acquire simultaneously, and the clinical equipment has inherent limitations in measurement accuracy. Hence, the clinical data set is not suitable for direct implementation into the pre-operative model. Discrepancies in each measurement might result in an inconsistent system unlikely to obey the law of conservation of mass. Despite these limitations such simulations need to work for 'real-world' clinical problems, emphasizing the importance of the interaction between clinicians and engineers to guide the selection of suitable data and ensure suitably representative and reproducible models. Identifying and excluding portions of clinical data where the patient's physiology has changed significantly, and finding alternative methods of confirming less reliable measurements is essential for a meaningful and consistent model.

In this case study, there was uncertainty about the accuracy of the pre-operative shunt geometry measured by CMR, which was used for the reconstruction of the pre-operative 3D model. While the original shunt used in surgery was 3.5 mm in diameter, quantifying the shunt size to 2.65 mm (see *Section 3.2*) in the pre-operative model agreed with the loss of luminal diameter observed in the CMR (diameter ranging from 2.3–3.0 mm along the length of the shunt, see Section 3.1). The small dimensions of the conduit and the turbulent nature of the flow inside it resulting in non-optimal signal resolution could cause underestimation of the shunt diameter from CMR data. Nevertheless, using shunt measurements from cardiac angiography, as a quality control measure, confirmed a generalized reduction in shunt lumen compared to original size at the time of surgery, consistent with neointimal proliferation and endothelialization of the tube graft following surgery.

4.2 Pre-operative model

An open-loop multi-scale model was used as the initial step to account for hemodynamics that are challenging to model. In fact, a closed-loop model is not necessary to evaluate the pulmonary model because the inlet flow is known and this simplifies the process of tuning the downstream impedances to the clinical data, yet taking into account 3D effects. Owing to the shunt and the ligated PA, the hemodynamics in the 3D models are particularly complex, with a jet coming from the shunt, impinging on the wall and leading to downstream complex flow structures (Figure 4(a)). It is imperative that the pre-operative model accounts for as many anatomical features of the surgical region and fluid dynamic variables of the remaining vasculature as possible. However, clinical investigations and bedside data are not intended, nor designed, for precise mathematical modelling, but to provide guidance to patient management. Therefore, the adaptation of clinical data in modelling studies, such as ours, can be challenging due to inconsistencies and a lack of precision. Moreover, the added complexity of the abnormal cardiovascular system in congenital heart defects makes lumped parameter identification and model simulations ever more difficult.

Pre-operative open-loop multi-scale modelling allows the lung vasculature to be adequately described. Closed-loop LPM allows fast tuning of parameters accounting for the whole system. In the present case study, the values of pulmonary impedances were modified during the tuning process (i.e. changing the distal-to-total resistance ratio and compliances) to reproduce the clinical pulmonary flow pulsatility.

In the LPM used in this study, respiratory effects have not been included since the pre-operative CMR and catheter data were averaged by cardiac cycle thereby removing respiratory variation. Doppler traces e.g. IVC, SVC could be used to indicate variation in flow with respiration, although timing of inspiration and expiration needs to be measured. The influence of respiration could be effectively implemented in the LPM as intra-thoracic and intra-abdominal pressure modulation due to diaphragm movement (Baretta et al. 2012), provided that enough respiratory data in the pre-operative analysis have been acquired.

The effect of gravity has not been included in the current model, although this is likely to be of most importance after stage 3 surgery.

In our approach, most of the tuning of the lumped parameters was done manually, starting from a LPM previously developed and the clinical data available; however, automatic tuning methods have already been implemented, such as the method presented by Spilker and Taylor (2010) that enables systematic optimisation of the LPM used as outlet BCs of 3D blood flow models (e.g. patient-specific abdominal aorta) in order to achieve the desired features of pressure and flow waveforms.

4.3 Post-operative models and virtual planning

The use of post-operative closed-loop multi-scale models is necessary to study different surgical options at the global and local scale. Constructing the possible post-operative surgical options is difficult since the exact reconstruction a surgeon will perform is unknown. In this case study, two options were considered (i.e. bi-directional Glenn and hemi-Fontan), after consulting several surgeons to ensure the reconstructions were technically feasible and realistic. In the future, it would be possible to consider several geometries of a similar theme for each option, e.g. a Glenn with different anastomosis locations or angles.

The post-operative 3D models were provided with appropriate BCs simulating the patient-specific circulation at the time of surgery. However, the potential change of cardiovascular parameters due to vascular self-regulation and adaptation to new local hemodynamics following the operation was not taken into account, posing a severe threat to reliability of virtual surgical predictions (Pennati et al. 2011). Moreover, the effects of different surgical options on the global hemodynamic variables were here compared only at rest (i.e. a clinically stable post-operative state), whereas extending the modelling to more extreme physiological states (e.g. crying in younger children, exercise in older children) would allow clinicians to catch differences in surgical options not apparent at rest.

4.4 Validation

The pre-operative LPM produced a good agreement between the modelled flows and clinical tracings (Figures 5 and 6). Qualitatively, the flow waveforms and maxima and minima were well reproduced, with $<4\%$ difference from the clinical data in average flow. Pressures in this case were less well matched ($<28\%$ difference); however, qualitatively the clinicians accepted the model as representative of the pre-operative state of the patient.

The patient investigated in this study underwent a hemi-Fontan procedure. Systemic arterial pressure was non-invasively monitored (brachial cuff pressure) throughout their entire hospital stay. This meant we could perform a direct comparison with our model using brachial cuff pressure. However, it was difficult to quantify an indicative value for mean arterial pressure since the baby experienced fluctuations according to the time of day, physical state (e.g. awake, asleep, crying) and drug administration. Overall, the patient had a substantial increase in mean arterial blood pressure compared to the pre-operative values, as correctly predicted by the hF model under resting conditions.

In the last 5 days while the patient was in hospital, systolic blood pressure was 73 to 116 mmHg (average 94 mmHg) and diastolic between 30 to 76 mmHg (average 52 mmHg), with a HR between 96 to 130 bpm (average 113 bpm). Assuming HR equal to 120 bpm as in the pre-operative conditions, the hF simulation produced results (systolic and diastolic pressures of 78 and 42 mmHg, respectively – Figure 9(b)) consistent with the lower range of values from the clinical data. This suggests a reasonable predictive capability of the model since the pre-operative model is based on measurements that were obtained under sedation and general anaesthesia when blood pressure is expected to be lower than when fully conscious. However, the challenges of modelling transient autonomic changes (Vignon-Clementel, Marsden, et al. 2010; Pennati et al. 2011) still need to be faced in order to more accurately predict hemodynamics when the patient is awake.

SVC pressure in the patient was 10–17 mmHg (average 13 mmHg), in good agreement with the model result (15.4 mmHg – Table 2). Moreover, the predicted SVC flow tracing (Figure 9(d)) showed damping of its pulsatility, matching the post-operative Doppler tracing (data not shown).

4.5 Modelling for clinical decision support and future directions

In this case study, we have performed a direct comparison between two surgical options – bi-directional Glenn and hemi-Fontan. The results of these simulations have shown that clinically there is little difference in the global performance of the two geometries at rest. However, there has been a significant change in both surgical options from the pre-operative state (i.e. decreased stroke volume, higher blood pressure and lower ventricular work) as would be expected with volume unloading of the ventricle with stage 2 surgery. There are some differences in local hemodynamics between the hF and bG geometry; however the clinical relevance of this is not known.

The potential benefits of using this type of modelling are both patient-specific and generalizable to all SV patients. Patients with specific geometric problems such as PA stenosis may undergo predictive modelling of different options, concentrating on local hemodynamics to aid

clinician decision making about the extent of the operation. Global hemodynamics are useful in cases where it is uncertain whether a patient would even be a suitable candidate for SV palliation.

One of the primary issues of this study is the clinical data acquisition. SV patients represent a particularly challenging population to study given the young age range, unstable nature of their physiology, and the small number of patients with the condition thereby limiting the numbers of potential participants. Ideally, all clinical data would be collected simultaneously ensuring identical physiological states and simplifying the construction of the pre-operative model. In practice, this is impossible with the technology available. Even measurements that are temporally close have errors due to the limitations of equipment such as fluid-filled catheters and the constantly changing physiology of the patient. Therefore, clinical data are often conflicting, incomplete, and limited. A major part of the collaboration between clinicians and engineers is in developing strategies to deal with the clinical data based on the experience of clinicians and engineers in their respective fields. Constant communication between the two fields is essential so that clinicians can help engineers to understand what can be modelled and what data are suitable for modelling, and engineers can perform clinically feasible and sensible simulations. While current state of the art in predictive modelling remains in the assessment of local flow dynamic variations between different surgical reconstructive options, the present methodology allows the evaluation of detailed, clinically-relevant global systemic effects in context of patient-specific simulations. To further affect the translation of this new modelling paradigm to the bedside, future work will focus on establishing a 'minimum' set of data that can be implemented to allow reliable and meaningful simulation results that can support clinical decision-making.

5. Conclusions

Multi-scale modelling of a patient-specific SV pathway is shown to effectively predict post-operative results for a patient approaching stage 2 palliation for SV heart disease. The complex process of utilizing clinical data appropriately to create pre-operative models, and using those models to test virtual operations, relies on comprehensive collaboration and integration between engineers and clinicians.

Acknowledgements

This study was supported by a grant from the Fondation Leducq, Paris, France. ALM received additional support from a Burroughs Wellcome Fund CASI award.

Notes

1. Joint first authors.
2. MOCHA investigators: Andrew Taylor, MD, Alessandro Giardini, MD, Sachin Khambadkone, MD, Silvia Schievano, PhD, Marc de Leval, MD, and T.-Y. Hsia, MD (Institute of Cardiovascular Sciences, UCL, London, UK); Edward Bove, MD and Adam Dorfman, MD (University of Michigan, Ann Arbor, MI, USA); G. Hamilton Baker, MD and Anthony Hlavacek (Medical University of South Carolina, Charleston, SC, USA); Francesco Migliavacca, PhD, Giancarlo Pennati, PhD, and Gabriele Dubini, PhD (Politecnico di Milano, Milan, Italy); Alison Marsden, PhD (University of California, San Diego, CA, USA); Jeffrey Feinstein, MD (Stanford University, Stanford, CA, USA); Irene Vignon-Clementel (INRIA, Paris, France); Richard Figliola, PhD and John McGregor, PhD (Clemson University, Clemson, SC, USA)

References

Alevriadou BR, McIntire LV. 1995. Rheology. In: Thrombosis and hemorrhage. Cambridge, MA: Blackwell Science. p. 369–381 Chapter 17.

Armillotta A, Bonhoeffer P, Dubini G, Ferragina S, Migliavacca F, Schievano S. 2007. Use of rapid prototyping models in the planning of percutaneous pulmonary valved stent implantation. Proc Inst Mech Eng H. 221:407–416.

Bardo DM, Frankel DG, Applegate KE, Murphy DJ, Saneto RP. 2001. Hypoplastic left heart syndrome. Radiographics. 21:705–717.

Baretta A, Corsini C, Yang W, Vignon-Clementel IE, Marsden AL, Feinstein JA, Hsia TY, Dubini G, Migliavacca F, Pennati G, et al., 2011. Virtual surgeries in patients with congenital heart disease: a multiscale modelling test case. Philos Trans R Soc A. 369:4316–4330.

Baretta A, Corsini C, Marsden AL, Vignon-Clementel IE, Hsia TY, Dubini G, Migliavacca F, Pennati G, the Modeling Of Congenital Hearts Alliance (MOCHA) Investigators. 2012. Respiratory effects on hemodynamics in patient-specific CFD models of the Fontan circulation under exercise conditions. Eur J Mech B/Fluids. 35:61–69.

Bove EL, Migliavacca F, de Leval MR, Balossino R, Pennati G, Lloyd TR, Khambadkone S, Hsia TY, Dubini G. 2008. Use of mathematical modeling to compare and predict hemodynamic effects of the modified Blalock-Taussig and right ventricle to pulmonary artery shunts for hypoplastic left heart syndrome. J Thorac Cardiovasc Surg. 136:312–320e2.

Corsini C, Cosentino D, Pennati G, Dubini G, Hsia TY, Migliavacca F. 2011. Multiscale models of the hybrid palliation for hypoplastic left heart syndrome. J Biomech. 44:767–770.

Dillman JR, Dorfman AL, Attili AK, Agarwal PP, Bell A, Mueller GC, Hernandez RJ. 2010. Cardiovascular magnetic resonance imaging of hypoplastic left heart syndrome in children. Pediatr Radiol. 40:261–274.

Dawson CA, Rickaby DA, Linehan JH, Bronikowski TA. 1988. Distributions of vascular volume and compliance in the lung. J Appl Physiol. 64:266–273.

de Zélicourt DA, Pekkan K, Parks J, Kanter K, Fogel M, Yoganathan AP. 2006. Flow study of an extracardiac connection with persistent left superior vena cava. J Thorac Cardiovasc Surg. 131:785–791.

de Zélicourt DA, Haggerty CM, Sundareswaran KS, Whited BS, Rossignac JR, Kanter KR, Gaynor JW, Spray TL, Sotiropoulos F, Fogel MA, et al., 2011. Individualized

computer-based surgical planning to address pulmonary arteriovenous malformations in patients with a single ventricle with an interrupted inferior vena cava and azygous continuation. J Thorac Cardiovasc Surg. 141(5):1170–1177.
Esmaily Moghadam M, Bazilevs Y, Hsia TY, Vignon-Clementel IE, Marsden AL. 2011. A comparison of outlet boundary treatments for prevention of backflow divergence with relevance to blood flow simulations. Comput Mech. 48:277–291.
Esmaily Moghadam M, Migliavacca F, Vignon-Clementel IE, Hsia TY, Marsden AL. 2012. Optimization of shunt placement for the Norwood surgery using multi-domain modeling. J Biomech Eng. 134(5):051002.
Fontan F, Baudet E. 1971. Surgical repair of tricuspid atresia. Thorax. 26:240–248.
Haggerty CM, de Zélicourt DA, Sundareswaran KS, Pekkan K, Whited B, Rossignac JR, Fogel MA, Yoganathan AP. 2009. Hemodynamic assessment of virtual surgery options for a failing Fontan using lumped parameter simulation. Comput Cardiol. 36:389–392.
Laganà K, Dubini G, Migliavacca F, Pietrabissa R, Pennati G, Veneziani A, Quarteroni A. 2002. Multiscale modelling as a tool to prescribe realistic boundary conditions for the study of surgical procedures. Biorheology. 39(3–4):359–364.
Laganà K, Balossino R, Migliavacca F, Pennati G, Bove EL, de Leval MR, Dubini G. 2005. Multiscale modeling of the cardiovascular system: application to the study of pulmonary and coronary perfusions in the univentricular circulation. J Biomech. 38:1129–1141.
Marsden AL, Vignon-Clementel IE, Chan F, Feinstein JA, Taylor CA. 2007. Effects of exercise and respiration on hemodynamic efficiency in CFD simulations of the total cavopulmonary connection. Ann Biomed Eng. 35(2):250–263.
Marsden AL, Bernstein AJ, Reddy VM, Shadden SC, Spilker RL, Chan FP, Taylor CA, Feinstein JA. 2009. Evaluation of a novel Y-shaped extracardiac Fontan baffle using computational fluid dynamics. J Thorac Cardiovasc Surg. 137:394–403e2.
Migliavacca F, Pennati G, Dubini G, Fumero R, Pietrabissa R, Urcelay G, Bove EL, Hsia TY, de Leval MR. 2001. Modeling of the Norwood circulation: effects of shunt size, vascular resistances, and heart rate. Am J Physiol Heart Circ Physiol. 280:H2076–H2086.
Pekkan K, de Zélicourt D, Ge L, Sotiropoulos F, Frakes D, Fogel MA, Yoganathan AP. 2005. Physics-driven CFD modelling of complex anatomical cardiovascular flows – a TCPC case study. Ann Biomed Eng. 33:284–300.
Pekkan K, Whited B, Kanter K, Sharma S, de Zélicourt D, Sundareswaran K, Frakes D, Rossignac J, Yoganathan AP. 2008. Patient-specific surgical planning and hemodynamic computational fluid dynamics optimization through free-form haptic anatomy editing tool (SURGEM). Med Biol Eng Comput. 46:1152–1139.
Pekkan K, Dasi LP, de Zélicourt D, Sundareswaran KS, Fogel MA, Kanter KR, Yoganathan AP. 2009. Hemodynamic performance of stage-2 univentricular reconstruction: Glenn vs. hemi-Fontan templates. Ann Biomed Eng. 37(1):50–63.
Pennati G, Fumero R. 2000. Scaling approach to study the changes through the gestation of human fetal cardiac and circulatory behaviors. Ann Biomed Eng. 28:442–452.
Pennati G, Corsini C, Cosentino D, Hsia TY, Luisi VS, Dubini G, Migliavacca F. 2011. Boundary conditions of patient-specific fluid dynamics modelling of cavopulmonary connections: possible adaptation of pulmonary resistances results in a critical issue for a virtual surgical planning. Interface Focus. 1:297–307.
Presson RG, Jr, Audi SH, Hanger CC, Zenk GM, Sidner RA, Linehan JH, Wagner WW, Jr, Dawson CA. 1998. Anatomic distribution of pulmonary vascular compliance. J Appl Physiol. 84(1):303–310.
Schievano S, Migliavacca F, Coats L, Khambadkone S, Carminati M, Wilson N, Deanfield JE, Bonhoeffer P, Taylor AM. 2007. Percutaneous pulmonary valve implantation based on rapid prototyping of right ventricular outflow tract and pulmonary trunk from MR data. Radiology. 242(2):490–497.
Snyder MF, Rideout VC. 1969. Computer simulation studies of the venous circulation. IEEE Trans Biomed Eng. 16(4):325–334.
Spilker RL, Feinstein JA, Parker DW, Reddy VM, Taylor CA. 2007. Morphometry-based impedance boundary conditions for patient-specific modeling of blood flow in pulmonary arteries. Ann Biomed Eng. Aug; 35:546–559.
Spilker RL, Taylor CA. 2010. Tuning multidomain hemodynamic simulations to match physiological measurements. Ann Biomed Eng. 38(8):2635–2648, doi: 10.1007/s10439-010-0011-9
Tang BT, Fonte TA, Chan FP, Tsao PS, Feinstein JA, Taylor CA. 2010. Three-dimensional hemodynamics in the human pulmonary arteries under resting and exercise conditions. Ann Biomed Eng. 39(1):347–358.
Troianowski G, Taylor CA, Feinstein JA, Vignon-Clementel IE. 2011. Three-dimensional simulations in Glenn patients: clinically based boundary conditions, hemodynamic results and sensitivity to input data. J Biomech Eng. 133(11):111006.
Vignon-Clementel IE, Figueroa CA, Jansen KE, Taylor CA. 2006. Outflow boundary conditions for three-dimensional finite element modeling of blood flow and pressure in arteries. Comput Methods Appl Mech Eng. 195:3776–3796.
Vignon-Clementel IE, Marsden AM, Feinstein JA. 2010. A primer on computational simulation in congenital heart disease for the clinician. Prog Pediatr Cardiol. 30(1-2):3–13.
Vignon-Clementel IE, Figueroa CA, Jansen KE, Taylor CA. 2010. Outflow boundary conditions for 3D simulations of non-periodic blood flow and pressure fields in deformable arteries. Comput Methods Biomech Biomed Eng. 13(5):625–640.

Appendix

The equations describing the pre-operative LPM (Figure 4(a)) are reported below. All constant parameters are listed in Tables A1 and A2.

Heart equations

The heart is described by two time-varying elastances, a SA and a SV respectively, whose contraction is ruled by two activation functions (AA(t) and AV(t), respectively). Both AA(t) and AV(t) are sinusoidal shape functions consecutive in time (Figure A1(a)), with duration of t_{SAs} and t_{SVs}, respectively.

Atrium

Blood flow across the atrial elastance :

$$\frac{dV_{SA}}{dt} = Q_{PV} + Q_{SVC} + Q_{THIVC} - Q_{AV}$$

SA pressure : $P_{SA} = P_{SA,\,active} \cdot AA(t) + P_{SA,\,passive}$, with

$$P_{SA,\,active} = \frac{1}{C_{SA}} \cdot (V_{SA} - V_{SA0}) \quad \text{and}$$

$$P_{SA,\,passive} = c_{SA} \cdot \left\{ e^{[d_{SA}(V_{SA} - V_{SA0})]} - 1 \right\}.$$

Ventricle

Blood flow across the ventricular elastance :

$$\frac{dV_{SV}}{dt} = Q_{AV} - Q_{AO}$$

SV pressure : $P_{SV} = P_{SV,\,active} \cdot \mathrm{AV}(t) + P_{SV,\,passive}$ with

$$P_{SV,\,active} = a \cdot (V_{SV} - V_{SV0})^2 + b \cdot (V_{SV} - V_{SV0}) \quad \text{and}$$

$$P_{SV,\,passive} = c_{SV} \cdot \left\{ e^{[d_{SV}(V_{SV} - V_{SV0})]} - 1 \right\}.$$

The pressure effectively generated by the SV is reduced by the viscous term due to the myocardium fibers: $P_{SV\,eff} = P_{SV} - R_{MYO} \cdot Q_{AO}$.

Valves

The AV and aortic (AO) valves are described by non-linear diodes, reproducing flow unidirectionality and resistance, with inertances accounting for inertial effects of blood flow (AO valve inertance is not present in the following equations because is included in the downstream arterial inertances L_{UBA} and L_{THAO}).

- AV valve

  Pressure drop across the AV valve: $P_{SA} - P_{SV} = L_{AV} \cdot (dQ_{AV}/dt) + K_{AV} \cdot Q_{AV}^2$

  Therefore, blood flow across the AV valve can be

Table A1. Parameter values for the heart and systemic circulation.

LPM blocks	Parameters	Values
Heart		
Atrium	C_{SA}	0.50
	c_{SA}	0.30
	d_{SA}	0.40
	V_{SA0}	1.63
	t_{SAs}	0.12
Ventricle	a	-0.115
	b	12
	c_{SV}	0.14
	d_{SV}	0.22
	V_{SV0}	3.80
	t_{SVs}	0.28
	R_{MYO}	4.03×10^{-2}
Valves	L_{AV}	2.64×10^{-5}
	K_{AV}	7.02×10^{-4}
	K_{AO}	7.39×10^{-5}
UB	R_{UBA}	8.43×10^{-1}
	L_{UBA}	6.47×10^{-4}
	C_{UB}	1.81
	R_{UBV}	2.46
	C_{SVC}	2.26×10^{-1}
	R_{SVC}	9.35×10^{-2}
LB		
Aorta	C_{AO}	1.41×10^{-1}
	R_{THAO}	2.23×10^{-1}
	L_{THAO}	2.20×10^{-3}
	C_{THAO}	2.96×10^{-2}
	R_{ABAO}	1.70
	L_{ABAO}	2.20×10^{-3}
	C_{ABAO}	6.26×10^{-2}
Legs	R_{LEGA}	4.63
	L_{LEGA}	2.20×10^{-3}
	C_{LEGA}	3.04×10^{-2}
	R_{LEGC}	10.9
	C_{LEGV}	6.20×10^{-1}
	R_{LEGV}	2.55
IVC	C_{ABIVC}	3.22×10^{-1}
	R_{ABIVC}	4.67×10^{-2}
	C_{THIVC}	9.65×10^{-1}
	R_{THIVC}	3.64×10^{-2}
Liver	R_{LA}	26.5
	C_{L}	7.79×10^{-1}
	R_{LV}	1.66×10^{-1}
Kidneys	R_{KA}	18.7
	C_{K}	3.24×10^{-1}
	R_{KV}	1.75
Intestine	R_{IA}	41.0
	C_{I}	1.94×10^{-1}
	R_{IV}	7.45×10^{-1}

Note: R [mmHg s cm^{-3}], C [cm^3 mmHg^{-1}], L [mmHg s^2 cm^{-3}], K [mmHg s^2 cm^{-6}], V [cm^3], a [mmHg cm^{-6}], b [mmHg cm^{-3}], c_{SA} and c_{SV} [mmHg], d_{SA} and d_{SV} [cm^{-3}], t_{SAs} and t_{SVs} [s].

Table A2. Parameter values for the pulmonary RCR blocks.

	Morphometric			Final LPM		
Block	$R_p + R_d$ (mmHg s cm^{-3})	$R_d/(R_p + R_d)$ (–)	C (cm^3 mmHg^{-1})	$R_p + R_d$ (mmHg s cm^{-3})	$R_d/(R_p + R_d)$ [–]	C (cm^3 mmHg^{-1})
Right lung						
1	9.64	0.87	1.53×10^{-2}	12.5	0.83	6.48×10^{-2}
2	37.9	0.92	3.14×10^{-3}	49.3	0.89	1.33×10^{-2}
3	1.61	0.73	1.43×10^{-1}	2.09	0.67	6.03×10^{-1}
Left lung						
1	49.5	0.93	2.39×10^{-3}	64.3	0.98	1.01×10^{-2}
2	21.0	0.89	5.90×10^{-3}	27.3	0.98	2.49×10^{-2}
3	2.69	0.82	7.41×10^{-2}	3.50	0.96	3.14×10^{-1}

Notes: '*Morphometric*' values are obtained from the Womersley-based impedances of the morphometric PA sub-trees (see Section 2.3). '*Final LPM*' values are obtained after the manual tuning (see Section 2.4), i.e. correction of the total resistance ($R_p + R_d$), compliance C and distal-to-total resistance ratio $R_d/(R_p + R_d)$.

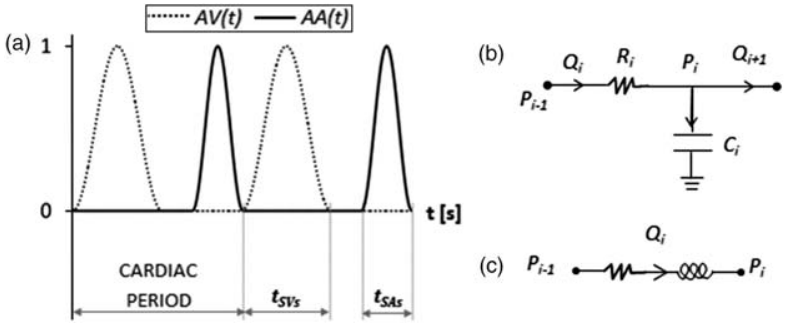

Figure A1. (a) Atrial and ventricular activation functions; (b) RC block; (c) RL block.

expressed by the following equations:

$$Q_{AV} = 0, \quad \text{if } Q_{AV} < 0$$

$$\frac{dQ_{AV}}{dt} = \begin{cases} 0, & \text{if } P_{SA} < P_{SVeff} \text{ and } Q_{AV} \leq 0, \\ \frac{P_{SA} - P_{SV} - K_{AV} \cdot Q_{AV}^2}{L_{AV}}, & \text{elseware.} \end{cases}$$

- AO valve

  Pressure drop across the AO valve: $P_{SV} - P_{AO} = R_{MYO} \cdot Q_{AO} + K_{AO} \cdot Q_{AO}^2$

  Therefore, blood flow across the AO valve can be expressed by the following equations:

$$Q_{AO} = \begin{cases} \frac{\sqrt{R_{MYO}^2 + 4K_{AO}(P_{SV} - P_{AO})} - R_{MYO}}{2K_{AO}}, & \text{if } P_{SV} > P_{AO}, \\ 0, & \text{if } P_{SV} < P_{AO}. \end{cases}$$

Systemic and pulmonary circulation equations

The systemic and pulmonary circulation is represented by RC and RL blocks, described by the following equations expressed for the generic resistance R_i, compliance C_i and inertance L_i of the block i.

RC blocks (Figure A1(b))

$$P_{i-1} - P_i = R_i \cdot Q_i,$$

$$Q_i - Q_{i+1} = C_i \frac{dP_i(t)}{dt}$$

RL blocks (Figure A1(c))

$$P_{i-1} - (P_i + R_i \cdot Q_i) = L_i \cdot \frac{dQ_i}{dt}.$$

Leg venous valve

A venous valve was included by means of a diode in the leg venous block. The following equation describes the flow Q_{LEGV} through the valve, with $(P_{LEGV} - P_{ABIVC})$ being the pressure drop across the valve and R_{LEGV} the resistance of leg veins:

$$Q_{LEGV} = \begin{cases} \frac{P_{LEGV} - P_{ABIVC}}{R_{LEGV}}, & \text{if } P_{LEGV} > P_{ABIVC}, \\ 0, & \text{if } P_{LEGV} < P_{ABIVC}. \end{cases}$$

Shunt equation

The expression for the pressure drop across the shunt is the following:

$$\Delta P = R_{SH} Q_{SH} + K_{SH} Q_{SH}^2 = \frac{k_1}{D^4} Q_{SH} + \frac{k_2}{D^4} Q_{SH}^2,$$

where R_{SH} and K_{SH} are the linear and non-linear terms, respectively, of shunt resistance, and Q_{SH} is the shunt flow. R_{SH} and K_{SH} can be expressed as functions of the shunt diameter D, with k_1 and k_2 being proportionality constants previously evaluated (Migliavacca et al. 2001).

Appendix B

Predictive modeling of the virtual Hemi-Fontan operation for second stage single ventricle palliation: Two patient-specific cases

Journal of Biomechanics 46 (2013) 423–429

Contents lists available at SciVerse ScienceDirect

Journal of Biomechanics

journal homepage: www.elsevier.com/locate/jbiomech
www.JBiomech.com

Predictive modeling of the virtual Hemi-Fontan operation for second stage single ventricle palliation: Two patient-specific cases

Ethan Kung [a], Alessia Baretta [b], Catriona Baker [c], Gregory Arbia [d], Giovanni Biglino [c], Chiara Corsini [b], Silvia Schievano [c], Irene E. Vignon-Clementel [d], Gabriele Dubini [b], Giancarlo Pennati [b], Andrew Taylor [c], Adam Dorfman [e], Anthony M. Hlavacek [f], Alison L. Marsden [a], Tain-Yen Hsia [c], Francesco Migliavacca [b,*], for the Modeling Of Congenital Hearts Alliance (MOCHA)+ Investigators[1]

[a] Mechanical and Aerospace Engineering Department, University of California San Diego, San Diego, CA, USA
[b] Laboratory of Biological Structure Mechanics, Department of Chemistry, Materials and Chemical Engineering "Giulio Natta", Politecnico di Milano, Piazza Leonardo da Vinci, 32, 20133 Milano, Italy
[c] Cardiorespiratory Unit, Great Ormond Street Hospital for Children and UCL Institute of Cardiovascular Science, London, UK
[d] INRIA, Paris-Rocquencourt, Le Chesnay, France
[e] Division of Pediatric Cardiology, Department of Pediatrics, University of Michigan Medical School, Ann Arbor, MI, USA
[f] Division of Pediatric Cardiology, Department of Pediatrics, Medical University of South Carolina, Charleston, SC 29425, USA

ARTICLE INFO

Article history:
Accepted 23 October 2010

Keywords:
Single-ventricle
Fontan
Multi-scale modeling
CFD
Hemi-fontan
Patient specific modeling

ABSTRACT

Single ventricle hearts are congenital cardiovascular defects in which the heart has only one functional pumping chamber. The treatment for these conditions typically requires a three-staged operative process where Stage 1 is typically achieved by a shunt between the systemic and pulmonary arteries, and Stage 2 by connecting the superior venous return to the pulmonary circulation. Surgically, the Stage 2 circulation can be achieved through a procedure called the Hemi-Fontan, which reconstructs the right atrium and pulmonary artery to allow for an enlarged confluence with the superior vena cava.

Based on pre-operative data obtained from two patients prior to Stage 2 surgery, we developed two patient-specific multi-scale computational models, each including the 3D geometrical model of the surgical junction constructed from magnetic resonance imaging, and a closed-loop systemic lumped-parameter network derived from clinical measurements. "Virtual" Hemi-Fontan surgery was performed on the 3D model with guidance from clinical surgeons, and a corresponding multi-scale simulation predicts the patient's post-operative hemodynamic and physiologic conditions. For each patient, a post-operative active scenario with an increase in the heart rate (HR) and a decrease in the pulmonary and systemic vascular resistance (PVR and SVR) was also performed. Results between the baseline and this "active" state were compared to evaluate the hemodynamic and physiologic implications of changing conditions.

Simulation results revealed a characteristic swirling vortex in the Hemi-Fontan in both patients, with flow hugging the wall along the SVC to Hemi-Fontan confluence. One patient model had higher levels of swirling, recirculation, and flow stagnation. However, in both models, the power loss within the surgical junction was less than 13% of the total power loss in the pulmonary circulation, and less than 2% of the total ventricular power. This implies little impact of the surgical junction geometry on the SVC pressure, cardiac output, and other systemic parameters. In contrast, varying HR, PVR, and SVR led to significant changes in theses clinically relevant global parameters.

Adopting a work-flow of customized virtual planning of the Hemi-Fontan procedure with patient-specific data, this study demonstrates the ability of multi-scale modeling to reproduce patient specific flow

* Corresponding author. Tel.: +39 02 2399 4316; fax: +39 02 2399 4286.
E-mail address: francesco.migliavacca@polimi.it (F. Migliavacca).

[1] +MOCHA Investigators: Andrew Taylor, MD; Alessandro Giardini, MD; Sachin Khambadkone, MD; Silvia Schievano, Ph.D.; Marc de Leval, MD; and T.-Y. Hsia, MD (Institute of Cardiovascular Sciences, UCL, London, UK); Edward Bove, MD and Adam Dorfman, MD (University of Michigan, Ann Arbor, MI, USA); G. Hamilton Baker, MD and Anthony Hlavacek (Medical University of South Carolina, Charleston, SC, USA); Francesco Migliavacca, Ph.D., Giancarlo Pennati, Ph.D., and Gabriele Dubini, Ph.D. (Politecnico di Milano, Milan, Italy); Alison Marsden, Ph.D. (University of California, San Diego, CA, USA); Jeffrey Feinstein, MD (Stanford University, Stanford, CA, USA); Irene Vignon-Clementel (INRIA, Paris, France); Richard Figliola, Ph.D., and John McGregor, Ph.D. (Clemson University, Clemson, SC, USA).

0021-9290/$ - see front matter
http://dx.doi.org/10.1016/j.jbiomech.2012.10.023

conditions under differing physiological states. Results demonstrate that the same operation performed in two different patients can lead to different hemodynamic characteristics, and that modeling can be used to uncover physiologic changes associated with different clinical conditions.

1. Introduction

Single ventricle physiology, in which the infant has only one functional pumping chamber, is one of the most severe forms of congenital heart disease. Without intervention, the condition is not compatible with life, requiring immediate surgical treatment after birth, followed by two additional surgeries within the first few years of life. The surgeries are staged such that at each stage the circulation provides adequate systemic oxygen delivery without severe, long-term volume overloading of the ventricle. The final goal is to bypass the heart by connecting the entire systemic venous return directly to the pulmonary arterial system, resulting in an in-series circulation driven by a single ventricle (Gale et al., 1980).

The Stage 1 surgery is performed within the first few days of life, with the patency of the ductus arteriosus ensured by infusion of prostaglandin E2 until the operation. In most cases a systemic-to-pulmonary shunt (Fig. 1a) provides balanced flow to the pulmonary circulation while maintaining an unrestricted aortic outflow and systemic venous return. The stage 2 surgery is performed at about 6 months of age, after the pulmonary vascular resistance has decreased due to lung growth (Bardo et al., 2001). The surgery removes the systemic-to-pulmonary shunt, or disconnects the pulmonary artery from the systemic arterial circulation (depending on stage 1 anatomy), and attaches the superior vena cava (SVC) to the pulmonary artery to provide pulmonary flow. After a few years of age as the proportion of systemic venous return from the lower body increases, the stage 3 surgery, the Fontan procedure, is performed, during which the inferior vena cava (IVC) is also connected to the pulmonary artery, completing the conversion to single ventricle circulation.

The transition from Stage 1 to Stage 2 circulation is particularly important as the single ventricle is relieved of the workload of providing pulmonary blood flow, which is then solely derived from the superior vena cava (SVC). In addition to requiring low pulmonary vascular resistance to allow for effective Stage 2 circulation, the surgical reconstruction required to provide a pulmonary blood flow devoid of a ventricular power source must be one that extracts little power or energy. The Hemi-Fontan (HF) operation has been adopted by many surgeons as the preferred procedure to achieve these goals. Fig. 1(b) demonstrates one version of this operation, in which the SVC remains connected to the right atrium, and a homograft patch is placed to redirect flow to the right and left pulmonary arteries through a small pouch or confluence.

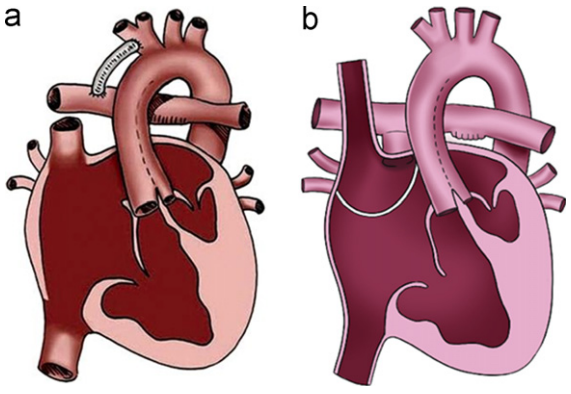

Fig. 1. Single ventricle palliation surgical procedures: (a) stage 1 and (b) stage 2 Hemi-Fontan. ((a) Republished with kind permission from Springer Science and Business Media, originally published in Pediatric Radiology 2010;40, Cardiovascular magnetic resonance imaging of hypoplastic left heart syndrome in children, Dillman, J.R., et al., p. 264, Fig. 4, illustration by Anne Phillips, University of Michigan Health System, Department of Radiology Media Services. (b) Produced by Carolyn Nowak, University of Michigan Health System, Department of Radiology Media Services.)

Due to the lack of animal models for single ventricle physiology, and the fact that direct clinical measurements are often difficult, the understanding of the impact of the surgical geometries and patient-specific anatomy on important clinical parameters, such as ventricular load, thrombotic risk, or systemic pressures and flows, remains challenging. Computational methods have been used to study patient-specific single ventricle physiology, and predict hemodynamic changes due to virtual surgery (Pekkan et al., 2008; Marsden et al., 2009, 2010; Sundareswaran et al., 2009; Vignon-Clementel et al., 2010; de Zélicourt et al., 2011). Using a coupled multi-scale and closed-loop modeling approach, realistic local and global hemodynamic interactions can be mimicked and detailed holistic, physiologic information can be extracted for in-depth analysis to better compare different surgical options.

In this study, we performed virtual HF operation on two patients who had undergone clinical investigation prior to conversion from Stage 1 to Stage 2 circulation. For each patient we investigated the local dynamics of the Hemi-Fontan circulation, and analyzed the global systemic physiology of each under a normal resting state, as well as an "active" state, which mimics voluntary arm and leg movements of the infant with increased heart rate and blood flow.

2. Methods

This study utilizes patient-specific computational models to describe various scenarios after the HF surgery for two single-ventricle patients. Each computational model contains a 3D domain of the surgical junction, and a 0D domain that describes the rest of the circulatory system. A total of 4 simulations were performed for this study, encompassing a resting and an active condition for the two patients.

2.1. Clinical data acquisition

The patients A and B were 5 and 6 months old at the time of surgery, respectively, with body surface areas (BSA) of 0.3 m^2 and 0.34 m^2. Patients A and B were recruited to the Medical University of South Carolina, Charleston, SC, and the University of Michigan, Ann Arbor, MI, respectively. The study was approved by the IRB at each institution. For patient A the MRI was performed 1.5 months prior to surgery, immediately following cardiac catheterization under the same general anesthesia. For patient B the MRI was performed immediately prior to surgery under the same anesthetic, and cardiac catheterization was performed 3 days prior to the MRI and surgery. MRI data was obtained using a standardized protocol, including a contrast-enhanced 3-dimensional MR angiogram, following the administration of 0.2 mmol/kg of gadoteridol (Prohance, Bracco Diagnostics, Princeton, New Jersey). In-plane spatial resolution for the angiogram was 1.0×1.0 mm^2, with slice thickness of 2.0 mm, interpolated to 1.0 mm.

2.2. Construction of 3D surgical junction geometries

Based on magnetic resonance imaging data of each patient prior to the Stage 2 surgery, we reconstructed the patient anatomy using commercial software (Mimics, Materialise NV, Leuven, Belgium). We selected regions of interest in the

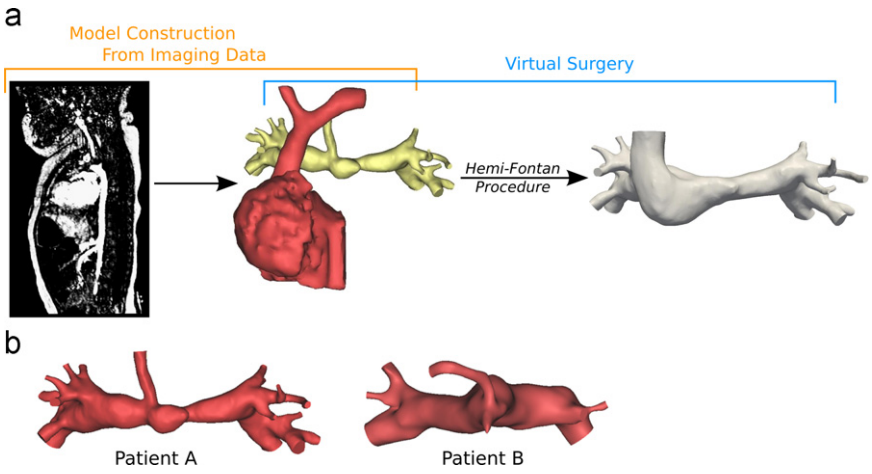

Fig. 2. (a) Work flow of model construction from imaging data, and virtual hemi-fontan surgery. (b) Pre-operative 3D anatomical models of Patients A and B.

imaging data, and used a segmentation and region-growing technique (Armillotta et al., 2007; Schievano et al., 2007) to obtain a 3D volume of the relevant vasculature. The resulting 3D model is a representation of the patient's pre-operative anatomy (Fig. 2b).

Once the pre-operative anatomical models are created, these can be manipulated using the same software (Mimics) in order to generate virtual post-operative scenarios. We performed the HF virtual surgery by modifying the pre-operative 3D model based on the geometric constraints relating to the organs and vessels surrounding the region. The post-operative models were created by following the clinical guidelines of the respective procedures, and by the same operator who generated the pre-operative models. The imaging-based virtual modification of the patient anatomy allows for patient-specific predictions of post-operative geometries. For example, the post-operative deformation of the SVC is affected by the pulmonary artery geometry at the point of anastomosis. Using this method, we can produce a predictive HF post-operative 3D geometrical model for each patient (Fig. 2a). Patient A had a left pulmonary stenosis that was palliated in the virtual surgery, mimicking a realistic clinical scenario. Both the HF virtual surgeries were performed by an engineer and a pediatric cardiac surgeon working together, and approved by a second surgeon from our research group.

2.3. 0D lumped-parameter network

To model the circulatory system outside of the 3D anatomical region, we use a 0D lumped-parameter network (LPN). The LPN consists of five main circuit blocks to model the heart, the upper and lower body vasculatures, and the right and left pulmonary vasculatures (Fig. 3). Two time-varying elastances represent the atrium and ventricle, where two activation functions properly shifted in time model contraction of the two chambers. The atrio-ventricular and aortic valves are modeled by non-linear diodes allowing for unidirectional flow with resistances proportional to the flow rate. In the lower body we modeled three organ systems (kidneys, liver and intestine) and a venous valve in the leg venous block. Corresponding to the outlets of the 3D model, a number of RCR blocks arranged in parallel describe the pulmonary circulation. Coronary circulation, gravity and respiratory effects are neglected (Migliavacca et al., 2001).

We prescribed the pulmonary LPN parameter values using a morphometric tree based impedance approach (Spilker et al., 2007; Troianowski et al., 2011). The parameters result from a 3D–0D preliminary study utilizing patient-specific pre-operative clinical data of the transpulmonary pressure gradient, total pulmonary flow, left–right pulmonary flow split, and the size of each pulmonary branch outlet (Troianowski et al., 2011). The pulmonary vascular resistance can be calculated as

$$PVR = \frac{P_{PA} - P_{SA}}{Q_{PA}} \tag{1}$$

where P_{PA}, P_{SA} and Q_{PA} are the mean pulmonary arterial pressure and atrial pressures, and total pulmonary flow, respectively.

For the systemic LPN parameters, we began with a set of values representing a healthy adult subject with BSA=1.8 m^2 (Noordergraaf et al., 1963; Snyder et al., 1968; Snyder and Rideout, 1969) and used allometric equations to scale the parameters according to the patient's BSA (Pennati and Fumero, 2000). This resulted in a BSA-adjusted generic LPN model, with resistance and capacitance values indicated as $R_{i\text{-}BSA}$ and $C_{i\text{-}BSA}$ for the ith-block . We then tuned the LPN to the patient's resting condition using the resistances of the upper and lower body (*UBSVR* and *LBSVR*, respectively) calculated by

$$UBSVR = \frac{P_{SysA} - P_{SA}}{Q_{UBA}}, \quad LBSVR = \frac{P_{SysA} - P_{SA}}{Q_{LBA}} \tag{2}$$

where P_{SysA}, Q_{UBA}, and Q_{LBA} are the pre-operative (stage 1) clinical measurements of the mean systemic arterial pressure, upper body flow, and lower body flow, respectively.

While maintaining the proportion of impedances among the different blocks, we modified the resistances of each block (resulting in R_i) such that the clinically measured *UBSVR* and *LBSVR* from Eq. (2) are achieved. We then calculated the patient-specific compliance C_i of the ith-block using (Pennati and Fumero, 2000; Baretta et al., 2011):

$$C_i = C_{i\text{-}BSA}\left(\frac{R_i}{R_{i\text{-}BSA}}\right)^{-4/3} \tag{3}$$

Lastly, we manually tuned the parameter values of the heart and the adjacent large vessels to best match both the mean values and waveform tracings from clinical flow measurements made during resting conditions. The heart rate for both patient models is set to 120 bpm, which is within the range of the measured heart rate in both patients.

For each patient, we also prescribed a set of LPN parameter values to reflect an "active" condition, which approximates the patient's physiology during voluntary movements of the limbs and increased blood flow. We chose an "active" state of an infant to parallel an "exercise" state of an older patient capable of exercising. For the active condition, we assume an increase in heart rate from 120 bpm to 160 bpm (Berg et al., 1971), and decreases in PVR and total SVR of 20% and 34%, respectively. Starting from the patient-specific tuned resting condition LPN model, parameters were systematically tuned, as above, to achieve a set of desired values to model the active state. The compliances were modified according to the equation:

$$C_{i\text{-}active} = C_i\left(\frac{R_{i\text{-}active}}{R_i}\right)^{-3/4} \tag{4}$$

where C_i, R_i are the compliances and resistances of the ith-block in the model under resting condition, and $R_{i\text{-}active}$ are the resistances of the ith-block under active condition (Baretta et al., 2012). All other model parameters and fluid properties were kept fixed. In patient A, the PVR and SVR were 0.62 and 4.30 mmHg s/ml for the resting condition, and 0.49 and 2.87 mmHg s/ml for the active condition, respectively; for patient B the PVR and SVR were 1.07 and 2.68 mmHg s/ml for resting and 0.86 and 1.75 mmHg s/ml for active condition, respectively.

2.4. Coupled multi-scale simulation and analysis

Each of the 3D anatomic models was discretized into an isotropic finite-element mesh with a maximum edge size of 0.03 cm and a total of 9.8×10^5–1.3×10^6 linear tetrahedral elements using commercial mesh generation software (MESHSIM, Simmetrix, Inc., New York). These mesh sizes were similar or higher compared to prior studies of corresponding anatomy (Bove et al., 2003; Pekkan et al., 2009; Yang et al., 2012). We coupled the 3D anatomical model to the 0D LPN model to produce a final computational model that described the entire circulation, and numerically solved the coupled system using custom software (Simvascular, www.simtk.org). Neumann boundary conditions were applied at all inlets and outlets of the 3D model using an implicit coupling algorithm described in our previous work (Esmaily Moghadam et al., 2011) in which the 3D domain receives pressure information from the 0D model, and returns flow information to the 0D model, thus completing the two-way coupling between the multi-scale domains. Flow and pressure in the 0D model were computed from a set of algebraic and ordinary differential equations derived from the LPN circuit, using a 4th order Runge–Kutta method. Velocity and pressure in the 3D domain were computed

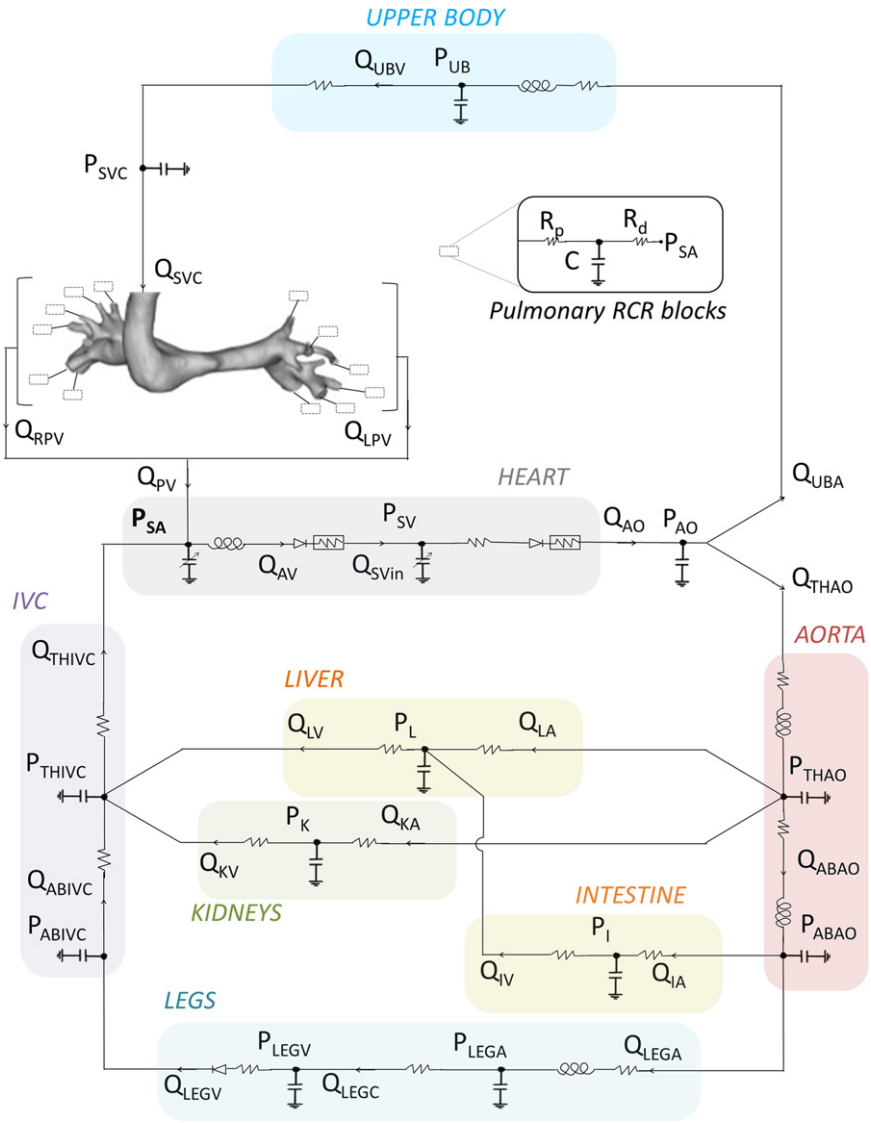

Fig. 3. The 0D lumped-parameter network model coupled to the 3D anatomical model.

using a custom incompressible finite element Navier–Stokes solver, assuming rigid walls and a Newtonian fluid with density of 1.06 g/cm^3 and dynamic viscosity of 0.04 dyn s/cm^2. The solver uses a stabilized scheme (Taylor et al., 1998) and outflow stabilization to prevent backflow divergence (Esmaily Moghadam et al., 2012). The method allows for modular coupling of the 3D and 0D domains without the need for intrusive changes to the finite element solver, and eliminates the small time step stability restriction imposed by explicit coupling methods in previous work. The choice of rigid walls is justified by our recent work (Long et al., 2012) showing little difference in energy loss and pressure levels, though non-negligible differences in wall shear stress (WSS), in rigid vs. deformable simulations. For each simulation we used a time step size of 1 ms for the 3D domain, and 1 μs for the 0D domain. 12 cardiac cycles were simulated and the last cycle was used in the analysis.

Based on the computed 3D velocity field from the simulation, we computed WSS and particle residence time (PRT), which is the time needed for entering particles to exit the 3D HF junction domain. We also obtained the local hemodynamic power dissipation in the surgical region by integrating the difference between the inlet and outlet energy fluxes of the 3D model, accounting for both the potential and kinetic energy terms (Marsden et al., 2007). Pressure and flow information at various points in the 0D LPN model were also extracted. The instantaneous pulmonary power loss is calculated as the sum of the power losses in all of the pulmonary blocks:

$$PW_{pul} = \sum_{outlet} (P_{outlet} - P_{SA}) * Q_{outlet} \tag{5}$$

where P_{outlet}, P_{SA}, and Q_{outlet} are the pressure at each outlet of the 3D model, the atrial pressure, and the volumetric flow through each outlet of the 3D model, respectively. The pulmonary power loss can then be averaged over the cardiac cycle to obtain a mean value. The ventricular output power is the difference between the work done to the blood by the ventricle, and vice versa, during the ejection and filling phases:

$$PW_{ven} = \left(\int_{systole} P_{SV} * V_{SV}\, dt - \int_{diastole} P_{SV} * V_{SV}\, dt / T \right) \tag{6}$$

where P_{SV}, V_{SV}, and T are the ventricular pressure, ventricular volume, and the cardiac cycle period, respectively.

3. Results

Figs. 4 and 5(a) show the volume rendered flow velocity field magnitude (color map) and directions (arrows) in the 3D surgical junction for patients A and B. For both patient models, the incoming flow from the SVC tends to glide along the curve of the confluence floor. In patient A the SVC flow transitions fairly smoothly into the pulmonary arteries. However, in patient B significant swirling is observed, leading to high velocities around the circumference, resulting in a low flow and stagnation region near the center of the confluence section.

Figs. 4 and 5(b) show the WSS distribution in the surgical junction for the two patients. In general, WSS is fairly uniformly distributed, with a band of high WSS corresponding to the orientation of the swirling flow in the junction. The spatial

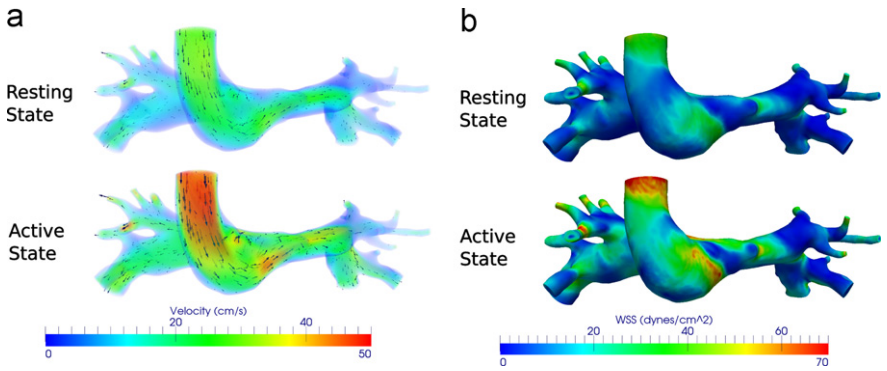

Fig. 4. Time-averaged 3D domain simulation results for patient A: (a) volume-rendered velocity magnitude (color map) and directions (arrows) and (b) wall shear stress distribution.

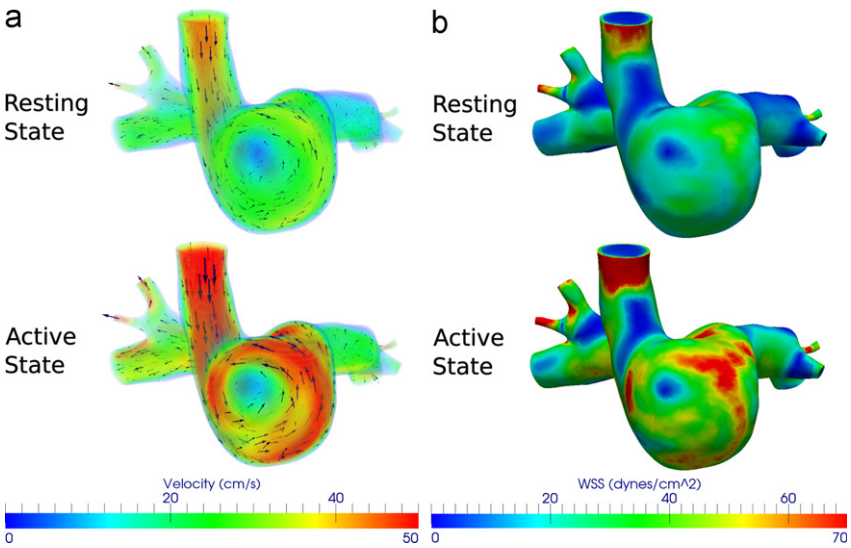

Fig. 5. Time-averaged 3D domain simulation results for Patient B: (a) volume-rendered velocity magnitude (color map) and directions (arrows) and (b) wall shear stress distribution.

Table 1
Mean values of simulated results. Pressures and flows are as labeled in Fig. 3.

	Patient A		Patient B	
	Resting	**Active**	**Resting**	**Active**
Q_{AO} **(mL/s)**	16.8	21.0	19.2	24.6
Q_{PV} **(mL/s)**	8.2	12.7	11.3	16.4
Q_{RPV}/Q_{PV}	0.54	0.53	0.63	0.62
Q_{PV}/Q_{AO}	0.49	0.60	0.59	0.67
P_{SA} **(mmHg)**	4.6	4.8	2.4	3.0
P_{SVC} **(mmHg)**	10.0	11.7	15.4	18.8
P_{AO} **(mmHg)**	74.9	62.0	53.1	46.3
Wall shear stress (dyn/cm^2)	10.62	19.34	20.64	36.05
Particle residence time (s)	0.27	0.18	0.31	0.22
Junction power loss (mW)	0.33	1.01	1.26	3.79
Pulmonary power loss (mW)	5.6	10.7	18.2	30.7
Ventricular power (mW)	193	209	168	193

pattern of WSS is similar between the resting and active conditions simulated.

Table 1 shows the average values of different parameters extracted from each simulation. The junction power loss associated with the HF in patient B is approximately 3 times of that in patient A, however, the amount of power loss associated with the HF region remained less than 13% of the total power loss in the pulmonary circulation, and less than 2% of the total ventricular output power in all cases.

For both patients, the systemic parameters are significantly affected by changes in the physiological condition, but with different magnitudes. The active state led to increased cardiac output and pulmonary blood flow, and a corresponding increase in SVC pressures in both models. Coupled with an already higher baseline SVC pressure of 15.5 mmHg, Patient B had a much higher SVC pressure in the active condition than patient A (18.8 vs. 11.7 mmHg, respectively).

Fig. 6 shows the ventricular pressure–volume loop and the SVC pressure for all cases. The area inside the pressure–volume loop for the active condition is smaller than that for the resting condition in both patients, indicating that less work is performed during each individual cardiac cycle. However, due to the higher heart rate, the ventricular output power (work divided by time) in the active condition is higher than that in resting.

The mean WSS is higher in the active state compared to the resting state (82% and 75% higher, for patients A and B, respectively). The mean PRT, on the other hand, is higher in the resting state compared to the active state (50% and 41% higher, for patients A and B, respectively).

4. Discussion

This study demonstrates the potential of multi-scale techniques to study the hemodynamics and physiology of Stage 2 circulation

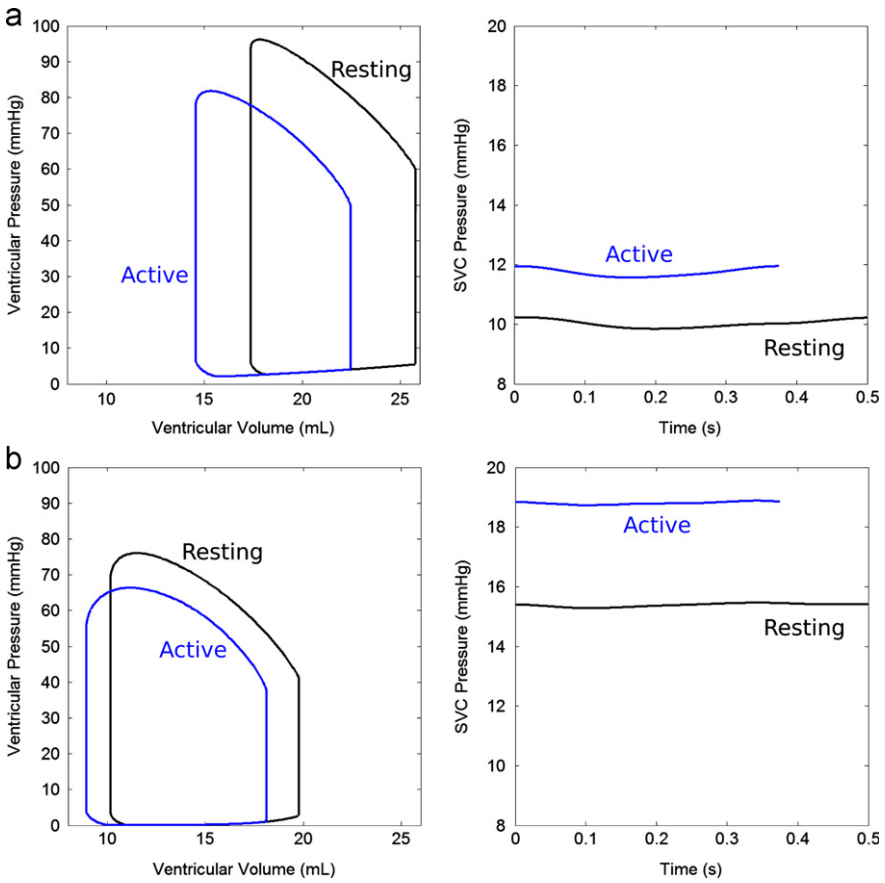

Fig. 6. Simulated results of ventricular pressure–volume loop and SVC pressure for: (a) patient A and (b) patient B.

with the HF procedure in patients with single ventricle circulation. A coupled closed-loop multi-scale modeling approach was used to mimic realistic post-operative scenarios in two patients based on pre-operative clinical data. This method allowed assessment of both local dynamic and global physiologic parameters in a patient-specific manner, and demonstrated that even with the same type of operation, differences in hemodynamic outcomes can occur. Moreover, these differences can be accentuated by virtually "stressing" the circulation by changing parameters to mimic physiologic conditions in an active state. By varying modeling parameters, such as heart rate and systemic/pulmonary vascular resistances, this methodology provides important insights into the effects of changes in physiologic condition on the Stage 2 circulation.

The power loss results are in the same range as reported by previous modeling studies of the HF anatomy (Bove et al., 2003; Pekkan et al., 2009). The simulation results show significant differences in the 3D velocity patterns in the surgical domains in the two different patients, leading to visible variations in power loss. Patient B exhibited three times higher power loss due to higher degrees of flow disturbances and flow rates. However, relative to the global systemic powers, such as the pulmonary circulation power loss and ventricular power, the power loss in the surgical domain is small and may not have a large influence on the overall circulation. The observed differences in global flow and pressures, for example cardiac output and SVC pressure, between Patients A and B were primarily due to differences in patient-specific physiologic parameters such as pulmonary vascular resistance. These results therefore imply that further refinement of the HF operation and improvements in the surgical junction power loss is likely to have minimal impact on the overall immediate post-operative circulation and physiology in terms of pressure and flow, at least during resting and regular active conditions.

Nevertheless, refinement of the HF operation may consider the optimization of minimizing thrombotic risk. Results from computational simulations such as PRT and WSS can contribute to assessing the relative thrombotic risks between the different cases. The lower PRT during the active condition may be beneficial for reducing thrombotic risk. However, the higher WSS during the active state may pose risks of platelet activation. The peaking levels of WSS observed in the scenarios investigated are within the range where shear-induced platelet activation is possible (Brown et al., 1975).

The observation that the active condition increased the surgical junction power loss can be explained by considering the junction as a non-linear resistance with a value proportional to the square of the flow rate (Whitehead et al., 2007). Auto-regulation mechanisms also act to increase vessel diameters during an active state, decreasing vascular resistance in response to increased flow (Goto et al., 2003). This was included in the models by the chosen changes in PVR and SVR. For these reasons, with increasing cardiac output, the surgical junction power loss increases at a faster rate than systemic power losses. The surgical junction power loss relative to systemic losses thus will become more significant at higher cardiac output. The power loss difference between the two HF models could become important and have more tangible effects on systemic parameters with more extreme physiological conditions such as strenuous activity (Marsden et al., 2007). As noted in the active condition simulation, the increase in SVC pressure for patient B is more exaggerated than patient A, with pressures reaching 19 mmHg. This has important clinical ramifications. While most patients would tolerate an SVC pressure up to 15–16 mmHg, at 19 mmHg it is likely that patient B would exhibit clinical signs of SVC syndrome or superior venous hypertension, with facial swelling, headache, and orbital edema, based on prior clinical experience.

This study demonstrates that, in the Stage 2 circulation, while differences in local dynamics and power loss can exist with the HF procedure between different patients, the impact on the global circulation is small compared to those of pulmonary power losses and ventricular power. In addition, the application of a multi-scale model was shown to accurately capture single ventricle patient physiology, incorporating clinical data for customized virtual planning and prediction of the stage 2 procedure, as well as utility in modeling systemic behaviors under different physiological states. Results show that differences in hemodynamic factors in different patient geometries can be accentuated by higher stress physiologic conditions, such as increased activity. The unique contributions of this study include the examination of different physiological conditions using a closed-loop multi-scale model, and the examination of parameters relevant to both thrombotic risk and energy loss. The results of this study provide an evaluation on the relative importance of various considerations for the clinical procedure design for the stage 2 surgery.

Thorough analyses on a sufficient population size are required in order to warrant changes in clinical procedures based on virtual simulation results. Future studies will apply these simulation methods to a larger number of patients, and examine additional parameters such as ventricular function, and compare different surgical options for the Stage 2 surgery. Limitations of this study include the need for further validation against both clinical and in vitro data, use of rigid walls, and a lack of clinical data to precisely model changes in PVR and other parameters from the pre- to post-operative state.

Conflict of Interest Statement

There are no conflict of interest associated with this work.

Acknowledgments

This work was supported by the Leducq Foundation as part of the Transatlantic Network of Excellence for Cardiovascular Research, a Burroughs Wellcome Fund Career award at the Scientific Interface, an American Heart Association Postdoctoral Fellowship, and NSF CAREER OCI-1150184. We also acknowledge Dr. Charles Taylor, Dr. Nathan Wilson, Mahdi Esmaily, and Weiguang Yang for their contributions to codes used in the simulations and analyses, and the open source Simvascular project at simtk.org.

References

Armillotta, A., Bonhoeffer, P., Dubini, G., Ferragina, S., Migliavacca, F., Sala, G., Schievano, S., 2007. Use of rapid prototyping models in the planning of percutaneous pulmonary valved stent implantation. Proceedings of the Institution of Mechanical Engineers, Part H: Journal of Engineering in Medicine 221, 407–416.

Bardo, D.M., Frankel, D.G., Applegate, K.E., Murphy, D.J., Saneto, R.P., 2001. Hypoplastic left heart syndrome. Radiographics 21, 705–717.

Baretta, A., Corsini, C., Marsden, A.L., Vignon-Clementel, I.E., Hsia, T.Y., Dubini, G., Migliavacca, F., Pennati, G., The Modeling Of Congenital Hearts Alliance (MOCHA), 2012. Respiratory effects on hemodynamics in patient-specific CFD models of the Fontan circulation under exercise conditions. European Journal of Mechanics-B/Fluids 35, 61–69.

Baretta, A., Corsini, C., Yang, W., Vignon-Clementel, I.E., Marsden, A.L., Feinstein, J.A., Hsia, T.Y., Dubini, G., Migliavacca, F., Pennati, G., Modeling of Congenital Hearts Alliance (MOCHA) Investigators, 2011. Virtual surgeries in patients with congenital heart disease: a multi-scale modelling test case. Philosophical Transactions of the Royal Society A: Mathematical, Physical and Engineering Sciences 369, 4316–4330.

Berg, K.M., Berg, W.K., Graham, F.K., 1971. Infant heart rate response as a function of stimulus and state. Psychophysiology 8, 30–44.

Bove, E.L., de Leval, M.R., Migliavacca, F., Guadagni, G., Dubini, G., 2003. Computational fluid dynamics in the evaluation of hemodynamic performance of cavopulmonary connections after the Norwood procedure for hypoplastic left heart syndrome. The Journal of Thoracic and Cardiovascular Surgery 126, 1040–1047.

Brown, C.H., Leverett, L.B., Lewis, C.W., Alfrey, C.P., Hellums, J.D., 1975. Morphological, biochemical, and functional changes in human platelets subjected to shear stress. The Journal of Laboratory and Clinical Medicine 86, 462–471.

de Zélicourt, D.A., Haggerty, C.M., Sundareswaran, K.S., Whited, B.S., Rossignac, J.R., Kanter, K.R., Gaynor, J.W., Spray, T.L., Sotiropoulos, F., Fogel, M.A., Yoganathan, A.P., 2011. Individualized computer-based surgical planning to address pulmonary arteriovenous malformations in patients with a single ventricle with an interrupted inferior vena cava and azygous continuation. The Journal of Thoracic and Cardiovascular Surgery 141, 1170–1177.

Esmaily Moghadam, M., Bazilevs, Y., Hsia, T.Y., Vignon-Clementel, I.E., Marsden, A.L., Modeling of Congenital Hearts Alliance (MOCHA), 2011. A comparison of outlet boundary treatments for prevention of backflow divergence with relevance to blood flow simulations. Computational Mechanics 48, 277–291.

Esmaily Moghadam, M., Migliavacca, F., Vignon-Clementel, I.E., Hsia, T.Y., Marsden, A.L., 2012. Optimization of shunt placement for the Norwood surgery using multi-domain modeling. Journal of Biomechanical Engineering 134, 051002.

Gale, A.W., Danielson, G.K., McGoon, D.C., Wallace, R.B., Mair, D.D., 1980. Fontan procedure for tricuspid atresia. Circulation 62, 91–96.

Goto, C., Higashi, Y., Kimura, M., Noma, K., Hara, K., Nakagawa, K., Kawamura, M., Chayama, K., Yoshizumi, M., Nara, I., 2003. Effect of different intensities of exercise on endothelium-dependent vasodilation in humans: role of endothelium-dependent nitric oxide and oxidative stress. Circulation 108, 530–535.

Long, C.C., Hsu, M.-C., Bazilevs, Y., Feinstein, J.A., Marsden, A.L., 2012. Fluid–structure interaction simulations of the Fontan procedure using variable wall properties. International Journal for Numerical Methods in Biomedical Engineering 28, 513–527.

Marsden, A.L., Bernstein, A.J., Reddy, V.M., Shadden, S.C., Spilker, R.L., Chan, F.P., Taylor, C.A., Feinstein, J.A., 2009. Evaluation of a novel Y-shaped extracardiac Fontan baffle using computational fluid dynamics. The Journal of Thoracic Cardiovascular Surgery 137, 394–403, e2.

Marsden, A.L., Reddy, V.M., Shadden, S.C., Chan, F.P., Taylor, C.A., Feinstein, J.A., 2010. A new multiparameter approach to computational simulation for Fontan assessment and redesign. Congenital Heart Disease 5, 104–117.

Marsden, A.L., Vignon-Clementel, I.E., Chan, F.P., Feinstein, J.A., Taylor, C.A., 2007. Effects of exercise and respiration on hemodynamic efficiency in CFD simulations of the total cavopulmonary connection. Annals of Biomedical Engineering 35, 250–263.

Migliavacca, F., Pennati, G., Dubini, G., Fumero, R., Pietrabissa, R., Urcelay, G., Bove, E.L., Hsia, T.Y., de Leval, M.R., 2001. Modeling of the Norwood circulation: effects of shunt size, vascular resistances, and heart rate. American Journal of Physiology: Heart and Circulatory Physiology 280, H2076–H2086.

Noordergraaf, A., Verdouw, D., Boom, H.B., 1963. The use of an analog computer in a circulation model. Progress in Cardiovascular Diseases 5, 419–439.

Pekkan, K., Dasi, L.P., de Zélicourt, D., Sundareswaran, K.S., Fogel, M.A., Kanter, K.R., Yoganathan, A.P., 2009. Hemodynamic performance of stage-2 univentricular reconstruction: Glenn vs. hemi-Fontan templates. Annals of Biomedical Engineering 37, 50–63.

Pekkan, K., Whited, B., Kanter, K., Sharma, S., de Zelicourt, D., Sundareswaran, K., Frakes, D., Rossignac, J., Yoganathan, A.P., 2008. Patient-specific surgical planning and hemodynamic computational fluid dynamics optimization through free-form haptic anatomy editing tool (SURGEM). Medical & Biological Engineering & Computing 46, 1139–1152.

Pennati, G., Fumero, R., 2000. Scaling approach to study the changes through the gestation of human fetal cardiac and circulatory behaviors. Annals of Biomedical Engineering 28, 442–452.

Schievano, S., Migliavacca, F., Coats, L., Khambadkone, S., Carminati, M., Wilson, N., Deanfield, J.E., Bonhoeffer, P., Taylor, A.M., 2007. Percutaneous pulmonary valve implantation based on rapid prototyping of right ventricular outflow tract and pulmonary trunk from MR data. Radiology 242, 490–497.

Snyder, M.F., Rideout, V.C., 1969. Computer simulation studies of the venous circulation. IEEE Transactions on Biomedical Engineering 16, 325–334.

Snyder, M.F., Rideout, V.C., Hillestad, R.J., 1968. Computer modeling of the human systemic arterial tree. Journal of Biomechanics 1, 341–353.

Spilker, R.L., Feinstein, J.A., Parker, D.W., Reddy, V.M., Taylor, C.A., 2007. Morphometry-based impedance boundary conditions for patient-specific modeling of blood flow in pulmonary arteries. Annals of Biomedical Engineering 35, 546–559.

Sundareswaran, K.S., de Zélicourt, D., Sharma, S., Kanter, K.R., Spray, T.L., Rossignac, J., Sotiropoulos, F., Fogel, M.A., Yoganathan, A.P., 2009. Correction of pulmonary arteriovenous malformation using image-based surgical planning. JACC Cardiovascular Imaging 2, 1024–1030.

Taylor, C.A., Hughes, T.J.R., Zarins, C.K., 1998. Finite element modeling of blood flow in arteries. Computer Methods in Applied Mechanics and Engineering 158, 155–196.

Troianowski, G., Taylor, C.A., Feinstein, J.A., Vignon-Clementel, I.E., 2011. Three-dimensional simulations in Glenn patients: clinically based boundary conditions, hemodynamic results and sensitivity to input data. Journal of Biomechanical Engineering 133, 111006.

Vignon-Clementel, I.E., Marsden, A.L., Feinstein, J.A., 2010. A primer on computational simulation in congenital heart disease for the clinician. Progress in Pediatric Cardiology 30, 3–13.

Whitehead, K.K., Pekkan, K., Kitajima, H.D., Paridon, S.M., Yoganathan, A.P., Fogel, M.A., 2007. Nonlinear power loss during exercise in single-ventricle patients after the Fontan: insights from computational fluid dynamics. Circulation 116, I165–I171.

Yang, W., Vignon-Clementel, I.E., Troianowski, G., Reddy, V.M., Feinstein, J.A., Marsden, A.L., 2012. Hepatic blood flow distribution and performance in conventional and novel Y-graft Fontan geometries: a case series computational fluid dynamics study. The Journal of Thoracic and Cardiovascular Surgery 143, 1086–1097.

Bibliography

[ABD+07] A Armillotta, P Bonhoeffer, G Dubini, S Ferragina, F Migliavacca, G Sala, and S Schievano. Use of rapid prototyping models in the planning of percutaneous pulmonary valved stent implantation. *Proceedings of the Institution of Mechanical Engineers, Part H: Journal of Engineering in Medicine*, 221(4):407–416, 2007.

[ACB+] Gregory Arbia, Chiara Corsini, Catriona Baker, Giancarlo Pennati, Tain-Yen Hsia, Irene E Vignon-Clementel, and for MOCHA. Multiscale modeling of pulmonary hemodynamics in first stage single ventricle patients: integrating clinical data and simulations. *submitted*.

[ACEM+14] Gregory Arbia, Chiara Corsini, Mahdi Esmaily Moghadam, Alison L Marsden, Francesco Migliavacca, Giancarlo Pennati, Tain-Yen Hsia, Irene E Vignon-Clementel, , and for MOCHA. Numerical blood flow simulation in surgical corrections: what do we need for an accurate analysis? *Journal of Surgical Research*, 186(1):44–55, 2014.

[AGHVC] G Arbia, J.F. Gerbeau, T.Y. Hsia, and I.E. Vignon-Clementel. A new approach for the outflow boundary conditions in three-dimensional hemodynamics. *in preparation*.

[BC14] Cristóbal Bertoglio and Alfonso Caiazzo. A tangential regularization method for backflow stabilization in hemodynamics. *Journal of Computational Physics*, 261:162–171, 2014.

[BCM+12] Alessia Baretta, Chiara Corsini, Alison L. Marsden, Irene E. Vignon-Clementel, Tain-Yen Hsia, Gabriele Dubini, Francesco Migliavacca, Giancarlo Pennati, and Mocha. Respiratory effects on hemodynamics in patient-specific cfd models of the fontan circulation under exercise conditions. *European Journal of Mechanics B-Fluids*, 35:61–69, 2012.

[BCMO88] C. Begue, C. Conca, F. Murat, and Pironneau O. Les équations de stokes et de navier-stokes avec des conditions aux limites sur la pression. *Seminaire College de France*, 1988.

[BdLM+03] Edward L. Bove, Marc R. de Leval, Francesco Migliavacca, Gualtiero Guadagni, and Gabriele Dubini. Computational fluid dynamics in the evaluation of hemodynamic performance of cavopulmonary connections after the norwood procedure for hypoplastic left heart syndrome. *The Journal of Thoracic and Cardiovascular Surgery*, 126(4):1040 – 1047, 2003.

[BDM13] Pablo J. Blanco, Simone Deparis, and A. Cristiano I. Malossi. On the continuity of mean total normal stress in geometrical multiscale cardiovascular problems. *Journal of Computational Physics*, 251(0):136–155, 2013.

[BF13] P. J. Blanco and R. A. Feijoo. A dimensionally-heterogeneous closed-loop model for the cardiovascular system and its applications. *Medical Engineering and Physics*, 35(5):652–667, 2013.

[BGH+09] Y. Bazilevs, J. R. Gohean, T. J. R. Hughes, R. D. Moser, and Y. Zhang. Patient-specific isogeometric fluid-structure interaction analysis of thoracic aortic blood flow due to implantation of the jarvik 2000 left ventricular assist device. *Computer Methods in Applied Mechanics and Engineering*, 198(45-46):3534–3550, 2009.

[BMG12] Cristobal Bertoglio, Philippe Moireau, and Jean-Frederic Gerbeau. Sequential parameter estimation for fluid–structure problems: Application to hemodynamics. *International Journal for Numerical Methods in Biomedical Engineering*, 28(4):434–455, 2012.

[BNAL05] B. Maury, N. Meunier, A. Soualah, and L. Vial. Outlet dissipative conditions for air flow in the bronchial tree. *ESAIM: Proc.*, 14:201–212, 2005.

[BSD68] J.S. Brody, E.J. Stemmler, and A.B. DuBois. Longitudinal distribution of vascular resistance in the pulmonary arteries, capillaries, and veins. *Journal of Clinical Investigation*, 47:783–799, 1968.

[BWF12] P.J. Blanco, S.M. Watanabe, and R.A. Feijóo. Identification of vascular territory resistances in one-dimensional hemodynamics simulations. *Journal of Biomechanics*, 45(12):2066 – 2073, 2012.

[CBK+13] C. Corsini, C. Baker, E. Kung, S. Schievano, G. Arbia, A. Baretta, G. Biglino, F. Migliavacca, G. Dubini, G. Pennati, A. Marsden, I. Vignon-Clementel, A. Taylor, T.-Y. Hsia, A. Dorfman, and for MOCHA. An integrated approach to patient-specific predictive modeling for single ventricle heart palliation. *Computer Methods in Biomechanics and Biomedical Engineering*, pages 1–18, 2013.

[CGN05] P. Causin, J. F. Gerbeau, and F. Nobile. Added-mass effect in the design of partitioned algorithms for fluid-structure problems. *Computer Methods in Applied Mechanics and Engineering*, 194(42-44):4506–4527, 2005.

[DDA+10] J. R. Dillman, A. L. Dorfman, A. K. Attili, P. P. Agarwal, A. Bell, G. C. Mueller, and R. J. Hernandez. Cardiovascular magnetic resonance imaging of hypoplastic left heart syndrome in children. *Pediatric Radiology*, 40(3):261–274, 2010.

[DeG08] C.G. DeGroff. Modeling the fontan circulation: Where we are and where we need to go. *Pediatric Cardiology*, 29(1):3–12, 2008.

[dLD10] M. R. de Leval and J. E. Deanfield. Four decades of fontan palliation. *Nature Reviews Cardiology*, 7(9):520–527, 2010.

[DO13] TK Dobroserdova and MA Olshanskii. A finite element solver and energy stable coupling for 3d and 1d fluid models. *Computer Methods in Applied Mechanics and Engineering*, 259:166–176, 2013.

[DSMDB+10] G De Santis, P Mortier, M De Beule, P Segers, P Verdonck, and B Verhegghe. Patient-specific computational fluid dynamics: structured mesh generation from coronary angiography. *Medical & Biological Engineering & Computing*, 48(4):371–380, 2010.

[dZMFY10] Diane A de Zélicourt, Alison Marsden, Mark A Fogel, and Ajit P Yoganathan. Imaging and patient-specific simulations for the fontan surgery: Current methodologies and clinical applications. *Progress in Pediatric Cardiology*, 30(1):31–44, 2010.

[FGNQ01] L. Formaggia, J.F. Gerbeau, F. Nobile, and A. Quarteroni. On the coupling of 3d and 1d navier-stokes equations for flow

problems in compliant vessels. *Computer Methods in Applied Mechanics and Engineering*, 191(6-7):561–582, 2001.

[FI14] Justine Fouchet-Incaux. Artificial boundaries and formulations for the incompressible Navier–Stokes equations: applications to air and blood flows. *SeMA Journal*, 64(1):1–40, 2014.

[FMN07] L. Formaggia, A. Moura, and F. Nobile. On the stability of the coupling of 3d and 1d fluid-structure interaction models for blood flow simulations. *ESAIM: Mathematical Modelling and Numerical Analysis*, 41:743–769, 7 2007.

[FQV13] L. Formaggia, A. Quarteroni, and C. Vergara. On the physical consistency between three-dimensional and one-dimensional models in haemodynamics. *Journal of Computational Physics*, 244:97–112, 2013.

[FVCJ+06] C. A. Figueroa, I. E. Vignon-Clementel, K. E. Jansen, T. J. R. Hughes, and C. A. Taylor. A coupled momentum method for modeling blood flow in three-dimensional deformable arteries. *Computer Methods in Applied Mechanics and Engineering*, 195(41-43):5685–5706, 2006.

[GCY+12] V. Gravemeier, A. Comerford, L. Yoshihara, M. Ismail, and W. A. Wall. A novel formulation for neumann inflow boundary conditions in biomechanics. *International Journal for Numerical Methods in Biomedical Engineering*, 28(5):560–573, 2012.

[GLT+06] Joan M. Greve, Andrea S. Les, Beverly T. Tang, Mary T. Draney Blomme, Nathan M. Wilson, Ronald L. Dalman, Norbert J. Pelc, and Charles A. Taylor. Allometric scaling of wall shear stress from mice to humans: quantification using cine phase-contrast mri and computational fluid dynamics. *American Journal of Physiology-Heart and Circulatory Physiology*, 291(4):H1700–H1708, 2006.

[GMC+13] Romain Guibert, Kristin Mcleod, Alfonso Caiazzo, Tommaso Mansi, Miguel Ángel Fernández, Maxime Sermesant, Xavier Pennec, Irene Vignon-Clementel, Younes Boudjemline, and Jean-Frédéric Gerbeau. Group-wise Construction of Reduced Models for Understanding and Characterization of Pulmonary Blood Flows from Medical Images. *Medical Image Analysis*, 18(1):63–82, October 2013.

[GR09] Christophe Geuzaine and Jean-Francois Remacle. Gmsh: A 3-d finite element mesh generator with built-in pre- and post-processing facilities. *International Journal for Numerical Methods in Engineering*, 79(11):1309–1331, 2009.

[GSE98] P. M. Gresho, R. L. Sani, and M. S. Engelman. *Incompressible Flow and the Finite Element Method.* John Wiley & Sons, 1998.

[GZ07] Baskar Ganapathysubramanian and Nicholas Zabaras. Sparse grid collocation schemes for stochastic natural convection problems. *J. Comput. Phys.*, 225(1):652–685, July 2007.

[HCC+11] Tain-Yen Hsia, Daria Cosentino, Chiara Corsini, Giancarlo Pennati, Gabriele Dubini, Francesco Migliavacca, and Hearts Modeling Congenital. Use of mathematical modeling to compare and predict hemodynamic effects between hybrid and surgical norwood palliations for hypoplastic left heart syndrome. *Circulation*, 124(11):S204–S210, 2011.

[HRT96] J. G. Heywood, R. Rannacher, and S. Turek. Artificial boundaries and flux and pressure conditions for the incompressible navier-stokes equations. *International Journal for Numerical Methods in Fluids*, 22(5):325–352, 1996.

[IE06] Vignon-Clementel IE. *A Coupled Multidomain Method for Computational Modeling of Blood Flow.* PhD thesis, Stanford, 2006.

[IGCW14] M Ismail, V Gravemeier, A Comerford, and WA Wall. A stable approach for coupling multidimensional cardiovascular and pulmonary networks based on a novel pressure-flow rate or pressure-only neumann boundary condition formulation. *International Journal For Numerical Methods in Biomedical Engineering*, 30(4):447–469, 2014.

[IWG13] M. Ismail, W. A. Wall, and M. W. Gee. Adjoint-based inverse analysis of windkessel parameters for patient-specific vascular models. *Journal of Computational Physics*, 244:113–130, 2013.

[KBB+13] E. Kung, A. Baretta, C. Baker, G. Arbia, G. Biglino, C. Corsini, S. Schievano, I. E. Vignon-Clementel, G. Dubini, G. Pennati, A. Taylor, A. Dorfman, A. M. Hlavacek, A. L. Marsden, T.-Y. Hsia, F. Migliavacca, and for MOCHA. Predictive modeling of

the virtual hemi-fontan operation for second stage single ventricle palliation: Two patient-specific cases. *Journal of Biomechanics*, 46(2):423 – 429, 2013.

[KED+11] Bon-Kwon Koo, Andrejs Erglis, Joon-Hyung Doh, David V. Daniels, Sanda Jegere, Hyo-Soo Kim, Allison Dunning, Tony DeFrance, Alexandra Lansky, Jonathan Leipsic, and James K. Min. Diagnosis of ischemia-causing coronary stenoses by noninvasive fractional flow reserve computed from coronary computed tomographic angiograms results from the prospective multicenter discover-flow (diagnosis of ischemia-causing stenoses obtained via noninvasive fractional flow reserve) study. *Journal of the American College of Cardiology*, 58(19):1989–1997, 2011.

[KKC+13] A. P. Kuprat, S. Kabilan, J. P. Carson, R. A. Corley, and D. R. Einstein. A bidirectional coupling procedure applied to multiscale respiratory modeling. *Multi-scale Modeling and Simulation of Biological Systems*, 244(0):148–167, 2013.

[Kli06] Andreas Klimke. *Uncertainty modeling using fuzzy arithmetic and sparse grids*. PhD thesis, Universit "at Stuttgart, Shaker Verlag, Aachen, 2006.

[Kli07] Andreas Klimke. Sparse Grid Interpolation Toolbox – user's guide. Technical Report IANS report 2007/017, University of Stuttgart, 2007.

[KOS+13] V. O. Kheyfets, W. O'Dell, T. Smith, J. J. Reilly, and E. A. Finol. Considerations for numerical modeling of the pulmonary circulation–a review with a focus on pulmonary hypertension. *Journal of biomechanical engineering*, 135(6):61011–15, 2013.

[KVCC+10] H. J. Kim, I. E. Vignon-Clementel, J. S. Coogan, C. A. Figueroa, K. E. Jansen, and C. A. Taylor. Patient-specific modeling of blood flow and pressure in human coronary arteries. *Annals of Biomedical Engineering*, 38(10):3195–3209, 2010.

[KVCF+10] H. J. Kim, I. E. Vignon-Clementel, C. A. Figueroa, K. E. Jansen, and C. A. Taylor. Developing computational methods for three-dimensional finite element simulations of coronary blood flow. *Finite Elements in Analysis and Design*, 46(6):514–525, 2010.

[LBB10] Jorge S. Leiva, Pablo J. Blanco, and Gustavo C. Buscaglia. Iterative strong coupling of dimensionally heterogeneous models. *International Journal for Numerical Methods in Engineering*, 81(12):1558–1580, 2010.

[LBMdW12] P. Luijendijk, S. M. Boekholdt, B. J. M. Mulder, and R. J. de Winter. Percutaneous treatment of native aortic coarctation in adults. *Netherlands Heart Journal*, 20(7-8):339–340, 2012.

[LDF+11] Jr. LaDisa, John F., Ronak J. Dholakia, C. Alberto Figueroa, Irene E. Vignon-Clementel, Frandics P. Chan, Margaret M. Samyn, Joseph R. Cava, Charles A. Taylor, and Jeffrey A. Feinstein. Computational simulations demonstrate altered wall shear stress in aortic coarctation patients treated by resection with end-to-end anastomosis. *Congenital Heart Disease*, 6(5):432–443, 2011.

[LDM+02] K. Lagana, G. Dubini, F. Migliavacca, R. Pietrabissa, G. Pennati, A. Veneziani, and A. Quarteroni. Multiscale modelling as a tool to prescribe realistic boundary conditions for the study of surgical procedures. *Biorheology*, 39(3-4):359–364, 2002.

[LSF+10] Andrea S. Les, Shawn C. Shadden, C. Alberto Figueroa, Jinha M. Park, Maureen M. Tedesco, Robert J. Herfkens, Ronald L. Dalman, and Charles A. Taylor. Quantification of hemodynamics in abdominal aortic aneurysms during rest and exercise using magnetic resonance imaging and computational fluid dynamics. *Annals of Biomedical Engineering*, 38(4):1288–1313, 2010.

[MBDQ11] A. Cristiano I. Malossi, Pablo J. Blanco, Simone Deparis, and Alfio Quarteroni. Algorithms for the partitioned solution of weakly coupled fluid models for cardiovascular flows. *International Journal for Numerical Methods in Biomedical Engineering*, 27(12):2035–2057, 2011.

[MBH+11] M. E. Moghadam, Y. Bazilevs, T. Y. Hsia, I. E. Vignon-Clementel, A. L. Marsden, and Allianc Modeling Congenital Hearts. A comparison of outlet boundary treatments for prevention of backflow divergence with relevance to blood flow simulations. *Computational Mechanics*, 48(3):277–291, 2011.

[MBP+06] F. Migliavacca, R. Balossino, G. Pennati, G. Dubini, T. Y. Hsia, M. R. de Leval, and E. L. Bove. Multiscale modelling in

biofluidynamics: Application to reconstructive paediatric cardiac surgery. *Journal of Biomechanics*, 39(6):1010–1020, 2006.

[MBX+13] P. Moireau, C. Bertoglio, N. Xiao, C. A. Figueroa, C. A. Taylor, D. Chapelle, and J. F. Gerbeau. Sequential identification of boundary support parameters in a fluid-structure vascular model using patient image data. *Biomechanics and Modeling in Mechanobiology*, 12(3):475–496, 2013.

[MKV+11] H. G. Morales, M. Kim, E. E. Vivas, M. C. Villa-Uriol, I. Larrabide, T. Sola, L. Guimaraens, and A. F. Frangi. How do coil configuration and packing density influence intraaneurysmal hemodynamics? *American Journal of Neuroradiology*, 32(10):1935–1941, 2011.

[MMVC+12] Mahdi Esmaily Moghadam, Francesco Migliavacca, Irene E. Vignon-Clementel, Tain-Yen Hsia, Alison L. Marsden, and Allianc Modeling Congenital Hearts. Optimization of shunt placement for the norwood surgery using multi-domain modeling. *Journal of Biomechanical Engineering-Transactions of the Asme*, 134(5), 2012.

[MPD+01] Francesco Migliavacca, Giancarlo Pennati, Gabriele Dubini, Roberto Fumero, Riccardo Pietrabissa, Gonzalo Urcelay, Edward L. Bove, Tain-Yen Hsia, and Marc R. de Leval. Modeling of the norwood circulation: effects of shunt size, vascular resistances, and heart rate. *American Journal of Physiology - Heart and Circulatory Physiology*, 280(5):H2076–H2086, 2001.

[MSL+05] J. Muller, O. Sahni, X. Li, K. E. Jansen, M. S. Shephard, and C. A. Taylor. Anisotropic adaptive finite element method for modelling blood flow. *Computer Methods in Biomechanics and Biomedical Engineering*, 8(5):295–305, 2005.

[MVCC+07] A. L. Marsden, I. E. Vignon-Clementel, F. P. Chan, J. A. Feinstein, and C. A. Taylor. Effects of exercise and respiration on hemodynamic efficiency in cfd simulations of the total cavopulmonary connection. *Annals of Biomedical Engineering*, 35(2):250–263, 2007.

[MVCF+13] Mahdi Esmaily Moghadam, Irene E. Vignon-Clementel, Richard Figliola, Alison L. Marsden, and Allianc Modeling Congenital Hearts. A modular numerical method for implicit

0d/3d coupling in cardiovascular finite element simulations. *Journal of Computational Physics*, 244:63–79, 2013.

[NLCC81] W. I. Norwood, P. Lang, A. R. Casteneda, and D. N. Campbell. Experience with operations for hypoplastic left heart syndrome. *The Journal of thoracic and cardiovascular surgery*, 82(4):511–9, 1981.

[OKP95] John N. Oshinski, David N. Ku, and Roderic I. Pettigrew. Turbulent fluctuation velocity: The most significant determinant of signal loss in stenotic vessels. *Magnetic Resonance in Medicine*, 33(2):193–199, 1995.

[OLFH96] C.E. O Leary, R. Fiori, and T.S. Hakim. Perioperative distribution of pulmonary vascular resistance in patients undergoing coronary artery surgery. *Anesthesia and analgesia*, 82:958–963, 1996.

[OMG+14] Jessica Oakes, Alison Marsden, L., Celine Grandmont, Shawn Shadden, C., Chantal Darquenne, and Irene Vignon-Clementel. Airflow and Particle Deposition Simulations in Health and Emphysema: From In Vivo to In Silico Animal Experiments. *Annals of Biomedical Engineering*, 42(4):899–914, April 2014.

[OTT+12] M. Oshima, R. Torii, S. Tokuda, S. Yamada, and A. Koizumi. Patient-specific modeling and multi-scale blood simulation for computational hemodynamic study on the human cerebrovascular system. *Current Pharmaceutical Biotechnology*, 13(11):2153–2165, 2012.

[PAH+98] R.G. Presson, S.H. Audi, C.C. Hanger, G.M. Zenk, R.A. Sidner, J.H. Linehan, and Dawson C.A. Wagner, W.W. Anatomic distribution of pulmonary vascular compliance. *Journal of Applied Physiology*, 84:303–310, 1998.

[PCC+11] G. Pennati, C. Corsini, D. Cosentino, T.-Y. Hsia, V. S. Luisi, G. Dubini, and F. Migliavacca. Boundary conditions of patient-specific fluid dynamics modelling of cavopulmonary connections: possible adaptation of pulmonary resistances results in a critical issue for a virtual surgical planning. *Interface Focus*, 1(3):297–307, 2011.

[PDZG+05] K. Pekkan, D. De Zelicourt, L. Ge, F. Sotiropoulos, D. Frakes, M. A. Fogel, and A. P. Yoganathan. Physics-driven cfd modeling of complex anatomical cardiovascular flows - a tcpc case study. *Annals of Biomedical Engineering*, 33(3):284–300, 2005.

[PFGVC14] Sanjay Pant, Benoit Fabrèges, Jean-Frédéric Gerbeau, and IreneE. Vignon-Clementel. A multiscale filtering-based parameter estimation method for patient-specific coarctation simulations in rest and exercise. In Oscar Camara, Tommaso Mansi, Mihaela Pop, Kawal Rhode, Maxime Sermesant, and Alistair Young, editors, *Statistical Atlases and Computational Models of the Heart. Imaging and Modelling Challenges*, volume 8330 of *Lecture Notes in Computer Science*, pages 102–109. Springer Berlin Heidelberg, 2014.

[PLCB11] Sanjay Pant, Georges Limbert, Nick P. Curzen, and Neil W. Bressloff. Multiobjective design optimisation of coronary stents. *Biomaterials*, 32(31):7755–7773, 2011.

[PTG+11] Anamika Prasad, Lillian K. To, Madhu L. Gorrepati, Christopher K. Zarins, and C. Alberto Figueroa. Computational analysis of stresses acting on intermodular junctions in thoracic aortic endografts. *Journal of Endovascular Therapy*, 18(4):559–568, 2011.

[PZVP12] A. Porpora, P. Zunino, C. Vergara, and M. Piccinelli. Numerical treatment of boundary conditions to replace lateral branches in hemodynamics. *International Journal for Numerical Methods in Biomedical Engineering*, 28(12):1165–1183, 2012.

[QLI+10] Y. Qian, J.L. Liu, K. Itatani, K. Miyaji, and M. Umezu. Computational hemodynamic analysis in congenital heart disease: Simulation of the norwood procedure. *Annals of Biomedical Engineering*, 38(7):2302–2313, 2010.

[RAC+08] A. G. Radaellia, L. Augsburger, J. R. Cebral, M. Ohta, D. A. Ruefenacht, R. Balossino, G. Benndorf, D. R. Hose, A. Marzo, R. Metcalfe, P. Mortier, F. Mut, P. Reymond, L. Socci, B. Verhegghe, and A. F. Frangi. Reproducibility of haemodynamical simulations in a subject-specific stented aneurysm model - a report on the virtual intracranial stenting challenge 2007. *Journal of Biomechanics*, 41(10):2069–2081, 2008.

[SDS+08] J. P. Schmidt, S. L. Delp, M. A. Sherman, C. A. Taylor, V. S. Pande, and R. B. Altman. The simbios national center: Systems biology in motion. *Proc IEEE Inst Electr Electron Eng*, 96(8):1266, 2008.

[SFP+07] RyanL. Spilker, JeffreyA. Feinstein, DavidW. Parker, V.Mohan Reddy, and CharlesA. Taylor. Morphometry-based impedance boundary conditions for patient-specific modeling of blood flow in pulmonary arteries. *Annals of Biomedical Engineering*, 35(4):546–559, 2007.

[SHF+13] David A. Steinman, Yiemeng Hoi, Paul Fahy, Liam Morris, Michael T. Walsh, Nicolas Aristokleous, Andreas S. Anayiotos, Yannis Papaharilaou, Amirhossein Arzani, Shawn C. Shadden, Philipp Berg, Gabor Janiga, Joris Bols, Patrick Segers, Neil W. Bressloff, Merih Cibis, Frank H. Gijsen, Salvatore Cito, Jordi Pallares, Leonard D. Browne, Jennifer A. Costelloe, Adrian G. Lynch, Joris Degroote, Jan Vierendeels, Wenyu Fu, Aike Qiao, Simona Hodis, David F. Kallmes, Hardeep Kalsi, Quan Long, Vitaly O. Kheyfets, Ender A. Finol, Kenichi Kono, Adel M. Malek, Alexandra Lauric, Prahlad G. Menon, Kerem Pekkan, Mahdi Esmaily Moghadam, Alison L. Marsden, Marie Oshima, Kengo Katagiri, Veronique Peiffer, Yumnah Mohamied, Spencer J. Sherwin, Jens Schaller, Leonid Goubergrits, Gabriel Usera, Mariana Mendina, Kristian Valen-Sendstad, Damiaan F. Habets, Jianping Xiang, Hui Meng, Yue Yu, George E. Karniadakis, Nicholas Shaffer, and Francis Loth. Variability of computational fluid dynamics solutions for pressure and flow in a giant aneurysm: The asme 2012 summer bioengineering conference cfd challenge. *Journal of Biomechanical Engineering-Transactions of the Asme*, 135(2), 2013.

[SMC+07] Silvia Schievano, Francesco Migliavacca, Louise Coats, Sachin Khambadkone, Mario Carminati, Neil Wilson, John E. Deanfield, Philipp Bonhoeffer, and Andrew M. Taylor. Percutaneous pulmonary valve implantation based on rapid prototyping of right ventricular outflow tract and pulmonary trunk from mr data. *Radiology*, 242(2):490–497, 2007.

[SMJ+06] O. Sahni, J. Muller, K. Jansen, M. Shephard, and C. Taylor. Efficient anisotropic adaptive discretization of the cardiovascular system. *Computer Methods in Applied Mechanics and Engineering*, 195:5634–5655, August 2006.

[SPB+12] SandyF C. Stewart, EricG Paterson, GregW Burgreen, Prasanna Hariharan, Matthew Giarra, Varun Reddy, StevenW Day, KeefeB Manning, Steven Deutsch, MichaelR Berman, MatthewR Myers, and RichardA Malinauskas. Assessment of cfd performance in simulations of an idealized medical device: Results of fda s first computational interlaboratory study. *Cardiovascular Engineering and Technology*, 3(2):139–160, 2012.

[ST10] RyanL. Spilker and CharlesA. Taylor. Tuning multidomain hemodynamic simulations to match physiological measurements. *Annals of Biomedical Engineering*, 38(8):2635–2648, 2010.

[SY76] B.D. Seeley and D.F. Young. Effect of geometry on pressure losses across models of arterial stenoses. *Journal of Biomechanics*, 9(7):439 – 448, 1976.

[TF09] C. A. Taylor and C. A. Figueroa. *Patient-Specific Modeling of Cardiovascular Mechanics*, volume 11 of *Annual Review of Biomedical Engineering*, pages 109–134. Annual Reviews, Palo Alto, 2009.

[TO12] Ryo Torii and Marie Oshima. An integrated geometric modelling framework for patient-specific computational haemodynamic study on wide-ranged vascular network. *Computer Methods in Biomechanics and Biomedical Engineering*, 15(6):615–625, 2012.

[TTFVC11] Guillaume Troianowski, Charles A Taylor, Jeffrey A Feinstein, and Irene E Vignon-Clementel. Three-dimensional simulations in glenn patients: clinically based boundary conditions, hemodynamic results and sensitivity to input data. *Journal of Biomechanical Engineering*, 133:111006, 2011.

[VCFJT06] I. E. Vignon-Clementel, C. A. Figueroa, K. E. Jansen, and C. A. Taylor. Outflow boundary conditions for three-dimensional finite element modeling of blood flow and pressure in arteries. *Computer Methods in Applied Mechanics and Engineering*, 195(29-32):3776–3796, 2006.

[VCFJT10] I. E. Vignon-Clementel, C. A. Figueroa, K. E. Jansen, and C. A. Taylor. Outflow boundary conditions for 3d simulations of non-periodic blood flow and pressure fields in deformable

arteries. *Computer Methods in Biomechanics and Biomedical Engineering*, 13(5):625–640, 2010.

[VCMF10] Irene E Vignon-Clementel, Alison L Marsden, and Jeffrey A Feinstein. A primer on computational simulation in congenital heart disease for the clinician. *Progress in Pediatric Cardiology*, 30(1):3–13, 2010.

[YCS+88] A. P. Yoganathan, E. G. Cape, H. W. Sung, F. P. Williams, and A. Jimoh. Review of hydrodynamic principles for the cardiologist: applications to the study of blood flow and jets by imaging techniques. *Journal of the American College of Cardiology*, 12(5):1344–53, 1988.

[YFS+13] Weiguang Yang, Jeffrey A. Feinstein, Shawn C. Shadden, Irene E. Vignon-Clementel, and Alison L. Marsden. Optimization of a y-graft design for improved hepatic flow distribution in the fontan circulation. *Journal of Biomechanical Engineering-Transactions of the Asme*, 135(1), 2013.

[YKA+06] Janice J. Yeung, Hyun Jin Kim, Thomas A. Abbruzzese, Irene E. Vignon-Clementel, Mary T. Draney-Blomme, Kay K. Yeung, Inder Perkash, Robert J. Herfkens, Charles A. Taylor, and Ronald L. Dalman. Aortoiliac hemodynamic and morphologic adaptation to chronic spinal cord injury. *Journal of Vascular Surgery*, 44(6):1254–1265, 2006.

[YVCT+12] Weiguang Yang, Irene E. Vignon-Clementel, Guillaume Troianowski, V. Mohan Reddy, Jeffrey A. Feinstein, and Alison L. Marsden. Hepatic blood flow distribution and performance in conventional and novel y-graft fontan geometries: A case series computational fluid dynamics study. *Journal of Thoracic and Cardiovascular Surgery*, 143(5):1086–1097, 2012.